UAB

Universitat Autònoma de Barcelona

On the road to improve glioblastoma therapy follow-up. Immune microenvironment: what is behind the MRSI-based nosological images?

Mª Pilar Calero Pérez

Ph.D Thesis

Universitat Autònoma de Barcelona

UAB

Universitat Autònoma
de Barcelona

Department of Biochemistry and Molecular Biology

Doctoral thesis

On the road to improve glioblastoma therapy follow-up. Immune microenvironment: what is behind the MRSI-based nosological images?

Mª Pilar Calero Pérez

2022

TABLE OF CONTENTS

INDEX OF FIGURES

INDEX OF TABLES

ABBREVIATION LIST

^{1}H	Hydrogen (also, Proton, nucleus of hydrogen)
3DiCSI	3D Interactive Chemical Shift Imaging
ADAMs	A Disintegrin and Metalloprotease
AIC	5-aminoimidazole-4-carboxamide
Ala	Alanine
APCs	Antigen presenting cells
AS	Surface area
BBB	Blood-brain barrier
BTDP	Below threshold detection period
CA	Contrast agent
CD206	Mannose receptor C type 1 gene
CD247	Programmed cell death-1 ligand 1 PD-L1 gene
Cho	Choline
CIBER	*Centro de Investigación Biomédica en Red*
CNS	Central Nervous System
CPA	Cyclophosphamide
Cr	Creatine
CRT	Calreticulin
CSF-1	Colony-stimulating factor 1
CT	Computer tomography
Ct	Cycle time
CTLA-4	Cytotoxic T-lymphocyte Antigen 4
DAMPs	Damage-associated molecular patterns
DCs	Dendritic cells
DDR	DNA damage repair
DMPM	Dynamic MRSI processing module
DMSO	Dimethyl sulfoxide
DN	Double-negative cells
DNA	Deoxyribonucleic acid
EDTA	Ethylenediaminetetraacetic acid

EGF	Epidermal growth factor
ETL	Echo time length
F4/80	EGF-like module containing mucin-like hormone receptor-like 1 gene
FasL	Fas ligand
FASTMAP	Fast Automatic Shimming Technique by Mapping Along Projections
FOV	Field of View
FoxP3	Forkhead box P3
GABRMN	*Grup d'Aplicacions Biomèdiques de la Ressonància Magnètica Nuclear*
GAMs	Glioma-associated microglia/macrophages
GB	Glioblastoma
GEM	Genetically engineered mice
Gln	Glutamine
Glu	Glutamate
Gly	Glycine
GM-CSF	Granulocyte Macrophage Colony-Stimulating Factor
Gy	Gray
HIF	Hypoxia-inducible factor
HMGB1	High Mobility Group Box 1
HTRP	Hypoxanthine guanine phosphoribosyl transferase gene
HVR	Hypervariable region
ICD	Immunogenic cell damage/death
IFN-γ	Interferon-γ
IL	Interleukin
IMS	Immune-Enhancing Metronomic Schedule
IS	Immune System
IT	Inter-slice thickness
Lac	Lactate
M1 GAMs	Anti-tumour glioma-associated microglia/macrophages
M2 GAMs	Pro-tumour glioma-associated microglia/macrophages
MCP-1	Monocyte Chemoattractant Protein-1
MDSCs	Myeloid-derived suppressor cells

MGMT	O6-methylguanine-DNA- methyltransferase
MHC	Major histocompatibility complex
mI	Myo-inositol
MLs	Mobile lipids
MM	Macromolecules
MR	Magnetic resonance
MRI	Magnetic resonance imaging
MRS	Magnetic resonance spectroscopy
MRSI	Magnetic resonance spectroscopic imaging
MTD	Maximum tolerated dose
MTIC	5-(3-methyltriazen-1-yl)-imidazole-4-carboxamide
MTX	Matrix size
NA	Number of averages
NAA	N-acetyl aspartate
NKs	Natural Killer cells
NMF	Non-negative matrix factorization
NMR	Nuclear magnetic resonance
Nos2	Inducible NO synthase gene
NS	Number of slices
O6-meG	O6-methyl-guanine
PBS	Phosphate buffered saline
PCr	Phosphocreatine
PD	Progressive disease
PD-1	Programmed cell death 1 receptor
PD-L1	Programmed cell death-1 ligand 1
PDX	Patient-derived xenografts
PET	Positron Emission Tomography
p.i.	Post-inoculation
ppm	Part per million
PR	Pattern recognition
PRe	Partial response

PRESS	Point-resolved spectroscopy
PUFAs	Polyunsaturated fatty acids
PVDF	Polyvinylidene fluoride
RANO	Response assessment in neuro-oncology
RARE	Rapid acquisition with relaxation enhancement
RECIST	Response Evaluation Criteria in Solid Tumours
RNA	Ribonucleic acid
ROI	Region of interest
RPMI	Roswell Park Memorial Institute
RT	Radiotherapy
rt-PCR	Real-time polymerase chain reaction
SDi	Stable disease
SDS-PAGE	Sodium dodecyl sulphate-polyacrylamide gel electrophoresis
sIL-6R	Soluble IL-6 receptor
sPD-L1	Soluble PD-L1
ST	Slice thickness
STR	Short tandem repeat
SW	Sweep width
T_1	Longitudinal relaxion time
T_2	Transverse relaxation time
T_1w	T_1-weighted image
T_2w	T_2-weighted image
TAT	Total acquisition time
TBP	Tata binding protein gene
TCR	T cell receptor
Tc	Cytotoxic T lymphocyte
TE	Echo time
TE_{eff}	Effective echo time
Th	Helper T lymphocyte
TME	Tumour microenvironment
TMZ	Temozolomide

TNF-α	Tumour necrosis factor-α
TNF-R1	Tumour Necrosis Factor Receptor 1
TLR	Toll-like receptors
Treg	Regulatory T lymphocyte
TR	Repetition time
TRI	Tumour responding index
TV	Tumour volume
UAB	*Universitat Autònoma de Barcelona*
UMR	Philipps University Marburg
VAPOR	Variable Power and Optimized Relaxation Delay
VOI	Volume of interest
WB	Western blot
WHO	World Health Organization
wt	Wild type
XS13	Acidic ribosomal protein RPLP0 gene

LIST OF PAPERS INCLUDED IN THIS THESIS:

1. Wu, S.; Calero-Pérez, P.; Villamañan, L.; Arias-Ramos, N.; Pumarola, M.; Ortega-Martorell, S.; Julià-Sapé, M.; Arús, C.; Candiota, A.P. Anti-tumour immune response in GL261 glioblastoma generated by Temozolomide Immune-Enhancing Metronomic Schedule monitored with MRSI-based nosological images. NMR Biomed. 2020, 33, e4229. doi:10.1002/nbm.4229. https://pubmed.ncbi.nlm.nih.gov/31926117/

2. Calero-Pérez, P.; Wu, S.; Arús, C.; Candiota, A.P. Immune system-related changes in preclinical GL261 glioblastoma under TMZ treatment: explaining MRSI-based nosological imaging findings with RT-PCR analyses. Cancers 2021, 13, 2363. doi:10.3390/cancers13112663. https://pubmed.ncbi.nlm.nih.gov/34071393/

The experimental work described in this PhD thesis was performed at the Biomedical Applications of Magnetic Resonance research group (GABRMN) at the *Universitat Autònoma de Barcelona* (UAB), except by the experimental part carried out during my research stage at the Department of Neurosurgery, Philipps University Marburg (UMR, Germany) under the supervision of Prof. Dr. Jörg-Walter Bartsch.

1. INTRODUCTION

1.1. GLIOMA

1.1.1. Epidemiology and classification

Tumours of the Central Nervous System (CNS) comprise less than 2% of all cases diagnosed in the year 2020 worldwide. Still, due to their poor prognosis, they are responsible for a mortality rate of 2.8% of all cancer patients [1]. Despite the low mortality, tumours of the CNS lead to quality of life losses and shorten patients' life (18.4 years of life lost on average)[2]. Among all primary brain tumours, gliomas account for almost 30% of the total. Furthermore, gliomas represent ca. 80% of all malignant tumours, being responsible for the majority of deaths due to primary brain tumours [3]. The average annual incidence of glioma was 5.26 per 100,000 people (Figure 1.1. Worldwide estimated age-standardised incidence rates of malignant brain tumours in 2020 *(Global Cancers Observatory: https://gco.iarc.fr/)*.Figure 1.1) or 17,000 new diagnoses per year during the years between 2000 and 2013 [4].

Estimated age-standardized incidence rates (World) in 2020, brain, central nervous system, both sexes, all ages
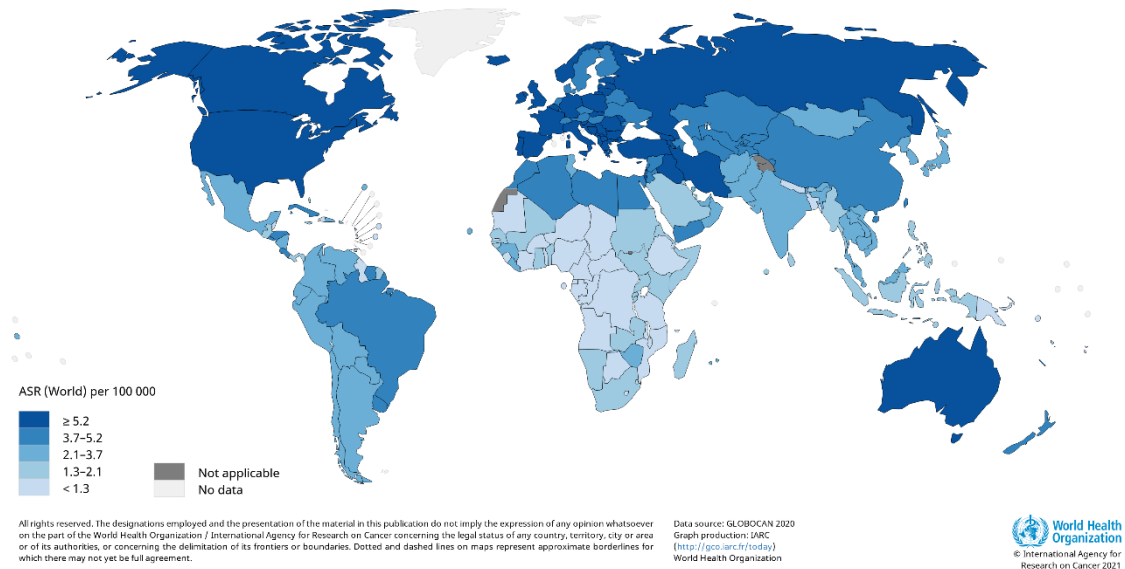
Figure 1.1. Worldwide estimated age-standardised incidence rates of malignant brain tumours in 2020 (Global Cancers Observatory: https://gco.iarc.fr/).

Gliomas originate from either mature glia or their less differentiated precursors which infiltrate the surrounding brain tissue [5]. The fifth edition of the World Health Organization Classification of Tumours of the CNS (WHO CNS5), published in 2021, classify brain and spinal cord tumours according to histological, immunohistochemical, and molecular findings, assigning grades 1-4. This classification indicates different degrees of malignancy, with WHO grade 1 showing the least malignant behaviour and WHO grade 4 indicating the most malignant behaviour [6].

Glioblastoma (GB) is the most fatal and frequently occurring type of primary astrocytoma, representing approximately 57% of all gliomas and 48% of all primary malignant CNS tumours [7,8], and has been designated Grade 4 by WHO [6]. GBs are included within the classification of adult-type diffuse gliomas, and present characteristic histology and genes/molecules that are key for diagnoses, such as microvascular proliferation or necrosis, Isocitrate Dehydrogenase wildtype gene, Telomerase Reverse Transcriptase promoter mutation, or Epidermal Growth Factor (EGF) Receptor gene amplification or +7/−10 chromosome copy number changes (combined whole chromosome 7 gain and whole chromosome 10 loss) [9]. Conversely, the IDH-mutant gene is present in that GBs that arises from a precursor diffuse or anaplastic astrocytoma, typically called secondary GBs, which represents approximately 10% of GBs tumours and generally carries a better prognosis [10].

Due to its heterogeneity, infiltrative nature, hypoxic tumour environment, presence of resistant cancer stem cells, and immunosuppressive microenvironment and despite application of aggressive standard of care therapeutic options such as surgery, radiation, and chemotherapy, GB patients present a median survival of less than 15 months, and the 5-year survival rate is less than 10% [11]. The complexity of the GB landscape reveals the need of constant investigation and improvement regarding therapeutic advancements [12].

1.1.2. GB diagnosis and follow-up

The detection of brain tumours occurs by the time they become symptomatic, and an imaging-based study is performed, since their growth is mostly silent until symptoms appear. GBs grow locally and, even being extremely invasive, rarely metastasize outside of the CNS. The clinical symptoms depend on the tumour location and size at diagnosis, being the most common headache and/or nausea when there is a large mass or significant edema, followed by symptoms related to intracranial hypertension (presented by 30% of patients), motor deficit (20%), epilepsy (15–20%), loss of body weight and condition (17%), confusion (15%) and visual or speech difficulties (13%) [13]. The initial assessment, localization and tentative diagnosis of brain tumours are based in non-invasive imaging approaches such as Magnetic Resonance Imaging (MRI), Computed Tomography (CT) and Positron Emission Tomography (PET). However, the definitive diagnosis in general requires the gold standard procedure, histopathological analysis from a tumour biopsy (taken from a stereotactic biopsy or surgical sample, depending on the case). This information may be also useful to gather molecular/cellular information from a given tumour, which may help in therapeutic decisions in some cases.

1.1.3. GB therapy

The current standard treatment used in clinical practice for GB patients consists of surgery, followed by radiotherapy (RT) plus temozolomide (TMZ) chemotherapy, followed by adjuvant TMZ chemotherapy. Even after aggressive therapy, the prognosis of patients with GB remains poor [14] and this standard clinical protocol has remained essentially the same for decades.

Developing novel therapeutic approaches and follow up methods is needed to improve the prognosis for GB patients. A comprehensive review of novel therapeutic approaches is described in [12], but only discrete, often non-significant, therapeutic improvements have been achieved. More details about the therapeutic standards of care are described below:

1.1.3.1. Surgery

Nowadays, surgery is the principal and the most effective component of standard care for GB patients, with the aim of maximal or supramaximal resection for mass reduction, while preserving neurological functions [15]. Its performance depends on the extent of resection, which is in turn determined by the site and eloquence of the brain area involved. In addition to the mentioned reduction in tumour volume, surgery also allows for accurate histological diagnosis and tumour genotyping that can determine subsequent therapy [10]. Surgical resection leads to prolonged survival and improves the quality of life of GB patients [15]. However, the infiltrative features of GB tumours make it difficult its complete resection. Consequently, the relapse occurs in approximately 80% of cases usually in the areas near to the original lesion [11]. Surgery is usually followed by RT and/or chemotherapy in an attempt to eradicate remaining tumour cells.

1.1.3.2. Radiotherapy

Following maximal safe resection, radio-chemotherapy is usually applied in GB patients in order to improve survival. Currently, conventional RT includes fractionated doses to a total of 60 Gy delivered in 30 to 33 fractions over a period of approximately 6 weeks [16]. Radiation is typically delivered to the gross tumour volume with an additional 2-3 cm surrounding margin to treat the infiltrating tumour, based on the observation that, following RT, GB recurs within 2 cm of the original tumour site in 80% – 90% of cases [17]. In addition to the direct effects of radiation, inducing deoxyribonucleic acid (DNA) damage and killing of tumour cells, RT can render cancer cells visible to the immune system through the expression of inflammatory and immunostimulatory mediators that modify the tumour microenvironment (TME), leading to improvement of patient's survival [18,19]. However, cancer stem cells play a relevant role in tumour resistance to RT [20,21] probably due to their plasticity and interactions with TME and their niches. This could be one of the challenges to face with the present therapeutic approaches, leading to GB relapse and patient death.

1.1.3.3. Chemotherapy – Temozolomide

Chemotherapeutic approaches in general induce death/proliferation arrest in cancer cells through different mechanisms such as apoptosis, autophagy, senescence, and/or necrosis [22]. TMZ is the current standard of care for chemotherapy of GB patients [23], since it was confirmed that RT with concomitant TMZ chemotherapy was more effective than RT alone (median survival after diagnosis of 14.6 months versus 12.1 months, respectively) [14]. The protocol used for TMZ treatment in GB patients is a daily dose of 75 mg/m² given 7 days concomitant with RT for up to

49 days. A four-week break is scheduled, and after that, patients receive up to six cycles of TMZ (150–200 mg/m²) for 5 days, every 28 days.

TMZ is an alkylating agent that can be administered orally and has the ability to cross the blood-brain barrier (BBB), achieving effective concentrations within the tumour site ($\approx$10 µg/ml) [24]. Following oral intake, TMZ is quickly absorbed intact through the gastrointestinal tract. In the neutral/alkaline pH of proliferating tumour cells, TMZ is spontaneously hydrolysed to 5-(3-methyltriazen-1-yl)-imidazole-4-carboxamide (MTIC), which is rapidly converted to the inactive 5-aminoimidazole-4-carboxamide (AIC) and to diazomethane, which is responsible for cytotoxicity, since it transfers a methyl group to the O6 of guanine residues in the DNA, giving rise to O6-methyl-guanine (O6-meG) (Figure 1.2). This was historically described to interrupt replication and cause a collapse of the replication fork, generating single-strands breaks, which induce double-strand breaks and ultimately cell death via apoptosis [25].
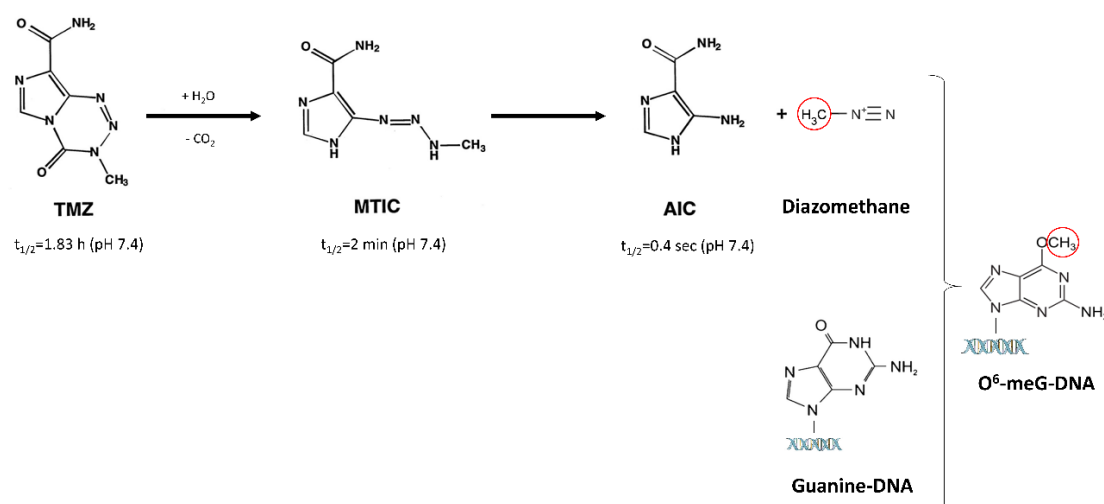
Figure 1.2. Prodrug activation of TMZ. TMZ is spontaneously hydrolysed to MTIC at neutral or alkaline pH. MTIC further fragments to AIC and the methyldiazonium ion, which in turn reacts with nucleophilic sites, for example, in the DNA. Abbreviations: TMZ, temozolomide; MTIC, 5-(3-methyltriazen-1-yl)-imidazole-4-carboxamide; AIC, 5-aminoimidazole-4-carboxamide; O6-meG, O5-methyl-guanine. Figure modified from H. Strober et al [26].

This cytotoxicity leading lesion in DNA can be removed by the enzyme O6-methylguanine-DNA- methyltransferase (MGMT), which transfers the methyl group from the adduct to its own cysteine residue. After repairing the DNA lesion, methylated MGMT is degraded. Therefore, MGMT confers tumour cell resistance to TMZ and hinders the success of the treatment In this respect its overexpression is linked to bad prognosis for patient survival [27–29].

Several research efforts have been devoted to the improvement of GB outcome, but only discrete results have been achieved. In this sense, surgery followed by chemo-radiotherapy and adjuvant therapy remains the approved first-line therapy that improves overall survival of patients with GB [30], and as previously mentioned, the overall survival of patients even after aggressive therapy is below 15 months. This highlights the urgent need to investigate novel

treatment approaches, as well as efficient follow-up strategies in order to improve patients' outcome.

<u>TMZ effect in GB cells: what is currently known?</u>

The beneficial effect of TMZ in preclinical/clinical settings has been historically attributed to its role as DNA alkylating agent and activator of the apoptotic cascade [31,32]. However, the TMZ effect could be also due to the methylation of other macromolecules, such as ribonucleic acid (RNA), proteins and lipids carrying nucleophilic groups, which implies post-transcriptional/translational modifications, and also mitochondrial DNA. This may lead to an alteration of mRNA folding, structure and maturation that can accelerate its decay. Furthermore, it results in remodelling of chromatin structure, causing alterations in gene expression, DNA replication, synthesis and repair, and lastly cell cycle disruption and cell death [26].

However, studies with cultured GB cells (e.g., GL261 GB cells) revealed that TMZ was not especially efficient in cell killing, mostly acting as cytostatic rather than cytotoxic drug [33]. Then, cell killing may not be the only reason for satisfactory results of survival increase obtained with TMZ in clinical and preclinical settings, being one of several possible explanations host immune system recruitment [34–40], mainly triggered by the exposure/release of damage-associated molecular patterns (DAMPs) by TMZ damaged cells.

1.1.4. Preclinical models for investigation in GB therapy

There are several limitations regarding therapy-related studies in GB patients. Due to evident ethical reasons, it is not possible to have 'untreated' (i.e., no therapy administered) groups of brain tumour patients. In the same line, it is not possible to perform repeated imaging exams in patients or collect biopsy samples at given time points of tumour growth/progression for research purposes, especially if standard surgical resection is feasible. This can be overcome with the use of preclinical models, which allow us to investigate the evolution of untreated animal groups, as well as to perform repeated explorations along treatment. Moreover, animal euthanasia can be performed in predetermined time points, providing a powerful tool to study new therapeutic targets, assess cellular/molecular local effects, as well as shed light on the situation of the TME, its influence on disease progression and outcome. The mouse genome has direct human orthologs in a relevant percentage of genes, thereby this is one of the dominant model organisms for cancer therapy studies [41].

There are different types of preclinical models (Figure 1.3**¡Error! No se encuentra el origen de la referencia.**) which have been used in various experimental settings with their advantages and disadvantages. However, it is worth noting that the relevance of a given preclinical model depends on how closely it replicates the original human disease (e.g., growing in the same organ/tissue of origin and displaying similar histopathological features), tumour growth

reproducibility, and its capacity to thrive in immunocompetent models [42]. Furthermore, given the relevance of the host immune system in events related to response to therapy (see section 1.3), the use of immunocompetent models is an important point to consider. Since in this thesis our work is centred in preclinical brain tumour models, some considerations about them will be made below.

Brain tumour models can be either spontaneous or transplantable. Spontaneous models are based on specific genetic alterations (genetically engineered mice, GEM) similar to human brain tumours, thus mirroring the histology and biology of human GBs. These models arise spontaneously, which turns into a challenge for standardisation within cohorts (especially in relation to the tumour initiation time point) [43]. Moreover, from our previous experience [44], the incidence of MR-detected brain tumours can be lower than expected from literature, hampering the formation of homogeneous groups for investigation. On the other hand, transplantable models are generated by cell lines or fragment tissues implantation into healthy mice. One intermediate possibility in this sense is the transplantation of cells/gliospheres obtained from GEM tumours for establishing transplantable lines [44].

Transplantable models can be divided into syngeneic and xenogeneic models depending on whether cells/tissues implanted comes from the same host species or not. Syngeneic models are generated by implantation of cells/tissues from the same genetic background of the host. This implies low or no host immune system action against tumour cells, which allows to study the full role of the immune system in case of therapy response investigation [45]. On the contrary, xenogeneic models are transplanted with cells from a different species, thus requiring the use of immunocompromised mice, in order to avoid rejection of the implanted cells. In general, in the case of brain tumours, the origin species is from human, either from established cell lines such as U87 or U258, or from brain tumour samples, also known as patient-derived xenografts (PDX). The investigation around better preclinical models is continuously evolving, and a "tolerized" PDX developed with human samples over immunocompetent strains was described by Semenkow et al [46], which can open a way for future studies.
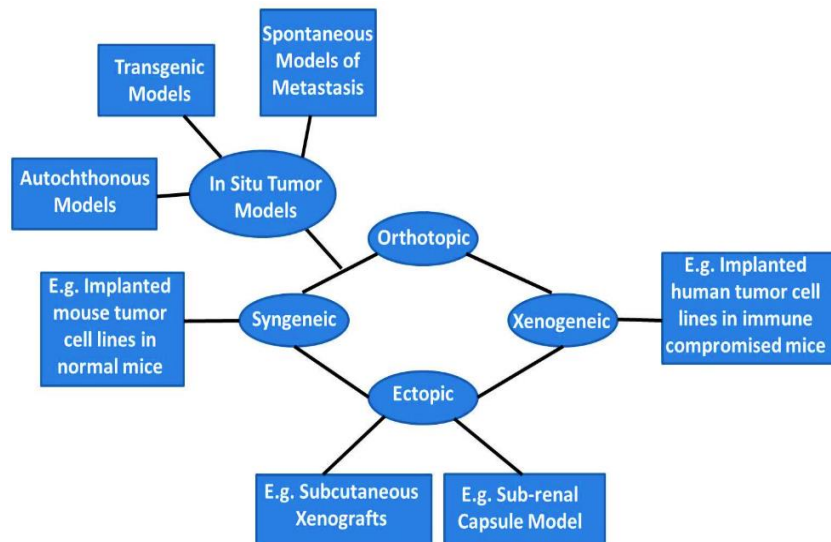
Figure 1.3. Preclinical cancer models scheme (obtained from [47]).

Considering the location, transplantable models can be also divided into ectopic and orthotopic. Ectopic models are generated by cells or tissues implanted in a location that differs from where disease naturally occurs. The subcutaneous injection (mice flank) is the most common procedure for these models, allowing easy monitoring of tumour evolution by calliper measurements. This model makes it difficult to recapitulate the original tumour behaviour and are known to provide over-optimistic therapy response results with respect to orthotopic models [42]. On the other hand, orthotopic models involve implantation of tumour cells into the same organ or tissue in which the disease naturally occurs, in our case, the brain. This mimics better the infiltrative nature of GB and the disease-relevant environment. Unfortunately, the assessment of tumour growth by calliper measurements is no longer possible, and evolution must be analysed through non-invasive imaging approaches.

GL261 GB model

The immunocompetent GL261 murine model, a transplantable and orthotopic model, was used in this thesis. It is generated by the stereotactic injection of the murine glioma cell line GL261 into the brain of C57BL/6 mice, resulting in tumours with invasive and infiltrative characteristics similar to those of human GB, growing in mice with an intact immune system [48]. Furthermore, this model presents ca. 100% take rate and allows for obtaining homogeneous experimental groups for therapy response studies.

The GL261 model is one of the best characterised mouse models of human GB and has been largely used as an *in vivo* model for GB research in our group [44,49–52] and other research groups worldwide [53–56]. It was generated by chemical mutagenesis in the late 30's [57] over the C3H background, i.e., it was not developed over the C57BL/6 background. Although it is usually described as syngeneic in literature, it may be rather considered isogenic due to its different background of origin. However, it would probably belong to the so-called "venerable

tumours" (i.e. any long-transplanted tumour) [58] where no or few immunological effects are expected against the tumour when inoculating those cells in immunocompetent mice. Accordingly, after the 1970s, the common practice was to grow GL261 tumours in the C57BL/6 mice strain, in which these tumours grow exponentially for about three weeks, the time when the tumour kill animals due to mass effect [59].

Regarding the GL261 cell line, studies on gene alterations show that these cells share several molecular modifications with human gliomas, such as K-Ras and p53 gene mutations. Moreover, they express basal Major Histocompatibility Complex I (MHCI) on its cell surface, but not Major Histocompatibility Complex II (MHCII) [48]. The immunological characteristics of the cell line GL261 growing in C57BL/6 mice make it a potent tool to investigate the antitumour effect of various treatment strategies such as immunotherapy, gene therapy, chemotherapy, radiotherapy or antiangiogenic therapy [48,59,60]. It has to be noted that the mutational load of GL261 [61] is much higher than an untreated human GB [62], which could trigger the host immune system stimulating rejection. On the other hand, relapsing human GB after several cycles of TMZ, may contain a similar mutational load [63] than GL261 tumours.

1.2. NUCLEAR MAGNETIC RESONANCE (NMR) AND ITS ROLE IN GB FOLLOW-UP

NMR, usually known in the clinical environment as MR[1], is the most common non-invasive technique for GB diagnosis and follow-up. MR was described in 1946 by Edward Purcell and Felix Bloch and started to be used *in vivo* in the 1970s. Since then, it has become a powerful tool in clinical diagnosis and follow-up, as well as in preclinical research. MR is based on the physical properties of certain atoms to absorb radiofrequency (non-ionizing) energy when they are placed in a magnetic field. This energy is released back to their surroundings during the transition of nuclei to their original state. This return to equilibrium conditions is a process known as relaxation. The most used nucleus in MR is the proton, ^1H, due to its close to 100% natural abundance, its high content in the human and animal bodies (we are ca. 70% water) and its large magnetic moment, resulting in an easily detectable signal. Depending on the parameters used in the acquisition, MR can inform about anatomical features such as tumour volume or contrast uptake (magnetic resonance imaging, MRI), metabolomic features (magnetic resonance spectroscopy, MRS), a combination of both (magnetic resonance spectroscopic imaging, MRSI), or biophysical parameters (diffusion/perfusion weighted imaging).

The following subsections will emphasise the main aspects related to MR approaches closely related to methods and results described in this thesis, with the main focus on brain tumour features. On the other hand, the detailed explanation of the physics behind the MR

---

[1] Magnetic Resonance is always Nuclear, but in order to avoid the undesirable connotations of the word <u>nuclear</u> among the lay public, this word is usually omitted in clinical settings.

technique are beyond the scope of this work and can be found in different resources such as [64].

1.2.1.   Magnetic Resonance Imaging

MRI is highly sensitive to pathologic alterations of normal brain parenchyma and has been widely used for diagnostic and follow-up of brain tumours. It provides high-quality images which inform about the size and local extension of the tumour mass [65], being useful for the diagnosis, surgery and therapy response assessment (informs about tumour volume evolution and contrast uptake). MRI is based on the signal from the ^{1}H nuclei, mostly from water and in some tissues from fat. Accordingly, images obtained, represented in a greyscale, primarily show the location of two molecules, water and triglycerides in fat. Thereby, the inherent contrast of MRI is achieved due to differences in proton density (essentially, the concentration of the sampled water) between brain regions. In addition to the proton density, the endogenous contrast is defined by two additional parameters intrinsic to a biological tissue: the longitudinal (T_1) and transversal (T_2) relaxation times of the water protons (mostly unbound mobile water). Thus, signal intensity in MRI is optimised through the adjustment of acquisition parameters such as echo time (TE, time elapsed between the application of the excitation pulse and the signal collection) or repetition time (TR, time elapsed between two excitation pulses). Accordingly, parameters chosen for the acquisition sequence determine which type of image will be obtained, e.g., proton density-weighted images, T_1-weighted (T_{1w}) images or T_2-weighted (T_{2w}) (Figure 1.4). T_{1w} images show cerebrospinal fluid and most tumours as low signal intensity (hypointense), while areas of fat and subacute haemorrhage appear as high signal intensity (hyperintense). T_{2w} images are more sensitive for lesion detection and show cerebrospinal fluid and most lesions as high signal intensity, whereas areas of haemorrhage may appear as low signal. Exogenous contrast agents (CA) can enhance endogenous contrast from MRI images, usually gadolinium-based or superparamagnetic iron oxide nanoparticles. MRI CAs decrease relaxation times of protons in tissues, enhancing contrast effect on T_{1w} and T_{2w} MRI, provided they are able to reach tumour sites. In brain tumours, the arrival of CAs to tumour sites is closely related to the impairment of BBB, which is in turn related to increase of tumour grade. Accordingly, CAs are broadly used in clinics to evaluate tumour borders and estimate grades, since the BBB impairment and abnormal perfusion allows CA extravasation and delayed clearance [66].
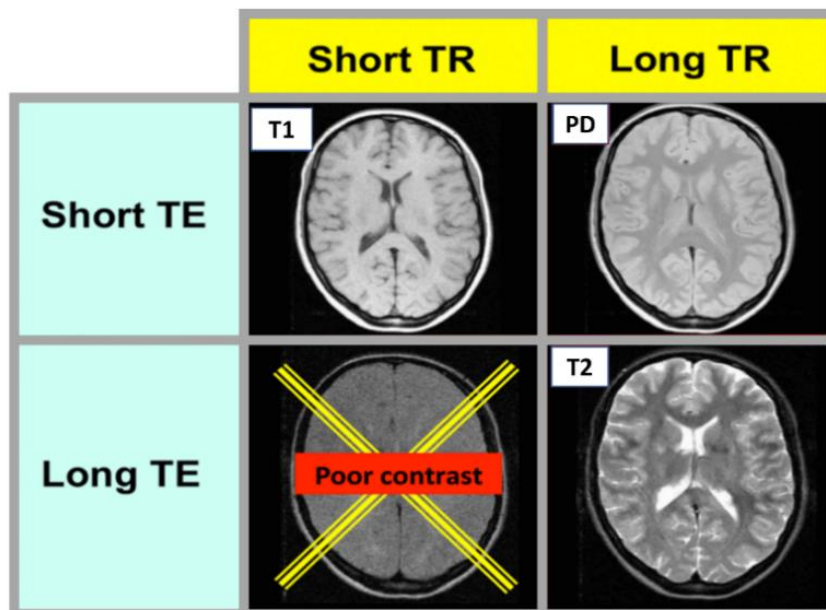
Figure 1.4. Human brain MRI examples obtained with different combination of TR and TE values. Both short TR and TE results in a T1w image, in which fluids such as cerebrospinal fluid (CSF) are hypointense, water-rich tissues are mid-grey and water-poor (e.g., high myeline/fat-tissues) are hyperintense. A combination of long TR and short TE results in a proton density weighted image, in which the maximum proton signal is obtained: the signal of tissue water is in the mid-grey scale and myelin/fat appears hyperintense. A combination of short TR and long TE result in a poor contrast image with insufficient signal. Both long TR and TE results in a T2w image, in which fluids have the highest intensity (hyperintense), and water- and fat- based tissues are mid-grey. Figure extracted from http://mriquestions.com/index.html.

1.2.2. Magnetic Resonance Spectroscopy

The anatomical information provided by MRI can be complemented by MRS, which allows obtaining information about the metabolomic profile of the investigated tissue [67,68] noninvasively. MRS can detect low molecular weight metabolites of interest that are present in adequate concentration (millimolar range) and with enough mobility, by means of suppression of the intense water signal, which is three to five orders of magnitude larger than the signal of the metabolites in tumour and brain. MRS can inform about a single region (single voxel) or different regions (multivoxel, also known as magnetic resonance spectroscopic imaging, MRSI, see section 1.2.3) within the region of interest. Single voxel provides a spectrum acquired from a small volume of tissue, in general a cubic volume. On the other hand, MRSI allows the study of the metabolic pattern across a larger region of the brain/tumour anatomy. This makes it possible to distinguish between different tissue types, tumour grades or the same tumour under different conditions (e.g., before or after therapy), as well as to predict the treatment response or failure and the clinical outcomes, allowing for an earlier change in treatment if needed, provided suitable interpretation of the spectroscopic pattern is achieved [69].

The information contained in MRS is essentially different from information provided by MRI and it is not as straightforward to interpret. As opposed to MRI, in which anatomical structures are delineated by different signal intensities, the MRS signal is contained in a spectral vector

composed by signals with different positions (chemical shifts). The <u>chemical shift</u> is the resonant frequency of a given nucleus (in part per million (ppm)) relative to a standard compound and informs about the chemical environment of the nucleus being detected. The proton MRS (^{1}H-MRS) information is represented as a spectrum, in which protons from different metabolites can be visualized at different chemical shifts (i.e., peak position along the x-axis) depending on their chemical environment and reflecting their relative concentration (along the y-axis) (Figure 1.5**¡Error! No se encuentra el origen de la referencia.**).
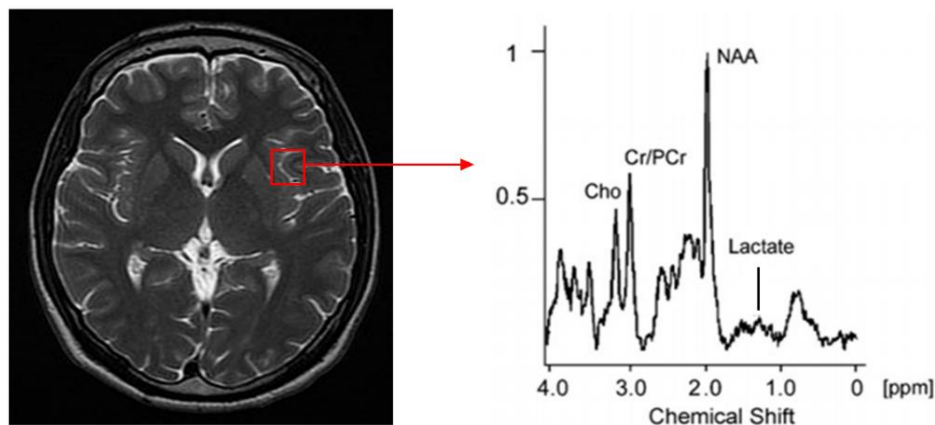
Figure 1.5. Example of a T2w MRI and a single voxel spectrum from healthy human brain. *The y-axis corresponds to amplitude (arbitrary units) and X-axis reflects the local chemical and magnetic environment of the molecule (chemical shift, ppm). Peaks are originated due to different chemical groups of the same metabolite. Thus, one metabolite can give rise to several peaks* [71]. *Major labelled resonances are indicated: Cho, choline (3.21 ppm); Cr/PCr, creatine/phosphocreatine (3.03 ppm); NAA, N-acetyl aspartate (2.01 ppm); Lac, lactate (1.31 ppm). See Table 1.1 for more details. Adapted from* [70].

1.2.3. Magnetic Resonance Spectroscopic Imaging

MRSI is a technique that combines MRI and MRS, thus it can provide metabolomic information superimposed to anatomical information, making it possible to investigate different regions of the studied tissue [72–74]. It is a method that superimposes metabolomic information to anatomical information, thus obtaining a spatial distribution of metabolites in different regions of the studied tissue (Figure 1.6). Thereby, MRSI can be a powerful tool to provide important clues about tumour heterogeneous biology and response to therapy, contributing to making early decisions about the efficacy of such therapies [50,75]. Although most reference clinical centres have full capabilities for MRS/MRSI implementation, these approaches are not currently used in the clinical pipeline for brain tumour follow-up, probably due to the prior biochemical knowledge needed for MR spectral interpretation, the lack of standardisation in MRS formats and the need of advanced tools for spectral processing and quantification.

After suitable processing and postprocessing, the information contained in MRSI acquisitions can be shown as an "image-like" output. However, most studies rely on a single metabolite assessment (NAA, Cho, Cre), metabolite ratios (NAA/Cho, NAA/Cre) [76], or specific indexes such as choline-to-NAA (CNI) [75]. This may be useful to distinguish between normal

brain parenchyma and tumour tissue or identify voxels at risk of progression [77]. However, the use of only a few metabolites may not be enough in some situations in which expected changes are more subtle. In addition, rich information provided by other metabolites in the spectral vector is disregarded. The use of the whole spectral pattern, instead of focusing on single metabolites or metabolite ratios, may help to tackle subtle changes affecting several metabolites at once. In this sense, approaches such as pattern recognition (PR, see section 1.2.4) are of great interest for the objective analysis of whole MRSI spectral patterns and integrate them in a suitable way to gain maximum information, which can be useful both in clinical and preclinical studies [49,50,78].

A) B) C)
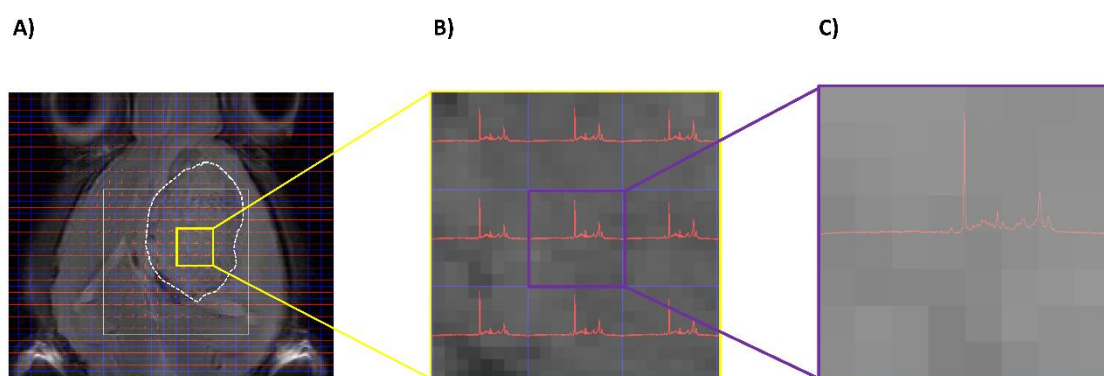
Figure 1.6. Examples of representative pixel spectra obtained in a 12x12 MRSI grid from a GL261 tumour-bearing mouse treated with TMZ. *A) Axial T2w MRI showing the volume of interest (VOI) from the GL261 GB tumour bearing mouse C1412 (unique GABRMN identifier for mice subjects, see section XXX) enlarged in B). The boundaries of the tumour mass are marked with a white discontinuous line. B) Examples of individual short echo time spectra (14 ms) from the acquired MRSI grid. C) Individual spectrum, shown for the 0.5-4.5 ppm range (see section 1.2.3.2 for more detailed information.*

1.2.3.1. Metabolites identified in normal murine brain parenchyma and GL261 GB.

The MRS spectral pattern can inform about a large list of metabolites provided their concentration ranges are over a minimum detection range (ca. 0.5 - 1.0 mM) (Figure 1.7). However, there is considerable overlapping of some signals of interest, especially with the resolution achieved in *in vivo* MR acquisitions. Metabolites of special interest for this PhD thesis are described below (Table 1.1):

Metabolite name	Chemical shift for main metabolite resonances in "in vivo" spectra (ppm)	Described biological meaning (increases/decreases)
N-Acetyl Aspartate (NAA)	2.01	Major signal in normal brain spectral pattern. Related to osmoregulation, N-acetylaspartylglutamic acid (NAAG) synthesis, fatty acid and myelin synthesis. Linked to neuronal density and functional integrity. Decreased in brain tumours due to neuronal dysfunction/loss [79,80].
(total) Creatine (Cr)	3.03, 3.93	Considered an indicator of brain cells energy production ability status. Generally used as internal concentration reference for assessing changes in other metabolites [81], it is described to decrease in tumour/damaged brain tissue [82,83].
(total) Choline (Cho)	3.21	Often referred as choline-containing compounds or total choline, due to considerable overlap in vivo (e.g., Phosphoryl choline, Glycerophosphocholine, free choline). Involved in membrane phospholipid synthesis/degradation [79]. Increased in tumour tissues due to elevated cell proliferation and membrane synthesis [84].
Lactate (Lac)	1.33, 4.10	End product of anaerobic glycolysis, increased in gliomas, which can metabolize glucose to lactate fast, even when oxygen is present [85]. Usually below detection in normal brain parenchyma, but increases in tumour tissue [80] especially in high grade tumours. The signal at 1.33 ppm can be partially contributed by fatty acids from NMR visible mobile lipids [86,87].
Myo-inositol (mI)	3.26, 3.55-3.56, 3.61 and 4.04	Considered a glial function marker and an osmotic agent regulator for cell volume; mI has been shown to inversely correlate with astrocytic grade in vivo, being lower in high grade tumours [88,89]. Overlaps with a possible glycine singlet signal at 3.56 ppm [89].

Glutamate & Glutamine (Glx)	2.01-2.35 (glutamate) 2.11-2.46 (glutamine)	Glutamate (Glu) is the major excitatory neurotransmitter in the brain and an important precursor for synthesis of glutathione. On the other hand, Glutamine (Gln), is a precursor and storage form of Glu located in astrocytes and is a complementary source of carbon for growing tumours [88,90]. Glu and Gln play a role in detoxification and regulation of neurotransmitters [88].
Glycine (Gly)	3.55	Gly is an inhibitory neurotransmitter that I also been known to be increased in high-grade gliomas [89,91] Due to overlap with the mI signal at clinical fields, their differential contribution can be estimated with the combined use of short/long echo times [89].
Mobile Lipids & Macromolecules (MLs & MM)	0.9, 1.3-1.4, 2.0 - 2.8 and 5.3 ppm	ML peaks are not observed in normal brain tissue but are known to be significant markers of tumour malignancy, their levels correlate with necrosis and membrane breakdown [92], a histopathological feature of high-grade gliomas caused by hypoxic stress [93], but also with proliferation rate [86,94]. Signal from MM probably arise due to post-translational modification of chemical groups in proteins (e.g., methylation, glycosylation, sialylation) [95].
Polyunsaturated fatty acids (PUFAs)	2.8	Constituents of cellular membranes essentially undetectable by MRS in normal brain tissue. It has been observed that PUFA levels increase in brain tumour after therapy in preclinical [60,96] probably due to apoptotic events.

Table 1.1. Summary of relevant metabolites identified in preclinical brain tumour MR spectra (main detectable signals), chemical shifts and biological relevance.
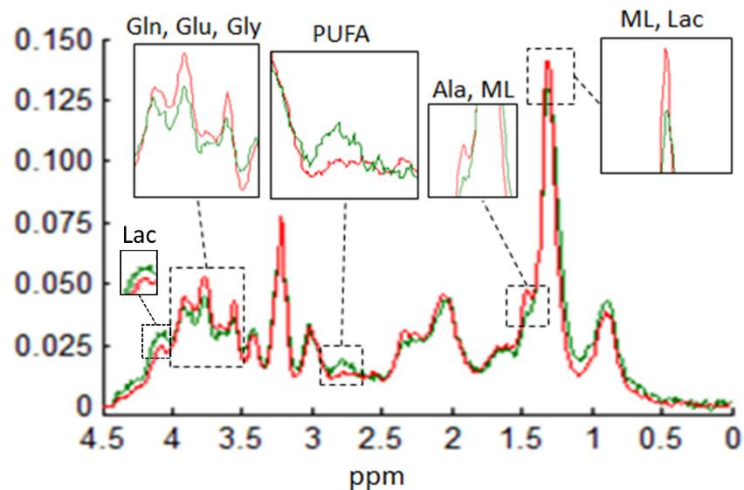
Figure 1.7. Main differences of extracted sources between the responsive (green) and unresponsive/untreated control (red) GL261 tumours. Tumour responding to TMZ show higher total ML (0.9 ppm), PUFA (2.8 ppm), and Lac (4.1 ppm), combined with lower Gln/Glu/Ala (ca. 3.8 ppm) and MLs/Lac (1.3 ppm). Figure adapted from [50]. (See "Pattern Recognition approaches" section 1.2.4. below for a more detailed explanation.

1.2.3.2. Pattern Recognition approaches

The individual analysis of MRSI spectral patterns is definitely time-consuming and requires specific spectroscopic expertise. Therefore, automated evaluation of the MRSI data as well as efficient display of the results are needed for routine clinical/preclinical application. This can be achieved through PR analyses, in which MRSI data can be analysed and classified into different categories according to differences spotted in their spectral pattern. In general, PR is defined as a description of measurements, with the final goal of inferring from a collection of measurements (training dataset) a mechanism for a decision-making process and to automate the aforementioned process [97]. The classification of new elements (test dataset, not part of training) is a prediction process, assigning those elements to one of the predefined categories or classes, based on the decision mechanism established through the training data. A detailed description of PR different approaches is beyond the scope of this PhD thesis, and only the methods applied in our described work will be mentioned.

When PR methods are applied to MRSI data, the automated decision-making processes can detect meaningful and key features (patterns) in order to distinguish between different categories analysed. Thus, robust PR algorithms combined with MRSI approaches make it possible to identify quantitative changes of different metabolites (even minor variations), which allows obtaining useful biochemical information related to biological and pathological processes. Those changes are difficult to spot without this type of approaches even for an expert observer. Based on the learning procedure used for classification, the classification strategies for PR could be supervised, unsupervised and semi-supervised.

With supervised methods, a set of data (the training dataset) is provided, consisting of a set of instances properly labelled with a known category. In the case of brain tumours, the

labelling of spectra is usually based on histopathological analysis of the tumour biopsy [98]. Once the system is trained, the classifier and mathematical algorithms extracted can be applied to different cases (the test dataset).

On the other hand, unsupervised methods assume unknown training data, which has not been manually-labelled, and aim to find inherent patterns in the data that can then be used to determine the correct output value for new data instances.

Non-negative matrix factorization (NMF) [99] is a common unsupervised method by which each class is represented by a "paradigmatic spectroscopy pattern" (i.e., a given metabolic profile), also known as "source". Biochemically, the source extraction technique for classifying the MRSI data assumes that a mixture of heterogeneous tissue patterns is present in each voxel and that the contribution of individual sources to the final pattern can be calculated. One of the advantages of this approach lies in the prevention of the confusing effect of mislabelled cases.

The semi-supervised methods [50,99] are a combination of both supervised and unsupervised PR approaches, which uses a combination of labelled and unlabelled data for training. The advantage is the prior knowledge regarding class membership to guide source extraction. The semi-supervised method previously developed in our group [60] was the approach used in this thesis to classify mouse brain tissues into normal brain parenchyma, actively proliferating (untreated/control) and responding to TMZ therapy (Figure 1.8), with no new source extraction or retraining.

1.2.3.3. Nosological imaging: visual assessment of response to therapy

One of the main challenges regarding the translation of metabolomics-based methods is, as previously mentioned, the need of advanced tools and previous knowledge on spectroscopy and PR methods, but also the general lack of imaging-like outputs that radiologists are used to. Then, past research work from our group was devoted to 'translate' the complex information into visual representations called nosological images [100].

In our case, the nosological image is a coloured-coded representation that is generated after application of PR techniques by estimating the contribution of each source ("paradigmatic spectra") to the individual voxels in the MRSI grid in order to assign each acquired voxel to one of the predetermined classes, namely normal brain tissue, responding or unresponsive tumour, extracted from the training dataset described in [60]. The most contributing paradigmatic spectrum is selected as the "winning source" for each voxel and each source is assigned a different colour, finally represented as nosological maps for each matrix.

In this PhD thesis, our previously semi-supervised PR method was used to test the response to TMZ therapy in GL261 GB bearing mice. In this sense, in the nosological images, the green colour was used when the GB responding to the treatment source contributed the most, red for actively proliferating GB, blue for normal brain parenchyma, and black for undetermined tissue

(Figure 1.8). See also Figure S1 of Chapter II for a summary of the steps required for this type of analysis.

A)   B)   C)

□ Responding tumour
□ Untreated/unresposive tumour
□ Normal brain parenchyma

Treated tumour   Control tumour   Treated tumour
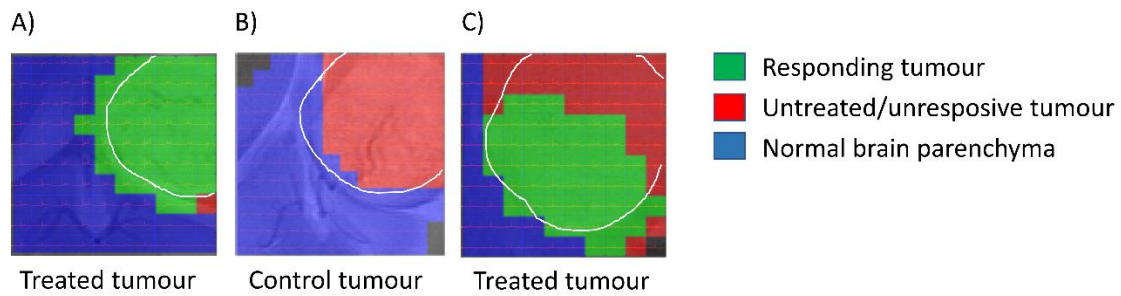
Figure 1.8. Examples of nosological images obtained with the semi-supervised PR method in TMZ-treated and control GL261 GB tumours. A) Homogeneous tumour from the treated case C1526 mostly identified as responding. B) Homogeneous tumour from the control case C1465 mostly identified as non-responding. C) Tumour from the treated case C1352 showing a heterogeneous pattern, with partial response to therapy.

1.3. TUMOURS ARE MORE THAN TUMOUR CELLS: ROLE OF TUMOUR MICROENVIRONMENT AND HOST IMMUNE SYSTEM

The environment in GB tissue is heterogeneous, involving interaction of tumour and non-tumour cell types, influencing their growth, progression and response to therapy. This tumour microenvironment (TME) represents not only non-cancerous cells but also extracellular biomolecules within the tumour. Glioma cells secrete numerous chemokines, cytokines and growth factors that promote infiltration of various cells such as peripheral macrophages, antigen-presenting cells (APCs), helper T cells (Th, CD4$^+$ lymphocytes), cytotoxic T cells (Tc, CD8$^+$ lymphocytes), regulatory T cells (Treg, CD4$^+$/FoxP3$^+$ lymphocytes) and natural killer cells (NK, CD49b$^+$ lymphocytes) within the tumour [101]. Indeed, Broekman et al. [102] described recruitment of healthy cells by GBs, which can modulate its growth and cross-talk with neighbouring cells. In addition, locally produced cytokines and chemokines may help to reprogram the infiltrating immune cells to acquire distinct functional phenotypes, thereby directing the immune system into inflammatory (anti-tumour) or anti-inflammatory (pro-tumour) responses [101]. In summary, proper response to therapy depends on suitable host immune responses.

1.3.1. The Cancer Immunity Cycle

For an anticancer effective immune response, a series of stepwise events are needed, which are repeating in cycles and constitute the Cancer Immunity Cycle (Figure 1.9). In the first step, DAMPs created by tumour cells due to therapy are exposed/released, being recognised by APCs through their Toll-like receptors (TLRs) and processed by them. After maturation, APCs migrate to the lymphatic nodes and present the captured antigens on MHCI and MHCII molecules to T cells in a process called cross-priming, resulting in the priming and activation of T cell responses. In this step, it is critical to achieve a balance between effector T cells (helper

and cytotoxic) and inhibitory Treg cells, which is key to satisfactory outcome [103]. During the next days, expansion and differentiation of T cells may take place, followed by migration of T cells to the tumour site, infiltration of the tumour bed and, together with macrophages, destroy matching antigen-expressing tumour cells [104]. The killing of the tumour cells releases additional antigens that are recognised by APCs, lead an increase in the breadth and depth of the response in the subsequent cycle [103]. Granulocyte Macrophage Colony-Stimulating Factor (GM-CSF), I interleukin (IL)-4, IL-12, and interferon-γ (IFN-γ) are central to the process of APCs maturation [105]. APCs in turn release cytokines like IL-1β, IL-6, IL-12 or tumour necrosis factor (TNF) that shape the NK and T cell responses [106].
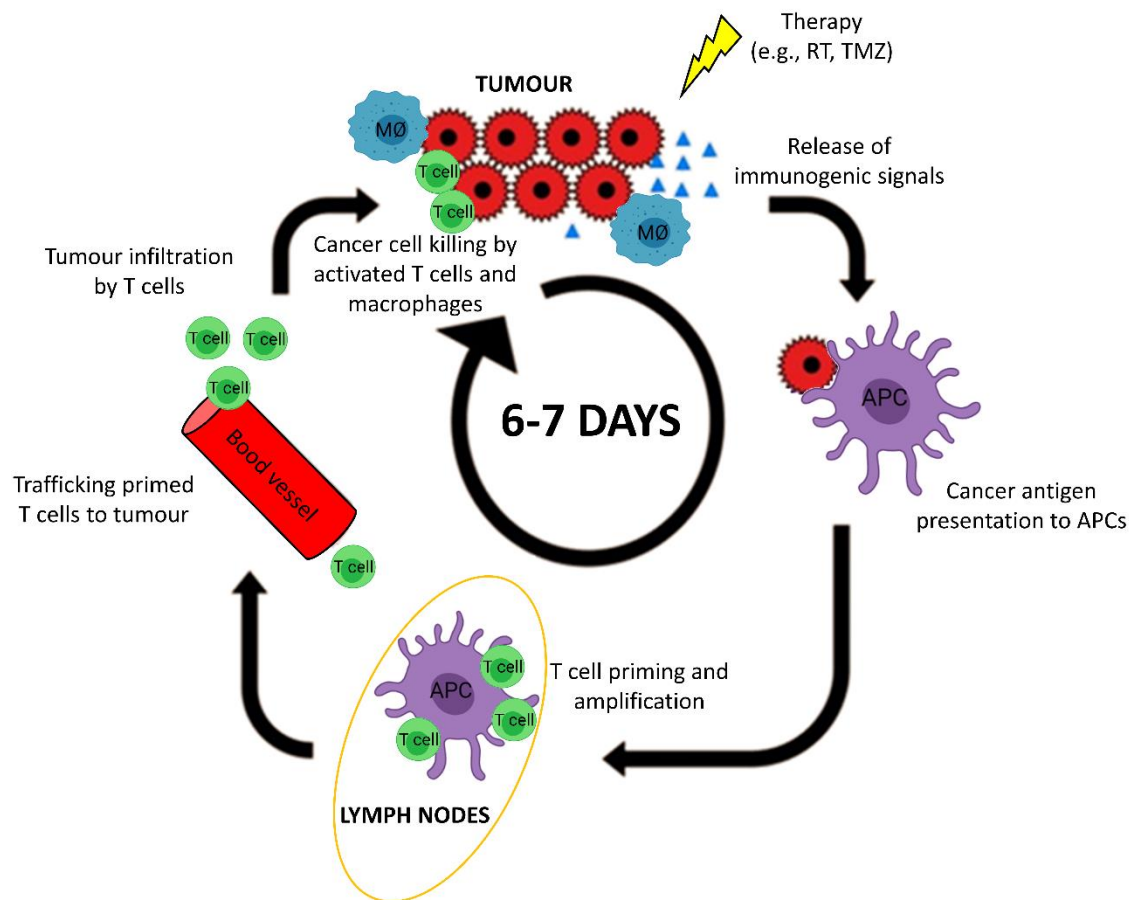
Figure 1.9. Scheme of the cancer immune cycle against a tumour. The whole cycle in mouse brain is assumed to take around 6–7 days [107]. The malignant cells may release immunogenic signals, after the therapeutic effects on them. These signals attract APC precursors to the tumour, where they are activated by compromised tumour cells. Then, activated APCs migrate to local lymph nodes, such as the dorsal cervical lymph node for brain, and present processed tumour-derived peptides to naïve T and B lymphocytes. In case of antigen match, they are then activated to become plasma cells producing antibodies, helper T lymphocytes or cytotoxic T lymphocytes. Activated lymphocytes leave lymph nodes to infiltrate brain tumour tissues and exert effector functions [108,109].This results in the recruitment and activation of innate immunity effector cells, including microglia/macrophages (MØ), NK and Natural Killer T cells, all of which are able to kill cancer cells. Immune tolerance may be induced by the activation of regulatory T cells (see section 1.3.3). Figure adapted from [49,103].

The Cancer Immunity Cycle may not perform optimally due to several reasons, namely: impairment of the amplification step in lymph nodes by antiproliferative agents, deregulation of

APCs, considering antigens as self rather than foreign, expansion of Treg cell responses rather than effector responses, deficient trafficking of T cells to tumours, inhibition of T cell tumour infiltration, or the suppression produced by factors in the microenvironment, such as Programmed Cell Death-1 ligand 1 (PD-L1) [110].

1.3.2. The GB immune microenvironment: its components and influencing factors

The immune system and its influencing factors (i.e., pathways which can modulate, enhance or decrease immune system activity) are critical regulators of tumour biology with the capacity to support or inhibit tumour development, growth, invasion and metastasis. Some of the relevant elements related to the work and results described in this PhD will be introduced.

1.3.2.1. Glioma-associated microglia/macrophages (GAMs)

Microglia (i.e. resident immune cells of the CNS), together with peripheral macrophages recruited by tumour cells from circulating blood [111], constitute the most common non-tumour cell types in the GB microenvironment [112], representing up to 30-40% of the tumour mass [111]. GAMs can be activated by various stimuli and polarized into a classically activated (M1) or alternatively activated (M2) phenotype, which in fact represent extreme situations of a continuum of activation states. Different pathologies are associated with dynamic changes in GAM activation. While M1 microglia is involved in proinflammatory and anti-tumour mechanisms, M2 microglia is involved in activities for promoting tumour survival and growth [113]. Accordingly, it is their gradual polarization state that determines the pathophysiological character of this cell population. Still, the fact that microglia/macrophages are significantly more abundant in GB than in low grade gliomas [112] may be suggestive of their possible active role in GB progression. Regarding GL261 GB model, it was described to be a complex environment composed by different tumour and immune cells. In this respect, a recent study has described the spatial localization of immune cell populations and mediators during GL261 tumour development [114].

1.3.2.2. Glioma infiltrating T helper, T cytotoxic and T regulatory cells

T cells are lymphocytes that play important roles in the antitumour immune response and determine the development and progression of tumour diseases, including GB [115]. The so-called Tc and Th are part of the adaptive immunity, which development is slower than innate immunity mediated by NK cells and macrophages [116]. These T lymphocytes are in a quiescent state in the lymph nodes and become effector T cells when an APC cell presents them with an adequate antigen on its surface [117,118]. Tc cells detect tumour-derived antigenic peptides presented by MHC class I molecules expressed on the surface of tumour cells or APCs [116], while Th cells interact with antigens in the context of MHC class II molecules on the surface of APCs [119].

Tc cells, also known as CD8^{+} T cells (i.e. expressing the CD8 coreceptor [120]), critically affect the development and progression of the tumour and are considered as a pivotal prognostic marker for cancer [115,121]; thus, a direct correlation between the proliferation of intratumoural Tc and the reduction of tumour size has been described [122]. Following Tc cell activation, effector Tc cells traffic to the tumour site to exert efficient responses [123] and kill tumour cells through granule exocytosis and apoptosis induction mediated by Fas ligand (FasL) [124].

Tc cells can develop positive cross-talking with immunostimulatory cells including NK cells, M1 GAMs, Th cells, and APCs, whereas these cells have negative cross-talking with immunoinhibitory elements including tumour cells, Treg cells, and M2 GAMs (Figure 1.10). When the TME is immunosuppressive this fosters cancer cell proliferation in an uncontrolled manner, allowing them to attain their invasive features.
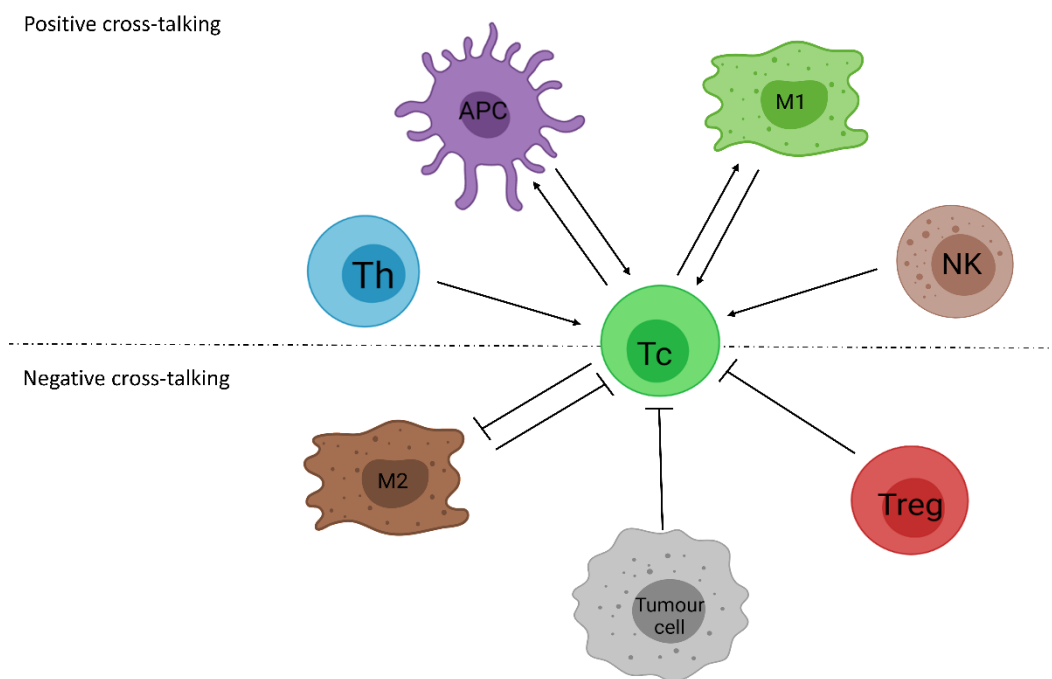
Figure 1.10. Cross-talk between Tc and other cells of TME. Tc cells have positive cross-talk with Th cells, APCs, M1 GAMs and NK cells, whereas they display negative cross with immunoinhibitory cells including M2 GAMs, tumour cells and Treg.

Th cells, also known as CD4^{+} T cells (i.e. expressing the CD4 coreceptor), mediate anti-tumour immunity by providing help for proliferation and function of Tc cells and antibody responses [118], as well as via secretion of effector cytokines such as IFN-γ and TNF-α. Moreover, under specific contexts, they can act via direct cytotoxicity against tumour cells, playing a fundamental role in a sustained effective anti-tumour response [125]. Additionally to cytokines secretion, the interaction between a Th cell and the MHC class II antigen of an APC can promote the induction of costimulatory signalling pathways between Th cells and Tc cells, such as CD80 and CD86 which activate both cell types for their further migration to the tumour site [118]. Furthermore, Th cells activate and enable APCs for maturation, expression of

costimulatory molecules and secretion of cytokines that are contributed to Tc cell priming [126]. It is also important to highlight the effect produced by IFN-γ and TNF-α released by effector Tc and Th cells inducing cytotoxicity in cancer cells [124]. Furthermore, IFN-γ stimulates M1 GAMs to exert antitumour effects [118].

Treg cells, also known as CD4$^+$/FoxP3$^+$ cells, represent a subset of cells that mitigate the immune response by secreting cytokines such as IL-10 and facilitating the inactivation of Tc cells by direct cell-to-cell interactions (Figure 1.11). Tumour cells can take advantage of Treg by attracting them into the tumour milieu and manipulating Treg-mediated immunosuppression in order to escape recognition and elimination by the host immune system [115]. Decreased infiltration of Treg results in reduced tumour growth and increased survival in murine models [127].
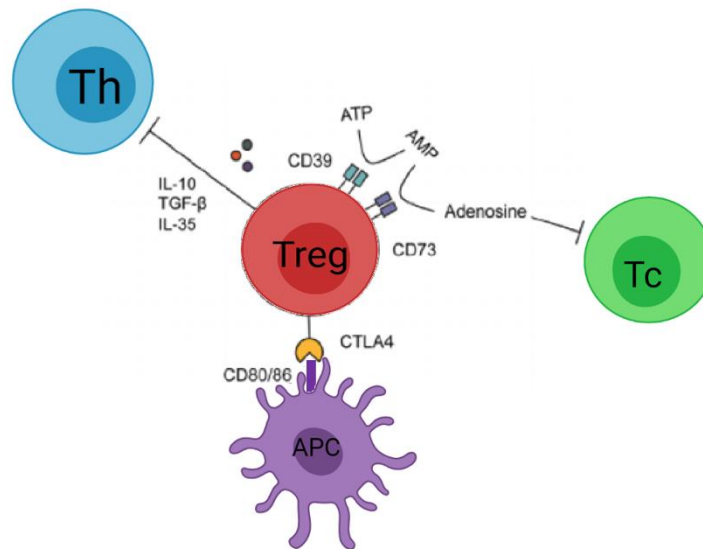
Figure 1.11. Immunosuppressive function of Treg cells. Regulatory T cells can inhibit effector Th and Tc cells through the production of immunosuppressive cytokines (IL-10, transforming growth factor-beta (TGF-β), and IL-35), the expression of inhibitory molecules such as CTLA-4, and by the release of adenosine through the CD39-CD73 pathway. Figure modified from [128].

1.3.2.3. Natural Killer cells

The NK cells, also known as CD49b$^+$ cells, are lymphocytes that secrete cytokines and chemokines known to participate in the innate immune response. They can recognize tumour cells due to the lack of MHC molecules on the surface, and kill them without any previous activation through the perforin/granzyme pathway or death receptor-related pathways [129]. NK cells are described to infiltrate in the gliomas, but in a lesser extent, reported as ca. 2.11% of the total [130], when compared with other IS populations such as macrophages.

1.3.2.4. Immune checkpoint pathways

Tumour cells develop different protection strategies for evading the immune system attack by high jacking inhibitory immune checkpoints, being able to create a strong immunosuppressive microenvironment. These checkpoints, such as the programmed cell death-1 ligand 1/ programmed cell death-1 receptor (PD-L1/PD-1) axis [131] and the Cytotoxic T-Lymphocyte Antigen 4 (CTLA-4) [132] (Figure 1.12), lead to the escape from immune surveillance allowing tumour cells to not be detected, thriving unchecked in the TME. Thus, therapeutic approaches based on immune checkpoint inhibitors that result in robust activation of the immune system and productive antitumour immune responses are a promising strategy in many types of cancer. However, despite the success of immune checkpoint inhibitors, resistance and immune-related adverse symptoms might eventually appear, which may make treatment ineffective [121]. Thus, better insight into their action mechanisms is needed.

PD-L1 / PD-1 axis

The tumour immune escape plays a very important role in the progression of tumour, and TME normally protects tumour cells from being killed by the immune system. Tumour-intrinsic factors involved in glioblastoma-associated immunosuppression include the induction of signalling pathways known to suppress immune responses [133]. The main mechanism to mediate immunosuppression in the TME is the interaction between PD-1 and PD-L1 [134]. PD-1 is an inhibitory receptor mainly expressed on activated T cells, including Th and Tc cells, natural killer T cells, B cells, macrophages and dendritic cells [135], while PD-L1 is highly expressed by malignant tumour cells [135], as well as by tumour-infiltrating myeloid cells, including macrophages [136,137].

Cytotoxic T-Lymphocyte Antigen 4

CTLA-4 is a protein with high homology to CD28, one of the main proteins expressed on T cells that provide co-stimulatory signals required for T cell activation and survival through its binding to B7 molecules, proteins presented on activated APCs. Thus CTLA-4 may compete with CD28 for binding to the B7 molecules (CD80 and/or CD86) expressed on the APCs. This binding would finally lead to reduced inducible activity of APCs on Tc cells with their subsequent suppression [138,139].
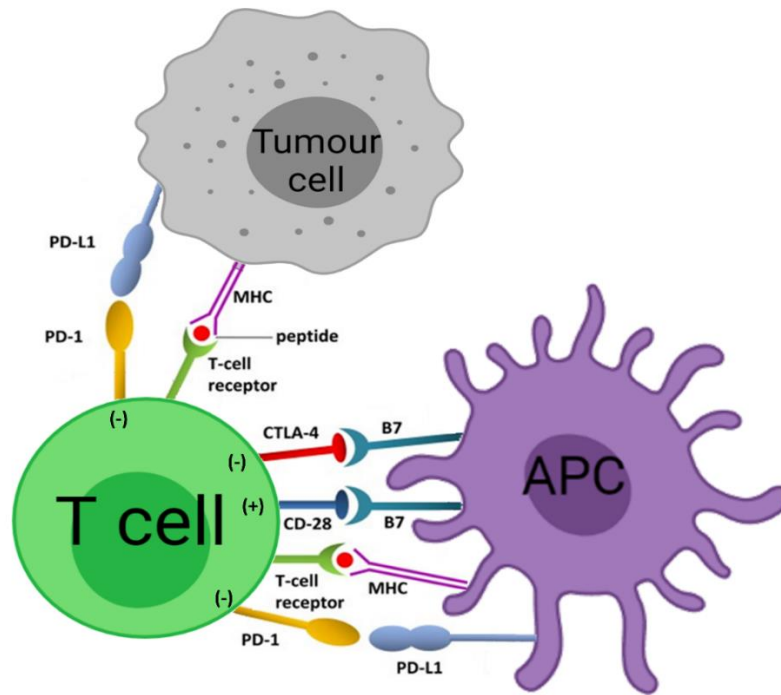
Figure 1.12. T Cells interact with dendritic cells and tumour cells through the inhibitory immune checkpoints PD-1 and CTLA-4. PD-1 is an inhibitory receptor expressed on activated T cells that bind PD-L1, a ligand highly expressed by malignant tumour cells and APCs. CTLA-4 is expressed on activated T cells and binds B7 molecules expressed on the APCs. The consequence of these interactions is the suppression of T cells. Figure modified from [140]*.*

1.3.3. The role of different metalloproteases

1.3.3.1. A Disintegrin and Metalloprotease (ADAMs)

The ADAM family proteins belong to the metalloprotease superfamily, which comprises a diverse group of multi-domain transmembrane and secreted proteins [141][142]. To date, 21 ADAM protein-coding genes have been identified in the human genome, whereas 24 ADAMs protein-coding genes have been named in the mouse genome (http://www.genenames.org/). ADAMs have been described to modulate the activities of membrane cytokines and growth factors, their receptors, and cell adhesion molecules. Their mechanism of action is related to cleavage of transmembrane proteins and solubilization of the complete ectodomain of cytokines, growth factors, receptors, and adhesion molecules. Thus, these molecules can initiate or inhibit signalling on the same cell, neighbouring cells, or distant cells by transport through blood [143]. ADAMs functions place them in pivotal positions regarding the regulation of tumour proliferation, inflammation, among others [141] and their specific roles in immunity have been reviewed in [144]. ADAMs are type I transmembrane proteins that consist of an N-terminal signal sequence followed by a pro-domain, a metalloprotease (catalytic) domain, a disintegrin-domain, an EGF domain-like (EGF-like) (cysteine-rich) domain, a single transmembrane domain, and a cytoplasmic tail (scheme in Figure 1.13). An exhaustive description of all existing ADAM proteins is beyond the scope of this PhD. Only subtypes related to results and discussion will be emphasized.
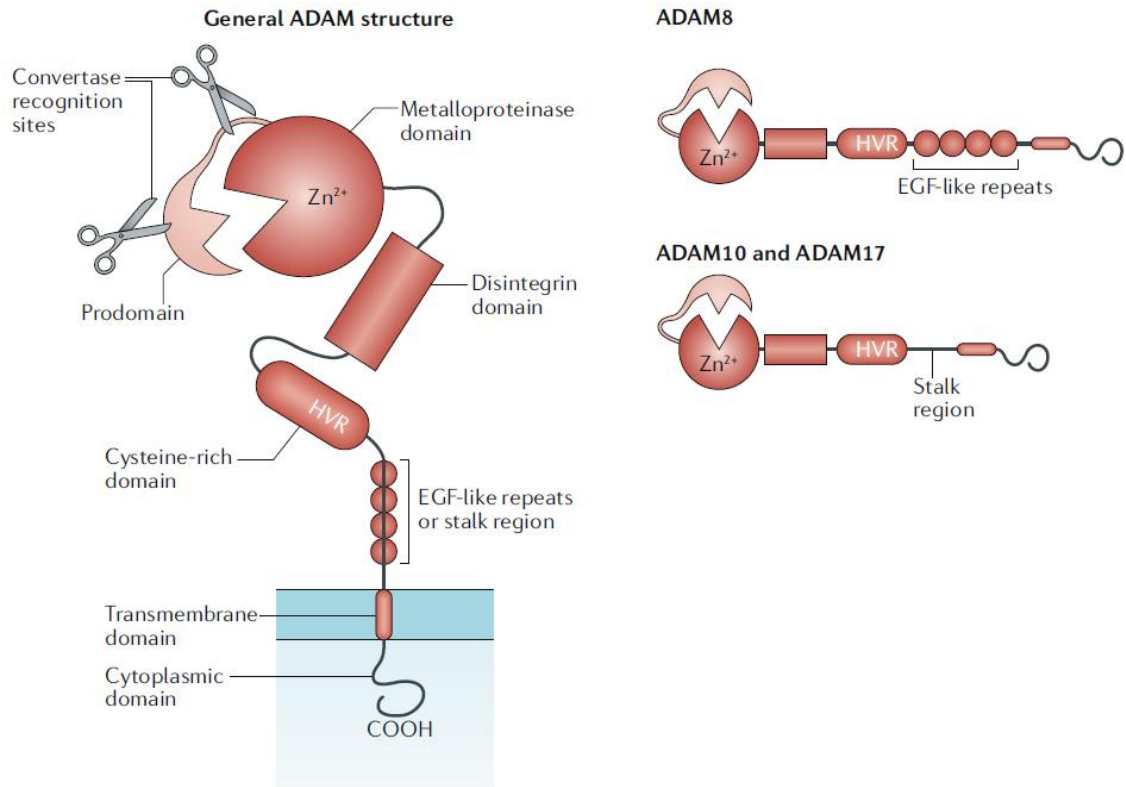
Figure 1.13. The general structure of ADAMs. *ADAMs consist of several domains, including a chaperone-like prodomain with two convertase recognition sites (keeps ADAMs inactive); a Zn2+-dependent metalloprotease domain (a key domain involved in catalytic activity and ligand shedding); a disintegrin-domain (interacts with integrins, supports adhesion and serves to maintain the structure of the extracellular region); a cysteine-rich domain containing a hypervariable region (HVR), an EGF domain-like (EGF-like) repeat domain (regulates substrate binding and shedding activity), a transmembrane domain and a carboxy- terminal SH3-binding cytoplasmic domain (interacts with signalling molecules and its phosphorylation regulates the activation, trafficking, and subcellular localization of ADAMs). In ADAM10 and ADAM17, the EGF-like repeat domain is absent, and the membrane-proximal region is often referred to as the stalk region. Figure modified from* [144]*.*

ADAM 8

ADAM8 is expressed mainly in immune system cells, such as monocytes, neutrophils, eosinophils, dendritic cells, and B- cells [145] and its expression is regulated by TNF-α in a dose-dependent manner. A study using wobbler mutant mice as a model for neurodegeneration and glial activation described ADAM8 upregulation in activated microglia, suggesting a role for ADAM8 in cell adhesion during neurodegeneration [146]. ADAM8 triggers the shedding of Tumour Necrosis Factor Receptor 1 (TNF-R1), thereby resulting in a reduction of the TNF action at cellular levels. Thus, the shedding of TNF-R1 by ADAM8 may protect cells from TNF-induced cell death [147]. Furthermore, ADAM8 that has been identified as a significant player in aggressive malignancies including breast, pancreatic, and brain cancer. High expression levels of ADAM8 are associated with invasiveness and predict a poor patient outcome [148].

ADAM10

ADAM10 endopeptidase is one of the primary enzymes responsible for ectodomain shedding of membrane proteins in eukaryotes, with a broad specificity in membrane protein ectodomain shedding, targeting ca. 100 substrates [149]. One of the described mechanisms of ADAM10 involving the immune system is the activation of Notch, a critical regulator of CD4^{+} cell differentiation which is activated through proteolytic cleavage carried out by ADAM10. Thus, ADAM10 action contributes to effective T-cell proliferation and differentiation [150].

ADAM17

It is the most thoroughly-studied ADAM protein. ADAM17 is an important regulator of cell signalling, expressed very broadly in somatic tissues, and it is present in cell membranes as a multimer. A variety of growth factors, cytokines, receptors, adhesion molecules, amongst others, have been described as substrates of ADAM 17, being some of these immunoregulatory molecules such as TNF-α, colony-stimulating factor 1 (CSF-1) and IL-6 receptor (IL-6R) [151,152].

ADAM17 plays an important role in the early APCs response. After TLR stimulation, APCs capture and process antigens for their presentation to naïve T lymphocytes at lymph nodes. In order to enhance antigen endocytosis, APCs need to disassembly of their podosomes, structure involved in their cellular mobility, and loss of podosomes depends on ADAM17 activity. TLR signalling induces cell surface recruitment and/or activation of ADAM17, which then cleaves surface proteins required for cell-substrate contact and podosome formation, causing podosome disassembly [153].

ADAM17 activity also influences the traffic of monocytes and T-cell differentiation and activation during the inflammatory processes. The soluble form of IL-6R (sIL-6R), which is able to bind IL-6, is produced by naïve and memory Th cells upon T cell receptor (TCR) activation through ADAM17-mediated shedding. Further on, the IL-6/sIL-6R complex stimulates the secretion of Monocyte Chemoattractant Protein-1 (MCP-1), a chemokine which attracts mononuclear cells, such as lymphocytes or macrophages. On the other hand, ADAM17 is involved in T-cell differentiation. T cells differentiate into Treg cells upon TGF-β stimulation, whereas triggering of the same cells with TGF-β plus IL-6 induces its differentiation toward CD4^{+} cells. Accordingly, stimulation of uncommitted T cells with TGF-β in the presence of IL-6 and sIL-6R leads to lower Treg differentiation when compared with IL-6 alone [154].

Inflammation is characterized by elevated levels of TNF-α. In this respect, ADAM17 mediates the shedding of membrane-bound TNF-α precursor to produce soluble TNF-α. This is a step needed for pro-inflammatory TNF-α activity, since membrane-bound TNF-α has rather anti-inflammatory properties [155]. Furthermore, it has been described that ADAM17- mediated shedding of colony-stimulating factor 1 (CSF-1) on the cell surface of neutrophils and macrophages can enhance macrophage proliferation [156].

1.3.3.2. Matrix Metalloproteases (MMPs)

The MMPs are a family of more than 25 structurally related zinc-dependent endopeptidases. In their active form, MMPs can degrade components of extracellular matrix such as collagen, fibrinogen and proteoglycan. MMPs can also affect bioactive molecules on cell surfaces and modulate various signalling pathways by cleaving cytokines, chemokines and growth factors. Thereby, MMPs have been shown to be relevant for cell biological processes such as cell proliferation, migration, differentiation, apoptosis, angiogenesis, tissue repair, and immune response. Low expression levels of MMPs have been described in unstimulated cultured cells and intact tissues in vivo, but their expression can be induced in TMEs [157]. It is still unclear which genes/molecules are responsible for MMPs overexpression in tumours, although TNF-α and IL-1 are often suggested to be involved [158]. Furthermore, alterations in MMP expression and activity have also been implicated in tumour progression and invasiveness [159]. MMPs structure consists of a signal peptide, a pro-domain, a catalytic domain, and a carboxy-terminal haemopexin domain (Figure 1.14). The pro-domain contains the cysteine switch sequence which complexes the catalytic Zn^{2+} in the zymogen form and allows MMPs to remain inactive in the extracellular space until they are activated by proteolytic cleavage providing a mechanism for their regulation. The carboxy-terminal hemopexin domain confers substrate specificity [158].
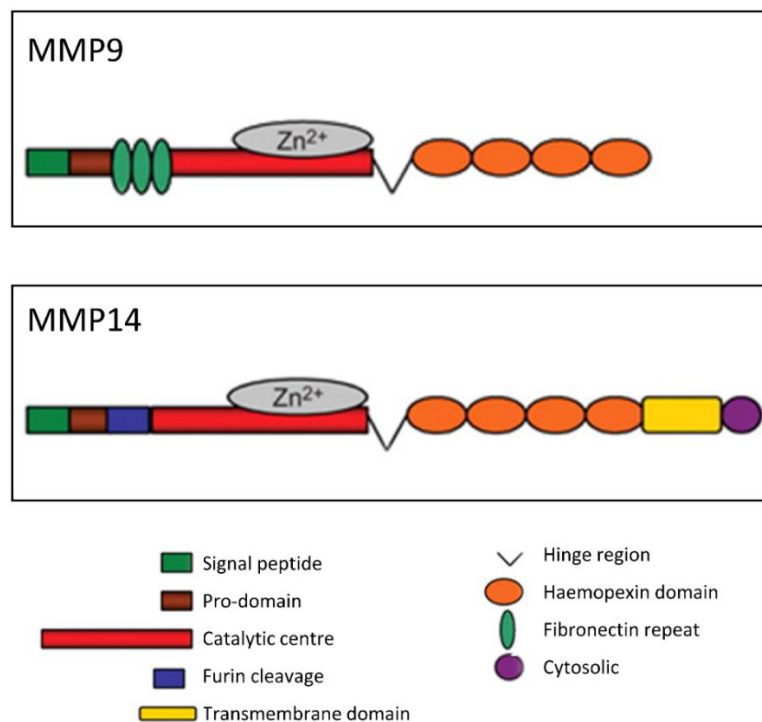
Figure 1.14. Domain structure of matrix metalloproteases MMP9 and MMP14. *All MMPs share the signal peptide, the pro-domain, and the catalytic domain. Specifically, MMP9 uniquely contain three fibronectin repeats within their catalytic domain and MMP14 presents a furin recognition site before the catalytic domain, which allows for intracellular activation of the zymogen by furin. The membrane-bound MMP-14 contains, in addition, a transmembrane and cytosolic domain. Both MMP9 and MMP14 have a flexible proline-rich hinge region and a haemopexin-like C-terminal domain, which helps in substrate recognition. Figure modified from* [160]*.*

MMP9

MMP9 is a metalloprotease capable of breaking down the extracellular matrix by type IV collagen degradation and damaging the tumour vascular endothelial barrier, leading to increased vascular permeability with the consequent extravasation of nutrients [161]. Furthermore, these changes contribute to neovascularization of gliomas and promote tumour growth and invasion. A study involving 45 cerebral glioma patients showed correlation between the expression of MMP9 and MRI features and histopathological grade of gliomas, indicating that MMP9 plays a significant role in tumour progression [162].

MMP14

MMP14 is a pericellular metalloprotease acting against extracellular matrix components directly. Potential substrates for MMP14 are proteins, including collagens, fibronectin, laminins, vitronectin, and aggrecan [163]. Previous studies have described that MMP14 is upregulated in different human tumours such as breast cancer, colon cancer, hepatocellular carcinoma, head and neck carcinoma, oral carcinoma, prostate cancer and pulmonary tumours [162,164–166], suggesting that MMP14 acts on the surrounding environment and promotes tissue remodelling, invasion, and metastasis. Furthermore, MMP14 is known to be over-expressed in glioma tissues and has also been demonstrated to correlate with grade and poor outcome in glioma patients [167,168].

1.4. ADJUSTING THE THERAPEUTIC SCHEDULE WITH IMMUNE-RESPECTFUL PROTOCOLS: MORE IS NOT ALWAYS BETTER

Chemotherapy regimens have usually exploited maximum tolerated doses (MTD) [169], alternated with rest periods to allow patients' organism to recover. However, this type of strategy can foster tumour re-growth, giving time to resistant clones to replenish the tumour. Moreover, most of the anticancer therapeutics are based in targeting cells actively replicating, but they are not selective. Accordingly, and having in mind the T-cell proliferative step occurring in lymph nodes (Figure 1.9), this type of regimen can hamper the achievement of a good resolution of the cancer treatment since it may also affect suitable proliferation of host immune system cells needed for tumour cell killing. In this sense, using a glioma and melanoma model, Litterman et al [170] demonstrated that alkylating agents, including TMZ, resulted in a decrease in lymphocytes and qualitative dysfunction of T and B cells. Then, considering the immune system role in response to TMZ therapy, it is essential to change paradigms for the administration of therapeutic agents with anti-proliferative action and respect/enhance the host immune system capabilities, setting rest periods between doses of therapy.

As opposed to the MTD intensive schedule interleaved with rest periods, metronomic chemotherapy was defined as the frequent and equally spaced administration of the minimum biological effective dose, significantly below the maximum tolerated dose, of chemotherapeutic

drugs, without the necessity of long rest periods for normal tissues recovery [171]. It has been demonstrated that following a metronomic schedule of chemotherapy drug administration every 6 days is effective in enhancing antitumour immune responses, both of the innate and adaptive systems, leading to tumour regression and avoiding tumour regrowth [172,173]. Note that this therapeutic spacing is in agreement with sparing the host immune system, avoiding application of antiproliferative agents during the T-cell proliferative period at the proximal ganglia. Specifically regarding TMZ, its toxicity effects to the host can be decreased by administration of TMZ on a metronomic schedule [174], maintaining the cytotoxicity to tumour cells and reducing the toxicity to non-tumour cells [175–177]. In this sense, TMZ metronomic low-dose schedules have been demonstrated to inhibit tumour growth, increase tumour cells autophagy, elicit antitumour immune responses in human, and show promising results in preclinical models [34].

Furthermore, the success of a given therapeutic approach is related with its capability to trigger immunogenic cell damage/death (ICD), a non-tolerogenic form of cell damage followed by emission of DAMPs in order to elicit host immune system to fight against tumours. ICD may involve changes in cell surface composition and/or release of soluble factors, while impairment in this process can contribute to therapeutic failure. It is accepted that three subclasses of DAMPs are characteristic of ICD (reviewed at [178]): a) DAMPs appearing on cell surface such as Calreticulin (CRT) exposure, which acts as an 'eat me' signal for macrophage engulfment. b) DAMPs released as end-stage degradation factors such as ATP secretion from cells experiencing physical or chemical stress, which is a prominent 'find me' signal for macrophage and APC precursors. c) DAMPs released extracellularly such as HMGB1 (nonhistone chromatin protein high-mobility group box 1, in its reduced state) released by injured cells during post-apoptotic necrosis and important for antigen presentation by APCs.

It is also well described that chemo-radiotherapy is capable of ICD triggering and DAMPs emission, eliciting host immune response against neoplastic cells and raising "indirect immunotherapy" (as opposed to "direct" immunotherapy, see section 1.3.3). Specifically regarding TMZ, its immunogenic effects are described to contribute in obtaining a positive outcome in anticancer therapy [35–40]. Contrary to what was historically described, TMZ does not need to completely kill all tumour cells, but rather produce enough damage triggering release/exposure of DAMPs in order to further attract immune system host elements. Our previous results with TMZ and preclinical GL261 GB support these findings: our group has reported in vitro investigation of TMZ in GL261 cultured cells had rather cytostatic than cytotoxic effects, but good ability to induce ICD [33], with results especially interesting regarding CRT exposure, in agreement with results reported by other authors [37]. Previous results from our group [172,179] also support that a regularly spaced therapeutic schedule improves outcome in GB-bearing mice. Altogether, results suggest that TMZ administration may trigger ICD and launch the cancer-immune cycle as described by Chen & Mellman [103] eventually leading to tumour cell killing, rather than killing cells directly. We coined the expression Immune-Enhanced

Metronomic Schedule (IMS) to define every 6 days chemotherapeutic administration protocol (see section 4, Chapter I).

2. GENERAL OBJECTIVES

The general objective of this PhD thesis was to gain insight into the validation of the MRSI-based developed biomarker as a robust method for therapy response follow-up in GB. This validation aims to explain cellular/molecular features triggering the MRSI-detected spectral pattern changes in IMS-TMZ-treated and untreated GL261 tumour-bearing mice. We planned to achieve this general goal through the following specific sub-objectives:

1.   Investigation of the robustness of the MRSI-based biomarker in longitudinal studies of the therapy response follow-up in GL261 GB tumour-bearing and control mice. Preliminary histopathological validation and possible explanation for relapse after transient response (Section 4, Chapter I).

2.   Evaluation of changes in tumour micro-environment regarding different sub-populations of GAMs, T lymphocytes and NK cells in GL261 GB tumour samples (control and transient response to IMS-TMZ) in order to explain the differential MRSI-detected pattern (Section 4, Chapters II and III).

3.   To investigate GL261 GB samples in different situations (control/untreated, transient response, relapsing and unresponsive) regarding gene expression in GAMs and of PD-L1, ADAMs and MMPs to better characterize their role in the whole therapy response process (Section 4, Chapter IV).

3. GENERAL MATERIALS AND METHODS

3.1. GL261 CELLS

GL261 glioma cells were obtained from the Tumor Bank Repository at the National Cancer Institute (NCI, Frederick, MD, USA) at passage 8. This cell batch was exhaustively tested as requested by NCI for the absence of pathogens and for being bona fide GL261 cells and absence of interspecies contamination. Tests were performed by IDEXX BioAnalytics and results can be found in Annex I. The GL261 cell line has been used by our group in different studies [49,170,171] due to the high take rate (close to 100%), reproducibility and reliability in generating glioblastomas when implanted into C57BL/6 mice.

3.1.1. Cell culture

GL261 cells were cultured in 75 cm^2 cell-culture flasks with RPMI-1640 culture medium (Sigma-Aldrich, Madrid, Spain) supplemented with 10% of foetal bovine serum (FBS) (Gibco, Invitrogen, UK), 0.285 g/l glutamine, 1% penicillin-streptomycin, and 2.0 g/L of sodium bicarbonate (all from Sigma-Aldrich, Madrid, Spain). Cells were incubated at 37°C in 5% CO_2 and 95% humidity (incubator HERAcell, 150i, Thermo Scientific). When cells covered 75%-85% of the flask surface, cells were sub-cultured (ca. after 7 days of cell culture start). For that, the medium was removed by aspiration with a vacuum pump. Then, the attached cells were washed with 10 ml of the sterile phosphate-buffered saline (PBS), PBS was removed by aspiration. Then, 2 ml of trypsin-ethylenediaminetetraacetic acid (EDTA) (0.5 g/l and 0.2 g/l, respectively) (Sigma-Aldrich, Madrid, Spain) was added in order to detach cells from the flask. After 3 min in the incubator, cells were resuspended in 8 ml of RPMI medium and centrifuged. The supernatant was discarded and the pellet resuspended in 10 ml fresh medium for cell counting (see section Cell count). Finally, cells (ca. 7x10^5 cells) were seeded in a new flask containing 25 ml RPMI medium. The medium was changed on days 3 and 5 after the culture passage. Cells were discarded after 25 passages in order to avoid the possible accumulation of genetic alterations; after that, a new aliquot was thawed and the process restarted.

3.1.2. Cell counting

For cell counting, aliquots of 10 µl of the cell resuspension described in 3.1.1 were added to 10 µl of trypan blue dye (Sigma-Aldrich, Madrid, Spain), and 10 µl of the mixture were loaded into the cell count slice for cell counting with the TC10^{TM} automatic cell counter (both from Bio-Rad, Hercules, California). Two replicates for each sample were performed.

3.2. GL261 GB PRECLINICAL MODEL GENERATION

3.2.1. C57BL/6 mice

The animal model used in this PhD thesis was the C57Bl/6 mice (females weighting 18-24 g and aged 13-23 weeks). They were obtained from Charles River Laboratories (Charles River Laboratories International, l'Abresle, France) and housed in the animal facility (*Servei d'Estabulari*, https://estabulari.uab.cat/) of the *Universitat Autònoma de Barcelona*. The husbandry conditions were as follows: light:dark cycles: 12:12 h (light from 8 am to 8 pm); temperature 20 °C (±2°); relative humidity 55% (±10%); water/food access ad libitum (2014 Teklad Global 14% protein rodent maintenance diet, Harlan, France); individually ventilated cages of five animals maximum (Tecniplast, Italy). Mice used in this work were housed in an enriched environment for at least 3 weeks before tumour generation, maintaining it over the whole mice life at our facility, since it has been reported that these approaches enhance host immune mechanisms [182]. All animal experiments were conducted according to the experimental protocol approved by the local ethics committee (*Comissió d'Ética en l'Experimentació Animal I Humana*, https://www.uab.cat)etica-recerca/) according to regional and state legislation (protocol CEEAH-3665, *Generalitat de Catalunya* order number 9685). The supervision protocol followed by animal facility staff for animal welfare and endpoint parameters can be found in Annex II. Each mouse studied in this thesis was attributed an alphanumeric identifier (CXXXX, being XXX a correlative increasing number). Furthermore, a unique ear notch combination was made with an ear punch divide in order to distinguish animals in the same cage, as shown in Figure 3.1.

Figure 3.1. Example of identification in mice by ear punching.

3.2.2. Generation of GL261 GB tumours by stereotactic injection of cells

For GL261 GB tumour generation into the brain parenchyma of C57BL/6 mice, analgesia (meloxicam at 1.0 mg/kg, Metacam, Boehringer Ingelheim) was administered to each mouse subcutaneously 15 minutes before anaesthesia, as well as 24 and 48 hours after implantation. Mice were anaesthetised with a mixture of ketamine (Parke-Davis SL, Madrid, Spain) at 80 mg/kg and xylazine (Carlier, Barcelona, Spain) at 10 mg/kg administered intraperitoneally. When they did not respond to a tail or toe pinch reflex, mice were immobilised in a stereotaxic holder (Kopf

Instruments, Tujunga/CA, USA) in a prone position. Then, the incision area was shaved and sterilised, and a 1 cm incision was made to expose the skull. Then, a 1 mm hole was drilled 0.1 mm posterior to Bregma and 2.32 mm to the right of the midline using a microdrill (Fine Science Tools, Heidelberg, Germany). A 26G Hamilton syringe (Reno, NV, USA) positioned on a digital push-pull microinjector (Harvard Apparatus, Holliston/MA, USA) was then used for the injection of 4 µl of RPMI cell culture medium containing 10^5 GL261 cells at a depth of 3.35 mm from the skull surface at a rate of 2 µl/min. Once injection was completed, the Hamilton syringe was left untouched for 2 minutes more before its removal to prevent cells leaking out of the brain. Finally, the Hamilton syringe was gently and slowly taken out and the scission site was closed with suture silk 6.0 (Braun, Barcelona, Spain) and the mouse was left in the cage to recover from anaesthesia under active supervision until total recovery.

3.3.   MRI AND MRSI ANALYSES – NOSOLOGICAL IMAGES

All MRI/MRSI analyses were carried out using standard protocols detailed and published by our research group. In order to avoid unnecessary text repetition in this section, please note that Chapter I and its supplementary material already detail the relevant parameters used in MR-based acquisitions, while supplementary material from Chapter II summarizes the steps performed for nosological image generation. Regarding Chapters III and IV, specific mention will be done whether animal selection was guided for MRI/MRSI or MRI parameters and the cut-off points used for each determined mice group (responding, relapsing, non-responding), but repetition of the technical parameters for MRI and MRSI will be avoided.

3.4.   STATISTICAL ANALYSES

Sample distribution was assessed with Kolmogorov-Smirnov test. Levene's test was used for assessing variance homogeneity. A two-tailed Student's t-test for independent measurements was used for comparisons. For comparisons with groups not sufficiently large to perform a Student's t-test, i.e., groups with an n=2, nonparametric tests were performed (Mann-Whitney U test) following the recommendation from the UAB Statistics Facility (https://sct-prv.uab.cat/estadistica/es). Relationships between different PCR-based markers were assessed with the Pearson correlation coefficient. The significance level for all tests was set to $p < 0.05$. A trend to significance was considered for analyses in which p values were in the range $0.05 < p < 0.01$.

For specific materials and methods of each section, please check each corresponding chapter for detailed description.

4. RESULTS/DISCUSSION

- **CHAPTER I:** Anti-tumour immune response in GL261 glioblastoma generated by Temozolomide Immune-Enhancing Metronomic Schedule monitored with MRSI-based nosological images. Published: https://pubmed.ncbi.nlm.nih.gov/31926117/

- **CHAPTER II:** Immune system-related changes in preclinical GL261 glioblastoma under TMZ treatment: explaining MRSI-based nosological imaging findings with rt-PCR analyses. Published: https://pubmed.ncbi.nlm.nih.gov/34071393/

- **CHAPTER III:** One step beyond for molecular profiling of the TME during TMZ response to treatment or relapse in GL261 GB bearing mice: GAM population, metalloproteases and PD-L1 expression profiles analyses by rt-PCR approaches.

- **CHAPTER IV:** Assessment of T cell and natural killer populations in control and TMZ-treated GL261 GB tumours by flow cytometry approaches.

Chapters I and II are included as published papers in this PhD thesis[2].

---

[2] Please note that due to copyright restrictions set by Publishers, Chapter I is presented in its pre-print format. Also consider that reference list at the end of this thesis is related to introduction, chapters III-IV and the general discussion. References regarding published papers as well as their supplementary materials may be found at the end of their corresponding subsection.

4.1. CHAPTER I: ANTI-TUMOUR IMMUNE RESPONSE IN GL261 GLIOBLASTOMA GENERATED BY TEMOZOLOMIDE IMMUNE-ENHANCING METRONOMIC SCHEDULE MONITORED WITH MRSI-BASED NOSOLOGICAL IMAGES.

Anti-tumour immune response in GL261 glioblastoma generated by Temozolomide Immune-Enhancing Metronomic Schedule monitored with MRSI-based nosological images

Shuang Wu [+] [1]| Pilar Calero-Pérez [+] [1, 4]| Lucia Villamañan [+] [1] | Nuria Arias-Ramos[1]| Martí Pumarola[2]| Sandra Ortega-Martorell[3] | Margarida Julià-Sapé[4, 5] | Carles Arús [1, 4, 5] | Ana Paula Candiota [4, 1, 5]

[+] These authors contributed equally to this work.

[1] Departament de Bioquímica i Biologia Molecular, Unitat de Bioquímica de Biociències, Edifici Cs, Universitat Autònoma de Barcelona, Cerdanyola del Vallès, Spain

[2] Unit of Murine and Comparative Pathology. Department of Animal Medicine and Animal Surgery, Veterinary Faculty, UAB, Cerdanyola del Vallès, Spain

[3] Department of Applied Mathematics, Liverpool John Moores University, Liverpool, UK

[4] Centro de Investigación Biomédica en Red en Bioingeniería, Biomateriales y Nanomedicina (CIBER-BBN), Spain

[5] Institut de Biotecnologia i de Biomedicina (IBB), Universitat Autònoma de Barcelona, Cerdanyola del Vallès, Spain

Correspondence:

Ana Paula Candiota, Centro de Investigación Biomédica en Red en Bioingeniería, Biomateriales y Nanomedicina (CIBER-BBN), Spain. Email: anpaula.candiota@uab.cat

ABSTRACT:

Glioblastomas (GB) are brain tumours with poor prognosis even after aggressive therapy. Improvements in both therapeutic and follow-up strategies are urgently needed. In previous work we described an oscillatory pattern of response to Temozolomide (TMZ) using a standard administration protocol, detected through MRSI-based machine learning approaches. In the present work, we have introduced the Immune-Enhancing Metronomic Schedule (IMS) with an every 6-days TMZ administration at 60mg/kg, and investigated the consistence of such oscillatory behaviour.

A total of n=17 GL261 GB tumour-bearing C57BL/6j mice were studied with MRI/MRSI every 2 days, and the oscillatory behaviour (6.2±1.5 days period from the TMZ administration day) was confirmed during response. Furthermore, IMS-TMZ produced significant improvement in mice survival (22.5±3.0 days for controls vs 135.8±78.2 for TMZ-treated), outperforming standard TMZ treatment.

Histopathological correlation was investigated in selected tumour samples (n=6) analyzing control and responding fields. Significant differences were found for CD3+ cells (lymphocytes, 3.3±2.5 vs 4.8±2.9 respectively) and Iba-1 immunostained area (microglia/macrophages, 16.8±9.7% and 21.9±11.4% respectively).

Unexpectedly, during IMS-TMZ treatment, tumours from some mice (n=6) fully regressed and remained undetectable without further treatment for one month. These animals were considered "cured" and a GL261 re-challenge experiment performed, with no tumour reappearance in 5 out of 6 cases.

Heterogeneous therapy response outcomes were detected in tumour-bearing mice, and a selected group was investigated (n=3 non-responders, n=6 relapsing tumours, n=3 controls). PD-L1 content was found ca. 3-fold increase in the relapsing group when comparing with control and non-responding groups, suggesting that increased lymphocyte inhibition could be associated to IMS-TMZ failure. Overall, data suggest that host immune response has a relevant paper in therapy response/escape in GL261 tumours under IMS-TMZ therapy. This is associated to changes in the metabolomics pattern, oscillating every 6 days, in agreement with immune cycle length, which is being sampled by MRSI-derived nosological images.

KEY WORDS: glioma; orthotopic tumours; immune response; metronomic therapy; immune memory, TMZ; PD-L1

Abbreviations used: **3DiCSI**, 3D Interactive Chemical Shift Imaging; **BTDP**, below threshold detection period; **CPA**, cyclophosphamide; **CTLs**, cytotoxic T lymphocytes; **DAMPs**, damage-associated molecular patterns; **DCs**, dendritic cells; **DMSO**, dimethyl sulfoxide; **DMPM**, dynamic MRSI processing module; **ETL**, echo train length; **FASTMAP**, fast automatic shimming technique by mapping along projections; **FOV**, field of view; **GB**, Glioblastoma; **HIF**, hypoxia-inducible factor; **IMS**, immune-enhancing metronomic schedule; **IT**, inter-slice thickness; **MDSCs**, myeloid-derived suppressor cells; **MTX**, matrix size; **MRI**, magnetic resonance imaging; **MRS**, magnetic resonance spectroscopy; **MRSI**, magnetic resonance spectroscopic imaging; **NA**, number of averages; **NMF**, non-negative matrix factorization; **NS**, number of slices; **PD**, progressive disease; **PD-1**, programmed death-1; **PD-L1**, programmed death-ligand 1; **PR**, pattern recognition; **PRe**, partial response; **PRESS**, point-resolved spectroscopy; **PVDF**, polyvinylidene fluoride; **RANO**, response assessment in neuro-oncology; **RARE**, rapid acquisition with relaxation enhancement; **RECIST**,

response evaluation criteria in solid tumours; **ROIs**, regions of interest; **SDi**, stable disease; **SDS-PAGE**, sodium dodecyl sulfate-polyacrylamide gel electrophoresis; **ST**, slice thickness; **SW**, sweep width; **T2w**, T2 weighted image; **TAT**, total acquisition time; **TE**, echo time; **TEeff**, effective echo time; **TMZ**, temozolomide; **TR**, repetition time; **TRI**, tumour responding index; **TV**, tumour volume; **VAPOR**, variable power and optimized relaxation delay; **VOI**, volume of interest; **WB**, western blot; **wt**, wild-type

1 | INTRODUCTION

Glioblastoma (GB) is the most frequent type of primary central nervous system malignancy in adults with very poor prognosis, which has not significantly improved despite the development of new diagnostic strategies and innovative therapies.[1] Combination chemotherapy after surgery such as Temozolomide (TMZ) with radiotherapy have been used as standard adjuvant therapeutic choice producing an average survival of 14.6 months.[2]

For therapy response assessment in GB, the most common monitoring approach is magnetic resonance imaging (MRI), which is the preferred modality to provide information about tumour size and local tumour tissue extension.[3] Radiological and clinical guidelines are used to evaluate GB response to therapy, particularly through the application of the response assessment in neuro-oncology (RANO)[4] and Response Evaluation Criteria in Solid Tumours (RECIST) criteria.[5] However, MRI information has been shown to be inaccurate due to the pseudoresponse and pseudoprogression phenomena occurring in some cases.[6] Functional and molecular imaging can provide more accurate information and has attracted a lot of attention in the last decade. Among functional methods, magnetic resonance spectroscopy (MRS) may provide information about the metabolomic profile of the investigated lesion.[7,8] Compared to MRS merely acquiring a single spectrum from a certain volume, magnetic resonance spectroscopic imaging (MRSI) is a technique that can provide metabolomic information superimposed to anatomical information, making it possible to gather this type of information from different regions of the studied tissue.[9,10] In this sense, MRSI might be an interesting approach to complement MRI information in evaluating tumour response to therapy.

Furthermore, the MRSI signal obtained from different types of tissue can be automatically categorized by pattern recognition (PR) techniques creating nosological maps potentially useful to detect and characterize therapy response in a noninvasive way.[11–13] In this respect, the tumour responding index (TRI) as an evaluation parameter has been put forward to measure the extent of response to treatment using the obtained nosological images.[14] In previous studies from our group, the multi-slice MRSI technique has allowed us to observe TRI oscillations (ca. 6 days period) in GL261-tumour bearing mice treated with TMZ.[14] Moreover, other authors have described that treatment with alkylating agents (e.g., TMZ) trigger the host immune system recruitment, eventually leading to tumour cell death.[15] Still, it has been described that the whole immune cycle in mice brain usually requires around six days[16], which agrees with the oscillation period found in previous studies.[14] Beyond

that, it was described that administering chemotherapy with consecutive cycles every 6 days could trigger immune system activation[17] and we coined the expression "Immune-Enhancing Metronomic Schedule" (IMS) for this type of administration protocol[18]. In the late steps of each immune cycle, activated T cells traffic to and infiltrate the tumour bed, specifically recognizing and binding cancer cells and killing their target.[19] In addition, microglial and macrophage cells, which can contribute up to 30% of a brain tumour mass, play a role in GB growth control.[20]

Programmed death-1 (PD-1) and its ligand (PD-L1) play a key role in tumour immune escape and the modulation of tumour microenvironment, closely related with tumour generation and development.[21] Chemotherapy can modify this tumour microenvironment. Thus, a recent study on 30 patients with thymic epithelial tumours revealed that PD-L1 expression increased in patient's tumours after chemotherapy.[22] Similar findings have been communicated in other types of tumour such as rectal adenocarcinoma and breast cancer.[23,24] These studies reveal a potential link between chemotherapy and tumour immunoresistance. However, little is known about how PD-L1 content changes in GB after chemotherapy, neither preclinical nor clinical.

Consequently, in this work, our goal was to observe the evolution of TRI in GL261 tumour-bearing mice treated with IMS-TMZ which was expected to enhance immune system participation in response to therapy. Furthermore, the tumour-associated immune population was characterized by histopathology studies, the contribution of PD-L1 to tumour relapse was investigated by western blot (WB) analysis, and the long-term antitumour immune memory was examined by re-challenging TMZ-cured mice with GL261 glioma cells.

2 | MATERIALS AND METHODS

2.1 | GL261 cells

GL261 mouse glioma cells were obtained from the Tumour Bank Repository at the National Cancer Institute (Frederick, MD, USA) and were grown as previously described.[25] Cells were checked for mouse STR profile and interspecies contamination, as well as PCR evaluation to discard Mycoplasma and virus contamination.

2.2 | Animal model

All studies were approved by the local ethics committee (*Comissió d'Ètica en Experimentació Animal i Humana* (CEEAH, https://www.uab.cat/web/experimentacio-amb-animals/presentacio-1345713724929.html), according to the regional and state legislation (protocol CEA-OH-9685 / CEEAH-3665).

A total of 37 C57BL/6 female wild-type (wt) mice weighing 22.4±2.2 g were used in this study. Six out of 37 C57BL/6 GL261 tumour bearing mice were generated in a previous study[14] and further analyzed by histopathology studies in the present work. Thirty-one C57BL/6 GL261 tumour bearing additional mice were generated for this work (See Figure 1 and Table 1). They were obtained from Charles River Laboratories (l'Abresle, France) and housed in the animal facility of the *Universitat Autònoma de Barcelona*. Tumours were induced in C57BL/6 mice by intracranial stereotactic injection of 10^5 GL261 cells as previously described by us.[26] Mice were weighed every other day and tumour volumes were followed twice a week using T2 weighted image (T2w) MRI acquisitions. Mice with the most homogeneous weights and tumour sizes were randomly chosen before therapy start to make experimental groups.

2.3 | Animal treatment

For *in vivo* experiments, TMZ (Sigma-Aldrich, Madrid, Spain) was dissolved in 10% dimethyl sulfoxide (DMSO) in saline solution (0.9% NaCl). IMS-TMZ 60 mg/kg was administered to n=19 tumour-bearing mice using an oral gavage, every 6 days, from day 11 post inoculation (p.i.), while control mice received 10% DMSO vehicle. After treatment, animals meeting endpoint criteria were euthanized by cervical dislocation according to animal welfare protocol advice for ethical reasons, the brain was removed, and tumour resected. Animals cured by the IMS-TMZ therapy were followed up and a re-challenge experiment was carried out (see section 2.4 for further details).

Regarding the histopathological analysis, six mice were used, four treated with TMZ and two controls from.[14] For these cases the TMZ administration scheme was the one described in previous studies, shown in Figure S1A. Still, control animals from [14] did not receive 10% DMSO vehicle.

2.4 | Tumour-specific Immune memory studies

2.4.1 |Criteria for cured mice

When GL261 tumours were reduced after IMS-TMZ treatment until abnormal mass detection by MRI was no longer possible, or its volume remained stable (usually below 2 mm^3) during at least 2 weeks, TMZ administration was halted. Then, MR images were acquired twice a week. Whenever the volume of the residual/abnormal mass was stable or decreased for one month, mice were transiently declared "cured" as in [17].

2.4.2 |Re-challenge experiment

Mice cured by the IMS-TMZ treatment (n=8) were inoculated with GL261 cells again, symmetric but contralateral to the initial injection site. For re-implantation, three C57BL/6 female wt mice were also implanted as controls, to check for consistency and

growth rate in contralateral side. All mice were followed-up (weight + welfare parameters) twice a week and volumetric T2w MRI was acquired once a week.
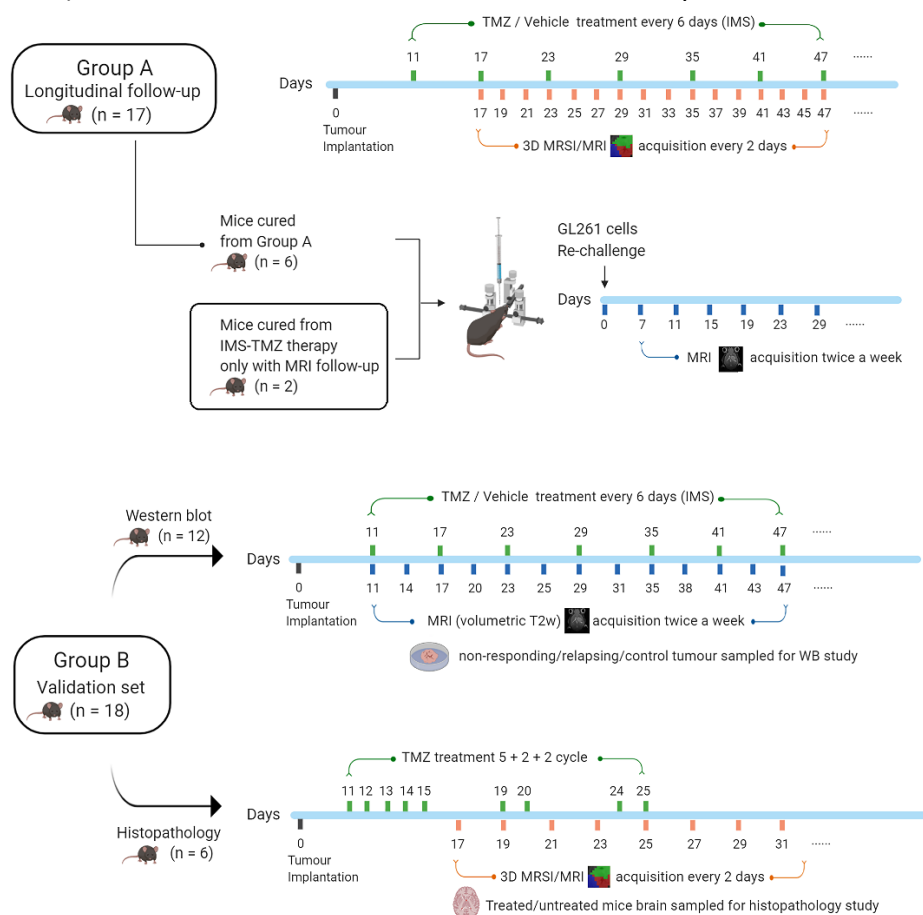
Figure 1. *Experimental schedule of the 37 mice harbouring a GL261 GB included in this work, corresponding to the contents of Table 1.*

2.5 | In vivo MRI and MRSI studies

2.5.1 | Data acquisition

In vivo MRI/MRSI studies were performed at the joint nuclear magnetic resonance facility of the *Universitat Autònoma de Barcelona* and *Centro de Investigación Biomédica en Red-Bioingeniería, Biomateriales y Nanomedicina (CIBER-BBN)* (Cerdanyola del Vallès, Spain), Unit 25 of NANBIOSIS (www.nanbiosis.es). The 7T Bruker BioSpec 70/30 USR spectrometer (Bruker BioSpin GmbH, Ettlingen, Germany) equipped with a mini-imaging gradient set (400 mT/m) was used. A 72 mm inner diameter linear volume coil was used as transmitter, and a mouse brain surface coil as a receiver for brain MRI studies.

Mice were positioned in a bed, which allowed delivery of anaesthesia (isoflurane, 1.5-2.0% in O_2 at 1 L/min), with an integrated heating water circuit for body temperature regulation. Respiratory frequency was monitored with a pressure probe and kept between 60–80 breaths/min.

Table 1. *Table illustrating animal distribution in different groups investigated in this work.*

Group	Longitudinal follow-up			Validation set				
				Western blot			Histopathology	
Treatment	IMS-TMZ		IMS-vehicle	IMS-TMZ		IMS-vehicle	5+2+2 TMZ	Non-treated
Mice codes	C1263	C1276#	C1258	C1288	C1343	C1300	C1100	C1110
	C1264	C1281#	C1260	C1319	C1349	C1317	C1108	C1111
	C1270	C1284#	C1261	C1356		C1266	C971	
	C1380	C1285#	C1359	C1290			C1022	
	C1383	C1286#	C1360	C1292				
		C1382#	C1361	C1341				
				C1342				
Number of animals	17			12			6	
MR data	MRSI/MRI			MRI			MRSI/MRI	

Note: # means cured cases (see Figure for representative cases and section 2.4.1 for the "cured mice" criteria). Total "n" (35) is different from the n stated in section 2.2 and 3.1 (37) because two cases (C1345 and C1351) did not have full longitudinal follow-up with MRI and MRSI, but still, were followed up only with MRI (see section 2.4.1).

MRI studies

GL261 tumour-bearing mice were screened by acquiring high resolution coronal T2w images using a Rapid Acquisition with Relaxation Enhancement (RARE) sequence to detect brain tumour presence and to monitor its evolution stage with repetition time (TR)/effective echo time (TEeff) = 4200/36 ms. The whole set of parameters used in MRI acquisitions can be found in the supplementary file. MRI data were acquired and processed on a Linux computer using ParaVision 5.1 software (Bruker BioSpin GmbH, Ettlingen, Germany).

MRSI studies

The MRSI acquisitions were performed every two days with mice in the longitudinal group, starting at day 15-17 post-implantation.

Consecutive 14 ms echo time (TE) MRSI with point-resolved spectroscopy (PRESS) localization grids were acquired individually across the tumour, using as a reference T2w high resolution images, as described in previous work.[14] Tumour was covered by 3-4 MRSI grids with matrix size of 10x10 or 12x12 (technical details of MRSI acquisitions can be found in the supplementary file). In order to ensure quality of the acquired data, shimming was performed individually for each MRSI grid. MRSI grids were spatially located such that the volume of interest (VOI) included most of the tumoural mass as well as normal/peritumoural brain parenchyma.

Water suppression was performed with Variable Power and Optimized Relaxation Delay (VAPOR), using a 300 Hz bandwidth. Linear and second order shims were automatically adjusted with Fast Automatic Shimming Technique by Mapping Along Projections (FASTMAP) and six saturation slices (ST, 10 mm; sech-shaped pulses: 1.0 ms/20250 Hz) were positioned around the VOI to minimize outer volume

contamination in the signals obtained.

2.5.2 | MRI and MRSI Processing and Post Processing

Tumour volume calculation

Manual segmentation of abnormal brain mass in T2w images was performed and tumour volumes were calculated from T2w high resolution horizontal images using the equation:

$$TV\ (mm^3) = [(AS_1 \times ST) + [(AS_2 + (...) + AS_{10}) \times (ST + IT)]] \times 0.075^2 \qquad \text{(Equation 1)}$$

Where TV is the tumour volume, AS is the number of pixels contained in the region of interest in each slice of the MRI sequence, ST is the slice thickness, IT the inter-slice thickness and 0.075^2 the individual pixel surface area in mm^2. The tumour area was calculated from pixels in each slice with ParaVision 5.1 software. The inter-slice volume was estimated adding the inter-slice thickness to the corresponding slice thickness in Equation 1.

Brain MRSI post‐processing and pattern recognition strategies

MRSI data were post-processed essentially as described in [25]. Briefly, data were initially pre-processed at the MR workstation with ParaVision 5.1, and then post-processed with 3D Interactive Chemical Shift Imaging (3DiCSI) software package version 1.9.17 (Courtesy of Truman Brown, Ph.D., Columbia University, New York, NY, USA) for line broadening adjustment (Lorentzian filter, 4 Hz), zero-order phase correction and exporting the data in ASCII format. Dynamic MRSI processing Module (DMPM), running over MatLab 2013a (The MathWorks Inc., Natick, MA, USA) was used to align all spectra within each MRSI matrix, using the choline signal as reference, 3.21 ppm). The 0–4.5 ppm region of each spectrum in the MRSI matrix was normalized to unit length and exported in ASCII format for performing the PR analysis. No baseline correction was performed in these spectra.

After that, the non-negative matrix factorization (NMF) semi-supervised methodology[27,28] was applied for the extraction of meaningful source signals from the MRSI investigated tumours. From the biochemical viewpoint, the source extraction technique to classify MRS data assumes that in each voxel there is a mixture of heterogeneous tissues and their metabolites from which the contribution of each source can be obtained. A previously described semi-supervised approach[29], which relies on Convex-NMF for the final source extraction, was used for classifying pixels into normal brain parenchyma, actively proliferating tumour and tumour responding to treatment; and for calculating nosologic maps representing the spatial response to treatment. Green colour is used when the GB responding to treatment source contributes the most, blue for normal brain parenchyma, red for actively proliferating

GB and black for undetermined tissue. A more detailed explanation on NMF can be found in the Supplementary file.

2.5.3 | Tumour Responding Index (TRI) calculations

In order to measure the extent of response to treatment using the obtained nosological images, a numerical parameter named TRI was calculated (Equation 2) [14].

$$TRI = \frac{Tumour\ responding\ pixels}{Total\ tumour\ pixels} \times 100 \qquad \text{(Equation 2)}$$

TRI is stated as the percentage of green, responding tumour pixels of all grids over the total tumour pixels of all recorded grids. Then, tentative ranges of TRI categories were established to classify the different response to treatment levels observed in the studied animals, taking into account both TRI percentage and volumetric data from MRI measurements according to RECIST criteria[5]. An adapted set of RECIST criteria was used to classify cases into Progressive disease (PD), Partial response (PRe) or Stable disease (SDi). See the Supplementary file for the adapted RECIST criteria.

In this work, a TRI cycle was defined provided a change between maximum and minimum TRI values was above 10%. Values below this threshold were attributed to possible experimental variability and were not counted as 'cycles'.

2.6 | Antibodies

For histopathology studies, Anti-CD3 antibody (dil. 1:300, rabbit, Ref A0452) was purchased from Dako (Santa Clara, CA, USA) and Anti-Iba-1 antibody (dil. 1:300, goat, Ref ab5076) was purchased from Abcam (Cambridge, UK).

For PD-L1 WB studies, Anti-PD-L1 antibody (dil. 1:400, rabbit, Ref ab233482) was purchased from Abcam (Cambridge, UK), β-tubulin antibody (dil. 1:1000, rabbit, Ref 2146) was purchased from Cell Signalling Technology (Beverly, MA, USA) and secondary antibody towards rabbit IgG (dil.1:2000), conjugated to horseradish peroxidase, was purchased from Bio-Rad (Richmond, CA, USA).

2.7 | Histopathology studies

TMZ-treated cases used for histopathological validation were the following: C1100 (TRI = 61.8%), C1108 (TRI = 70.3%), C971 (TRI = 44.1%) and C1022 (TRI = 46.5%). In addition, two control (non-treated) tumour-bearing mice were also explored (C1110 and C1111). MRI/MRSI data, nosological images and TRI calculations are described in.[14]

Fixed brains were embedded in paraffin and serial horizontal sections were cut, taking into account MRSI slices in order to ensure spatial correlation. Brain was split in half and each half was cut in 20 sections of 5 μm. The upper half of the brain corresponded to MRSI Grids 1 and 2, while the lower half of the brain corresponded to MRSI Grids 3 and 4.

One section corresponding to each MRSI Grid position was selected for CD3+ immunohistochemical staining for detecting the presence of T lymphocytes and Iba-1 immunohistochemical staining for detecting the presence of activated macrophages/microglia in treated and control tumours.

After immunostaining, the preparations were digitized for quantification using a Nanozoomer 2.0HT (Hamamatsu Photonics France, Massy, France). Then, CD3+ positive cells and percentage of Iba-1 positive immunostained cellular areas were counted in each section in fields that corresponded to green or red tumour areas in nosological images. From each chosen area, 5 fields of 0.025 mm^2 were randomly selected at 40x magnification, using NDPview 1.2.53 software (Hamamatsu Photonics France SARL, Massy, France). Fields were placed in the more highly cellular areas, avoiding poor or acellular areas. Exceptionally, in some samples, fewer fields were counted if the corresponding area of the nosological image was not large enough to evaluate 5 fields.

2.8 | PD-L1 expression by Western blotting

Cases used for PD-L1 expression were those with the following codes: fast growth tumours escaping IMS-TMZ therapy right from the start, defined as "non-responding" (C1288, C1319 and C1356, n=3); cases showing transient tumour shrinkage but eventually relapsing, defined as "relapsing" (C1290, C1292, C1341, C1342, C1343 and C1349, n=6). Control cases received 10% DMSO vehicle with the same schedule (C1266, C1300 and C1317, n=3).

Tissue Homogenization and Protein Extraction. Whole GL261 tumours obtained after euthanization at endpoint were weighted and protein extracted as described in [30], details can be found in Supplementary file. Protein concentration was determined by Bradford assay (Bio-Rad) and equal amounts of protein (80 μg) were loaded on 12% Sodium Dodecyl Sulfate Polyacrylamide Gel Electrophoresis (SDS-PAGE), blotted on polyvinylidene fluoride (PVDF) Immobilon-P membranes (Millipore, Darmstadt, Germany), and immunodetected with the corresponding antibodies using a chemiluminescent detection method (Clarity™ Western ECL Blotting Substrates, Bio-Rad, California, U.S.A.). Chemiluminescent signal was obtained with Chemidoc MP Image System and quantified with the ImageJ software.

2.9 | Statistical analysis

Variance homogeneity was assessed with the Levene's test. Sample distribution was assessed with the Kolmogorov-Smirnov test. A two-tailed Student's t-test for independent measurements was used for comparisons, for samples of equal or different variances (depending on the Levene's test result). Comparisons of survival

rates were performed with the Log-Rank test. The significance level for all tests was p<0.05.

3 | RESULTS

Table 1 summarizes the cases described in this study and the analyses performed with each one.

3.1 | IMS-TMZ treatment and follow up in GL261 tumour-bearing mice

In this part of the study 19 mice were used. Among them, 13 mice were treated with TMZ using an IMS protocol and 6 were administered with vehicle, also in an IMS administration (see Table 1 for individual codes). The IMS administration scheme can be found in Figure S1A. All mice were followed-up according to the supervision parameters for animal health status and weighted (Figure S1C). The tumour volume at therapy starting (day 11 p.i.) in this section was 5.4 ± 2.6 mm^3, close to tumour volumes in previous work with similar TMZ schedule (6.0 ± 1.2 mm^3)[30]. Tumour volume evolution of vehicle and TMZ-treated mice is shown in Figure S1B. As described before,[31] TMZ treatment with the IMS administration has a positive impact in the survival of GL261 tumour-bearing mice (Figure S1D). Thus, the average survival rate for control mice was 22.5 ± 3.0 days whereas the TMZ-treated animals survived significantly more, 135.8 ± 78.2 days (p<0.05 according to Log Rank Test), being 61.5% of TMZ treated mice alive at day 150 p.i. and some individuals still alive at 464 days p.i.

3.2 | Multi-slice MRSI-based volumetric analysis of therapy response assessment under IMS-TMZ treatment

A longitudinal study was performed with eleven TMZ-treated GL261 tumour-bearing mice and six vehicle treated mice (see Table 1 for individual codes). Mice were studied every two days (see Figure S2A) until endpoint. The start of MRSI explorations was conditioned by the measured tumour volume. According to our experience and data described by our group[31], tumour volumes below 10-20 mm^3 are not properly segmented by MRSI, and this was the cut-off point to start MRSI acquisitions. An example can be seen in Figure S2B. Results are summarized below.

3.2.1| TMZ-treated mice

The relationship between TRI and tumour volume evolution, as well as the corresponding nosological images of three most representative cases of TMZ treated mice are shown in Figure 2 (for the remaining cases, refer to Figures S3 and S4).

Several TRI oscillations were observed in the TMZ-treated mice, and these were generally coincident with SDi and PRe tumour stages (Table S2), according to the

47

adapted RECIST criteria. Oscillations were observed between days 17 and 39 p.i. depending on the case observed. It is worth mentioning that in the first MRSI time points (days 15-19 depending on the case), where the evolution tumour would be still classified as PD, TRI oscillations can already be seen.

In five cases (C1263, C1264, C1270, C1380 and C1383) tumour escaped from therapy and met PD criteria, leading to the euthanization of the mice. During this relapse, which started between days 35-41, either TRI cycles were not found anymore, or this value was no longer reliable. When the slope of the tumour growth increased dramatically or tumour relapsed beyond volumes of ca. 50 mm^3, TRI do not seem to suggest response, even if oscillating features are seen. Moreover, the combination of high tumour volume (>70mm^3) and relatively low TRI (e.g., C1270, TRI <40%) resulted in bad survival outcome in comparison with other cases, and tumour grew uncontrolled until the second TRI oscillation appearance.

Regarding cases with complete follow-up, a total of 48 doses of TMZ were given, resulting in 26 TRI oscillation peaks, 21 of them corresponding with tumour growth arrest or volume decrease, whereas 5 TRI peaks were no longer able to coincide with controlled tumour growth (almost exclusively at relapsing time points). In addition, 8 TMZ doses corresponded to periods in which tumour volume were below the minimum volume for nosological imaging segmentation while 2 TMZ doses corresponded to endpoint with no further explorations made.

It is worth mentioning that TRI peak appears ca. 6-8 days after the first therapy administration period. The only case which delayed this appearance – 12 days, but only 6 days after the second therapy dose, C1383– could be due to segmentation problems due to borderline tumour volume between therapy cycles one and two. For all followed tumours, the first TRI peak agreed with a certain decrease in the tumour growth slope.

Spectra acquired were of overall good quality and examples of chosen MRSI spectra for case C1263 are shown in Figure S2A.
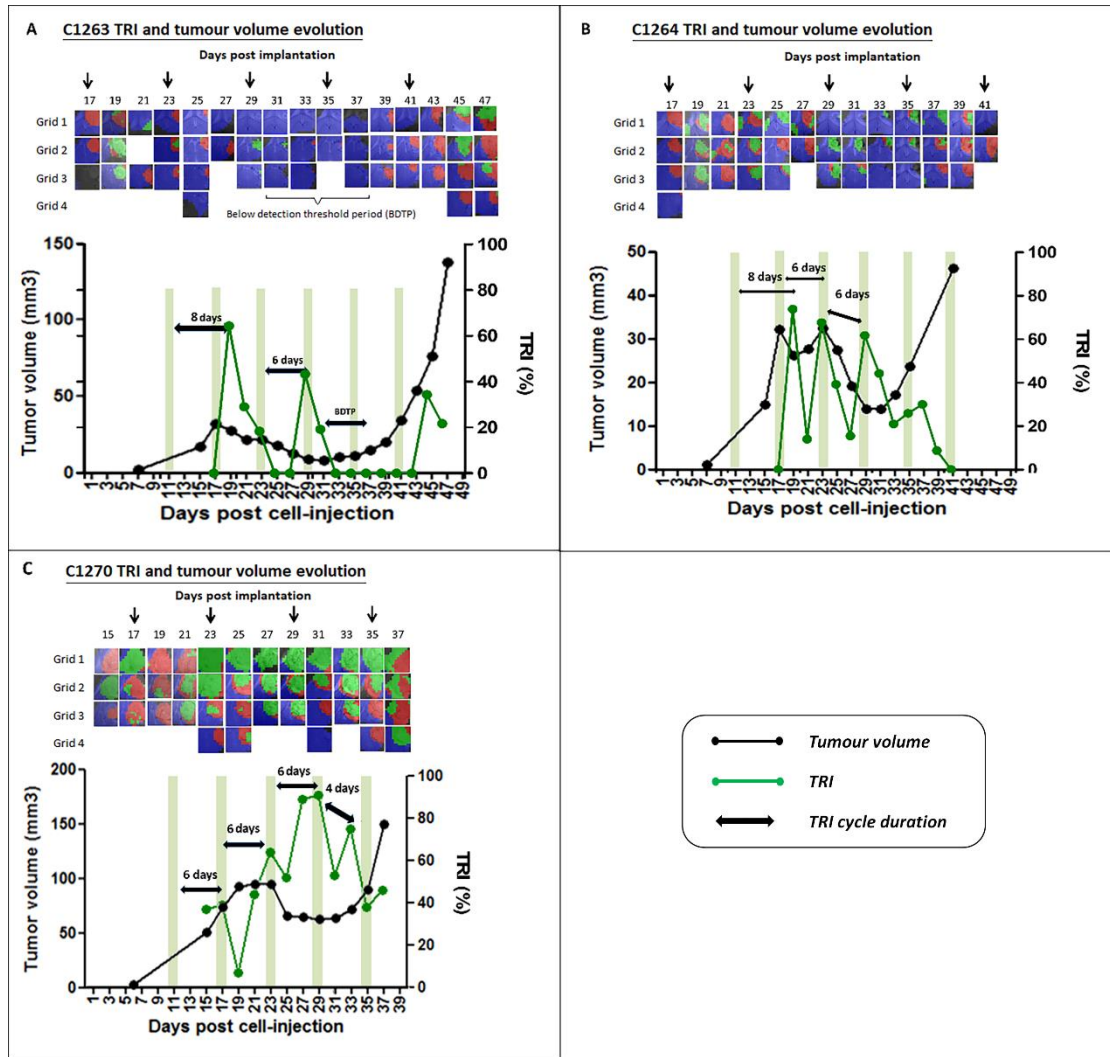
Figure 2. *Nosological images and graphical representation of the tumour volume evolution for the tumour region in the cases (a) C1263, (b) C1264 and (c) 1270. Tumour volume in mm^3 (black line, left axis) and the percentage of green, responding pixels (TRI) obtained taking into account total pixels counting (green line, right axis). In the upper part of every image, chosen time points show the evolution of the nosological images in four rows of colour-coded grids superimposed to the T2w-MRI for each slice. Vertical arrows indicate days of therapy administration. In the graph below, green shaded columns indicate TMZ administration days. TRI cycle duration (therapy administration to next peak maxima) is highlighted in every image. In (a), from Day 31 to Day 37 it was not possible to evaluate TRI evolution because tumour volume was below the limit for confident MRSI segmentation, which we called below detection threshold period (BDTP).*

3.2.2| Additional cases from cured mice

For mice with full MRI/MRSI follow-up, six of the TMZ treated mice analyzed (see Table 1 for individual codes) had tumours which disappeared after IMS-TMZ treatment, which obviously prevents the generation of nosological images. Details about their tumour volume and TRI evolution can be found in the supplementary material (Figure S3).

As in other TMZ-treated mice, TRI oscillations or punctual increases could be found for most cases. For example, in the first days of MRSI monitoring, TRI cycles were found in four out of six cases. After that time, the relationship between tumour volume evolution and TRI changes was different in every case.

The maximum volume achieved in this group was 37.4 mm^3, and tumour volume decrease was found around the second TMZ therapy dose, lasting until ca. day 30 p.i. For cases with enough volume for nosological imaging segmentation, oscillations were seen during active response. For example, case C1276 (Figure S3A) showed TRI oscillations from days 17 till 27 p.i., when the tumour was classified either as SDi or PRe. Case C1382 presented TRI oscillations at days 17 and 21 p.i., followed by a gradual decrease which concurred with tumour disappearance.

Cured mice had tumours with a trend to smaller volumes at therapy start (average 4.3 ± 1.4 mm^3 vs 6.9 ± 3.4 mm^3 in non-cured mice from this work), although this difference was not statistically significant.

3.2.3| Vehicle-treated mice

Six vehicle-treated mice were analysed for comparison purposes (Figures S5 and S6). The tumour evolution in this group was classified as PD throughout the period of MRSI analysis (Table S2), as expected. The TRI oscillatory pattern is not observed in any of the cases, except in the C1258, where a possible TRI cycle is observed (Figure S5), although tumour growth slope did not decrease. In the remaining 5 cases, no TRI cycles were observed, indicating that clear TRI oscillations are only present when tumour-bearing mice respond to IMS-TMZ treatment.

3.3 | Histopathology validation

Six mice were used for histopathological analysis, 4 treated with TMZ and two non-treated. Comparison of responsive and unresponsive zones (i.e., green and red areas of the nosological images) was performed (see Figure 3). Responsive zones presented significantly higher CD3+ positive cell counting and higher percentage of Iba-1 immunostained area in comparison with unresponsive zones. Values for CD3+ were 4.8 ± 2.9 and 3.3 ± 2.5 CD3+ positive cells in responsive and unresponsive zones, respectively (n=53 and n=94 fields). For Iba-1, the percentage of positive immunostained area was 21.9 ± 11.4% for responsive and 16.8 ± 9.7% for unresponsive zones (n=53 and n=95 fields). Individual fields from responsive zones could achieve values up to 42% of area occupancy by Iba-1 positive cells while unresponsive zones could reach values as low as 1.4%. Although it could be contributing to the MRSI-detected spectral pattern changes, there is variability, and differences between regions within the same tumour are not so clear cut in certain individual cases.
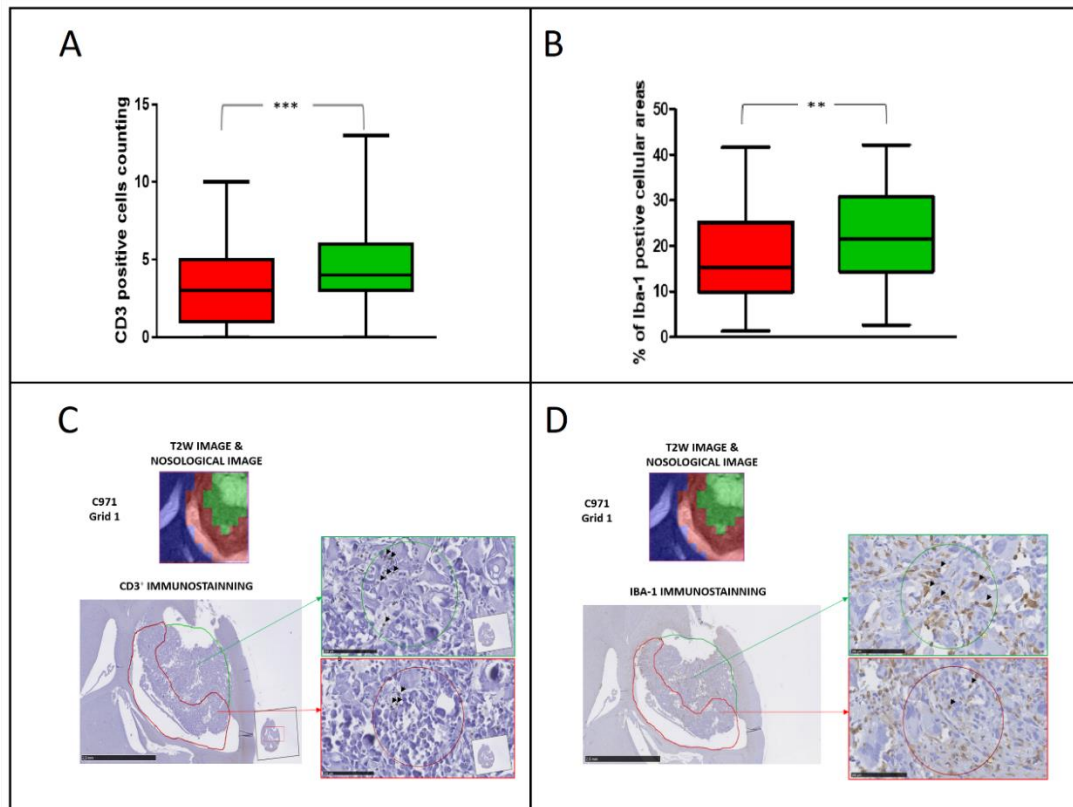
Figure 3. Boxplot showing (a) CD3$^+$ positive cells/field (n=147) and (b) % of Iba-1 positive immunostained cellular areas/field (n=148) in red and green areas of each MRSI grid of TMZ-treated and control cases. Significant differences were observed for CD3$^+$ positive cell counting (P = .0009) and for Iba-1 positive immunostained cellular areas (P = .0011) with unpaired Student's t test. The limits of the box represent quartiles 1 (Q1) and 3 (Q3) of the distribution, the central line corresponds to the median (quartile 2). The whiskers symbolize the maximum and minimum values in each distribution. Examples of (c) CD3$^+$ and (d) Iba-1 immunostaining in different analyzed fields of case C971 corresponding with green (responsive) and red (unresponsive zones). Nosological images obtained from Grid 1 of the case C971 superimposed to the T2w-MRI. Both green and red zones could be distinguished within the tumour, showing a heterogeneous pattern of response. The red and green areas from the nosological image have been manually drawn over the tumour (shown in red and green lines). One representative field has been selected in each area (red and green circle have the same area). In the circular fields shown, cell count was 6 and 3 positive cells for CD3+ and 15.54% and 10.49% of positive immunostained cellular areas for Iba-1, for green and red areas, respectively. Arrows point to positive cells. Magnification (40×).

3.4 | PD-L1 content in GL261 tumours

PD-L1 content was analyzed in 12 frozen dissected GL261 tumours: 9 from IMS-TMZ treated mice and 3 control, with growth curves shown in Figure S7. WB results and quantification are shown in Figure 4. After normalization to Tubulin, PD-L1 band intensity was 0.23 ± 0.04 in the GL261 control group whereas it was 0.64 ± 0.14 in the relapsing GL261 group and 0.19 ± 0.02 in non-responding group. The PD-L1 content was found significantly higher (p<0.001) in the relapsing group when comparing with control group (2.8-fold) and non-responding group (3.4-fold), whereas no differences

were found for PD-L1 content between non-responding and control tumours.
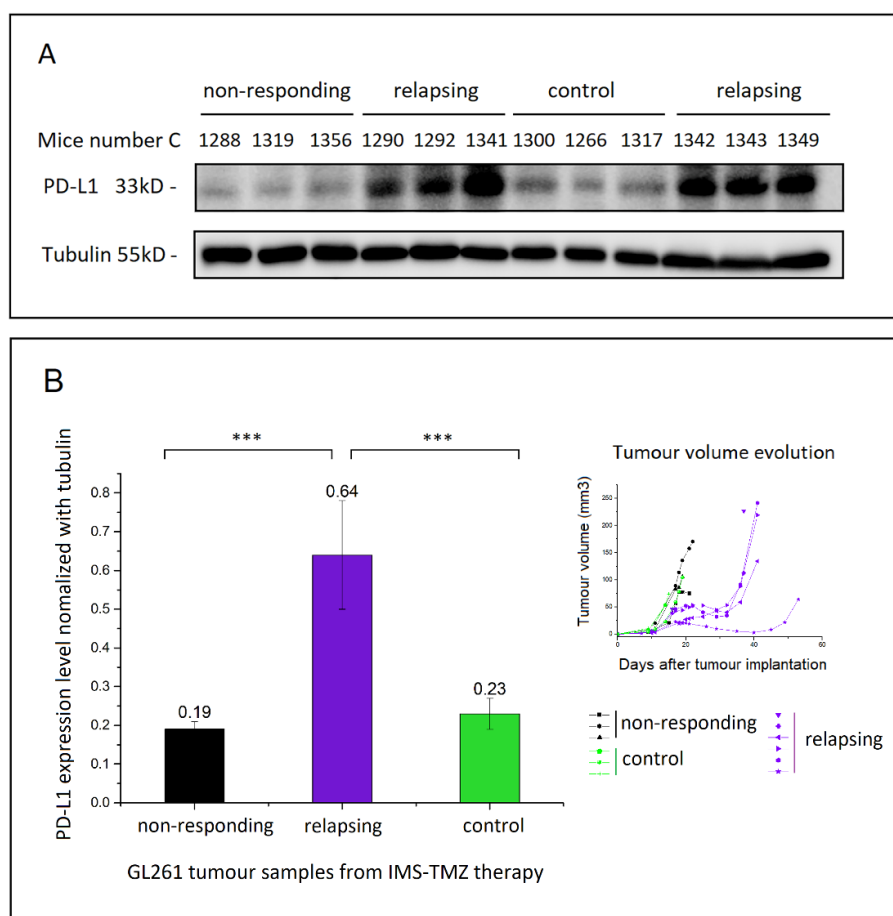
Figure 4. *Frozen dissected tumours from IMS-TMZ-treated mice (a) WB for tumour total protein homogenate (80 µg) from different mice treated with IMS-TMZ (nonresponding and relapsing tumours), n = 9, compared with vehicle-treated mice, n = 3. PD-L1 and Tubulin proteins were analyzed. (b) Quantification of WB result including the non-responding, relapsing and control tumour samples, PD-L1 band intensity (after normalization to Tubulin) are 0.19 ± 0.02 in the non-responding group, 0.64 ± 0.14 in the relapsing group and 0.23 ± 0.04 in the control group. ***P < .001 for Student's t test for the comparison among nonresponding, relapsing and control group.*

3.5 | IMS-TMZ activates Tumour-specific immune memory

We were also interested in a preliminary evaluation of whether IMS-TMZ treatment could induce long-term antitumour immunity in the cured C57BL/6 mice (tumour growth curves shown in *Figure S8*). For that, the re-challenge experiment described in section 2.4.2 was performed. Three wt mice were implanted in parallel as controls. Control tumours grew normally and no significant differences were found with standard GL261 tumour doubling time of 2.4 ± 0.3 days[32]. Regarding the re-challenged mice, only one of re-implanted tumours in the TMZ-cured mice (case C1286) grew after 10 days while the rest remained tumour-free until present time (range 150-464 days post-implantation). With respect to case C1286, TMZ was administered as usual in an

IMS protocol and tumour disappeared after only one TMZ dose. After being cured again, this mouse has been followed-up (weight + welfare parameters) twice a week and MRI acquisitions were acquired once a week, for the rest of its lifetime (until 175 days post-implantation) and no tumour mass has been detected in its brain.

This high rate (100 %) of tumour rejection (Table 2) suggests that the cured mice seem to be acquiring antitumour immune memory to GL261.

	Primary tumour implantation wt control mice	Tumour re-challenge IMS-TMZ cured mice
Mice with growing tumour	3	0
Mice rejecting tumour	0	8
Tumour rejection rate	0%	100%

Table 2. *Comparison of GL261 tumour take rates between primary tumour implantation, and GL261 re-challenge in IMS-TMZ-cured mice.*

The tumour volume and TRI graph of a representative case (C1276) displaying immune memory is shown in Figure 5. For this specific case, tumour reached a maximum volume of 18.2 mm^3 at day 17 p.i., decreasing to 1.5 mm^3 after 7 TMZ doses. Two TRI cycles were observed during tumour-shrinking (Figure S4). The scar/residual abnormal mass caused by tumour growth was stable for one month; therefore, the mouse was declared as cured (see section 2.4.1). On day 74 p.i. this cured mouse was re-implanted on the other side of the brain parenchyma with GL261 cells. No tumour mass was detected in the cured mouse brain within 3 months after tumour re-implantation.

53
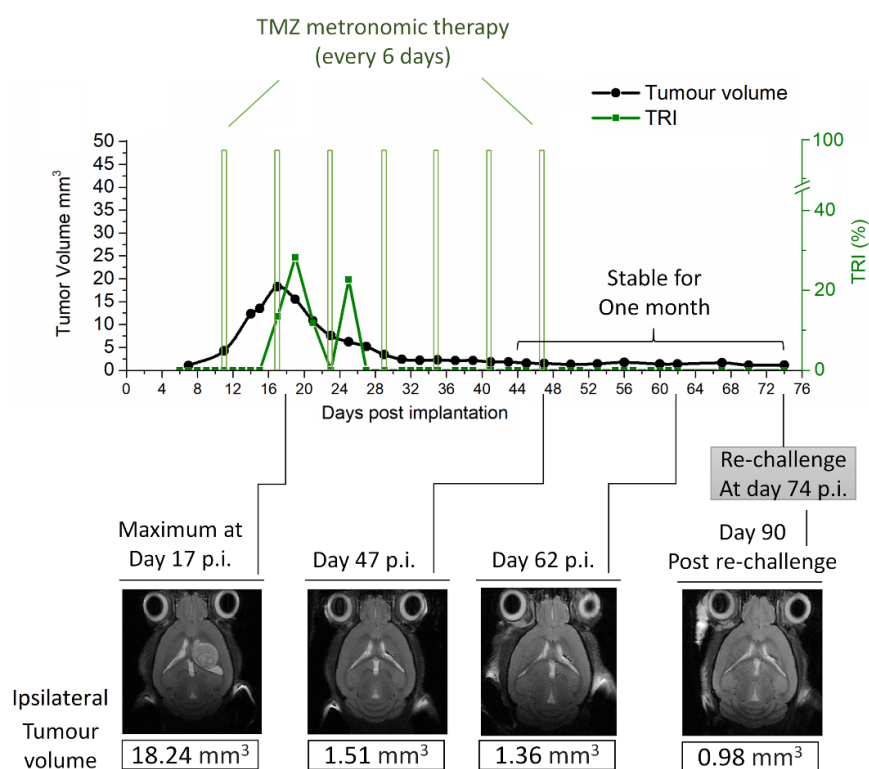
Figure 5. *Graphical representation of the tumour volume evolution, TRI cycles and re-challenge time point of cured mouse (C1276). T2w images shows that the tumour reached the maximum volume, 18.2 mm^3 at Day 17 p.i., then tumour was ablated after seven doses of IMS-TMZ therapy, and the scar caused by tumour growth was stable for 1 mo. (cured). On Day 74 p.i., cured mouse was re-implanted on the other side of the brain parenchyma with GL261 cells, and no tumour mass was detected in the cured mouse brain within 3 mo. (90 d post–re-challenge) after tumour cells re-injection.*

4 | DISCUSSION

4.1 | IMS-TMZ therapy triggering a repeated oscillatory TRI behavior

During this work, eleven TMZ-treated and six vehicle treated tumour-bearing mice were analyzed by MRSI-based nosological images (representative cases shown in Figures 1, S3-S6). Results confirmed the oscillatory response level (i.e., TRI values) of TMZ-treated mice due to changes in the metabolomic spectral pattern. This was already shown in a previous study with the standard 5-2-2 TMZ administration protocol in a smaller cohort of animals [14] but its reproducibility with the IMS-TMZ protocol had not yet been tested. Multi-slice MRSI acquisitions allowed us not only to monitor TRI oscillations along the period of transient response to therapy, but also to sample intratumoural heterogeneity. The TMZ administration seems to be the responsible of "setting" cycles, since the period between therapy administration and appearance of a TRI peak is consistent along different cases, ranging 4-8 days during regular transient response periods. Also, it has been shown that, prior or during tumour relapse, these oscillations disappeared, with a different TRI behavior: it either assumed an increasing, non-oscillating trend or only showed small, incipient increases. This confirms that consistent TRI oscillations are related to metabolomic changes due to tumour response, but mostly absent during tumour relapse. The average value for time lapse recorded between TMZ administration and TRI peak appearance (being TRI peak average 66.8 ± 22.3 % in all studied cases, n = 11) was 6.2 ± 1.5 days.

In control cases (Figures S5-S6), no TRI oscillations were observed, with the possible exception of case C1258, although no coherent tumour decrease was seen at possible TRI peak in C1258. This suggests that the lack of response to therapy leads to absence of clear TRI oscillation. In such cases, an increase in TRI could suggest local metabolomics changes resembling the ones observed during therapy (e.g., spontaneous host immune response), although these are clearly not enough to arrest tumour growth.

Results from TMZ-treated mice suggest that TMZ administration "resets" the immune system cycle clock, since TRI maximum peaks appear in average 6.2 ± 1.5 days after therapy administration (Figures 1, S3 and S4). This value is in agreement with work

previously published by us with a non-metronomic TMZ administration schedule (distance between TRI maxima, 6.3 ±1 .3 days, n=4 [14]) and also with calculations approached in single-slice acquired cases (distance between TRI maxima, 6.2 ± 2.0 days, calculated for n=3 cases from [29]). This value is also in line with the length of immune cycle in mice brain, described to be of ca. 6 days [33]. Moreover, taking into account that TMZ has already been described to behave as an immunogenic drug, which triggers the exposure and release of immunogenic signals [34,35], we hypothesize that each TMZ cycle is triggering a new 'turn' of the immune cycle leading to an arrival of new sub-clones of immune system cells within tumours ca. 6 days later. This would contribute to metabolomic pattern changes sampled by MRSI acquisitions, leading to changes in nosological images (see figure 6 for a schematic explanation).

Still, it is worth noting that TRI peak maxima are also accompanied, in some instances, by a reduction of the tumour volume characterizing either a partial response case (see Figure 2, case C1263 and C1270) or stable disease (case C1264). This reproducible behavior may underlie that a high TRI is indicating an active anti-tumoural response triggered by the immunogenic potential of TMZ.

The monitoring of TRI evolution could enable the design of personalized therapeutic schemes, adapting the TMZ therapy schedule in order to obtain an optimal anti-tumour effect. Once fully validated that the 'green pattern' is associated with a productive action of the host immune system against the tumour, its presence would indicate that no further TMZ doses are needed until TRI starts decreasing, which would mean that a new, resistant clone of tumour cells is replacing cells killed by immune system action. The new TMZ administration would trigger a new turn in the immune system cycle, with priming and amplification of lymphocytes enabling them to kill this new tumour cells sub-clone.
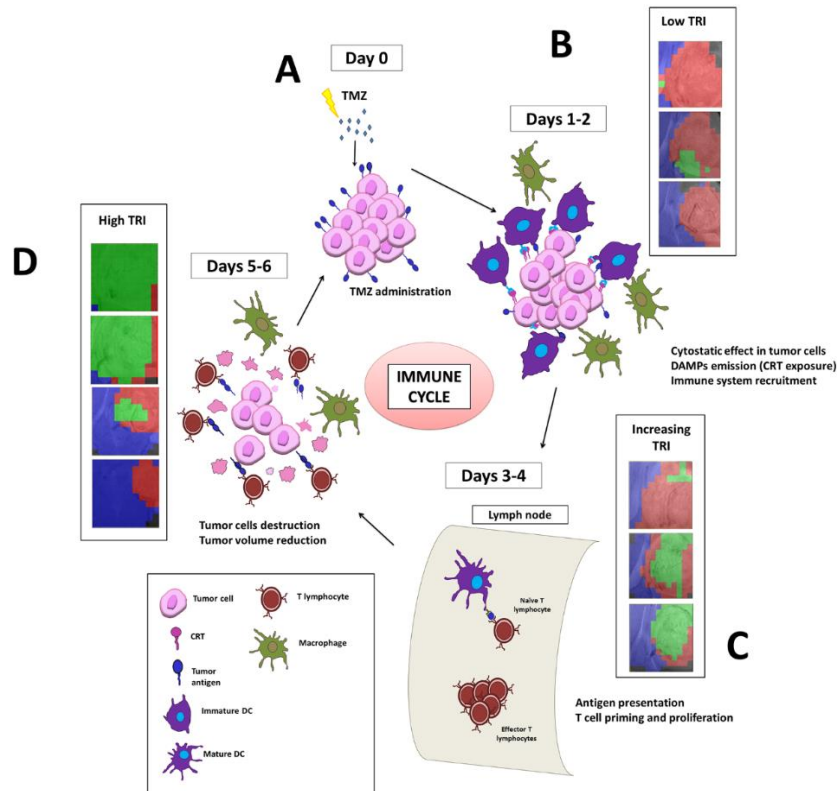
Figure 6. Hypothetic schema of the cycle for immune response against a preclinical GB tumour after two therapy cycles and resulting nosological images, using as example images from case C1270. The whole cycle is thought to last 6 to 7 d in mouse brain. When treated with TMZ at Day 0 (A), tumour cells release and expose immunogenic signals which attract dendritic cells (DCs) and macrophages to the tumour site. Initially (Days 1 and 2), the immune system is not especially active against these particular tumour cell clones and the nosological images correspond mostly to actively proliferating tumour, and thus TRI is low (B). At Days 3 and 4, DCs migrate to the lymph nodes and prime naïve CD8+ effector T cells, which start to proliferate. It is important that TMZ (or any antiproliferative agent) not to be administered in this period because it would impair lymphocytes proliferation and hamper proper immune response. TRI may start increasing between Day 3 and Day 4 (allowing for inter-subject variability) partially due to innate immune system action against tumour or to primed lymphocytes from a previous therapy cycle attacking the tumour again (C). At Days 5 and 6 of the cycle, a new wave of effector T cells arrive at the tumour site and jointly with macrophages efficiently attack the tumour. In this period, we may observe a TRI peak maximum and, in some instances, even reduction in tumour volume (D).

One of the handicaps of the MRSI-based nosological image calculation technique is that small sized tumours do not produce confident segmentation (e.g. case C1263 in which the tumour zone was mislabeled as normal brain parenchyma, Figure S2B). We named this period "below threshold detection period" (BTDP) since the semi-supervised source analysis software was not able to properly segment the tumour. However, since small tumours have a trend to better survival or either cure, the metabolomics signature would not be as relevant as in tumours with larger volumes, in which this information is relevant to assess the efficacy of a therapeutic strategy.

These results demonstrate how non-invasive methods based on PR analysis of MRSI acquisition can be applied in order to improve therapeutic success, making it possible to develop enhanced and personalized therapies based on metabolomic information, which takes place before or in the absence of MRI volume-related changes.

Finally, if the relationship between TRI cycles and efficient host immune system attraction for tumour fighting is fully confirmed, we should be also able to evaluate and quantify the response level in combined treatments (e.g. synergistic TMZ+ anti-PD-1 or TMZ + CX-4945, an ATP-competitive CK2 protein kinase inhibitor described for preclinical GB treatment[30]), as well as to refine administration timing. Our surrogate biomarker for therapy response, coded in nosological images, was developed with TMZ-treated cases [29] and one of the fundamental questions then was whether it would be useful with other therapeutic agents. Indeed, it was also proven robust to detect tumour response in cyclophosphamide (CPA) treated mice[31], suggesting that the changes sampled are not restricted to TMZ, but rather being related to local changes during different treatments. Those would be probably related to immune system action against tumours, which could be an extremely valuable biomarker in tuning therapy administration to obtain maximal effectiveness and improve outcome.

4.2 | Histopathology results

Our working hypothesis is that the recorded TRI oscillations could be at least partially due to local metabolic changes resulting from immune system action within the tumour tissue. This hypothesis is supported by histopathological findings (section 3.3 of this manuscript), obtained from samples reported in [14]: TMZ-treated samples presented a higher number of lymphocyte-like cells in comparison with untreated samples. This was further confirmed with immunostaining for CD3^{+} (T lymphocytes marker) and Iba-1 (microglia/macrophages marker). Values were significantly higher in tumour zones classified as "responding", in comparison with control cases or "unresponsive" areas. Moreover, the TRI imaging biomarker was proven to be correlated with the proliferation index Ki67 [14,29], also reflecting that metabolomics changes could be related to the proliferation status of tumour cells.

Results obtained in the present work reinforce the concept of IMS-TMZ as a good alternative for GB treatment. This hypothesis needs to be further validated in future work by assessing the recruitment of the host immune system elements through histopathological validation during TRI maximum and minimum values: in addition to CD3 and Iba-1, other markers such as FoxP3 (regulatory T lymphocytes) or specific markers for different polarization extremes of macrophages (M1 and M2 subtypes) will be useful. Importantly, this may be of relevance due to the fact that macrophages/microglia intimately interact with tumour cells and may contribute,

depending on the cellular subtype, to tumour growth, migration and invasion of tumour cell, destruction of the extracellular matrix, neoangiogenesis and an immunosuppressive microenvironment. [36] Also, their quantification at different time points along therapy protocols would be of help to understand better their potential contribution to the metabolomics pattern of responding and non- responding tumours.

4.3 | A possible explanation for resistance to TMZ therapy in GL261 tumours: PD-L1 content increase

Immune evasion is one of the features of cancer[37], and overexpression of PD-L1 on the surface of the cancer cells is one way of escaping the immune system attack.[38] Several studies reveal that up-regulated expression of PD-L1 on tumour cells could be a potential link between chemotherapy and tumour immunoresistance [22–24]. In some cases studied in this work, we observed a transient therapy response to IMS-TMZ followed by fast tumour regrowth. WB results shows that increased PD-L1 content was found in late relapsing tumours when comparing to vehicle-treated tumours, which could provide a possible explanation for relapse in these mice.

In this respect, other authors have already described that treatment with alkylating agents (e.g., TMZ) trigger host immune system recruitment.[15] Our hypothesis is that one of the reasons contributing to GL261 tumour regrowth during IMS-TMZ would be the appearance of tumour cell sub-clones which up-regulate PD-L1. These PD-L1 over expressing tumour cells would be protected from productive T-lymphocyte attack and, consequently, would replace the tumour cell population not overexpressing PD-L1. This would finally lead to tumour escape due to the immunosuppressive effect of increased PD-L1 content. With respect to control tumours, they should barely trigger the production of immunogenic signals due to the lack of damage caused by TMZ, thus resulting in less T cell infiltration into tumour tissue. Accordingly, no selection of tumour cells with increased PD-L1 expression for clonal expansion would happen.

In the case of "non-responding" GL261 tumours, results show that the expression level of PD-L1 is equivalent to vehicle-treated tumours, and lower than in late relapsing ones. Our hypothesis to explain this difference is that "non-responding" tumours would escape therapy by a different mechanism, not yet clarified, rather than "late relapsing" tumours, which could use high PD-L1 content for this. Initial tumour mass duplication time and, eventually, overall tumour mass could probably hamper on its own immune system capability of the host[39], then, no positive selection for PD-L1 high expression clones would be required in this instance for tumours to grow unencumbered. This result brings us significant insight for future research in preclinical GL261 GB, indicating that anti- PD-1 immunotherapy should be more effective as second line treatment in late relapsing GL261 tumours, while combined TMZ and kinase inhibitors such as CX-

4945 may be best for fast growth, "non-responding" GL261 tumours. In addition, kinase inhibitors could contribute an added value through another pathway, impairing hypoxia-inducible factor (HIF) stabilization which in turn could lead to decrease of PD-L1 content.[40] These hypotheses are amenable to test in future work and can lead to further improvement of the outcome of tumour-bearing mice.

4.4 | IMS-TMZ therapy may establish long-term specific anti-tumour immunity.

Alkylating agents such as CPA and TMZ have been described to induce the immunogenic cell death of tumour cells by activating the immune system through the exposure and emission of damage-associated molecular patterns (DAMPs), triggering the recruitment of the host immune system [15,34,41,42]. However, as relevant as eliciting the immune system is avoiding impairing its amplification, and here the IMS gains importance. In the GL261 mouse model, TMZ produces a significantly better survival rate when administered in a 6-day cycle [30] instead of in daily schedule of 5 consecutive days [43]. Alkylating agents, including TMZ, are known to induce side effects related to the immune system such as leukopenia and neutropenia, when administered daily [44]. If TMZ is administered in a continuous schedule, the anti-tumour immune cycle may be hampered due to the inhibition of the proliferation of immune cells, such as primed CD8+ T lymphocytes. On the other hand, in a metronomic administration schedule, TMZ would not interfere with the proliferation of immune cells (time period in Figure 6C), since the next TMZ dose is administered after completion of the amplification step. This would be of benefit to establishing long-term specific anti-tumour immunity. Whereas all control, vehicle-treated mice developed rapidly growing GL261 tumours, IMS-TMZ-cured mice resisted secondary re-challenge tumour development. Our preliminary findings in this suggest that antitumour immunological memory is established by the host immune system of cured mice. The efficiency to trigger antitumour immunity may be supported by the induction of immunogenic cell death by the TMZ effect on GL261 tumour cells[18]. In this respect, we cannot ignore that GL261 is a moderately immunogenic cell line[45]. Thus, a basal part of the response to therapies may be helped by this basal immunogenicity, like in "hot" tumours[46]. Nonetheless, it seems clear that this basal immunogenicity alone is not able to make C57BL/6 mice resistant to GL261 GB growth, in the absence of IMS-TMZ therapy (Figure S1B). Accordingly, this IMS-TMZ may promote long-term therapeutic responses through generation of immunological memory with concomitant prevention of tumour relapse. Wu and Waxman[17] found an increased number of CD8+ T cells and decreased number of circulating macrophages and myeloid-derived suppressive cells (MDSCs) populations in cured mice treated with "metronomic" IMS-like CPA treatment, which rejected the GL261 tumour on re-challenge[17]. In this sense, further work will be needed to explore the actual mechanism of antitumour immune memory in our

system; thus, assessment of different immune populations could be performed in mice that rejected the re-implanted GL261 tumours compared to control tumours. Animal models of cancer are used to produce results of relevance for translation to human patients, eventually. In this respect, one relevant corollary of the described work from the imaging part should be that MRS/MRSI studies of glioblastoma patients during treatment should consider whether oscillatory variations comparable to the ones described in this work for GL261 GB under therapy may be happening, and exercise due caution interpreting single datapoint results to predict response to therapeutic strategies being evaluated.

In addition to the beneficial effects related to immune system, the IMS administration schedule also allows us to reduce the cumulative amount of administered TMZ and avoid consequent development of other tumours due to the mutagenic effects of TMZ, such as lymphomas[31]. Moreover, if a translational protocol reaches the clinical pipeline, the reduction of TMZ dosage should also decrease undesired side effects in patients. The curative effect of the IMS-TMZ protocol alone in 38% of the overall investigated mice, indicates that similar protocols, avoiding damage to the amplification phase of the immune cycle, could be of relevance to patients.

5 | CONCLUSIONS

Results in this work confirmed that the IMS-TMZ protocol produced the expected oscillatory changes in the metabolomic pattern sampled by MRSI-based nosological images. This oscillatory pattern could act as a biomarker of the effective attack of the host immune system onto the GL261 tumour during therapy monitoring, especially during transient response. TMZ administered using the Immune-Enhancing Metronomic Schedule produces significantly better survival rate than non-IMS protocols and may even establish long-term specific anti-tumour immunity in cured mice. With regard to GL261 GB tumours showing transient response to therapy followed by tumour regrowth, PD-L1 content increase in the tumour tissue could be a possible explanation for the recurrence. Further studies will be needed to assess the presence, type, and amount of recruited host immune system elements at the point of maximum and minimum TRI values. This will help us to understand better their potential contributions to the metabolomic pattern changes detected. Finally, whenever the relationship between TRI oscillations and productive host immune system attraction for tumour fighting is fully demonstrated, we should be also able to use this to evaluate and quantify the extent of response in combination therapies, thereby further improving therapy scheduling and allowing for its personalization.

REFERENCES

1. Buckner JC. Factors influencing survival in high-grade gliomas. *Semin Oncol*. 2003;30:10-14.

2. Stupp R, Hegi ME, Mason WP, et al. Effects of radiotherapy with concomitant and adjuvant temozolomide versus radiotherapy alone on survival in glioblastoma in a randomised phase III study: 5-year analysis of the EORTC-NCIC trial. *Lancet Oncol*. 2009;10(5):459-466.

3. Dhermain FG, Hau P, Lanfermann H, Jacobs AH, van den Bent MJ. Advanced MRI and PET imaging for assessment of treatment response in patients with gliomas. *Lancet Neurol*. 2010;9(9):906-920.

4. Vogelbaum MA, Jost S, Aghi MK, et al. Application of novel response/progression measures for surgically delivered therapies for gliomas: Response Assessment in Neuro-Oncology (RANO) Working Group. *Neurosurgery*. 2012;70(1):234-43; discussion 243-4.

5. Eisenhauer EA, Therasse P, Bogaerts J, et al. New response evaluation criteria in solid tumours: revised RECIST guideline (version 1.1). *Eur J Cancer*. 2009;45(2):228-47.

6. Hygino da Cruz LC, Rodriguez I, Domingues RC, Gasparetto EL, Sorensen AG. Pseudoprogression and Pseudoresponse: Imaging Challenges in the Assessment of Posttreatment Glioma. *Am J Neuroradiol*. 2011;32(11):1978-1985.

7. Pichler BJ, Wehrl HF, Judenhofer MS. Latest Advances in Molecular Imaging Instrumentation. *J Nucl Med*. 2008;49(Suppl_2):5S-23S.

8. Horská A, Barker PB. Imaging of Brain Tumors: MR Spectroscopy and Metabolic Imaging. *Neuroimaging Clin N Am*. 2010;20(3):293-310.

9. Hattingen E, Jurcoane A, Bahr O, et al. Bevacizumab impairs oxidative energy metabolism and shows antitumoral effects in recurrent glioblastomas: a 31P/1H MRSI and quantitative magnetic resonance imaging study. *Neuro Oncol*. 2011;13(12):1349-1363.

10. Nelson SJ. Assessment of therapeutic response and treatment planning for brain tumors using metabolic and physiological MRI. *NMR Biomed*. 2011;24(6):734-749.

11. Ortega-Martorell S, Julià-Sapé M, Lisboa P, Arús C. Pattern Recognition Analysis of MR Spectra. In: *EMagRes*. Vol 5. Chichester, UK: John Wiley & Sons, Ltd; 2016:945-958.

12. Laudadio T, Martínez-Bisbal MC, Celda B, Van Huffel S. Fast nosological imaging using canonical correlation analysis of brain data obtained by two-dimensional turbo spectroscopic imaging. *NMR Biomed*. 2008;21(4):311-321.

13. Simões RV, Ortega-Martorell S, Delgado-Goñi T, et al. Improving the classification of brain tumors in mice with perturbation enhanced (PE)-MRSI. *Integr Biol (Camb)*. 2012;4(2):183-91.

14. Arias-Ramos N, Ferrer-Font L, Lope-Piedrafita S, et al. Metabolomics of Therapy Response in Preclinical Glioblastoma: A Multi-Slice MRSI-Based Volumetric Analysis for Noninvasive Assessment of Temozolomide Treatment. *Metabolites*. 2017;7(2):20.

15. Liikanen I, Ahtiainen L, Hirvinen ML, et al. Oncolytic Adenovirus With Temozolomide Induces Autophagy and Antitumor Immune Responses in Cancer Patients. *Mol Ther*. 2013;21(6):1212-1223.

16. Karman J, Ling C, Sandor M, Fabry Z. Initiation of Immune Responses in Brain Is Promoted by Local Dendritic Cells. *J Immunol*. 2004;173(4):2353-2361.

17. Wu J, Waxman DJ. Metronomic cyclophosphamide eradicates large implanted GL261 gliomas by activating antitumor Cd8^{+} T-cell responses and immune memory. *Oncoimmunology*. 2015;4(4):e1005521.

18. Villamañán L. Unraveling CK2 inhibition and temozolomide contribution to therapy response in preclinical GL261 glioblastoma: immune system implications and magnetic resonance based nosological

imaging. *PhD Thesis, Univ Autònoma Barcelona*. January 2019. https://tdx.cat/handle/10803/666881.

19. Chen DS, Mellman I. Oncology Meets Immunology: The Cancer-Immunity Cycle. *Immunity*. 2013;39(1):1-10.

20. Lorger M. Tumor Microenvironment in the Brain. *Cancers (Basel)*. 2012;4(1):218-243.

21. He J, Hu Y, Hu M, Li B. Development of PD-1/PD-L1 Pathway in Tumor Immune Microenvironment and Treatment for Non-Small Cell Lung Cancer. *Sci Rep*. 2015;5(1):13110.

22. Katsuya Y, Horinouchi H, Asao T, et al. Expression of programmed death 1 (PD-1) and its ligand (PD-L1) in thymic epithelial tumors: Impact on treatment efficacy and alteration in expression after chemotherapy. *Lung Cancer*. 2016;99:4-10.

23. Hecht M, Büttner-Herold M, Erlenbach-Wünsch K, et al. PD-L1 is upregulated by radiochemotherapy in rectal adenocarcinoma patients and associated with a favourable prognosis. *Eur J Cancer*. 2016;65:52-60.

24. Zhang P, Su D-M, Liang M, Fu J. Chemopreventive agents induce programmed death-1-ligand 1 (PD-L1) surface expression in breast cancer cells and promote PD-L1-mediated T cell apoptosis. *Mol Immunol*. 2008;45(5):1470-1476.

25. Simões RV, Delgado-Goñi T, Lope-Piedrafita S, Arús C. 1 H-MRSI pattern perturbation in a mouse glioma: the effects of acute hyperglycemia and moderate hypothermia. *NMR Biomed*. 2010;23(1):23-33.

26. Simões R V, García-Martín ML, Cerdán S, Arús C. Perturbation of mouse glioma MRS pattern by induced acute hyperglycemia. *NMR Biomed*. 2008;21(3):251-264.

27. Ortega-Martorell S, Ruiz H, Vellido A, et al. A Novel Semi-Supervised Methodology for Extracting Tumor Type-Specific MRS Sources in Human Brain Data. Monleon D, ed. *PLoS One*. 2013;8(12):e83773.

28. Ortega-Martorell S, Lisboa PJG, Vellido A, et al. Convex Non-Negative Matrix Factorization for Brain Tumor Delimitation from MRSI Data. Monleon D, ed. *PLoS One*. 2012;7(10):e47824.

29. Delgado-Goñi T, Ortega-Martorell S, Ciezka M, et al. MRSI-based molecular imaging of therapy response to temozolomide in preclinical glioblastoma using source analysis. *NMR Biomed*. 2016;29(6):732-743.

30. Ferrer-Font L, Villamañan L, Arias-Ramos N, et al. Targeting Protein Kinase CK2: Evaluating CX-4945 Potential for GL261 Glioblastoma Therapy in Immunocompetent Mice. *Pharmaceuticals*. 2017;10(4):24.

31. Ferrer-Font L, Arias-Ramos N, Lope-Piedrafita S, et al. Metronomic treatment in immunocompetent preclinical GL261 glioblastoma: effects of cyclophosphamide and temozolomide. *NMR Biomed*. 2017;30(9):1-12.

32. Ciezka M, Acosta M, Herranz C, et al. Development of a transplantable glioma tumour model from genetically engineered mice: MRI/MRS/MRSI characterisation. *J Neurooncol*. 2016;129(1):67-76.

33. Karman J, Ling C, Sandor M, Fabry Z. Initiation of Immune Responses in Brain Is Promoted by Local Dendritic Cells. *J Immunol*. 2004;173(4):2353-2361.

34. Kim T-G, Kim C-H, Park J-S, et al. Immunological Factors Relating to the Antitumor Effect of Temozolomide Chemoimmunotherapy in a Murine Glioma Model. *Clin Vaccine Immunol*. 2010;17(1):143-153.

35. Curtin JF, Liu N, Candolfi M, et al. HMGB1 Mediates Endogenous TLR2 Activation and Brain Tumor Regression. Weil R, ed. *PLoS Med*. 2009;6(1):e1000010.

36. Roesch S, Rapp C, Dettling S, Herold-Mende C. When Immune Cells Turn Bad—Tumor-Associated Microglia/Macrophages in Glioma. *Int J Mol Sci*. 2018;19(2):436.

37. Hanahan D, Weinberg RA. Hallmarks of Cancer: The Next Generation. *Cell*. 2011;144(5):646-674.

38.   Dong H, Strome SE, Salomao DR, et al. Tumor-associated B7-H1 promotes T-cell apoptosis: A potential mechanism of immune evasion. *Nat Med*. 2002;8(8):793-800.

39.   Hanson HL, Donermeyer DL, Ikeda H, et al. Eradication of Established Tumors by CD8+ T Cell Adoptive Immunotherapy. *Immunity*. 2000;13(2):265-276.

40.   Samanta D, Park Y, Ni X, et al. Chemotherapy induces enrichment of CD47 + /CD73 + /PDL1 + immune evasive triple-negative breast cancer cells. *Proc Natl Acad Sci*. 2018;115(6):E1239-E1248.

41.   Wu J, Jordan M, Waxman DJ. Metronomic cyclophosphamide activation of anti-tumor immunity: tumor model, mouse host, and drug schedule dependence of gene responses and their upstream regulators. *BMC Cancer*. 2016;16(1):623.

42.   Schiavoni G, Sistigu A, Valentini M, et al. Cyclophosphamide Synergizes with Type I Interferons through Systemic Dendritic Cell Reactivation and Induction of Immunogenic Tumor Apoptosis. *Cancer Res*. 2011;71(3):768-778.

43.   Dai B, Qi N, Li J, Zhang G. Temozolomide combined with PD-1 Antibody therapy for mouse orthotopic glioma model. *Biochem Biophys Res Commun*. 2018;501(4):871-876.

44.   Gilbert MR, Wang M, Aldape KD, et al. Dose-Dense Temozolomide for Newly Diagnosed Glioblastoma: A Randomized Phase III Clinical Trial. *J Clin Oncol*. 2013;31(32):4085-4091.

45.   Szatmári T, Lumniczky K, Désaknai S, et al. Detailed characterization of the mouse glioma 261 tumor model for experimental glioblastoma therapy. *Cancer Sci*. 2006;97(6):546-553.

46.   Galon J, Bruni D. Approaches to treat immune hot, altered and cold tumours with combination immunotherapies. *Nat Rev Drug Discov*. 2019;18(3):197-218.

ANTI-TUMOUR IMMUNE RESPONSE IN GL261 GLIOBLASTOMA GENERATED BY TEMOZOLOMIDE IMMUNE-ENHANCING METRONOMIC SCHEDULE MONITORED WITH MRSI-BASED NOSOLOGICAL IMAGES

Shuang Wu [+], Pilar Calero Pérez [+], Lucia Villamañan [+], Nuria Arias-Ramos, Martí Pumarola Batlle, Sandra Ortega-Martorell, Margarita Julia Sape, Carles Arús and Ana Paula Candiota

[+] These authors contributed equally to this work.

SUPPLEMENTARY MATERIALS

MRI studies

The acquisition parameters were as follows: repetition time (TR)/effective echo time (TEeff) = 4200/36 ms; echo train length (ETL) = 8; field of view (FOV) = 19.2 × 19.2 mm; matrix size (MTX) = 256 × 256 (75 × 75 μm/pixel); number of slices (NS) = 10; slice thickness (ST) = 0.5 mm; inter-ST = 0.1 mm; number of averages (NA) = 4; total acquisition time (TAT) = 6 min and 43 s.

MRSI studies

Consecutive 14 ms echo time (TE) MRSI with point-resolved spectroscopy (PRESS) localization grids were acquired individually across the tumour, using as a reference T2w high resolution images, as described in previous work.[1] First upper (dorsal) grid (Grid 1) had a matrix size of 10 × 10. Then, Grid 2 was acquired 1 mm below Grid 1 with a matrix size of 12 × 12. Grid 3 was acquired 1 mm below Grid 2, also with a matrix size of 12 × 12. Finally, if tumour volume was not completely covered with 3 grids, a final Grid 4 was acquired 1 mm below Grid 3 with a matrix size of 10 × 10.

Acquisition parameters for all grids were: FOV, 17.6 mm × 17.6 mm; VOI in Grids 1 and 4 was 5.5 mm × 5.5 mm × 1.0 mm. VOI in Grids 2 and 3 was 6.6 mm × 6.6 mm × 1.0 mm. ST, 1 mm; TR, 2500 ms; Sweep Width (SW), 4006.41 Hz; NA, 512; TAT, 21 min 30 s each grid. Water suppression was performed with Variable Power and Optimized Relaxation Delay (VAPOR), using a 300 Hz bandwidth. Linear and second order shims were automatically adjusted with Fast Automatic Shimming Technique by Mapping Along Projections (FASTMAP) in a 5.8 mm × 5.8 mm × 5.8 mm volume which contained the VOI region. Six saturation slices (ST, 10 mm; sech-shaped pulses: 1.0 ms/20250 Hz) were positioned around the VOI to minimize outer volume contamination in the signals obtained.

MRSI postprocessing: outline of NMF methods

In general, NMF methods belong to a group of multivariate data analysis techniques designed to estimate meaningful latent components, also known as sources, from non-negative data. Standard NMF methods decompose a given data matrix "X" into two non-negative matrices: the sources ("S") and the mixing matrix ("A"). The differences between NMF methods are given by the different cost functions used for measuring the divergence between X and S*A. A more recent variant of NMF that is also able to handle negative data, namely convex-NMF, was used in this work[2]. Convex-NMF has proven to be able to identify a reduced number of sources that can be confidently recognized as representing brain tumor/tissue types in a way that other source extraction methods, including other NMF variants, cannot detect with the same degree of specificity[3,4].

Adapted RECIST criteria

Classification of adapted RECIST criteria was applied as follows: Progressive disease (PD): 20% increase with respect to the smallest tumour volume so far. Partial response (PRe): tumour decrease by 30%, taking into account the biggest volume so far. Stable disease (SDi): less than 20% increase and no more than 30% decrease in tumour volume.

Protein extraction for WB studies

Whole GL261 tumours obtained after euthanization at endpoint were weighted and 200 µL of cold lysis buffer for each 50 mg of tissue was added (cold lysis buffer: 50 mM Tris-HCl pH 7.7, 150 mM NaCl, 15 mM $MgCl_2$, 0.4 mM ethylenediaminetetraacetic acid, 0.5 mM dithiothreitol, 100 µg/ml of leupeptin, aprotinin and benzamidin and 2 mM of phenylmethanesulfonyl fluoride or phenylmethylsulfonyl fluorid). Samples were homogenized with a 20 G needle 10 times and with a 26 G needle 10 more times. Then, sonication (Fisher Sonic Dismembrator Model 300, Thermo Fisher Scientific, Waltham, MA, USA) was performed five times for 5-s intervals at 30% amplification. After remaining 30 min on ice, the lysate was centrifuged at 13,000× g for 20 min at 4 °C. Finally, supernatant was collected and used for WB analysis.

SUPPLEMENTARY FIGURES:
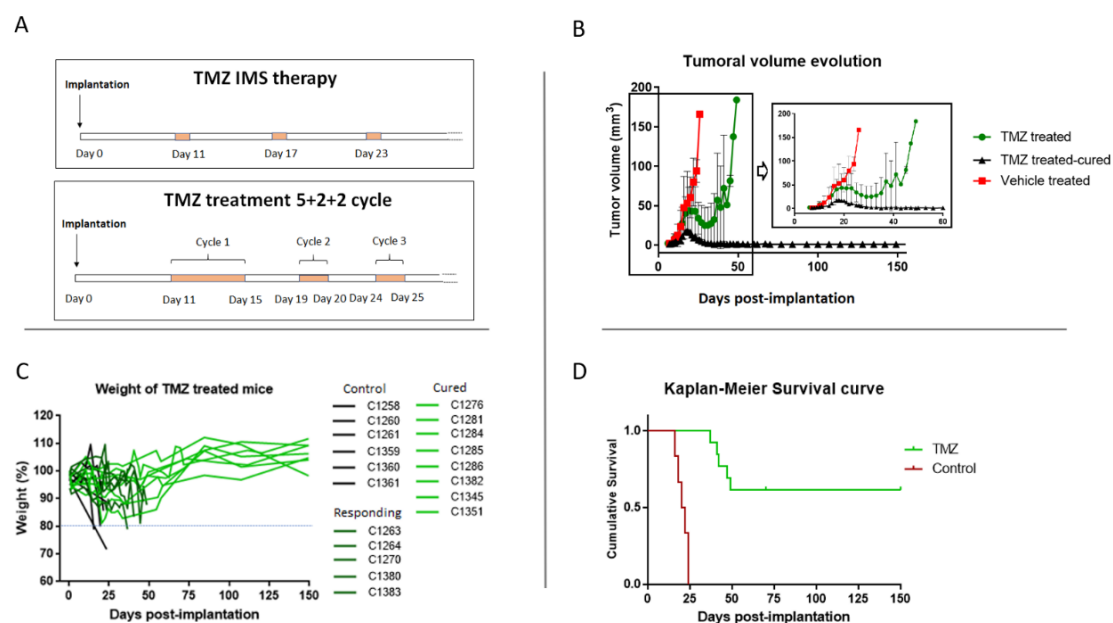
Figure S1. (A) Therapeutic schemes for TMZ treatment used in the studies described in this work. First, Immune-Enhancing Metronomic Schedule (IMS) used for GL261 GB therapy in mice- TMZ is administered every six days. Second, TMZ administration schema with 3 therapy cycles with a 3-day interleave, as described previously by us [1]. In both protocols TMZ therapy started at day 11 p.i., except for cases C1100 and C1108, for which the starting day was adapted to tumor volume (see details in supplementary reference 1) (B) Tumour volume evolution for control, vehicle treated (n=6, C1258, C1260, C1261, C1359, C1360 and C1361) and TMZ-treated GL261 tumour-bearing mice with the IMS protocol. For TM-treated mice two groups are shown: responding mice (n=5, cases C1263, C1264, C1270, C1380 and C1383) and cured mice, in which tumour disappeared due to TMZ treatment (n=8, C1276, C1281, C1284, C1285, C1286, C1345, C1351 and C1382). Mean ± SD values are shown. (C) Body weight evolution of GL261 tumour-bearing mice during TMZ treatment with the IMS protocol. Weight is expressed in %, assuming 100% for the weight at day 0; dashed horizontal blue line indicates the 20% weight reduction point, below which animals must be euthanized due to welfare parameters. (D) Kaplan Meier survival comparing GL261 tumour-bearing mice treated with vehicle (n=6) and TMZ (n=13) in an IMS protocol.
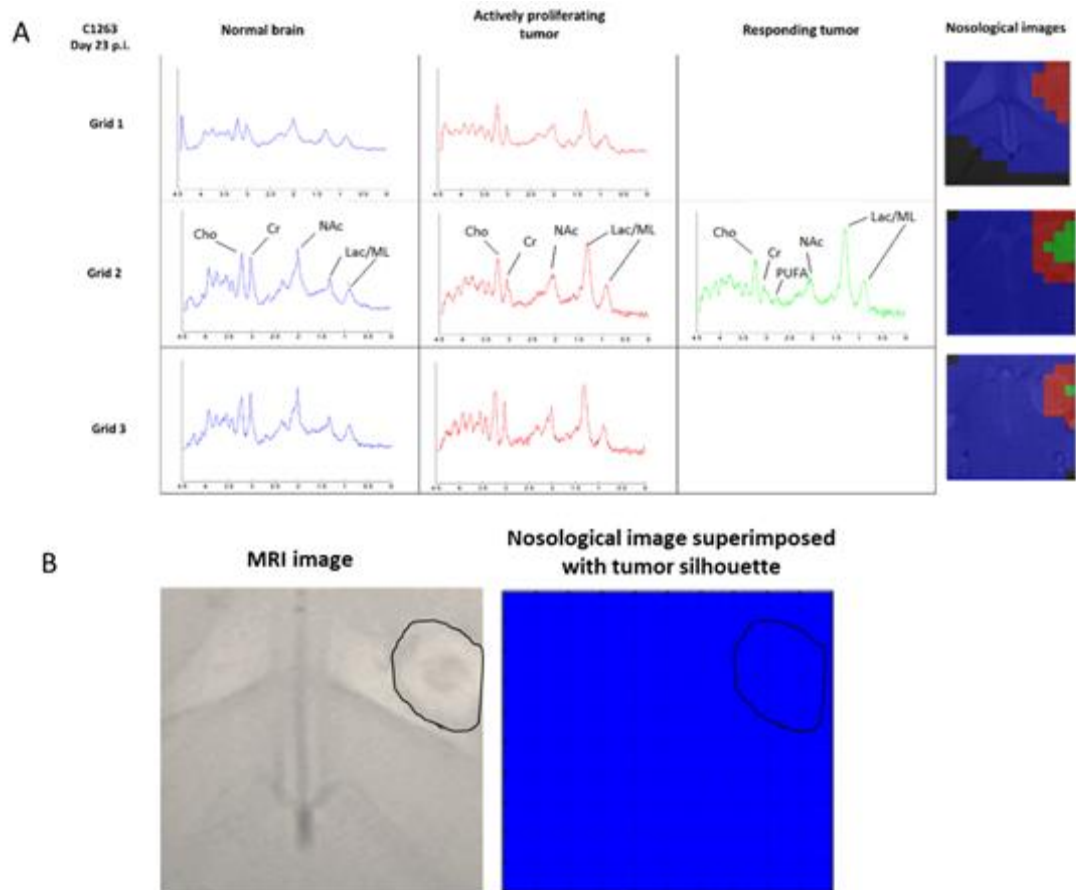
Figure S2. (A) Examples of mean spectra calculated from chosen zones of nosological images classified as normal brain parenchyma, actively proliferating tumour and responding tumour in case C1263. Normal brain is shown in blue (n=301 pixels), actively proliferating tumour in red (n=35) and responding tumour in green (n=9). Cho= choline, Cr= creatine, NAc= N-acetyl containing compounds, Lac= lactate, ML= mobile lipids. As expected, tumour zones present higher Cho/Cr and Cho/NAc ratio in comparison with normal brain parenchyma and higher Lac/ML signals. Still, responding zones present more noticeable 2.8 ppm signal, compatible with Polyunsaturated fatty acids (PUFA) chemical shift. (B) Example from case 1263 in which the tumour was not recognized by the semisupervised system analysis due to its small size (C1263, day 29 p.i., grid 1) showing one of the handicaps of the technique. In the left side, the MRI image with the tumour mass surrounded in black continuous line. On the right, the nosological imaging mislabeled 'normal' blue over the tumour zone superimposed to the tumour silhouette.
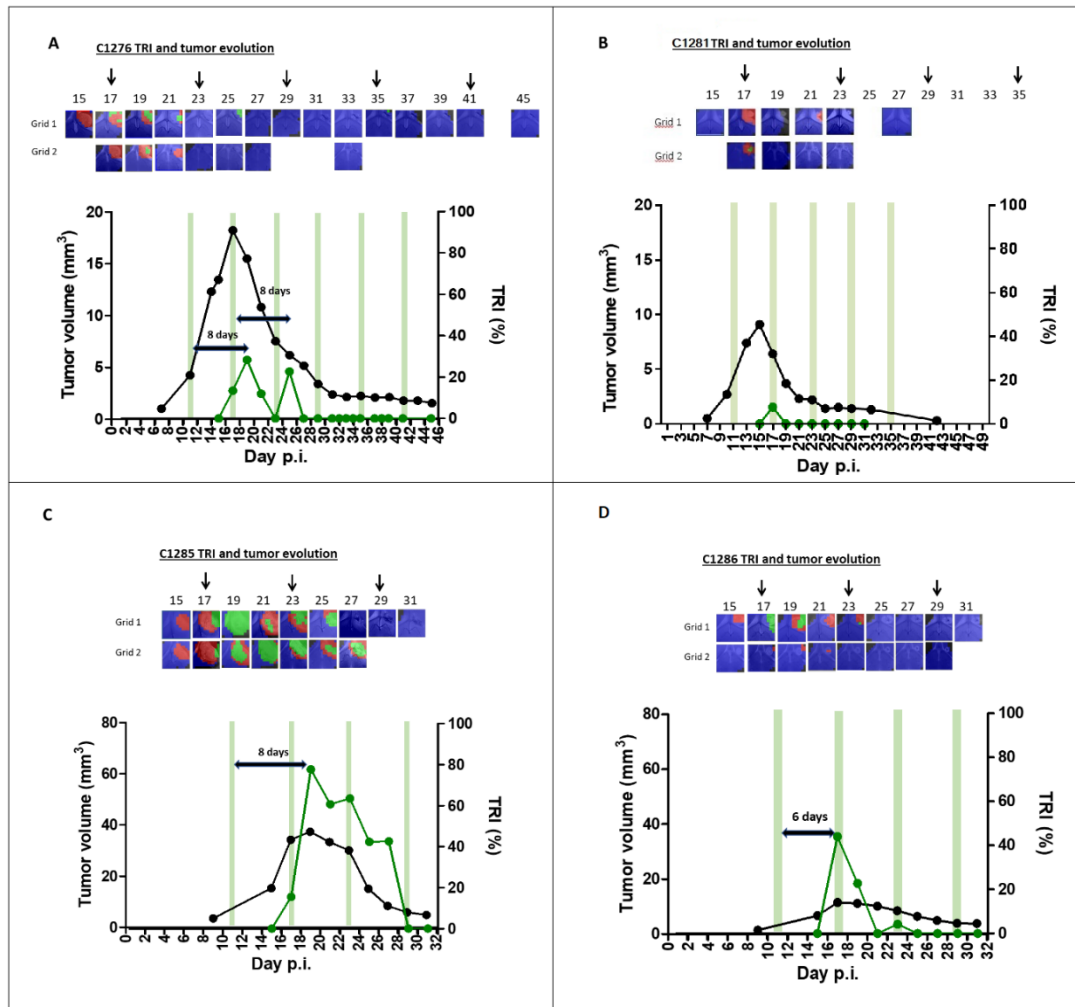
Figure S3. Nosological images and graphical representation of the tumour volume evolution for the tumour region in cases (A) C1276, (B) C1281, (C) C1285 and (D) C1286 of "cured" animals. Tumour volume in mm3 (black line, left axis) and the percentage of green, responding pixels (TRI) obtained taking into account total pixels counting (green line, right axis). In the upper part of every image chosen time points show the evolution of the nosological images in two rows of color-coded grids superimposed to the T2w-MRI for each slice. Below, green shaded columns indicate TMZ administration days. Case C1284 is not shown because TRI was always below the detection point due to small tumour volume.
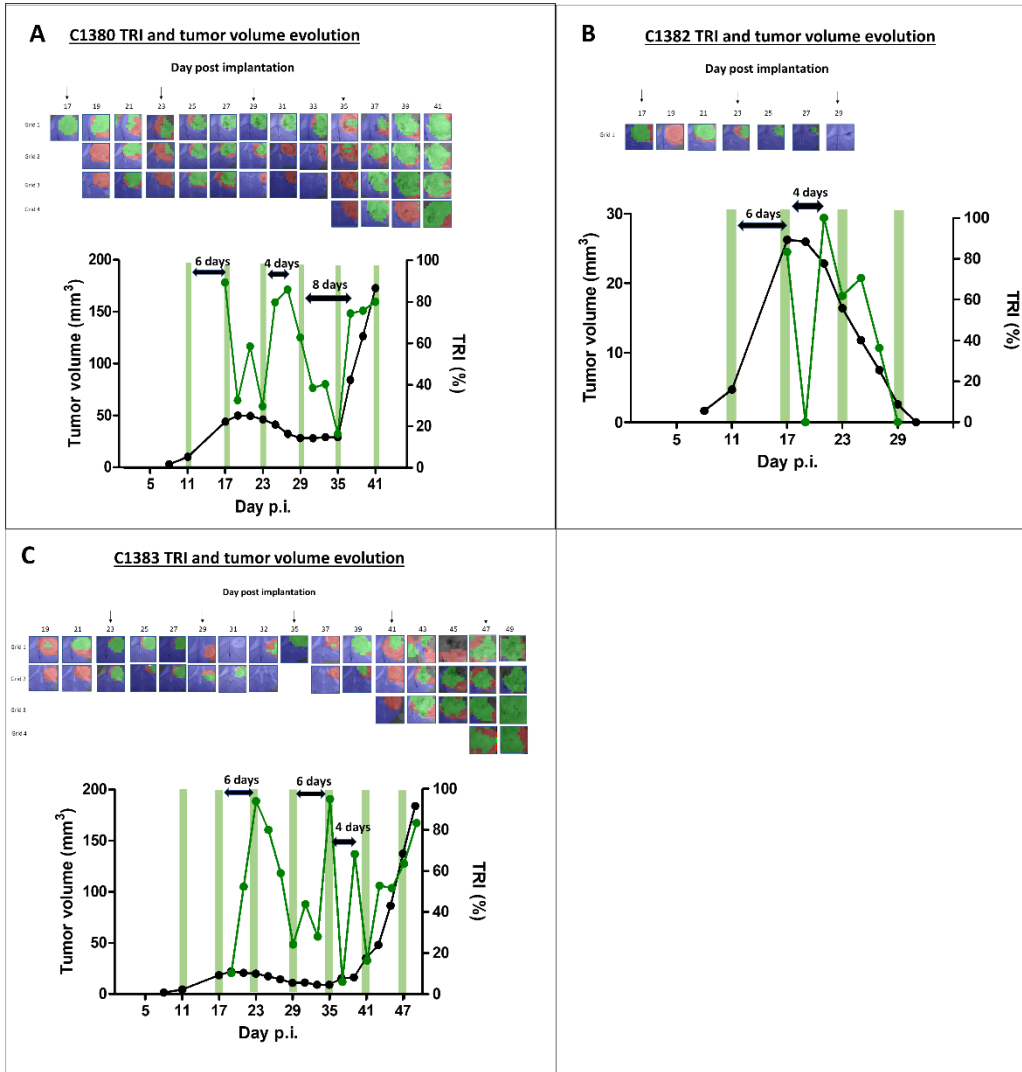
Figure S4. Nosological images and graphical representation of the tumour volume evolution for the tumour region in cases (A) C1380, (B) C1382 and (C) C1383. Tumour volume in mm3 (black line, left axis) and the percentage of green, responding pixels (TRI) obtained taking into account total pixels counting (green line, right axis). In the upper part of every image chosen time points show the evolution of the nosological images in one to four rows of color-coded grids superimposed to the T2w-MRI for each slice. Below, green shaded columns indicate TMZ administration days.
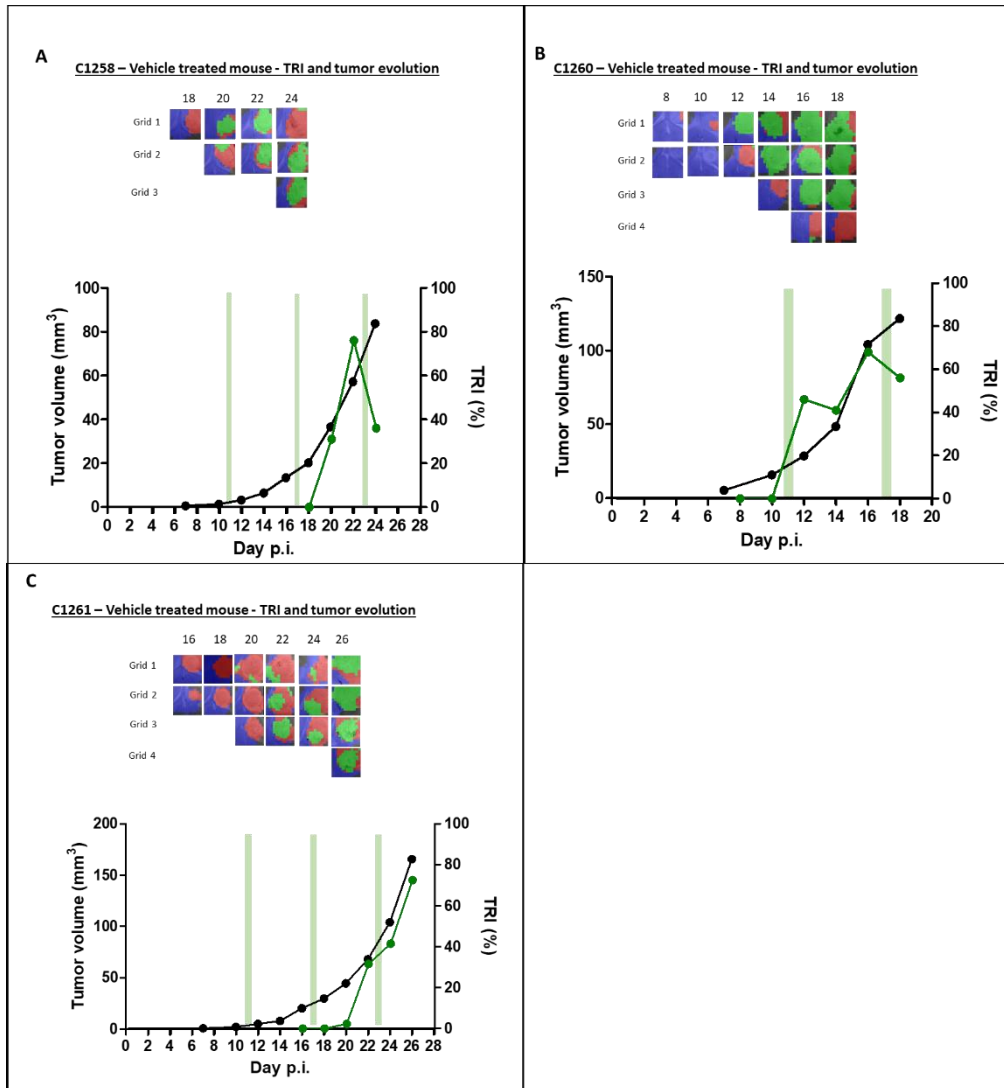
Figure S5. Nosological images and graphical representation of the tumour volume evolution for the tumour region in the vehicle treated cases (A) C1258, (B) C1260 and (C) C1261. Tumour volume in mm3 (black line, left axis) and the percentage of green, responding pixels (TRI) obtained taking into account total pixels counting (green line, right axis). In the upper part of every image chosen time points show the evolution of the nosological images in two rows of color-coded grids superimposed to the T2w-MRI for each slice. Below, green shaded columns indicate TMZ administration days.
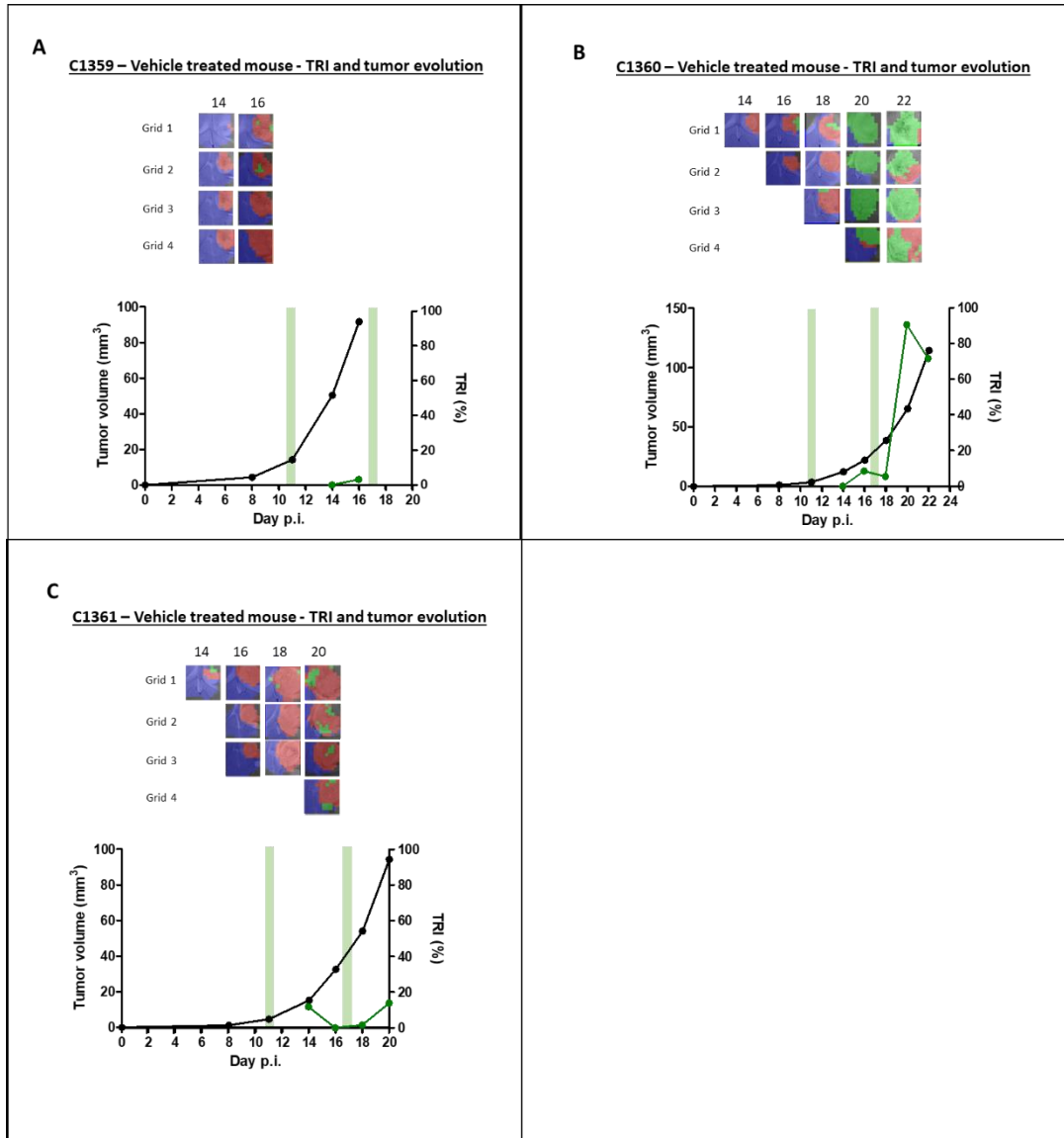
Figure S6. Nosological images and graphical representation of the tumour volume evolution for the tumour region in the vehicle treated cases (A) C1359, (B) C1360 and (C) C1361. Tumour volume in mm3 (black line, left axis) and the percentage of green, responding pixels (TRI) obtained taking into account total pixels counting (green line, right axis). In the upper part of every image chosen time points show the evolution of the nosological images in two rows of color-coded grids superimposed to the T2w-MRI for each slice. Below, green shaded columns indicate TMZ administration days.

Tumour volume evolution of samples for Western Blot analysis
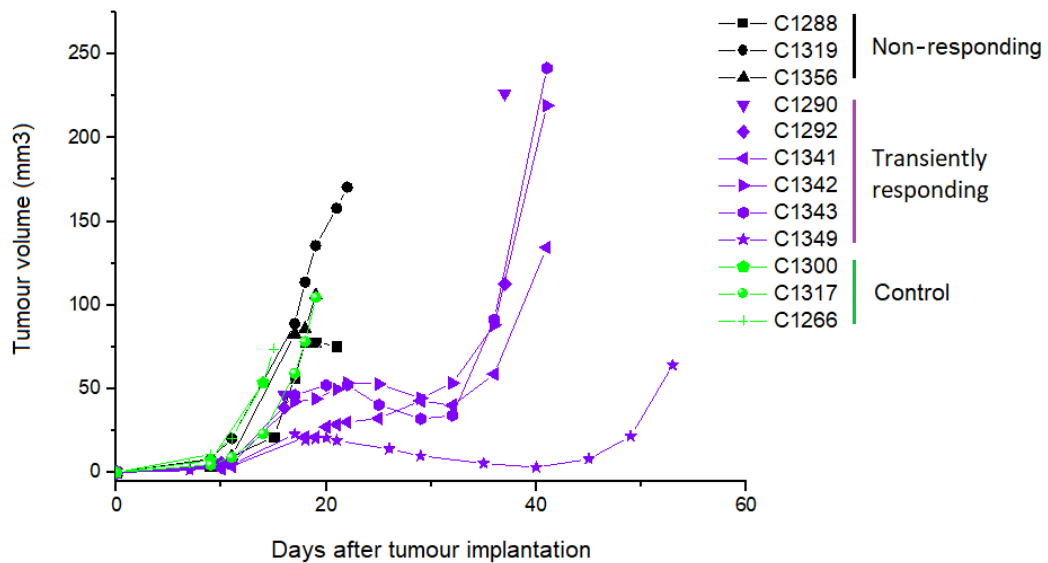
Figure S7. Tumour volume evolution for control, vehicle treated (n=3, C1300, C1317 and C1266) and TMZ-treated GL261 tumour-bearing mice with the IMS protocol. For TMZ treated mice two groups are shown: non responding mice (n=3, C1288, C1319 and C1356) and mice showing transient response, in which tumour had transient shrinkage but re-grew after several doses of IMS-TMZ treatment (n=6, C1290, C1292, C1341, C1342, C1343 and C1349). Data for C1290 and C1292 is incomplete (gap from day 16p.i. to day 37p.i.) because of technical issues related to MR scanner time availability in this time period.

Tumour volume evolution of cured mice
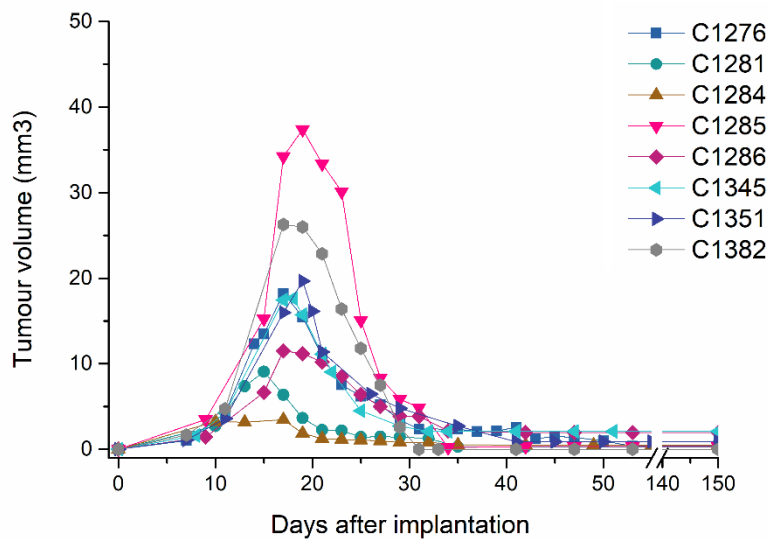
Figure S8. Tumour volume evolution of mice cured from TMZ treated group: (n=8, C1276, C1281, C1284, C1285, C1286, C1345, C1351 and C1382).

73

SUPPLEMENTARY TABLES:

Table S1. Evolution of the TMZ treated GL261 cases considering TRI and tumour volume changes over time. Classification of adapted RECIST criteria were applied as follows: Progressive disease: 20% increase with respect to the smallest tumour volume so far. Partial response: tumour decrease of 30% taking into account the biggest volume so far. Stable disease: less than 20% of increase and no more of 30% decrease.

Case	Day p.i.	Classification of RECIST criteria	TRI behavior
C1263	17-19	Stable disease	TRI cycles
	21-31	Partial Response	
	33-47	Progressive disease	BDTP and no cycles
C1264	17	Progressive disease	TRI cycles
	19-31	Stable disease	
	33-35	Progressive disease	
	37	Stable disease	No cycles
	39-41	Progressive disease	
C1270	15-19	Progressive disease	TRI cycles
	21-23	Stable disease	
	25-31	Partial Response	
	33	Stable disease	
	35-37	Progressive disease	No cycles
C1276	15-17	Progressive disease	TRI cycles
	19	Stable disease	
	21-27	Partial Response	
C1281	15-17	Stable disease	No cycles
	19-27	Partial Response	

C1284	15-17	Stable disease	No cycles
	19-27	Partial Response	
C1285	15-17	Progressive disease	TRI cycles
	19-23	Stable disease	TRI cycles, then no cycles
	25-31	Partial Response	No cycles
C1286	15-17	Progressive disease	TRI cycles
	19-21	Stable disease	
	23-31	Partial Response	No cycles
C1380	11-17	Progressive disease	
	19-25	Stable disease	TRI cycles
	27-35	Partial Response	
	37-41	Progressive disease	No cycles
C1382	17	Progressive disease	TRI cycles
	19-21	Stable disease	
	23-29	Partial Response	No cycles
C1383	17	Progressive disease	
	19-25	Stable disease	TRI cycles
	27-35	Partial Response	
	37-49	Progressive disease	TRI cycles / No cycles

Table S2. Evolution of the vehicle-treated cases considering TRI and tumour volume changes over time.

Classification of adapted RECIST criteria were applied as follows: Progressive disease: 20% increase with respect to the smallest tumour volume so far. Partial response: tumour decrease of 30% taking into account the biggest volume. Stable disease: less than 20% of increase and no more of 30% decrease.

Case	Day p.i.	Classification of RECIST criteria	TRI behavior
C1258	18-24	Progressive disease	One TRI cycle
C1260	8-18	Progressive disease	No cycles
C1261	16-26	Progressive disease	No cycles
C1359	14-16	Progressive disease	No cycles
C1360	14-22	Progressive disease	No cycles
C1361	14-20	Progressive disease	No cycles

SUPPLEMENTARY REFERENCES:

1.   Arias-Ramos N, Ferrer-Font L, Lope-Piedrafita S, et al. Metabolomics of Therapy Response in Preclinical Glioblastoma: A Multi-Slice MRSI-Based Volumetric Analysis for Noninvasive Assessment of Temozolomide Treatment. *Metabolites*. 2017;7(2):20.

2.   Ding C, Li T, Jordan MI. Convex and semi-nonnegative matrix factorizations. *IEEE Trans Pattern Anal Mach Intell*. 2010;32(1):45-55.

3.   Ortega-Martorell S, Lisboa PJG, Vellido A, et al. Convex Non-Negative Matrix Factorization for Brain Tumor Delimitation from MRSI Data. Monleon D, ed. *PLoS One*. 2012;7(10):e47824.

4.   Ortega-Martorell S, Lisboa PJG, Vellido A, Julia-Sape M, Arus C. Non-negative Matrix Factorisation methods for the spectral decomposition of MRS data from human brain tumours. *BMC Bioinformatics*. 2012;13(1):38.

4.2. CHAPTER II: IMMUNE SYSTEM-RELATED CHANGES IN PRECLINICAL GL261 GLIOBLASTOMA UNDER TMZ TREATMENT: EXPLAINING MRSI-BASED NOSOLOGICAL IMAGING FINDINGS WITH RT-PCR ANALYSES.

Article

Immune System-Related Changes in Preclinical GL261 Glioblastoma under TMZ Treatment: Explaining MRSI-Based Nosological Imaging Findings with RT-PCR Analyses

Pilar Calero-Pérez [1,2], Shuang Wu [1], Carles Arús [1,2,3] and Ana Paula Candiota [1,2,3,*]

[1] Departament de Bioquímica i Biologia Molecular, Unitat de Bioquímica de Biociències, Edifici Cs, Universitat Autònoma de Barcelona, 08193 Cerdanyola del Vallès, Spain; Pilar.Calero@uab.cat (P.C.-P.); psychews@gmail.com (S.W.); Carles.Arus@uab.cat (C.A.)
[2] Centro de Investigación Biomédica en Red en Bioingeniería, Biomateriales y Nanomedicina (CIBER-BBN), 08193 Cerdanyola del Vallès, Spain
[3] Institut de Biotecnologia i de Biomedicina (IBB), Universitat Autònoma de Barcelona, 08193 Cerdanyola del Vallès, Spain
[*] Correspondence: AnaPaula.Candiota@uab.cat

Simple Summary: Glioblastoma (GB) is an aggressive brain tumour with poor survival. Tumour microenvironment is a key element in GB evolution and response to therapy. We assessed presence and phenotypes of microglia/macrophages in preclinical GL261-GB microenvironment under Temozolomide (TMZ) treatment to unveil its possible relationship with MRSI-detected metabolomics changes. Microglia/macrophage polarisation towards an anti-tumour phenotype prevailed in TMZ-treated tumours. Since microglia/macrophages can represent 30–40% of the GB tumour volume, they must contribute the metabolomic pattern change. PD-L1 expression also correlated with the anti-tumour microglia/macrophage phenotype. These results highlight the potential of MRSI-detected metabolomics as non-invasive biomarker for immune system action.

Abstract: Glioblastomas (GB) are brain tumours with poor prognosis even after aggressive therapy. Previous work suggests that magnetic resonance spectroscopic imaging (MRSI) could act as a biomarker of efficient immune system attack onto GB, presenting oscillatory changes. Glioma-associated microglia/macrophages (GAMs) constitute the most abundant non-tumour cell type within the GB and can be polarised into anti-tumour (M1) or pro-tumour (M2) phenotypes. One of the mechanisms to mediate immunosuppression in brain tumours is the interaction between programmed cell death-1 ligand 1 (PD-L1) and programmed cell death-1 receptor (PD-1). We evaluated the subpopulations of GAMs in responding and control GB tumours to correlate PD-L1 expression to GAM polarisation in order to explain/validate MRSI-detected findings. Mice were evaluated by MRI/MRSI to assess the extent of response to treatment and with qPCR for GAMs M1 and M2 polarisation analyses. M1/M2 ratios and PD-L1 expression were higher in treated compared to control tumours. Furthermore, PD-L1 expression was positively correlated with the M1/M2 ratio. The oscillatory change in the GAMs prevailing population could be one of the key causes for the differential MRSI-detected pattern, allowing this to act as immune system activity biomarker in future work.

Keywords: glioblastoma; orthotopic immunocompetent tumours; immune-enhancing metronomic schedule; TMZ; magnetic resonance spectroscopic imaging; immune system activity imaging biomarker; cancer immune cycle; glioma-associated microglia/macrophages; PD-L1

1. Introduction

Glioblastoma (GB) is the most frequent primary central nervous system malignancy in adults. These tumours have poor prognosis, which has not significantly improved

despite new diagnostic strategies and innovative therapies have been developed [1]. The combination of chemotherapy (Temozolomide, TMZ) plus radiotherapy is still used as the standard therapeutic choice after surgery, resulting in an average survival rate of only 14.6 mo [2], which highlights the urgent need for investigating novel therapeutic approaches/follow-up strategies in order to improve patient outcome. Nowadays, the implication of the immune system in cancer surveillance and therapy response is widely accepted [3]. This is especially relevant in GB, since GB cells have the capacity for creating an immunosuppressive microenvironment and employ various methods to escape immune surveillance through several pathways [4]. Therefore, understanding these strategies and the biology of such tumour microenvironment will be helpful for developing novel therapeutic approaches and follow-up methods, which should lead to improved prognosis for GB patients.

Glioma-associated microglia/macrophages (GAMs), i.e., microglia, together with peripheral macrophages recruited by tumour tissue from circulating blood [5], constitute the most common non-tumour cell type in the GB microenvironment [6] and are characterised by considerable diversity and plasticity. Over the last decade, it has become clear that this cellular population interacts with numerous other cell types to actively influence brain tumour biology [7]. These cells can be activated by various stimuli and polarised into classically activated (M1) or alternatively activated (M2) phenotype, which represent extreme situations of a continuum of activation states. M1 microglia/macrophages are usually involved in proinflammatory and anti-tumour mechanisms. In contrast, M2 microglia/macrophages are involved in activities for promoting tumour survival and growth [8]. Accordingly, their gradual polarisation state determines the pathophysiological character of this cell population, while subpopulations differ with respect to receptor expression, effector function, and cytokine and chemokine production. The antitumor effect of M1 microglia/macrophages was described to involve several mechanisms, such as proinflammatory cytokines release and activation of cytotoxic T lymphocytes. Indeed, complex interactions between innate and adaptive immune responses such as antitumour microglia/macrophages and T-cells have been described [9] and are key elements in sustained therapy response. On the other hand, M2 microglia/macrophages can increase the proportion of T-regulatory lymphocytes and lead to the inhibition of the cytotoxic T-cell responses [10]. The fact that microglia/macrophages had been described to be more abundant in GB than in low-grade gliomas [6] hints at their possible active role in glioma progression. GAMs undergoing phenotype polarisation display changes in their molecular and metabolic profiles, also triggering the expression of different markers such as Nos2 and CD206 characterising M1 and M2 microglia/macrophages, respectively [11,12]. However, more than a bilateral all or none option, the M1/M2 signature rather implies a continuum between two extremes with specific abilities (e.g., epigenetic marks, metabolic reprogramming) and local signalling (e.g., cytokines, chemokines, and immune checkpoints) [13].

Furthermore, one of the main mechanisms known to mediate immunosuppression in the brain tumour microenvironment is the interaction between programmed cell death-1 ligand 1 (PD-L1) and its receptor (PD-1) [14]. PD-1 is an inhibitory receptor mainly expressed on activated T cells, B cells, macrophages, and dendritic cells, while PD-L1 is highly expressed by malignant tumour cells [15], as well as by tumour-infiltrating myeloid cells, including macrophages [16,17]. It is a notable immune checkpoint initially described to cause T cell anergy [18], although its role in other cellular populations is still a matter of discussion.

The preclinical GB model GL261 growing into C57BL/6 mice is widely accepted as an immunocompetent model suitable for assessing therapeutic approaches and immune system participation in therapy response [9,19–21]. Our group has studied the evolution and behaviour of this tumour model under TMZ and other therapeutic approaches [22–25]. We have described the non-invasive assessment of response to therapy in preclinical GL261 GB (control and under TMZ therapy) with magnetic resonance spectroscopic imaging (MRSI) approaches. MRSI combines anatomical information from magnetic resonance

imaging (MRI) [26], and magnetic resonance spectroscopy (MRS), which provides information regarding the metabolomic profile of the investigated tissue [27–29]. When using MRSI is coupled to advanced machine learning analysis (source extraction as described in [30]), spectral pattern differences between actively proliferating GB and GB responding to therapy can be shown colour-coded (the nosological images) in single-slice [23] or multislice volumetric approaches [24]. Using volumetric MRSI-based nosological images, we have defined the tumour responding index (TRI) as an evaluation parameter to estimate/measure the extent of response to treatment. The level of detected response, TRI, showed consistent oscillations with 6–7 day frequency during transient response to TMZ therapy [24,31]. These oscillations were not detected regarding tumour volume changes. We hypothesised that this could be a surrogate biomarker for immune system-contributed local changes triggered by response to therapy, since this periodicity coincides with the cancer immune cycle length described in [32], also supported by immunohistochemistry data related to lymphocytes (CD3$^+$) and microglia/macrophage (Iba1$^+$) content [31].

The purpose of this work was to assess the origin of the oscillating pattern changes spotted by MRSI in TMZ-treated/responding GL261 GB bearing mice under Immune-Enhancing Metronomic Schedule (IMS) [31]. Since it was described that macrophages can represent up to 30–40% of tumour masses [5], consistent with our results in [31], it is reasonable to investigate whether the spectral pattern changes could be related to different macrophage phenotypes present in such samples. Accordingly, we wanted to characterise the different subpopulations of GAMs in MRSI-evaluated responding and control GL261 GB tumours by quantitative real-time polymerase chain reaction (qPCR). Furthermore, PD-L1 gene expression was investigated by qPCR to correlate GAMs polarisation with immunosuppression within the tumour microenvironment.

2. Materials and Methods

2.1. GL261 GB Preclinical Model Generation and Treatment

GL261 mouse glioma cells have been obtained from the Tumour Bank Repository at the National Cancer Institute (Frederick, Maryland) and were grown as previously described by us [33]. Cells were checked for mouse short tandem repeat (STR) profile as well as interspecies contamination. In addition, PCR studies were performed in order to discard mycoplasma and virus presence. All studies involving animals were approved by the local ethics committee (*Comissió d'Ètica en Experimentació Animal i Humana*, CEEAH, www. uab.cat/web/experimentacio-amb-animals/presentacio-1345713724929.html, accessed on 26 May 2021), according to regional and state legislations (protocol references CEA-OH-9685/CEEAH-3665). Mice were purchased from Charles River Laboratories (l'Abresle, France) and housed at the animal facility of the *Universitat Autònoma de Barcelona*. An enriched environment was used, similar to the one described in [34], and mouse spent at least three weeks in this environment prior to tumour implantation. In order to obtain reproducible and well-categorised groups regarding tumour volume and evolution prior to therapy and ensuring proper TRI and tumour volume for qPCR studies (see Sections 2.2.4 and 2.4), tumours were induced in a total of 110 C57BL/6 female wild-type (wt) mice by intracranial stereotactic injection of 10^5 GL261 cells as already described by us [33]. Only 20 C57BL/6 mice (weighing 21.1 ± 1.5 g, aged 15.9 ± 3.3 weeks) fulfilling inclusion conditions (e.g., TRI value, equal or higher than 60% for TMZ-treated mice and TRI = 0%, or as close as possible, for control mice, see SM for further details) were eventually used for the evaluation of the origin of the recorded MRSI patterns. Mice were weighed twice a week and tumour volumes were followed up using T2 weighted image (T2w) MRI acquisitions. Multi-slice MRSI studies (Section 2.2) were performed to assess the extent of the response to treatment using the obtained nosological images. Tumour volumes were chosen aiming to ensure enough volume to allow for proper MRSI acquisition and segmentation at the desired time points, with no significant differences between groups.

GL261 GB treatment. For in vivo experiments, TMZ (Sigma-Aldrich, Madrid, Spain) was dissolved in 10% dimethyl sulfoxide (DMSO) in saline solution (0.9% NaCl) and was

administered using an oral gavage. Treated tumour-bearing mice (*n* = 10) received IMS-TMZ 60 mg/kg, every 6 d (two or three times depending on the euthanasia day), from day 11 post-implantation (p.i.), as described in [31], while tumour-bearing control mice (*n* = 10) received 10% DMSO vehicle following the same administration schedule.

2.2. In Vivo MRI and MRSI Studies

In vivo MRI/MRSI studies were conducted at the joint nuclear magnetic resonance facility of the *Universitat Autònoma de Barcelona* and *Centro de Investigación Biomédica en Red-Bioingeniería, Biomateriales y Nanomedicina* (CIBER-BBN) (Cerdanyola del Vallès, Spain), Unit 25 of NANBIOSIS (www.nanbiosis.es, accessed on 18 March 2021). Mice were positioned in a dedicated bed, which allowed suitable anaesthesia delivery (isoflurane, 1.5–2.0% in O_2 at 1 L/min), with an integrated circuit of heating water for maintaining proper body temperature. Respiratory frequency was monitored with the help of a pressure probe and kept between 60–80 breaths/min. The 7T Bruker BioSpec 70/30 USR spectrometer (Bruker BioSpin GmbH, Ettlingen, Germany) equipped with a mini-imaging gradient set (400 mT/m) was used for acquisitions. A 72-mm inner-diameter linear volume coil was used as transmitter, and a dedicated mouse brain quadrature surface coil was used as receiver for MRI studies.

2.2.1. MRI Studies

GL261 GB-bearing mice were screened with high-resolution coronal T2w images using a Rapid Acquisition with Relaxation Enhancement (RARE) sequence to evaluate brain tumour presence and to monitor its evolution stage, using repetition time (TR)/effective echo time (TEeff) = 4200/36 ms. The detailed set of parameters used in MRI acquisitions can be found in Supplementary Material file. MRI data of tumour-bearing mice were acquired and processed on a Red Hat Linux computer using ParaVision 5.1 software (Bruker BioSpin GmbH, Ettlingen, Germany).

2.2.2. MRSI Studies

Consecutive point-resolved spectroscopy (PRESS), 14 ms echo time (TE) MRSI were acquired individually across the tumour, using T2w high-resolution images as reference, as described in [24]. Shimming was individually performed for each MRSI grid. MRSI grids were spatially placed in order that the volume of interest (VOI) would include most of the tumoral mass as well as part of the normal/peritumoral brain parenchyma. The whole set of MRSI acquisition parameters can be found in the Supplementary Material file.

2.2.3. MRI and MRSI Processing and Post-Processing

- Tumour volume calculation

Abnormal brain masses observed in T2w images were manually segmented and each tumour volume was calculated from T2w high-resolution horizontal images using the following equation:

$$TV \ mm^3 = [(AS1 \times ST) + [(AS2 + (\dots) + AS10) \times (ST + IT)]] \times 0.0752 \quad (1)$$

where TV is the tumour volume, AS is the number of pixels in the region of interest in each MRI slice, ST is slice thickness, IT the inter-slice thickness, and 0.0752 accounts for the individual pixel surface area in mm^2. The tumour area was calculated from pixels in each slice with ParaVision 5.1 software. The inter-slice volume was estimated through addition of the inter-slice thickness to the corresponding slice thickness in Equation (1).

- Brain MRSI post-processing and machine learning strategies

MRSI data were post-processed as described by us in [35]. Briefly, data were initially pre-processed with ParaVision 5.1. Further post-processing was performed with 3D Interactive Chemical Shift Imaging (3DiCSI) software package version 1.9.17 (Courtesy of Truman Brown, PhD, Columbia University, New York, NY, USA) for the fol-

lowing: line broadening adjustment (Lorentzian filter, 4 Hz), zero-order phase correction, and ASCII format exportation. Then, dynamic MRSI processing module (DMPM, http://gabrmn.uab.es/?q=dmpm, accessed on 26 May 2021), running over MatLab 2013a (The MathWorks Inc., Natick, MA, USA), was used for spectral alignment within each MRSI matrix, using the 3.21 ppm choline signal as reference). The 0–4.5 ppm region of each MRSI spectrum was unit length normalised and exported in ASCII format used for pattern recognition (PR) analysis. No baseline correction was performed in these spectra.

After that, spectral vectors were analysed following the methodology based in non-negative matrix factorization (NMF) semi-supervised protocol described in [23] for classifying pixels into normal brain parenchyma, actively proliferating tumour and tumour responding to treatment, and calculating nosologic maps representing the spatial response to treatment. Green colour is used when the GB responding to treatment source contributes the most, red for actively proliferating GB, blue for normal brain parenchyma, and black for undetermined tissue. See Section 4.3 for further details about metabolites originating the differences in the control or responding GB pattern metabolome (also SM and Figure S1).

2.2.4. Tumour Responding index (TRI) Calculations

In order to measure the extent of response to treatment using the obtained nosological images, a numerical parameter named TRI was calculated (Equation (2)) [24],

$$\text{TRI} = \frac{Tumour\ responding\ pixels}{Total\ tumour\ pixels} \times 100 \tag{2}$$

TRI is stated as the percentage of green (colour-coded), responding tumour pixels of all grids over the total tumour pixels of all recorded grids.

Then, extreme values for TRI were selected, as homogeneously green/red as possible. For TMZ-treated mice, tumours with TRI values >60% were selected while TRI = 0% (or as close as possible) was selected for vehicle-treated mice. Regarding cases responding to TMZ treatment, tumour volume meeting criteria for "stable disease" according to Response Evaluation Criteria in Solid Tumors (RECIST) [36] adapted as described in [23] were chosen.

2.3. Animal Euthanasia

Whenever a mouse met criteria to be included in the study regarding MRI and MRSI parameters, euthanasia was performed by cervical dislocation, and samples were dissected and stored in liquid nitrogen.

2.4. RNA Isolation, cDNA Synthesis and qPCR

RNA isolation was performed following the protocol for purification of total RNA from animal tissues (RNeasy Mini Kit, QIAGEN, GmbH, Hilden, Germany). RNA concentration was quantified at 260 nm (Qubit, Thermo Fisher Scientific, Massachusetts, EEUU), and RNA integrity and quality were determined with 260/280 and 260/230 ratios (NanoDrop, München, Germany). One hundred ng of RNA from each sample was transcribed into cDNA with the iScript cDNA synthesis kit (Bio-Rad, California, EEUU) according to manufacturer's instructions.

The qPCR amplification was carried out to investigate five genes: EGF-like module containing mucin-like hormone receptor-like 1 (F4/80), inducible NO synthase (Nos2), mannose receptor C type 1 (CD206) programmed cell death-1 ligand 1 PD-L1 (CD274 antigen), purchased from BioRad (California, EEUU, Ref 13,733; 18,126; 17,533; and 60,533, respectively). F4/80 has been established as a global microglia/macrophage population marker, Nos2 has been described as a marker of M1 phenotype, and CD206 has been defined as a marker of M2 phenotype [37–40].

An amount of 2 ng of cDNA was used for qPCR, all reactions were performed twice, and results were averaged. qPCR analysis was carried out using the Bio-Rad CFX qPCR System. Primers and the Power SYBR Green Master Mix were purchased from Bio-Rad. The PCR amplification reactions were performed in 10 μL reaction volumes, and PCR protocol

consisted of 40 cycles of denaturation at 95 °C for 10 s and annealing/extension at 60 °C for 30 s. Relative mRNA expression levels were normalised to two housekeeping genes (tata binding protein (TBP) and hypoxanthine guanine phosphoribosyl transferase (HPRT), purchased from BioRad (California, EEUU, Ref 21,374 and 15,452, respectively). Primers sequences are described in the Supplementary Material file. The cycles threshold-values (ct-values) average of the two reference genes for normalization purposes was used. For each gene, the $2^{-\Delta\Delta Ct}$ method [41] (a method to calculate relative gene expression levels between different samples that directly uses the ct-values generated by the qPCR system) for calculation was performed to analyse relative quantities.

2.5. Statistical Analysis

Sample distribution was assessed with Kolmogorov-Smirnov test. Levene's test was used for assessing variance homogeneity. A two-tailed Student's t-test for independent measurements was used for comparisons. Relationships between different markers were assessed with the Pearson correlation coefficient. The significance level for all tests was $p < 0.05$.

3. Results

3.1. Follow up of GL261 Tumour-Bearing Mice and Endpoint Criteria

In this study, 20 mice were used (n = 10 IMS-TMZ-treated and n = 10 vehicle-treated). The average tumour volume at therapy start (day 11 p.i.) was 7.5 ± 3.2 mm^3 for TMZ-treated mice and 9.1 ± 8.4 mm^3 for control mice, with no significant differences between both groups.

Tumour volume was followed up by MRI, and MRSI acquisitions were carried out in order to measure the extent of response to treatment using the obtained nosological images. Extreme values for TRI were searched for, as well as homogeneous response levels, avoiding heterogeneous samples as much as possible. For TMZ-treated mice, MRSI studies were performed when tumour volume showed decrease in comparison with previous explorations, meeting criteria for "stable disease" according to adapted RECIST [23] (see Supplementary Material file). The time point chosen for TMZ-treated mice was when TRI values were equal or higher than 60%, and average TRI obtained was $76.97 \pm 11.22\%$, corresponding to intermediate/high response categories (see [24] for category definition). The average tumour volume was 58.64 ± 26.43 mm^3, at day 23.6 ± 1.6 p.i. For vehicle-treated mice, the time point chosen for study was at the moment tumours showed TRI = 0% (or as close as possible, average $4.59 \pm 6.31\%$) and tumour had enough size to provide samples for qPCR experiments (71.61 ± 29.18 mm^3 at day 18.3 ± 3.8 p.i.). At chosen time points, mice were euthanised by cervical dislocation, brain was removed, and tumour was resected. All collected samples are described in Table S1, and tumour volume evolution is shown in Figure 1.

3.2. Microglia/Macrophage Global Population, As Well As M1 and M2 Subtypes, Are Increased in IMS-TMZ-Treated Tumours

In order to characterise the microglia/macrophage population in the GL261 GB microenvironment during TMZ treatment, gene expression level analyses were performed in TMZ-treated and control mice: the F4/80 gene as general GAMs marker, Nos2 gene as M1 subtype marker, and CD206 gene as M2 subtype marker.

F4/80 gene showed significantly higher expression levels in TMZ-treated group than in control group ($p < 0.0001$), with 0.71 ± 0.32 relative expression for treated tumours vs. 0.18 ± 0.08 for control tumours. The same trend was observed for Nos2 gene (0.05 ± 0.03 relative expression for treated tumours vs. 0.01 ± 0.01 for control tumours) and CD206 gene (0.23 ± 0.09 relative expression for treated tumours vs. 0.13 ± 0.06 for control tumours), with significant differences ($p = 0.0002$ and $p = 0.0073$, respectively). Table 1 shows detailed description of gene expression levels and Figure 2 shows gene comparisons. These results suggest that both M1 and M2 subtype populations may increase in TMZ-

treated tumours when compared to vehicle-treated tumours, also supported by the larger global microglia/macrophage population detected with the F4/80 gene expression level.
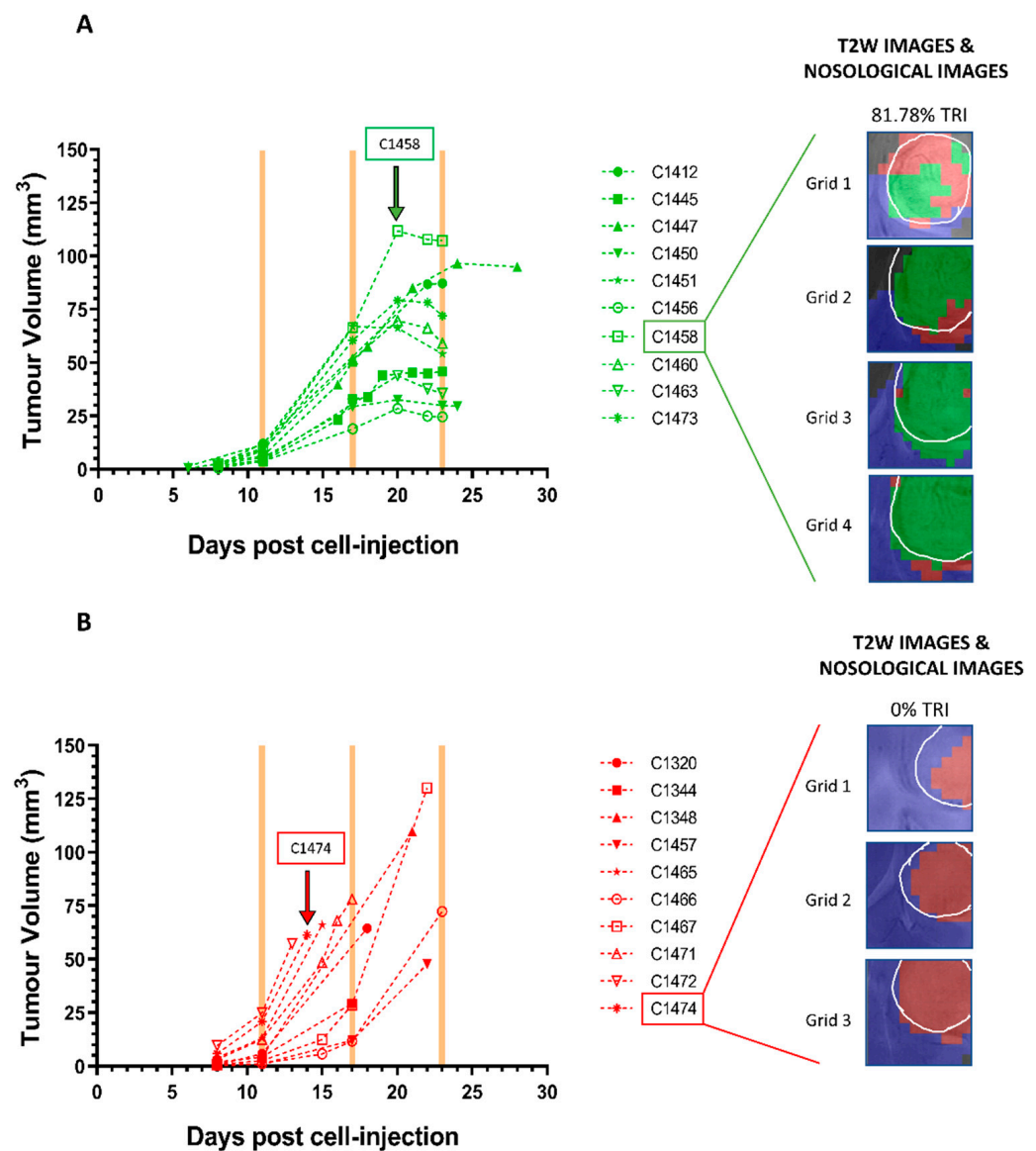
Figure 1. Tumour volume evolution (in mm^3) of (**A**) responding TMZ-treated (*n* = 10) and (**B**) vehicle-treated (*n* = 10) cases. In all responding cases, tumour volumes were in growth arrest, while in all control cases, tumour volume increased fast. Yellow shaded columns indicate TMZ administration days. The last point in the tumour volume evolution line designates the euthanasia day. The tumour volume at therapy start (day 11 p.i.) was 7.50 ± 3.22 mm^3 for TMZ-treated mice and 9.07 ± 8.44 mm^3 for control mice. At the endpoint, the tumour volume was 58.64 ± 26.43 mm^3 and the TRI was 76.97 ± 11.22% for TMZ-treated mice, while the tumour volume was 71.61 ± 29.18 mm^3 and TRI was 4.59 ± 6.31% for control mice. C1458 (unique GABRMN mice identifier) is shown as an example of a responding TMZ-treated mouse, and C1474 is shown as an example of a control mouse. Nosological images obtained from Grids 1–4 of case C1458 and Grids 1–3 of case C1474 were superimposed to the T2w-MRI. The tumour areas from the nosological images have been manually drawn over the tumour (shown in white line), and TRI was calculated from it. Rectangles over arrows at left indicate the cases and time points at which the MRSI-derived nosological images shown at right were acquired.

Table 1. Relative normalised expressions obtained in qPCR studies with IMS-TMZ and IMS-vehicle-treated samples: average ± SD of F4/80, Nos2, CD206, and PD-L1 genes, and ratios of M1/GAMs, M2/GAMs, and M1/M2. Significant differences between groups are indicated by asterisks (*** $p \leq 0.001$, ** $p < 0.005$, and * $p < 0.05$)).

| | Relative Expression | | | | | | |
	F4/80 ***	Nos2 ***	CD206 **	PD-L1 ***	M1/GAMs	M2/GAMs **	M1/M2 *
IMS-TMZ-treated	0.71 ± 0.32	0.05 ± 0.03	0.23 ± 0.09	1.07 ± 0.34	0.07 ± 0.02	0.35 ± 0.16	0.26 ± 0.16
IMS-vehicle treated	0.18 ± 0.08	0.01 ± 0.01	0.13 ± 0.06	0.46 ± 0.16	0.08 ± 0.05	0.84 ± 0.34	0.11 ± 0.09
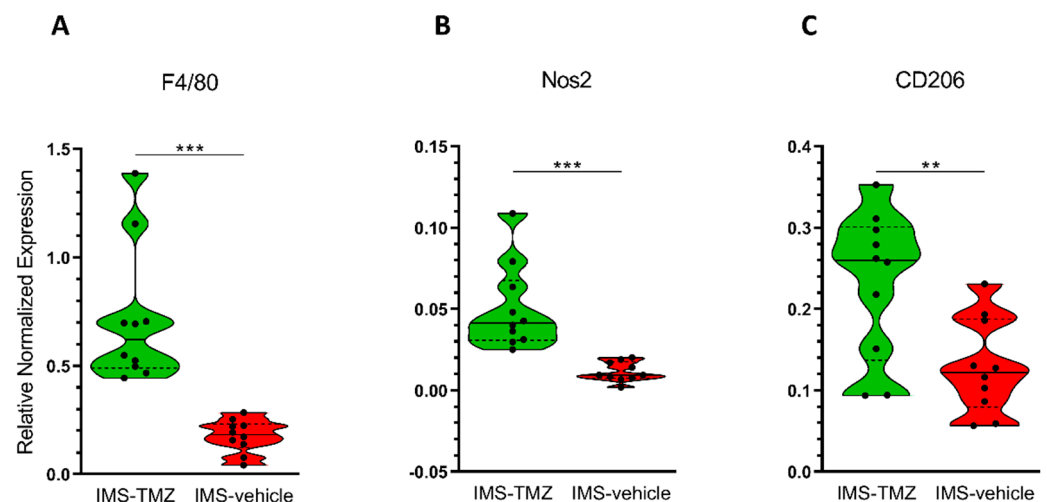
Figure 2. Violin plot for estimation of different cell populations in IMS-TMZ-treated GL261 GB and control mice, for comparisons of (**A**) global GAMs population through F4/80 expression level analysis ($p = 0.0004$), (**B**) M1 macrophage subtype population through Nos2 expression level analysis ($p = 0.001$), and (**C**) M2 macrophage subtype population through CD206 expression level analysis ($p = 0.009$). Data are the mean ± S.D. and significant differences between groups are indicated by asterisks (*** $p \leq 0.001$, ** $p < 0.005$), $n = 10$ for each group. Solid horizontal line in violin plots indicates median and the dashed lines indicate 1st and 3rd quartiles. Note that graphs are shown with different "y" scaling for better appreciation of data distribution.

Moreover, we were also interested in assessing whether the increased levels of global GAMs population would reflect predominant M1 or M2 subtypes. In order to gain more insight into this question, correlation studies were performed with the aforementioned markers F4/80, Nos2 and CD206. Pearson correlation showed significant values for F4/80 vs. Nos2 expression levels in IMS-TMZ-treated samples ($p = 0.0096$), suggesting a positive association (see Figure S2A). This association was not seen in vehicle-treated samples, while CD206 expression was not significantly correlated with F4/80 in any of the instances evaluated (see Figure S2B). These results suggest that the global GAMs population biomarker increase observed in IMS-TMZ-treated tumours (ca. 4-fold) would be mainly related to the increase in the M1 phenotype population and, to a lesser extent, to the increase in the M2 phenotype population.

3.3. Assessing Different Macrophage Population Subtypes Regarding Global GAMs Values

Since the purpose of this work was to provide insight about the relationship between microglia/macrophage subpopulations and the MRSI-sampled pattern in control and IMS-TMZ-treated GL261 GB, M1/GAMs and M2/GAMs ratios were analysed (Figure 3A,B) using the corresponding individual markers (F4/80, Nos2, CD206). Thus, in order to check whether the predominant microglia/macrophage subtype population was different in responding IMS-TMZ-treated and vehicle-treated samples, M1/M2 ratio was calculated taking into account the relation of Nos2 gene to CD206 gene expression (Figure 3C). See Table 1 for M1/GAMs, M2/GAMs, and M1/M2 ratio values. Results essentially show

that there is indeed a change in the M1/M2 subtype proportions in GL261 tumours upon response to treatment. A significantly higher ratio of M1/M2 microglia/macrophages ($p = 0.0249$) was found in responding IMS-TMZ-treated tumours compared to vehicle-treated tumours, while the ratio M1/GAMs showed no differences ($p = 0.7944$). This apparent discrepancy can be explained when we take into account that both M1 sub type and total GAM increase in responding tumours (Figure 2A,B). Furthermore, lower M2/GAMs ratio ($p = 0.0006$) is also found in responding tumours. Even though M2s are seen to increase in responding tumours (Figure 2C), this increase does not compensate for the higher increase of total GAM, thus their ratio decreases (Figure 3B).
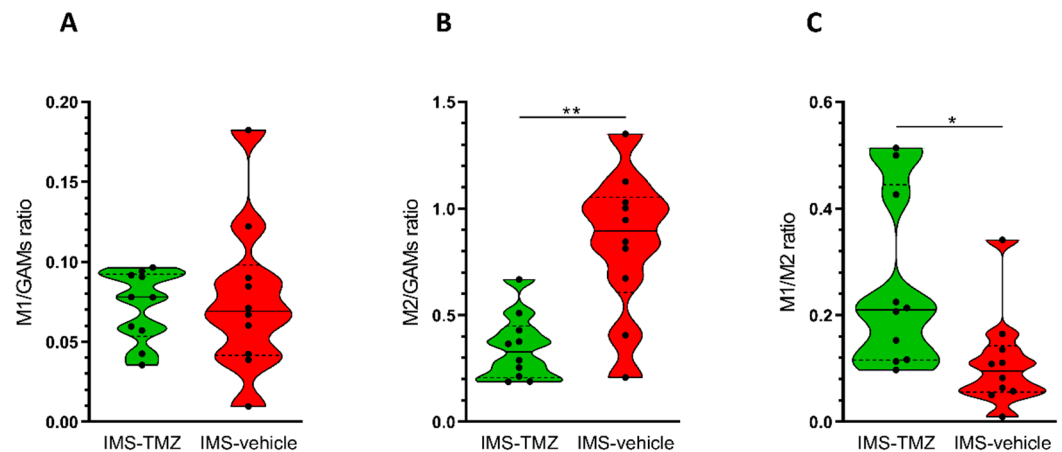
Figure 3. Ratios of (**A**) M1/GAMs, (**B**) M2/GAMs, and (**C**) M1/M2 were calculated in IMS-TMZ-treated ($n = 10$) and control ($n = 10$) tumours using, respectively, the specific markers Nos2 to F4/80, CD206 to F4/80 and Nos2 to CD206. No significant differences were observed ($p = 0.858$) for the ratio of M1/GAMs between TMZ-treated (0.07 ± 0.02 M1/GAMs ratio) and control (0.08 ± 0.05 M1/GAMs ratio) groups. On the other hand, significant differences were found for M2/GAMs ratio ($p = 0.001$) and for M1/M2 ratio ($p = 0.03$) between TMZ-treated (0.35 ± 0.16 M2/GAMs ratio and 0.26 ± 0.16 M1/M2 ratio) and control (0.84 ± 0.34 M2/GAMs ratio and 0.11 ± 0.09 M1/M2 ratio) groups. Data are mean $\pm$ SD and significant differences between groups are indicated by asterisks (** $p < 0.005$, * $p < 0.05$). Explanations for violin plots as in Figure 2. Note that graphs are shown in different "y" scaling for better appreciation of data distribution.

3.4. PD-L1 Gene Is Highly Expressed in IMS-TMZ-Treated Tumours, and These Increases May Be Correlated with the Polarisation State of Microglia/Macrophage Population

The PD-L1 gene level expression was assessed, and values were compared between IMS-TMZ-treated and vehicle-treated groups. Results suggest a significantly higher PD-L1 gene expression in responding TMZ-treated tumours in comparison with control tumours ($p < 0.0001$), with a 1.07 ± 0.34 relative expression found for TMZ-treated tumours and a 0.46 ± 0.16 relative expression for control tumours (see Figure 4A for visual comparison). Furthermore, to investigate whether PD-L1 gene expression levels were correlated with the polarisation state of GAMs, Pearson correlation analyses were performed, and PD-L1 expression level was shown to be positively correlated to the M1/M2 ratio ($p = 0.0127$) (Figure 4B and Figure S2C), suggesting that for higher M1/M2 ratios, a higher PD-L1 expression level was found.
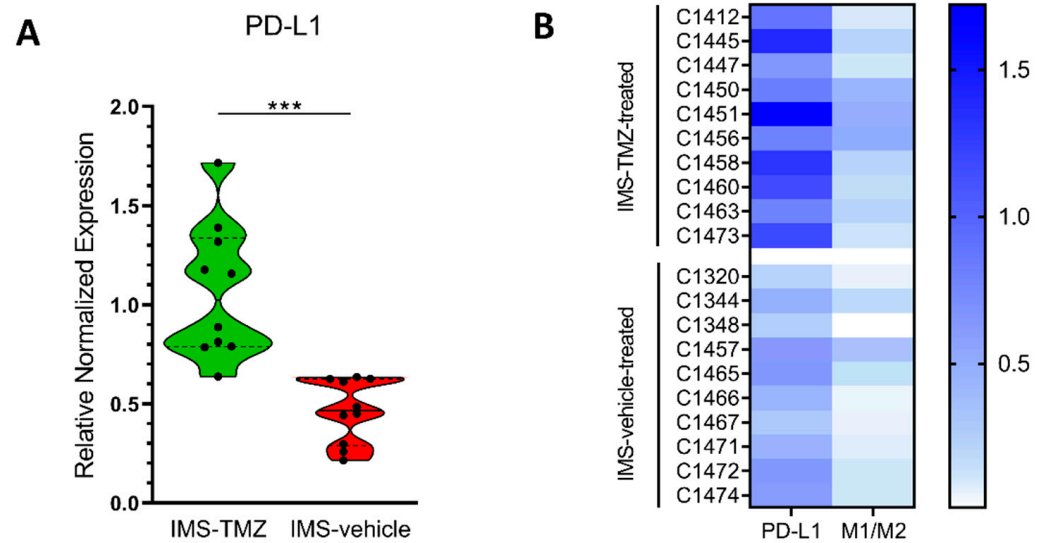
Figure 4. (**A**) Violin plot for comparisons of PD-L1 level analysis expression in tumour samples from IMS-TMZ-treated GL261 GB and control mice ($p < 0.0001$). Data are the mean $\pm$ SD and significant differences between groups are indicated by asterisks (*** $p < 0.001$). Explanations for violin plots as in Figure 2. (**B**) Visual coloured map for normalised expression representing PD-L1 expression level (from Figure 4A) and M1/M2 ratio (from Figure 3C) in each individual case. Pearson correlation analysis in the whole group showed overall significance ($p = 0.013$), although when pairs of values were analysed separately for control and IMS-TMZ-treated groups, only the control set of values showed significance ($p = 0.048$), which was lost for values from treated cases.

4. Discussion

4.1. Immune System Populations Change during Response to Therapy

During this work, samples from GL261 GB-bearing mice treated with IMS-TMZ ($n = 10$) or vehicle ($n = 10$) were analysed by qPCR in order to characterise the microglia/macrophage population into the tumour site. Tumours were excised at chosen time points, guided by the response level spotted by MRSI-based nosological images, reflecting specific changes in their spectral pattern. Our results reinforce the idea of the microglia/macrophages role in tumour evolution: both control and treated tumours presented relevant microglia/macrophage content. Still, an overall increase (ca. 4-fold change in average) in such content was observed in IMS-TMZ-treated tumours responding to therapy, through F4/80 gene level expression (Figure 2A). This trend is in line with previous Iba-1 immunohistochemistry data [31], which reported a 2.4-fold increase in the percentage of Iba-1 stained area for TMZ-treated tumours (when narrowing groups to control vs. high response cases, see [24,31] for further details). Since different methodological approaches were used in [24,31] and in this work, direct comparison of results is not straightforward, as already described by others [42], although the trend is clear.

Increased infiltration of immune cells into tumour sites after therapy and its relationship with effective response has been described for cancer types such as colorectal [43], breast [44], ovarian [45], and brain [46], in agreement with results described in this work. Immune infiltration has been described as a good prognostic factor, and certain chemotherapeutic agents were described to actually enhance the host immune response through presentation of tumour antigen peptides to T-cells, or upregulation of tumour antigens, rendering these tumour cells more susceptible to immune system attack [47]. This is also related to the corollary that effective therapeutic strategies should convert a 'cold' tumour (noninflamed) with low immune cell infiltration into a 'hot' tumour (inflamed) with high immune cell infiltration [48].

In our study, response to IMS-TMZ treatment increased the infiltrating microglia/macrophage population. The beneficial effect of TMZ in preclinical/clinical settings was mainly attributed to its effect as DNA alkylating agent and activation of the apoptotic cascade [49,50].

However, it is worth noting that TMZ alone has a cytostatic rather than cytotoxic mechanism, when added to GL261 cultured cells at concentrations similar to the ones used in preclinical studies, as described in [9,51–53]. Thus, the main beneficial effects observed with TMZ therapy may have a different explanation. In this respect, the potential immunogenic effects of TMZ are gaining prominence [9,54–58]. Through the release/exposure of immunogenic signals, TMZ administration may launch the cancer immune cycle as described by Chen and Mellman [59], eventually leading to tumour cell killing. On the other hand, it was also described that DNA damage repair (DDR) mechanisms triggered after TMZ exposure could lead to reprogramming of macrophages to a tumor-supportive state (M2) and TMZ-resistant cells would display upregulated DDR cytokines (preclinical and database human samples) [60], in line with overall results described in [61] with GL261 cells. Hence, TMZ can have an indirect role in microglia/macrophage polarisation changes, with an M2 polarization being supported by different authors [62,63], although none of them used an IMS schedule. Still, we should also have in mind a possible indirect effect of TMZ over the lymphocytes anergy status after striking the tumour, which may superimpose in time with the periodic TMZ administration. One of the goals of our work was to investigate whether local changes in IMS-TMZ-treated tumours, especially with respect to immune system, would be related to MRSI-detected spectral pattern changes, as previously proposed [24,25,31]. The cancer immune cycle involves several cellular populations and local factors. However, in order to be detected by MRSI-based approaches (i.e., to significantly contribute to the spectral pattern), these cellular populations must represent a significant proportion of the tumour volume. Hence, the GAM population is a suitable candidate to be at least partially responsible for the observed changes, since they are the most common non-tumoural cell within GB masses, reaching values up to 30–40% of the overall volume [5]. Other cellular populations such as lymphocytes would represent only a small fraction of the GB mass volume (ca 1% in GL261 GB, unpublished GABRMN data) and may not have a direct impact in spectral pattern changes.

4.2. Not All GAMs Are Equal (I): Polarisation of Microglia/Macrophages and Its Role in Therapy Response in GB

In the majority of solid tumours, progression is associated with a phenotype prevalence changing from M1 to M2 [64], which can trigger the suppression of effector T cell immunity, improved tumour cell survival, promotion of angiogenesis, and chemoresistance [65]. In this sense, we assessed the GAM polarisation profile when GL261 tumours showed a clear MRSI-detected responding pattern and compared them with untreated control tumours. Our goal was to better understand the oscillatory behaviour of the MRSI-detected pattern in terms of a transient/permanent response to therapy in GL261 GB [24,31].

Our studies with Nos2 and CD206 gene markers suggest, first, that both control and IMS-TMZ-treated tumours contain M1 and M2 microglia/macrophages (Figure 3A,B), in line with data for control GL261 tumours described in [66]. More interestingly, our results point to a significantly higher ratio of M1/M2 microglia/macrophage content in IMS-TMZ-treated responding tumours (Figure 3C), being ca. 2.3-fold times higher than in control tumours. This result indicates a phenotype switch of GAM from M2 to M1 in responding tumours compared to control tumours. In other words, more cells infiltrating the tumour with the ability to start and sustain inflammatory responses and to exhibit antitumour activity and leading to tumour tissue disruption. This specific M1/M2 ratio was also evaluated by other authors in various cancer tumour types and in relation to outcome prognosis. For example, high content of M1 macrophages was associated with best prognosis in treated ovarian cancer patients, suggesting a correlation between efficacy of antineoplastic regimens and M1 polarisation [67]. On the other hand, authors in [68] studied the prevalence of M2-polarised macrophages in different lung neoplastic lesions, with high M2 infiltration predicting poor prognosis. In lung adenocarcinomas, 79.71% of tumour-associated macrophages were M2 polarised and the remaining 20.35% were M1 polarised [68]. Regarding brain tumour-related studies, investigation with clinical

glioma samples have found an association between high CD163$^+$ cells (M2 marker) and glioma progression [69]. In the same line, authors in [37] have found that predominant M1 polarisation was associated with better overall prognosis of GB patients, using CXCL10 and CCL13 as markers for M1 and M2 macrophages, respectively. Moreover, the M1/M2 ratio was described to be correlated with survival rate in GB patients after TMZ treatment [70]. Further work reported in [71] revealed mixed profiles of M1 and M2 macrophages in human GB while the ratio M1/M2 correlated with survival in IDH1 wild type GB. It is then clear that achieving suitable M1/M2 ratios is desirable and will be determinant for outcome in preclinical and clinical GB.

4.3. Not All GAMs Are Equal (II): The Polarisation Status of Microglia/Macrophages Affects Their Metabolomic Pattern

It has been described that microglia/macrophage polarisation implies metabolic changes, involving pathways such as glycolysis, the Krebs cycle, and fatty acid metabolism, enabling the specialised activities of these cells [72,73]. Furthermore, changes in key metabolic regulatory events in microglia/macrophages can be initiated in response to changes in the tumour microenvironment [74]. In relation to this, M1 macrophages rely on glycolysis for energy production, while M2 macrophages mostly use mitochondrial oxidative metabolism (Krebs cycle) for ATP biogenesis. This entails that M1 microglia/macrophages increase lactate release and fatty acid synthesis, while the synthesis of N-acetyl group-containing compounds, glutamine, glycine, and alanine, among others, is upregulated in the M2 microglia/macrophage population [11,72,75,76]. Besides, the differential induction of fatty acid synthesis and fatty acid oxidation elicits microglia/macrophage polarisation towards M1 or M2 profiles, respectively [11].

The different metabolic pathways should contribute, at least partially, to the differential metabolomic pattern detected in vivo by MRSI-based analyses in GL261 GB transiently responding to therapy compared with control, untreated tumours. In this respect, the prototypical source of TMZ-responding tumours [23] shows large amounts of mobile lipids/lactate (1.33 ppm signal) and increased lactate at 4.1 ppm, combined with higher polyunsaturated fatty acids (PUFA, 2.8 ppm signal) and other changes in the glutamine, glutamate, and alanine regions, which would be consistent with the metabolic profiles expected for the M1 subtype compared to the M2 subtype (e.g., higher lactate in M1s), related to the limitation of pyruvate entrance into the Krebs cycle triggering formation of high amounts of lactate from pyruvate [77]).

However, more detailed studies will be needed to further assess the actual impact of metabolic changes related to microglia/macrophage polarization on the in vivo MRSI differential metabolomic pattern. In this respect, it is worth remembering that the tumour spectroscopic pattern also contains contributions from tumour cells and extracellular metabolites/macromolecules/lipids present in the tumour microenvironment in suitable concentration to be detected by MRSI. In any case, the MRSI-based nosological images and the changes in spectral pattern (sources) behind those images seem to be coherent with changes in M1/M2 ratios. This reinforces the potential of those images for early in vivo detection of whether a certain therapeutic approach is properly eliciting efficient host immune response against GB tumours.

Finally, we may also consider that literature describes M2 macrophages being able to re-polarise to M1, but not the reverse; M1 macrophages are mostly consumed during the inflammatory response [78]. Then, after a first "wave" of macrophage M1 polarisation and tumour cell killing, probably driven by interaction with T-cells [9], M1 sub-population decrease would bring down M1/M2 ratios, close to levels found in untreated actively proliferating tumours. Figure S3 combines a hypothetic scheme of events taking place during IMS-TMZ therapy in GL261 GB demonstrated in this work (GAM changes, M1/M2 polarisation) with the corresponding changes in the MRSI-based nosological images described in previous work [23–25,31] and used here to select adequate time points for sampling. Its potential relevance for translational studies is also highlighted there.

4.4. PD-L1 Gene Expression in GL261 GB

PD-L1 expression level is considered a major positive prognostic biomarker for immune therapy in many cancers, but not yet in glioma [79]. The expression and subcellular distribution of PD-L1 in the tumour tissue exhibits great variability reflecting the specificities of cellular and structural microenvironment in the brain, preventing the confident use of PD-L1 as a prognostic biomarker in glioma [80].

Results obtained in the present work have assessed the PD-L1 gene level expression in IMS-TMZ-treated and vehicle-treated GL261 GB groups. A significantly higher PD-L1 gene expression (2.3-fold) was found in responding TMZ-treated tumours compared to untreated ones. Chemotherapy has been described to modify the tumour microenvironment, increasing PD-L1 expression [81,82], and our previous work with Western-blot analysis for control, treated-relapsing, and unresponsive data from GL261 GB samples [31] seems to partially agree with those results. This is in line with results described by authors in [83], who also suggested that PD-L1 increase was related to STAT3 signalling. Furthermore, a significant positive correlation was found between PD-L1 gene expression level and the M1/M2 ratio (see Figure 4B and Figure S2C), indicating that increased PD-L1 content could be associated with increased M1-polarised macrophages.

PD-L1 is known to be expressed in a variety of cell types, including macrophages. For example, a study of patient GB samples showed that monocytes cultured in glioma-conditioned medium expressed high levels of PD-L1 [84]. The role of PD-L1 in tumour cells and macrophages seems to be different, though. An interesting study with murine melanoma and breast cancer cells by Singhal et al. [85] showed that only PD-L1 on target tumour cells clearly inhibited the effector functions of T cells. PD-L1 expressed by macrophages exerted a regulatory role only during the interaction of macrophages presenting tumour antigen to effector T cells. Thus, in this case PD-L1 could be simply limiting excessive activation of T cells and protecting PD-L1 harbouring macrophages from being killed by approaching T cells [85]. In short, available evidence indicates that PD-L1 from both tumour cells and microglia/macrophages is relevant for assessing prognosis [86]. In our case, the origin of the reported PD-L1 expression level changes is still unclear, since samples analysed contain both tumour cells and GAMs and further studies will be needed for better clarification of this extreme.

4.5. Wrap-up: Incoporating the Measured Gene Expression Results into the Explanation of the Oscillatory Behaviour of the MRSI-Based Biomarker of Response

In longitudinal studies of IMS-treated response assessment, we have reported periodic oscillations of the MRSI-based biomarker showing increases in the detected response level (TRI) every 6 days. In this sense, we also assume that there are tissue events/changes that originate this oscillation, alternating a high response nosological image profile with periods showing tissue characteristics that resemble more an actively proliferating tumour.

Figure S3 summarises how we correlate cellular/molecular events taking place with results obtained in this work. At the therapy starting point, GL261 GB tumours display an essentially protumoural microglia/macrophage phenotype, supported by qPCR results and encoded in the red colour over the tumour mass of the nosological images. TMZ therapy may lead to release/exposure of immunogenic signals [53], which set the cancer immunity cycle [59]. In the meanwhile, both M1 and M2 populations increase (see also Figure 2A): M1 microglia/macrophages will participate in tumour cell killing [9], and M2 microglia/macrophages are waiting for M1 polarisation. The M1/M2 ratio changes towards higher values in tumours showing transient response to IMS-TMZ (Figure 3C). Maximum response is spotted by our noninvasive biomarker (green colour in nosological images) after ca. 6 days of therapy administration, in line with the length of the immune cycle described in [32]. At this point, an increase in PD-L1 gene expression is observed (Figure 4A), although its origin could be either in tumour cell population, microglia/macrophages or both together. Since M1 microglia/macrophages are mostly consumed during the antitumour response events, after such interval, the ratio M1/M2 may shift towards the

control values, T lymphocytes may be approaching exhaustion, and surviving tumour cells may start proliferating again leading to tumour regrowth (day +9, red colour over the tumour image) until the previous therapeutic administration point (at day +6) resets the immune cycle and produces the next response oscillation (day +12).

Having this hypothesis in mind, how can we obtain an advantage regarding this biomarker? It is worth noting that therapy can modulate/change macrophage profiles towards an inflammatory M1 profile with satisfactory results, as already described in preclinical GB models using amphotericin B [87], CSF-1R inhibition [88], immunovirotherapy [89], or recombinant adeno-associated virus [90], although the latter presented only modest result in phase II clinical phases [91]. On the other hand, work described in [92] focused into blocking relevant pathways in protumoural macrophages with minocycline in preclinical murine GB models. Our results suggest that our imaging biomarker findings are at least partially explained by changes in microglia/macrophage profiles within brain tumours (hence, in the expected antitumour/protumour actions). Thus, we may be able, in a near future, to follow-up different therapies and foresee results in an early fashion gathering hints about the prevailing macrophage population at a given moment. A word of caution may be issued here, since the mutational load of GL261 [93] is much higher than untreated human GB [94] and this could be a determinant for host immune system eliciting. In this respect, relapsing human GB contain a similar mutational load [95] to GL261 tumours. Further confirmation of the potential of such imaging biomarker in human GB therapy response follow-up may be worthwhile to investigate.

5. Conclusions

Our results confirm that TMZ administered in an immune-enhancing metronomic schedule increases the GB-associated microglia/macrophage population infiltrating the tumour. The M2/GAMs ratio was shown to be remarkably lower in responding IMS-TMZ-treated mice, while the M1/M2 ratio was significantly higher when compared to vehicle-treated mice. These results indicate that TMZ treatment applied in IMS protocols contributes to immune system activation, suggesting M2-to-M1 polarisation, improving the anti-tumoural response mediated by microglia/macrophages. Since it is well known that GAMs can represent 30–40% of cells in GB and M1 and M2 microglia/macrophages have different metabolic profiles, this relative population change could be one of the reasons for the differential MRSI-sampled pattern during response to therapy reinforcing its proposed role as immune system activity biomarker for future work.

It remains unclear whether the increase of the PD-L1 gene level expression in the responding IMS-TMZ-treated tumours originates from changes in tumour cells, the M1/M2 microglia/macrophages polarisation, or both. Further studies will be needed to assess the relative roles of the two cell types in the detected increase of the PD-L1 expression upon response to therapy in the GL261 GB.

Institutional Review Board Statement: All animal studies were conducted according to the protocol approved by the local ethics committee (*Comissió d'Ètica en l'Experimentació Animal i Humana*, https://www.uab.cat/etica-recerca/, accessed on 26 May 2021) according to regional and state legislations (protocol CEEAH-3665 approved on 5 February 2018).

Informed Consent Statement: Not applicable.

Data Availability Statement: The data presented in this study are available on request from the corresponding author.

Conflicts of Interest: The authors declare no conflict of interest.

References

1. Hanif, F.; Muzaffar, K.; Perveen, K.; Malhi, S.M.; Simjee, S.U. Glioblastoma Multiforme: A Review of its Epidemiology and Pathogenesis through Clinical Presentation and Treatment. *Asian Pac. J. Cancer Prev.* **2017**, *18*, 3–9.
2. Stupp, R.; Hegi, M.E.; Mason, W.P.; Bent, M.J.V.D.; Taphoorn, M.J.B.; Janzer, R.C.; Ludwin, S.K.; Allgeier, A.; Fisher, B.; Belanger, K.; et al. Effects of radiotherapy with concomitant and adjuvant temozolomide versus radiotherapy alone on survival in glioblastoma in a randomised phase III study: 5-year analysis of the EORTC-NCIC trial. *Lancet Oncol.* **2009**, *10*, 459–466. [CrossRef]
3. Pardoll, D. Cancer and the Immune System: Basic Concepts and Targets for Intervention. *Semin. Oncol.* **2015**, *42*, 523–538. [CrossRef]
4. Razavi, S.-M.; Lee, K.E.; Jin, B.E.; Aujla, P.S.; Gholamin, S.; Li, G. Immune Evasion Strategies of Glioblastoma. *Front. Surg.* **2016**, *3*, 11. [CrossRef] [PubMed]
5. Hambardzumyan, D.; Gutmann, D.; Kettenmann, H. The role of microglia and macrophages in glioma maintenance and progression. *Nat. Neurosci.* **2016**, *19*, 20–27. [CrossRef] [PubMed]
6. Lisi, L.; Ciotti, G.; Braun, D.; Kalinin, S.; Currò, D.; Russo, C.D.; Coli, A.; Mangiola, A.; Anile, C.; Feinstein, D.; et al. Expression of iNOS, CD163 and ARG-1 taken as M1 and M2 markers of microglial polarization in human glioblastoma and the surrounding normal parenchyma. *Neurosci. Lett.* **2017**, *645*, 106–112. [CrossRef] [PubMed]
7. Gutmann, D.H.; Kettenmann, H. Microglia/Brain Macrophages as Central Drivers of Brain Tumor Pathobiology. *Neuron* **2019**, *104*, 442–449. [CrossRef] [PubMed]
8. Bingle, L.; Brown, N.J.; E Lewis, C. The role of tumour-associated macrophages in tumour progression: Implications for new anticancer therapies. *J. Pathol.* **2002**, *196*, 254–265. [CrossRef]
9. Von Roemeling, C.A.; Wang, Y.; Qie, Y.; Yuan, H.; Zhao, H.; Liu, X.; Yang, Z.; Yang, M.; Deng, W.; Bruno, K.A.; et al. Therapeutic modulation of phagocytosis in glioblastoma can activate both innate and adaptive antitumour immunity. *Nat. Commun.* **2020**, *11*, 1–12. [CrossRef]
10. Zhao, P.; Wang, Y.; Kang, X.; Wu, A.; Yin, W.; Tang, Y.; Wang, J.; Zhang, M.; Duan, Y.; Huang, Y. Dual-targeting biomimetic delivery for anti-glioma activityviaremodeling the tumor microenvironment and directing macrophage-mediated immunotherapy. *Chem. Sci.* **2018**, *9*, 2674–2689. [CrossRef]
11. Viola, A.; Munari, F.; Sánchez-Rodríguez, R.; Scolaro, T.; Castegna, A. The Metabolic Signature of Macrophage Responses. *Front. Immunol.* **2019**, *10*, 1462. [CrossRef] [PubMed]
12. Thapa, B.; Lee, K. Metabolic influence on macrophage polarization and pathogenesis. *BMB Rep.* **2019**, *52*, 360–372. [CrossRef] [PubMed]
13. Grégoire, H.; Roncali, L.; Rousseau, A.; Chérel, M.; Delneste, Y.; Jeannin, P.; Hindré, F.; Garcion, E. Targeting Tumor Associated Macrophages to Overcome Conventional Treatment Resistance in Glioblastoma. *Front. Pharmacol.* **2020**, *11*, 368. [CrossRef]
14. Zhang, X.; Zhu, S.; Li, T.; Liu, Y.-J.; Chen, W.; Chen, J. Targeting immune checkpoints in malignant glioma. *Oncotarget* **2017**, *8*, 7157–7174. [CrossRef] [PubMed]
15. Keir, M.E.; Butte, M.J.; Freeman, G.J.; Sharpe, A.H. PD-1 and Its Ligands in Tolerance and Immunity. *Annu. Rev. Immunol.* **2008**, *26*, 677–704. [CrossRef] [PubMed]
16. Mirghorbani, M.; Van Gool, S.; Rezaei, N. Myeloid-derived suppressor cells in glioma. *Expert Rev. Neurother.* **2013**, *13*, 1395–1406. [CrossRef]

17. Antonios, J.P.; Soto, H.; Everson, R.; Moughon, D.; Orpilla, J.R.; Shin, N.P.; Sedighim, S.; Treger, J.; Odesa, S.; Tucker, A.; et al. Immunosuppressive tumor-infiltrating myeloid cells mediate adaptive immune resistance via a PD-1/PD-L1 mechanism in glioblastoma. *Neuro-Oncology* **2017**, *19*, 796–807. [CrossRef] [PubMed]

18. Lu, D.; Ni, Z.; Liu, X.; Feng, S.; Dong, X.; Shi, X.; Zhai, J.; Mai, S.; Jiang, J.; Wang, Z.; et al. Beyond T Cells: Understanding the Role of PD-1/PD-L1 in Tumor-Associated Macrophages. *J. Immunol. Res.* **2019**, *2019*, 1–7. [CrossRef]

19. Wu, J.; Waxman, D. Metronomic cyclophosphamide eradicates large implanted GL261 gliomas by activating antitumor Cd8+T-cell responses and immune memory. *OncoImmunology* **2015**, *4*, e1005521. [CrossRef]

20. Iorgulescu, J.B.; Gokhale, P.C.; Speranza, M.C.; Eschle, B.K.; Poitras, M.J.; Wilkens, M.K.; Soroko, K.M.; Chhoeu, C.; Knott, A.; Gao, Y.; et al. Concurrent Dexamethasone Limits the Clinical Benefit of Immune Checkpoint Blockade in Glioblastoma. *Clin. Cancer Res.* **2021**, *27*, 276–287. [CrossRef]

21. Tran, T.-A.-T.; Kim, Y.-H.; Duong, T.-H.-O.; Jung, S.; Kim, I.-Y.; Moon, K.-S.; Jang, W.-Y.; Lee, H.-J.; Lee, J.-J.; Jung, T.-Y. Peptide Vaccine Combined Adjuvants Modulate Anti-tumor Effects of Radiation in Glioblastoma Mouse Model. *Front. Immunol.* **2020**, *11*, 1165. [CrossRef]

22. Ferrer-Font, L.; Arias-Ramos, N.; Lope-Piedrafita, S.; Julià-Sapé, M.; Pumarola, M.; Arús, C.; Candiota, A.P. Metronomic treatment in immunocompetent preclinical GL261 glioblastoma: Effects of cyclophosphamide and temozolomide. *NMR Biomed.* **2017**, *30*, e3748. [CrossRef]

23. Delgado-Goñi, T.; Ortega-Martorell, S.; Ciezka, M.; Olier, I.; Candiota, A.P.; Julià-Sapé, M.; Fernández-Flores, F.; Pumarola, M.; Lisboa, P.J.; Arús, C. MRSI-based molecular imaging of therapy response to temozolomide in preclinical glioblastoma using source analysis. *NMR Biomed.* **2016**, *29*, 732–743. [CrossRef]

24. Arias-Ramos, N.; Ferrer-Font, L.; Lope-Piedrafita, S.; Mocioiu, V.; Julià-Sapé, M.; Pumarola, M.; Arús, C.; Candiota, A.P. Metabolomics of Therapy Response in Preclinical Glioblastoma: A Multi-Slice MRSI-Based Volumetric Analysis for Noninvasive Assessment of Temozolomide Treatment. *Metabolites* **2017**, *7*, 20. [CrossRef] [PubMed]

25. Wu, S.; Calero-Pérez, P.; Arús, C.; Candiota, A. Anti-PD-1 Immunotherapy in Preclinical GL261 Glioblastoma: Influence of Therapeutic Parameters and Non-Invasive Response Biomarker Assessment with MRSI-Based Approaches. *Int. J. Mol. Sci.* **2020**, *21*, 8775. [CrossRef] [PubMed]

26. Chronaiou, I.; Stensjøen, A.L.; Sjøbakk, T.E.; Esmaeili, M.; Bathen, T.F. Impacts of MR spectroscopic imaging on glioma patient management. *Acta Oncol.* **2014**, *53*, 580–589. [CrossRef] [PubMed]

27. Horská, A.; Barker, P.B. Imaging of Brain Tumors: MR Spectroscopy and Metabolic Imaging. *Neuroimaging Clin. N. Am.* **2010**, *20*, 293–310. [CrossRef]

28. Pandey, R.; Caflisch, L.; Lodi, A.; Brenner, A.J.; Tiziani, S. Metabolomic signature of brain cancer. *Mol. Carcinog.* **2017**, *56*, 2355–2371. [CrossRef]

29. Julià-Sapé, M.; Candiota, A.P.; Arús, C. Cancer metabolism in a snapshot: MRS(I). *NMR Biomed.* **2018**, *32*, e4054. [CrossRef]

30. Ortega-Martorell, S.; Lisboa, P.J.G.; Vellido, A.; Simões, R.V.; Pumarola, M.; Julià-Sapé, M.; Arús, C. Convex Non-Negative Matrix Factorization for Brain Tumor Delimitation from MRSI Data. *PLoS ONE* **2012**, *7*, e47824. [CrossRef]

31. Wu, S.; Calero-Pérez, P.; Villamañan, L.; Arias-Ramos, N.; Pumarola, M.; Ortega-Martorell, S.; Julià-Sapé, M.; Arús, C.; Candiota, A.P. Anti-tumour immune response in GL261 glioblastoma generated by Temozolomide Immune-Enhancing Metronomic Schedule monitored with MRSI-based nosological images. *NMR Biomed.* **2020**, *33*. [CrossRef] [PubMed]

32. Karman, J.; Ling, C.; Sandor, M.; Fabry, Z. Initiation of Immune Responses in Brain Is Promoted by Local Dendritic Cells. *J. Immunol.* **2004**, *173*, 2353–2361. [CrossRef] [PubMed]

33. Simoes, R.V.; García-Martín, M.L.; Cerdan, S.; Arús, C. Perturbation of mouse glioma MRS pattern by induced acute hyperglycemia. *NMR Biomed.* **2007**, *21*, 251–264. [CrossRef] [PubMed]

34. Garofalo, S.; Porzia, A.; Mainiero, F.; Di Angelantonio, S.; Cortese, B.; Basilico, B.; Pagani, F.; Cignitti, G.; Chece, G.; Maggio, R.; et al. Environmental stimuli shape microglial plasticity in glioma. *eLife* **2017**, *6*, e33415. [CrossRef] [PubMed]

35. Simões, R.; Delgado-Goñi, T.; Lope-Piedrafita, S.; Arús, C. 1 H-MRSI pattern perturbation in a mouse glioma: The effects of acute hyperglycemia and moderate hypothermia. *NMR Biomed.* **2009**, *23*, 23–33. [CrossRef]

36. Eisenhauer, E.A.; Therasse, P.; Bogaerts, J.; Schwartz, L.H.; Sargent, D.; Ford, R.; Dancey, J.; Arbuck, S.; Gwyther, S.; Mooney, M.; et al. New response evaluation criteria in solid tumours: Revised RECIST guideline (version 1.1). *Eur. J. Cancer* **2009**, *45*, 228–247. [CrossRef]

37. Gjorgjevski, M.; Hannen, R.; Carl, B.; Li, Y.; Landmann, E.; Buchholz, M.; Bartsch, J.W.; Nimsky, C. Molecular profiling of the tumor microenvironment in glioblastoma patients: Correlation of microglia/macrophage polarization state with metalloprotease expression profiles and survival. *Biosci. Rep.* **2019**, *39*. [CrossRef]

38. Zhu, Y.; Zhang, L.; Lu, Q.; Gao, Y.; Cai, Y.; Sui, A.; Su, T.; Shen, X.; Xie, B. Identification of different macrophage subpopulations with distinct activities in a mouse model of oxygen-induced retinopathy. *Int. J. Mol. Med.* **2017**, *40*, 281–292. [CrossRef]

39. Hannen, R.; Selmansberger, M.; Hauswald, M.; Pagenstecher, A.; Nist, A.; Stiewe, T.; Acker, T.; Carl, B.; Nimsky, C.; Bartsch, J.W. Comparative Transcriptomic Analysis of Temozolomide Resistant Primary GBM Stem-Like Cells and Recurrent GBM Identifies Up-Regulation of the Carbonic Anhydrase CA2 Gene as Resistance Factor. *Cancers* **2019**, *11*, 921. [CrossRef]

40. Watters, J.J.; Schartner, J.M.; Badie, B. Microglia function in brain tumors. *J. Neurosci. Res.* **2005**, *81*, 447–455. [CrossRef]

41. Rao, X.; Huang, X.; Zhou, Z.; Lin, X. An improvement of the 2ˆ(–delta delta CT) method for quantitative real-time polymerase chain reaction data analysis. *Biostat. Bioinform. Biomath.* **2013**, *3*, 71–85.

42. Sinn, H.-P.; Schneeweiss, A.; Keller, M.; Schlombs, K.; Laible, M.; Seitz, J.; Lakis, S.; Veltrup, E.; Altevogt, P.; Eidt, S.; et al. Comparison of immunohistochemistry with PCR for assessment of ER, PR, and Ki-67 and prediction of pathological complete response in breast cancer. *BMC Cancer* **2017**, *17*, 1–10. [CrossRef]

43. Matsutani, S.; Shibutani, M.; Maeda, K.; Nagahara, H.; Fukuoka, T.; Nakao, S.; Hirakawa, K.; Ohira, M. Significance of tumor-infiltrating lymphocytes before and after neoadjuvant therapy for rectal cancer. *Cancer Sci.* **2018**, *109*, 966–979. [CrossRef]

44. Ladoire, S.; Mignot, G.; Dabakuyo, S.; Arnould, L.; Apetoh, L.; Rébé, C.; Coudert, B.; Martin, F.; Bizollon, M.H.; Vanoli, A.; et al. In situ immune response after neoadjuvant chemotherapy for breast cancer predicts survival. *J. Pathol.* **2011**, *224*, 389–400. [CrossRef]

45. Liu, R.; Hu, R.; Zeng, Y.; Zhang, W.; Zhou, H.-H. Tumour immune cell infiltration and survival after platinum-based chemotherapy in high-grade serous ovarian cancer subtypes: A gene expression-based computational study. *EBioMedicine* **2020**, *51*, 102602. [CrossRef]

46. Nesseler, J.P.; Schaue, D.; McBride, W.H.; Lee, M.-H.; Kaprealian, T.; Niclou, S.P.; Nickers, P. Irradiation to Improve the Response to Immunotherapeutic Agents in Glioblastomas. *Adv. Radiat. Oncol.* **2019**, *4*, 268–282. [CrossRef]

47. Jochems, C.; Schlom, J. Tumor-infiltrating immune cells and prognosis: The potential link between conventional cancer therapy and immunity. *Exp. Biol. Med.* **2011**, *236*, 567–579. [CrossRef] [PubMed]

48. Haanen, J.B. Converting Cold into Hot Tumors by Combining Immunotherapies. *Cell* **2017**, *170*, 1055–1056. [CrossRef] [PubMed]

49. Roos, W.P.; Batista, L.F.Z.; Naumann, S.C.; Wick, W.; Weller, M.; Menck, C.F.M.; Kaina, B. Apoptosis in malignant glioma cells triggered by the temozolomide-induced DNA lesion O6-methylguanine. *Oncogene* **2006**, *26*, 186–197. [CrossRef]

50. De Salvo, M.; Maresca, G.; D'Agnano, I.; Marchese, R.; Stigliano, A.; Gagliassi, R.; Brunetti, E.; Raza, G.H.; De Paula, U.; Bucci, B. Temozolomide induced c-Myc-mediated apoptosisviaAkt signalling in MGMT expressing glioblastoma cells. *Int. J. Radiat. Biol.* **2011**, *87*, 518–533. [CrossRef] [PubMed]

51. Strobel, H.; Baisch, T.; Fitzel, R.; Schilberg, K.; Siegelin, M.D.; Karpel-Massler, G.; Debatin, K.-M.; Westhoff, M.-A. Temozolomide and Other Alkylating Agents in Glioblastoma Therapy. *Biomedicines* **2019**, *7*, 69. [CrossRef] [PubMed]

52. Günther, W.; Pawlak, E.; Damasceno, R.; Arnold, H.; Terzis, A.J. Temozolomide induces apoptosis and senescence in glioma cells cultured as multicellular spheroids. *Br. J. Cancer* **2003**, *88*, 463–469. [CrossRef] [PubMed]

53. Villamañan, L.; Martínez-Escardó, L.; Arús, C.; Yuste, V.; Candiota, A. Successful Partnerships: Exploring the Potential of Immunogenic Signals Triggered by TMZ, CX-4945, and Combined Treatment in GL261 Glioblastoma Cells. *Int. J. Mol. Sci.* **2021**, *22*, 3453. [CrossRef] [PubMed]

54. Fritzell, S.; Sandén, E.; Eberstål, S.; Visse, E.; Darabi, A.; Siesjö, P. Intratumoral temozolomide synergizes with immunotherapy in a T cell-dependent fashion. *Cancer Immunol. Immunother.* **2013**, *62*, 1463–1474. [CrossRef] [PubMed]

55. Curtin, J.F.; Liu, N.; Candolfi, M.; Xiong, W.; Assi, H.; Yagiz, K.; Edwards, M.R.; Michelsen, K.S.; Kroeger, K.M.; Liu, C.; et al. HMGB1 Mediates Endogenous TLR2 Activation and Brain Tumor Regression. *PLoS Med.* **2009**, *6*, e1000010. [CrossRef]

56. Kim, T.-G.; Kim, C.-H.; Park, J.-S.; Park, S.-D.; Kim, C.K.; Chung, D.-S.; Hong, Y.-K. Immunological Factors Relating to the Antitumor Effect of Temozolomide Chemoimmunotherapy in a Murine Glioma Model. *Clin. Vaccine Immunol.* **2009**, *17*, 143–153. [CrossRef] [PubMed]

57. Karachi, A.; Dastmalchi, F.; A Mitchell, D.; Rahman, M. Temozolomide for immunomodulation in the treatment of glioblastoma. *Neuro-Oncology* **2018**, *20*, 1566–1572. [CrossRef]

58. Opzoomer, J.W.; Sosnowska, D.; Anstee, J.E.; Spicer, J.F.; Arnold, J.N. Cytotoxic Chemotherapy as an Immune Stimulus: A Molecular Perspective on Turning Up the Immunological Heat on Cancer. *Front. Immunol.* **2019**, *10*, 1654. [CrossRef]

59. Chen, D.S.; Mellman, I. Oncology Meets Immunology: The Cancer-Immunity Cycle. *Immunity* **2013**, *39*, 1–10. [CrossRef]

60. Meng, X.; Duan, C.; Pang, H.; Chen, Q.; Han, B.; Zha, C.; Dinislam, M.; Wu, P.; Li, Z.; Zhao, S.; et al. DNA damage repair alterations modulate M2 polarization of microglia to remodel the tumor microenvironment via the p53-mediated MDK expression in glioma. *EBioMedicine* **2019**, *41*, 185–199. [CrossRef]

61. Azambuja, J.H.; da Silveira, E.F.; de Carvalho, T.R.; Oliveira, P.S.; Pacheco, S.; Couto, C.T.D.; Beira, F.T.; Stefanello, F.M.; Spanevello, R.M.; Braganhol, E. Glioma sensitive or chemoresistant to temozolomide differentially modulate macrophage protumor activities. *Biochim. Biophys. Acta (BBA)—Gen. Subj.* **2017**, *1861*, 2652–2662. [CrossRef]

62. Panzarini, E.; Tacconi, S.; Carata, E.; Mariano, S.; Tata, A.M.; Dini, L. Molecular Characterization of Temozolomide-Treated and Non Temozolomide-Treated Glioblastoma Cells Released Extracellular Vesicles and Their Role in the Macrophage Response. *Int. J. Mol. Sci.* **2020**, *21*, 8353. [CrossRef] [PubMed]

63. Hudson, A.L.; Parker, N.R.; Khong, P.; Parkinson, J.F.; Dwight, T.; Ikin, R.J.; Zhu, Y.; Chen, J.; Wheeler, H.R.; Howell, V.M. Glioblastoma Recurrence Correlates With Increased APE1 and Polarization Toward an Immuno-Suppressive Microenvironment. *Front. Oncol.* **2018**, *8*, 314. [CrossRef]

64. Sica, A.; Mantovani, A. Macrophage plasticity and polarization: In Vivo veritas. *J. Clin. Investig.* **2012**, *122*, 787–795. [CrossRef] [PubMed]

65. Larionova, I.; Cherdyntseva, N.; Liu, T.; Patysheva, M.; Rakina, M.; Kzhyshkowska, J. Interaction of tumor-associated macrophages and cancer chemotherapy. *OncoImmunology* **2019**, *8*, e1596004. [CrossRef] [PubMed]

66. Szulzewsky, F.; Pelz, A.; Feng, X.; Synowitz, M.; Markovic, D.; Langmann, T.; Holtman, I.R.; Wang, X.; Eggen, B.J.L.; Boddeke, H.W.G.M.; et al. Glioma-Associated Microglia/Macrophages Display an Expression Profile Different from M1 and M2 Polarization and Highly Express Gpnmb and Spp1. *PLoS ONE* **2015**, *10*, e0116644. [CrossRef]

67. Macciò, A.; Gramignano, G.; Cherchi, M.C.; Tanca, L.; Melis, L.; Madeddu, C. Role of M1-polarized tumor-associated macrophages in the prognosis of advanced ovarian cancer patients. *Sci. Rep.* **2020**, *10*, 1–8. [CrossRef]

68. Zhang, B.; Yao, G.; Zhang, Y.; Gao, J.; Yang, B.; Rao, Z.; Gao, J. M2-Polarized tumor-associated macrophages are associated with poor prognoses resulting from accelerated lymphangiogenesis in lung adenocarcinoma. *Clinics* **2011**, *66*, 1879–1886. [CrossRef]

69. Vidyarthi, A.; Agnihotri, T.; Khan, N.; Singh, S.; Tewari, M.K.; Radotra, B.D.; Chatterjee, D.; Agrewala, J.N. Predominance of M2 macrophages in gliomas leads to the suppression of local and systemic immunity. *Cancer Immunol. Immunother.* **2019**, *68*, 1995–2004. [CrossRef]

70. Geisenberger, C.; Mock, A.; Warta, R.; Rapp, C.; Schwager, C.; Korshunov, A.; Nied, A.-K.; Capper, D.; Brors, B.; Jungk, C.; et al. Molecular profiling of long-term survivors identifies a subgroup of glioblastoma characterized by chromosome 19/20 co-gain. *Acta Neuropathol.* **2015**, *130*, 419–434. [CrossRef] [PubMed]

71. Zeiner, P.S.; Preusse, C.; Golebiewska, A.; Zinke, J.; Iriondo, A.; Muller, A.; Kaoma, T.; Filipski, K.; Müller-Eschner, M.; Bernatz, S.; et al. Distribution and prognostic impact of microglia/macrophage subpopulations in gliomas. *Brain Pathol.* **2018**, *29*, 513–529. [CrossRef] [PubMed]

72. O'Neill, L.A.J.; Kishton, R.J.; Rathmell, R.J.K.J. A guide to immunometabolism for immunologists. *Nat. Rev. Immunol.* **2016**, *16*, 553–565. [CrossRef] [PubMed]

73. Jha, A.K.; Huang, S.C.-C.; Sergushichev, A.; Lampropoulou, V.; Ivanova, Y.; Loginicheva, E.; Chmielewski, K.; Stewart, K.M.; Ashall, J.; Everts, B.; et al. Network Integration of Parallel Metabolic and Transcriptional Data Reveals Metabolic Modules that Regulate Macro-phage Polarization. *Immunity* **2015**, *42*, 419–430. [CrossRef]

74. O'Neill, L.A.; Pearce, E.J. Immunometabolism governs dendritic cell and macrophage function. *J. Exp. Med.* **2016**, *213*, 15–23. [CrossRef]

75. Abuawad, A.; Mbadugha, C.; Ghaemmaghami, A.M.; Kim, D.-H. Metabolic characterisation of THP-1 macrophage polarisation using LC–MS-based metabolite profiling. *Metabolomics* **2020**, *16*, 1–14. [CrossRef]

76. De Santa, F.; Vitiello, L.; Torcinaro, A.; Ferraro, E. The Role of Metabolic Remodeling in Macrophage Polarization and Its Effect on Skeletal Muscle Regeneration. *Antioxidants Redox Signal.* **2019**, *30*, 1553–1598. [CrossRef]

77. Fuchs, A.L.; Schiller, S.M.; Keegan, W.J.; Ammons, M.C.B.; Eilers, B.; Tripet, B.; Copié, V. Quantitative 1H NMR Metabolomics Reveal Distinct Metabolic Adaptations in Human Macrophages Following Differential Activation. *Metabolites* **2019**, *9*, 248. [CrossRef] [PubMed]

78. Italiani, P.; Boraschi, D. From Monocytes to M1/M2 Macrophages: Phenotypical vs. Functional Differentiation. *Front. Immunol.* **2014**, *5*, 514. [CrossRef]

79. Chen, R.Q.; Liu, F.; Qiu, X.Y.; Chen, X.Q. The Prognostic and Therapeutic Value of PD-L1 in Glioma. *Front. Pharmacol.* **2019**, *9*, 1503. [CrossRef]

80. Huang, J.; Liu, F.; Liu, Z.; Tang, H.; Wu, H.; Gong, Q.; Chen, J. Immune Checkpoint in Glioblastoma: Promising and Challenging. *Front. Pharmacol.* **2017**, *8*, 242. [CrossRef]

81. Zhang, P.; Su, D.-M.; Liang, M.; Fu, J. Chemopreventive agents induce programmed death-1-ligand 1 (PD-L1) surface expression in breast cancer cells and promote PD-L1-mediated T cell apoptosis. *Mol. Immunol.* **2008**, *45*, 1470–1476. [CrossRef] [PubMed]

82. Katsuya, Y.; Horinouchi, H.; Asao, T.; Kitahara, S.; Goto, Y.; Kanda, S.; Fujiwara, Y.; Nokihara, H.; Yamamoto, N.; Watanabe, S.-I.; et al. Expression of programmed death 1 (PD-1) and its ligand (PD-L1) in thymic epithelial tumors: Impact on treatment efficacy and alteration in expression after chemotherapy. *Lung Cancer* **2016**, *99*, 4–10. [CrossRef] [PubMed]

83. Wang, S.; Yao, F.; Lu, X.; Li, Q.; Su, Z.; Lee, J.-H.; Wang, C.; Du, L. Temozolomide promotes immune escape of GBM cells via upregulating PD-L1. *Am. J. Cancer Res* **2019**, *9*, 1161–1171. [PubMed]

84. Bloch, O.; Crane, C.A.; Kaur, R.; Safaee, M.; Rutkowski, M.J.; Parsa, A.T. Gliomas Promote Immunosuppression through Induction of B7-H1 Expression in Tumor-Associated Macrophages. *Clin. Cancer Res.* **2013**, *19*, 3165–3175. [CrossRef] [PubMed]

85. Singhal, S.; Stadanlick, J.; Annunziata, M.J.; Rao, A.S.; Bhojnagarwala, P.S.; O'Brien, S.; Moon, E.K.; Cantu, E.; Danet-Desnoyers, G.; Ra, H.-J.; et al. Human tumor-associated monocytes/macrophages and their regulation of T cell responses in early-stage lung cancer. *Sci. Transl. Med.* **2019**, *11*, eaat1500. [CrossRef] [PubMed]

86. Sepesi, B.; Cuentas, E.P.; Canales, J.R.; Behrens, C.; Correa, A.M.; Vaporciyan, A.; Weissferdt, A.; Kalhor, N.; Moran, C.; Swisher, S.; et al. Programmed Death Cell Ligand 1 (PD-L1) Is Associated With Survival in Stage I Non–Small Cell Lung Cancer. *Semin. Thorac. Cardiovasc. Surg.* **2017**, *29*, 408–415. [CrossRef]

87. Sarkar, S.; Döring, A.; Zemp, F.J.; Da Silva, C.L.; Lun, X.; Wang, X.; Kelly, J.; Hader, W.J.; Hamilton, M.; Mercier, P.; et al. Therapeutic activation of macrophages and microglia to suppress brain tumor-initiating cells. *Nat. Neurosci.* **2014**, *17*, 46–55. [CrossRef]

88. Pyonteck, S.M.; Akkari, L.; Schuhmacher, A.J.; Bowman, R.L.; Sevenich, L.; Quail, D.F.; Olson, O.C.; Quick, M.L.; Huse, J.T.; Teijeiro, V.; et al. CSF-1R inhibition alters macrophage polarization and blocks glioma progression. *Nat. Med.* **2013**, *19*, 1264–1272. [CrossRef]

89. Saha, D.; Martuza, R.L.; Rabkin, S.D. Macrophage Polarization Contributes to Glioblastoma Eradication by Combination Immunovirotherapy and Immune Checkpoint Blockade. *Cancer Cell* **2017**, *32*, 253–267. [CrossRef]

90. Chiu, T.-L.; Wang, M.-J.; Su, C.-C. The treatment of glioblastoma multiforme through activation of microglia and TRAIL induced by rAAV2-mediated IL-12 in a syngeneic rat model. *J. Biomed. Sci.* **2012**, *19*, 45. [CrossRef]

91. Carpentier, A.F.; Metellus, P.; Ursu, R.; Zohar, S.; Lafitte, F.; Barrié, M.; Meng, Y.; Richard, M.; Parizot, C.; Laigle-Donadey, F.; et al. Intracerebral administration of CpG oligonucleotide for patients with recurrent glioblastoma: A phase II study. *Neuro-Oncology* **2010**, *12*, 401–408. [CrossRef]

92. Markovic, D.; Vinnakota, K.; van Rooijen, N.; Kiwit, J.; Synowitz, M.; Glass, R.; Kettenmann, H. Minocycline reduces glioma expansion and invasion by attenuating microglial MT1-MMP expression. *Brain Behav. Immun.* **2011**, *25*, 624–628. [CrossRef]

93. Genoud, V.; Marinari, E.; Nikolaev, S.I.; Castle, J.C.; Bukur, V.; Dietrich, P.-Y.; Okada, H.; Walker, P.R. Responsiveness to anti-PD-1 and anti-CTLA-4 immune checkpoint blockade in SB28 and GL261 mouse glioma models. *OncoImmunology* **2018**, *7*, e1501137. [CrossRef]

94. Schumacher, T.N.; Schreiber, R.D. Neoantigens in cancer immunotherapy. *Science* **2015**, *348*, 69–74. [CrossRef]

95. Pich, O.; Muiños, F.; Lolkema, M.P.; Steeghs, N.; Gonzalez-Perez, A.; Lopez-Bigas, N. The mutational footprints of cancer therapies. *Nat. Genet.* **2019**, *51*, 1732–1740. [CrossRef]

Supplementary Materials: Immune System-Related Changes in Preclinical GL261 Glioblastoma under TMZ Treatment: Explaining MRSI-Based Nosological Imaging Findings with RT-PCR Analyses

Pilar Calero-Pérez, Shuang Wu, Carles Arús and Ana Paula Candiota.

Supplementary Introduction

MRSI analysis: outline of NMF methods

Non-negative matrix factorization (NMF) methods are multivariate data analyses designed for meaningful components (also known as sources) estimation, originating from non-negative data. Standard NMF methods decompose data "X" into 2 non-negative matrices: sources ("S") and mixing matrices ("A"). The divergence between X and S*A is measured by cost functions, which may differ for different NMF methods. There are NMF variants which can also handle negative data, such as convex-NMF, which was the basis of the analysis used in this study [1]. Convex-NMF was capable to spot a reduced number of sources confidently recognized as representative from brain tumour/tissue types much better than other NMF variants [2,3]. Original sources were extracted from TMZ-treated and control mice individuals, as described in [4], defining prototypic metabolomic patterns related to normal or unaffected brain, GL261 tumours actively proliferating and TMZ-treated, responding tumours. The source-based analysis used in this work and other studies mentioned [5–7] made use of previously extracted sources in order to study new cases and assign one of the three predefined classes to each investigated voxel, thus generating the so-called nosological images.

Supplementary Materials and Methods

MRI studies

The acquisition parameters for MRI studies were as follows: repetition time (TR)/effective echo time (TEeff) = 4200/36 ms; echo train length (ETL) = 8; field of view (FOV) = 19.2 × 19.2 mm; matrix size (MTX) = 256 × 256 (75 × 75 μm/pixel); slice thickness (ST) = 0.5 mm; inter-ST = 0.1 mm; number of slices (NS) = 10; number of averages (NA) = 4; total acquisition time (TAT) = 6 min and 43 s.

MRSI studies

Grid 1 was the first upper (dorsal) grid and was acquired with 10 × 10 matrix size. Then, Grid 2 was acquired 1 mm below using 12 × 12 matrix size, and grid 3 was acquired 1 mm below Grid 2, with the same matrix size. Finally, in case that tumour volume was not completely covered, a final Grid 4 was acquired 1 mm below Grid 3 with 10 × 10 matrix size.

Variable Power and Optimized Relaxation Delay (VAPOR) was used for water suppression, using a 300-Hz bandwidth. Fast Automatic Shimming Technique by Mapping Along Projections (FASTMAP) was used for linear and second order shims automatic adjustment. Finally, 6 saturation slices (ST, 10 mm; sech-shaped pulses: 1.0 ms/20250 Hz) were positioned around the VOI for minimizing outer volume contamination in the signals obtained.

Acquisition parameters for all grids were as follows: FOV, 17.6 mm × 17.6 mm; VOI in Grids 1 and 4 was 5.5 mm × 5.5 mm × 1.0 mm, while Grids 2 and 3 had 6.6 mm × 6.6 mm × 1.0 mm. TR, 2500 ms; ST, 1 mm; Sweep Width (SW), 4006.41 Hz; NA, 512; TAT, 21

min 30 s each grid. Water suppression was performed with Variable Power and Optimized Relaxation Delay (VAPOR), using a 300 Hz bandwidth. Linear and second order shims were automatically adjusted with Fast Automatic Shimming Technique by Mapping Along Projections (FASTMAP) in a 5.8 mm × 5.8 mm × 5.8 mm volume which contained the original VOI region. Six saturation slices (ST, 10 mm; sech-shaped pulses: 1.0 ms/20250 Hz) were positioned around the VOI to minimize outer volume contamination in the signals obtained.

Nosological images

The nosological images are generated combining MRSI techniques with robust machine learning analyses, which take the whole spectral pattern changes into account (considers the 0 to 4.5 ppm spectral vector, see figure S1B). This makes it possible to use quantitative changes of different metabolites and to detect even subtle variations in metabolomic profile, enabling to classify the tissue into mostly (majority source vote) normal brain tissue, responding or unresponsive tumour.

The labelling of the MRSI data acquired is based on the source extraction technique, which assumes that a mixture of the heterogeneous tissue patterns is present in each voxel and that the contribution of individual source to the final pattern can be calculated. In this sense, the nosological imaging is generated by estimating the contribution of each source ("paradigmatic spectra") to the individual voxels in the MRSI grid in order to assign each acquired voxel to one of the predetermined classes. The quantitative most relevant paradigmatic spectrum of the voxel is selected as the "winning source" and the voxel is correspondingly coloured, finally represented as nosological maps for each matrix. Green colour is used when the GB responding to treatment source contributes the most, red for actively proliferating GB, blue for normal brain parenchyma, and black for undetermined tissue. These nosological images can provide a visual representation of MRSI results and be used as an imaging biomarker to determine therapy-caused response.

The most remarkable changes between responding and unresponsive tumours can be summarised. Main metabolites contributing to different patterns of responding and non-responding spectra are mobile lipids 0.9 + macromolecules (ML, MM, 0.9 ppm), mobile lipids 1.3 + lactate (ML/Lac, 1.3 ppm), N-acetyl-aspartate and N-acetyl group-containing compounds (NAA and NAc, 2.02 ppm), glutamate + glutamine (Glx, 2.1–2.4 ppm), polyunsaturated fatty acids in mobile lipids (PUFA, 2.8 ppm), total creatine (Cre, 3.03 ppm), choline-containing compounds (Cho, 3.21 ppm), myo-inositol + glycine (Ins + Gly, 3.55 ppm), glutamine + glutamate (Glx, 3.8 ppm, which is also partially contributed by alanine), and lactate (Lac, 1.3 and 4.1 ppm).

Figure S1 provides a summary of the steps performed in this type of analysis.

Inclusion criteria for mice fully evaluated in this study

Not all studied mice accomplished criteria to be included in this particular study, which searched for homogeneous and clear control and therapy-responding examples to explain the associated MRSI patterns. Inclusion criteria were as follows:

1. Homogeneous tumour appearance at MRI exploration, avoiding tumour volumes at inclusion decision time outside the usual tumour volume range values (average 9.3 ± 6.1 mm^3) considered in current GABRMN group cohort studies [5–9]. Tumours growing towards the skull or lower part of the brain, in which MRSI signals can be spurious and have poor spectral quality, were also discarded. Total number discarded due to criteria 1 = 44.
2. Extreme values for Tumour Responding Index (See [5]) were searched for (i.e., TRI values >60% for treated tumours and close to 0% for control tumours). In addition, not only the TRI value itself but its homogeneous distribution within the tumour mass

was preferred, since it was not feasible to 'dissect' samples in different tumour regions. Thus, tumours showing heterogeneous response pattern distributions in nosological images were avoided. Total number discarded due to criteria 2 = 30.

3. Maintenance or reduction in the tumour size was searched for in the treated group, pointing towards clear growth arrest. The reduction was mostly in agreement with 'stable disease' according to RECIST values (4.43 ± 6.32% tumour volume reduction in comparison with previous explorations). The lack of further follow-up prevents us to define whether it would meet partial or complete response criteria. Total number discarded due to criteria 3 = 3.

4. Tumour tissue available volume had to be large enough (more than 20 mm^3) to obtain the amount of RNA suitable to carry out qPCR experiments (i.e. > 70 ng/μL). Total number discarded due to criteria 4 = 13.

It is worth noting that mice discarded from this study because of inclusion criteria, were allocated to other studies performed by our group in order to minimize animal waste and maximize knowledge obtained from this particular animal model.

Adapted RECIST criteria

Classification based on adapted RECIST criteria was applied as follows, considering the GL261 GB tumour volumes registered in the previous exploration:

- Progressive disease (PD): 20% increase in tumour volume, or higher.

- Partial response (PRe): tumour volume decreases by 30%, or higher.

- Stable disease (SDi): less than 20% increase and no more than 30% decrease in tumour volume.

Amplicon Context Sequence

- F4/80:

TATGCCATCCACTTCCAAGATGGGTTAACATCCTTTCTTGCTTTTAAATATATTATGGAACAATGTCTGAAGATTGTAAGTGCTTTAAGGATCATACTTTTAATAAC

- Nos2:

ACCACACCAAACTGTGTGCCTGGAGGTTCTGGATGAGAGCGGCAGCTACTGGGTCAAAGACAAGAGGCTGCCCCCCCTGCTCACTCAGCCAAGCCCTCACCTACTTCCTGGACATTACGACCCCTCCCACCC

- CD206:

TGGAATAATATCCACTGTTCTTCGTACAAAGGATTTATTTGTAAAATGCCAAAAATTATTGATCCTGTAACTACACACTCATCCATTACAACCAAAGCTGACCAAAGGAAGATGGATC

- PD-L1:

GCTAGATGTGGAGAAATGTGGCGTTGAAGATACAAGCTCAAAAAACCGAAATGATACACAATTCGAGGAGACGTAAGCAGTGTTGAACCCTC

- TBP:

TCTGAGTACTGAAGAAAGGGAGAATCATGGACCAGAACAACAGCCTTCCACCTTATGCTCAGGGCTTGGCCTCCCCACAGGGCGCCATGACTCCTGGAATTCCCATCTTTAGTCCAATGATGCCTTACGGCA

- HPRT:

TTTTATCAGACTGAAGAGCTACTGTAATGATCAGTCAACGGGGGACATAAAAGTTATTGGTGGAGATGATCTCTCAACTTTAACTGGAAAGAATGTCTTGA

Supplementary Figures:
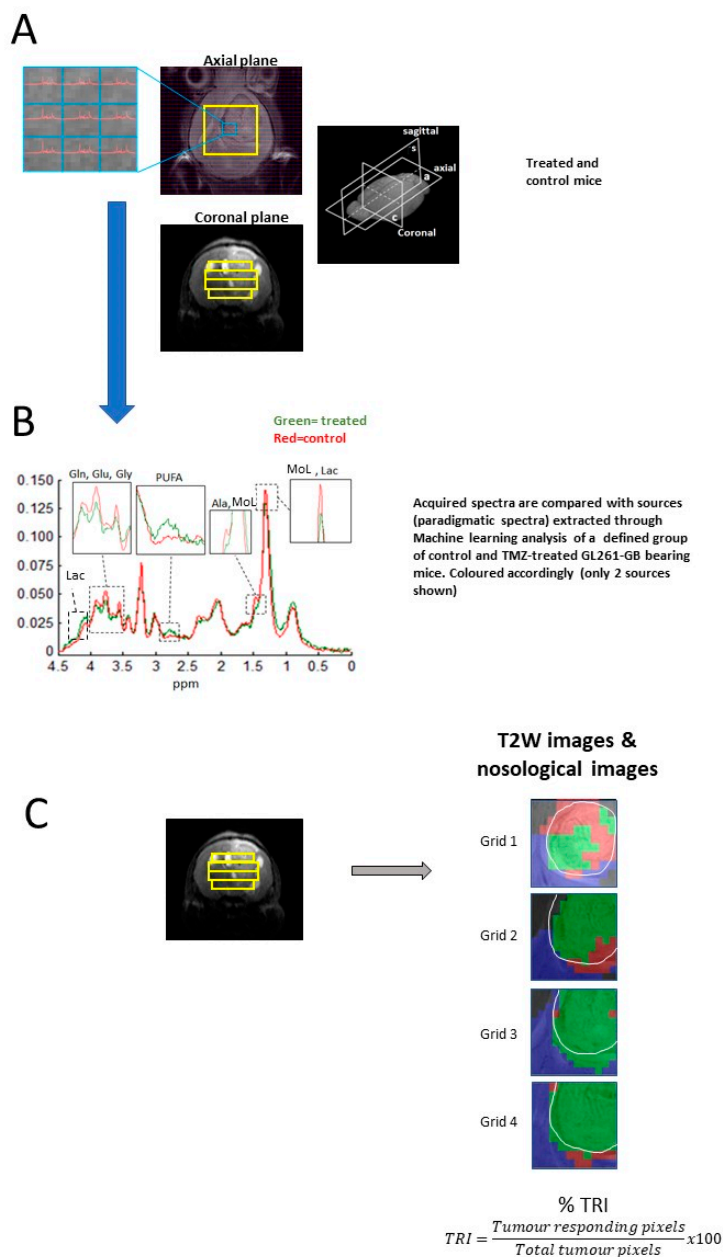
Figure S1. Summary of steps performed for nosological images calculation mentioned in this work. **A**) MRSI spectra are acquired. Both coronal and axial imaging orientation are shown for better understanding of different anatomical levels studied. Each individual spectrum of the MRSI grid (blue square in A) is analysed as a unique spectral vector. **B**) Spectra are compared with fixed sources (paradigmatic spectra), obtained from a defined group of TMZ-treated and control mice [4]. In fact, 3 sources were acquired but only sources corresponding to control – actively proliferating- and TMZ-treated mice, transiently responding to therapy, are shown, respectively in red and green. Those are the sources relevant to this particular study. Main contributing metabolites are shown in expansion regions. **C**) Spectra, and volume elements, are then coloured according to whether they show more correlation with the control, TMZ-treated or normal brain parenchyma source. If the correlation between the spectrum of a voxel and the sum of the percentages contributed by the sum of the three tissue sources was below a threshold of 50%, this voxel was labelled as 'undecided' and coloured in black [4]. The Tumour Responding Index (TRI) is then calculated as shown in the formula at the bottom, considering spectra (pixels) identified as responding regarding to the total tumour pixels, taking into account manual drawing over the abnormal section in T2w MRI.
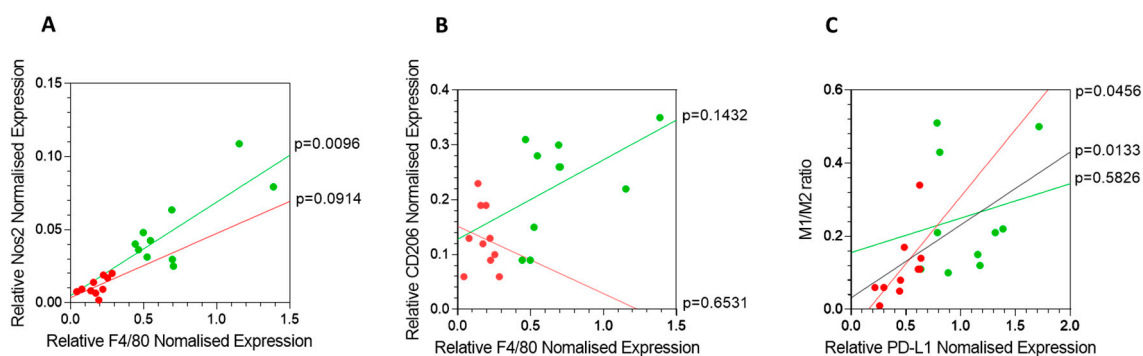
Figure S2. Pearson correlation analysis between F4/80 gene expression level and **A**) Nos2 and **B**) CD206 gene expression levels; and between **C**) PD-L1 gene expression level and M1/M2 ratio (see section 3.4. of the main manuscript for definition) in IMS-TMZ-treated GL261 GB (green line) and control (red line) mice samples. **C**) Also shows the correlation between PD-L1 gene expression level and M1/M2 ratio when treated and control cases are combined (black line). P values for each group are indicated in the graphs.
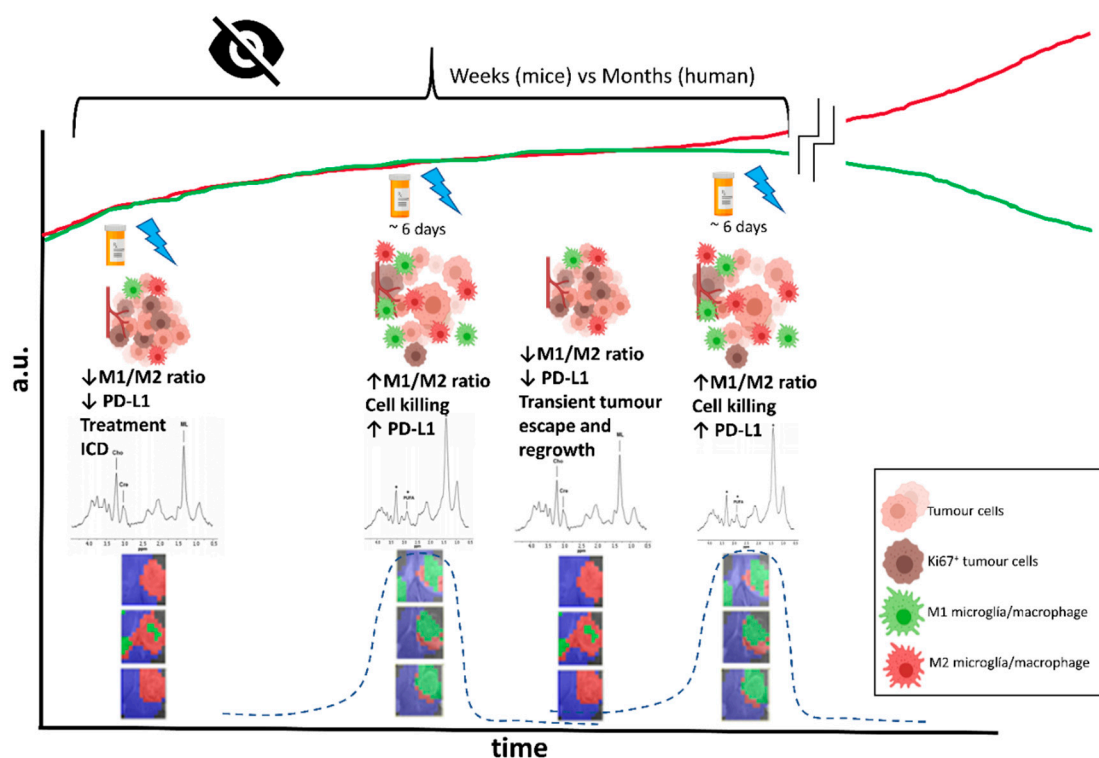
Figure S3. Hypothetical scheme for the rationale behind changes in the nosological images coding for response in MRSI of IMS-TMZ treated GB GL261 bearing mice (see main text for further details). The oscillation in cellular populations such as Ki67 positive tumour cells or microglia/macrophages, changes in their polarisation status, in surface receptor such as PD-L1 and their subsequent effects, as well as changes in tissue microstructure (giant cells, acellular spaces [5,10]) should all contribute to the MRSI-detected imaging biomarker differences. Those show periodic oscillations that agree with the length of the immune cycle (ca. 6 days) and should be related to events triggered by TMZ therapy.

This may be extended [7] to any therapeutic approach eliciting the host immune system. It is also worth noting that these events take place early in the timeline, far before any changes are seen in tumour volumes (red and green lines). Hence detection of such oscillatory changes could provide early indication about immune system-driven response to therapy, while tumour volume changes may be 'blind' to these early local metabolomics changes. At the therapy starting point, GL261 GB tumours display an M2/GAMs ratio which is more than 10-fold higher the M1/GAMs ratio, thus an essentially protumoural microglia/macrophage phenotype (encoded in the red colour over the tumour mass of the

nosological images). Launching TMZ therapy may trigger immunogenic cell damage and release/exposure of immunogenic signals [11] which will turn on the cancer immunity cycle and elicit the host immune system [12]. In the meanwhile, both M1 and M2 populations infiltrating the tumour increase (see also Figure 2A): while M1 microglia/macrophages will participate in tumour cell killing, probably after interaction with T-cells [13], and M2 microglia/macrophages are waiting for M1 polarisation. In this respect, M1/M2 ratio changes towards higher values in tumours showing transient response to IMS-TMZ (Figure 3C of the main manuscript). The point of maximum response spotted by our non-invasive biomarker (i.e., green colour over the GB tumour mass in nosological images) is ca. 6 days after therapy administration, in line with the length of the immune cycle described in [14]. At this point, an increase in PD-L1 gene expression is observed (Figure 4A of the main manuscript), although it could be either due to expression by the tumour cell population to evade lymphocyte attack, to expression in microglia/macrophages or both together. Since M1 microglia/macrophages are mostly consumed during the antitumour response events, after such interval, the ratio M1/M2 may shift towards the control values, T lymphocytes may be approaching exhaustion and surviving tumour cells may start proliferating again leading to tumour regrowth (day +9, red colour over the tumour image) until the previous therapeutic administration point (at day +6) resets the immune cycle and produces the next response oscillation (day +12).

Supplementary Tables:

Table S1. Description of IMS-TMZ and IMS-vehicle treated mice, including tumour volume at therapy start point and at endpoint, euthanasia day and percentage of TRI shown at that time.

Group	Case	Tumour volume at therapy start point (mm^3)	Tumour volume at endpoint (mm^3)	Euthanization (day p.i.)	TRI (%)
IMS-TMZ	C1412	12.05	87.17	23	95.21
	C1445	3.74	45.99	23	60.13
	C1447	6.17	94.92	28	78.70
	C1450	5.45	29.61	24	72.83
	C1451	11.60	54.09	23	64.24
	C1456	3.63	24.50	23	71.18
	C1458	9.95	107.24	23	81.78
	C1460	9.30	59.12	23	93.57
	C1463	4.37	35.55	23	76.47
	C1473	8.69	71.96	23	75.61
IMS-vehicle	C1320	5.80	64.36	18	3.26
	C1344	4.26	29.30	17	0.00
	C1348	4.35	109.67	21	5.37
	C1457	1.12	54.86	23	6.84
	C1465	13.02	66.05	15	0.85
	C1466	1.21	72.36	23	0.00
	C1467	2.56	130.03	22	6.00
	C1471	12.55	78.08	17	20.96
	C1472	24.92	57.26	13	2.66
	C1474	20.87	61.26	14	0.00

SM additional References.

1. Ding, C.; Li, T.; Jordan, M.I. Convex and Semi-Nonnegative Matrix Factorizations. *IEEE Trans. Pattern Anal. Mach. Intell.* **2010**, *32*, 45–55.

2. Ortega-Martorell, S.; Lisboa, P.J.G.; Vellido, A.; Julia-Sape, M.; Arus, C. Non-negative Matrix Factorisation methods for the spectral decomposition of MRS data from human brain tumours. *BMC Bioinformatics* **2012**, *13*, 38, doi:10.1186/1471-2105-13-38.

3. Ortega-Martorell, S.; Lisboa, P.J.G.; Vellido, A.; Simões, R. V.; Pumarola, M.; Julià-Sapé, M.; Arús, C. Convex Non-Negative Matrix Factorization for Brain Tumor Delimitation from MRSI Data. *PLoS One* **2012**, *7*, e47824, doi:10.1371/journal.pone.0047824.

4. Delgado-Goñi, T.; Ortega-Martorell, S.; Ciezka, M.; Olier, I.; Candiota, A.; Julià-Sapé, M.; Fernández, F.; Pumarola, M.; Lisboa, P.; Arús, C. MRSI-based molecular imaging of therapy response to temozolomide in preclinical glioblastoma using source analysis. *NMR Biomed.* **2016**, *29*, 732–743, doi:10.1002/nbm.3521.

5. Arias-Ramos, N.; Ferrer-Font, L.; Lope-Piedrafita, S.; Mocioiu, V.; Julià-Sapé, M.; Pumarola, M.; Arús, C.; Candiota, A.P. Metabolomics of therapy response in preclinical glioblastoma: A multi-slice MRSI-based volumetric analysis for noninvasive assessment of temozolomide treatment. *Metabolites* **2017**, *7*, pii: E20, doi:10.3390/metabo7020020.

6. Wu, S.; Calero-Pérez, P.; Villamañan, L.; Arias-Ramos, N.; Pumarola, M.; Ortega-Martorell, S.; Julià-Sapé, M.; Arús, C.; Candiota, A.P. Anti-tumour immune response in GL261 glioblastoma generated by Temozolomide Immune-Enhancing Metronomic Schedule monitored with MRSI-based nosological images. *NMR Biomed.* **2020**, *33*, e4229, doi:10.1002/nbm.4229.

7. Wu, S.; Calero-Pérez, P.; Arús, C.; Candiota, A.P. Anti-PD-1 immunotherapy in preclinical gl261 glioblastoma: Influence of therapeutic parameters and non-invasive response biomarker assessment with mrsi-based approaches. *Int. J. Mol. Sci.* **2020**, *21*, 8775, doi:10.3390/ijms21228775.

8. Ferrer-Font, L.; Villamañan, L.; Arias-Ramos, N.; Vilardell, J.; Plana, M.; Ruzzene, M.; Pinna, L.A.; Itarte, E.; Arús, C.; Candiota, A.P. Targeting protein kinase CK2: Evaluating CX-4945 potential for GL261 glioblastoma therapy in immunocompetent mice. *Pharmaceuticals* **2017**, *10*, 24, doi:10.3390/ph10010024.

9. Ferrer-Font, L.; Arias-Ramos, N.; Lope-Piedrafita, S.; Julià-Sapé, M.; Pumarola, M.; Arús, C.; Candiota, A.P. Metronomic treatment in immunocompetent preclinical GL261 glioblastoma: effects of cyclophosphamide and temozolomide. *NMR Biomed.* **2017**, *30(9)*, doi:10.1002/nbm.3748.

10. Delgado-Goñi, T.; Julià-Sapé, M.; Candiota, A.P.; Pumarola, M.; Arús, C. Molecular imaging coupled to pattern recognition distinguishes response to temozolomide in preclinical glioblastoma. *NMR Biomed.* **2014**, *27*, 1333–1345, doi:10.1002/nbm.3194.

11. Villamañan, L.; Martínez-escardó, L.; Arús, C.; Yuste, V.J.; Candiota, A.P. Successful partnerships: Exploring the potential of immunogenic signals triggered by TMZ, CX-4945, and combined treatment in Gl261 glioblastoma cells. *Int. J. Mol. Sci.* **2021**, *22*, 3453, doi:10.3390/ijms22073453.

12. Chen, D.S.; Mellman, I. Oncology meets immunology: The cancer-immunity cycle. *Immunity* **2013**, *39*, 1–10, doi:10.1016/j.immuni.2013.07.012.

13. von Roemeling, C.A.; Wang, Y.; Qie, Y.; Yuan, H.; Zhao, H.; Liu, X.; Yang, Z.; Yang, M.; Deng, W.; Bruno, K.A.; et al. Therapeutic modulation of phagocytosis in glioblastoma can activate both innate and adaptive antitumour immunity. *Nat. Commun.* **2020**, *11*, 1508, doi:10.1038/s41467-020-15129-8.

14. Karman, J.; Ling, C.; Sandor, M.; Fabry, Z. Initiation of immune responses in brain is promoted by local dendritic cells. *J. Immunol.* **2004**, *173*, 2353–2361, doi:10.4049/jimmunol.173.4.2353.

4.3. CHAPTER III: ONE STEP BEYOND FOR MOLECULAR PROFILING OF THE TUMOUR MICROENVIRONMENT IN GL261 GB BEARING MICE: GAM POPULATION, METALLOPROTEASES AND PD-L1 EXPRESSION ANALYSES DURING TMZ THERAPY RESPONSE, RELAPSE OR UNRESPONSIVE SITUATIONS

4.3.1. Context and specific objectives

Results described in the previous chapter were relevant, in the sense that significant changes in TME were found during response to IMZ-TMZ treatment, with regard to one of the relevant populations, i.e., the GAM population, as well as aspects related to PD-L1 expression. Accordingly, one of the arising questions was to check whether these profiles would also change in mice relapsing or unresponsive to IMS-TMZ therapy.

Moreover, in addition to the significant role described for GAM polarisation through M1 or M2 phenotype and the PD-1/PD-L1 axis in the response to therapy, it has been described that zinc-dependent proteases of the metzincin superfamily, such as ADAMs and MMPs, are important modulators of the TME [143,159]. As previously mentioned in the Introduction (section 1.3.4.1, The role of different metalloproteases), these protease families have been described to be related to several biological processes such as inflammatory responses, immune regulation, angiogenesis, cell migration and proliferation, apoptosis, tissue repair, among others.

Thus, since ADAMs and MMPs proteases may act as important modulators of the TME, the distinct populations of GAMs might be also correlated with specific protease profiles in GB [183,184]. Some of these proteases (ADAM8, 10 and 17 and MMP9 and 14) were shown to be associated with microglia/macrophage functions, thus profiling these protease genes in conjunction with M1/M2 polarization markers in GB could provide novel insights into the molecular signature of these cells and might prove beneficial as a diagnostic tool and predictor of patient survival. Within the TME, ADAM10 and ADAM17 are expressed not only in cancer cells but also in tumour-infiltrating immune cells. ADAM10 or ADAM17 might cleave membrane PD-L1 in immune cells and the ubiquitous expression of these two ADAMs and regulation of their activities by a number of physiological signals clearly positions them as new modulators of the PD-1/PD-L1 immune checkpoint pathway [185].

Accordingly, the specific objective of Chapter III was to analyse samples from IMS-TMZ-treated mice either responding or non-responding to treatment, as well as relapsing and vehicle-treated tumours using rt-PCR in order to characterise the different subpopulations of GAMs and PD-L1 gene expression, as well as the molecular profile of different protease genes, known to be associated with GB progression (ADAM8, ADAM10, ADAM17, MMP9 and MMP14). Furthermore, we studied the correlation between GAM population, both M1/M2 subtypes, and metalloproteases expression. The metalloproteases profiles were also associated with expression of PD-L1 in order to provide information on their role in the immunosuppression in

TME. For that, a predoctoral stage was carried out in the laboratory of Prof. Jörg-Walter Bartsch, from Philipps University of Marburg (UMR), Department of Neurosurgery, due to his wide expertise in the metalloproteases field and TME characterization.

4.3.2. Specific materials and methods

A total of 31 C57BL/6 mice (weighing 21.4 ± 1.4 g, aged 15.5 ± 2.8 weeks) were used for the work described in this Chapter. The GL261 glioma generation, the IMS-TMZ treatment, and the *in vivo* MRI studies were performed with parameters described in Chapters I and II. MRI was used to categorize individuals according to their evolution. It is worth clarifying that n=10 responding IMS-TMZ-treated mice and n=10 IMS-vehicle-treated (control) mice are the same individuals described in chapter II regarding M1/M2/PD-L1 profiling. In this chapter, we have enlarged the cohort of mice including individuals belonging to relapsing (after transient response) and unresponsive groups, and also enlarged the IMS-TMZ treated responding group with n=2 additional cases each.

4.3.2.1. RNA isolation, cDNA synthesis and rt-PCR

Analysis of relative mRNA expression levels of F4/80, Nos2, CD206, CD274 (PD-L1), ADAM8, ADAM10, ADAM17, MMP9 and MMP14 were carried out in all the samples collected. RNA isolation and cDNA synthesis were performed following the same experimental approach described in Chapter II.

For F4/80, Nos2, CD206, and PD-L1 rt-PCR analyses, experimental steps were already described in Chapter II. For ADAM8, ADAM10, ADAM17, MMP9 and MMP14 rt-PCR analyses, 2 ng of cDNA were used, all reactions were performed twice, and results were averaged. The rt-PCR was performed using a StepOne-Plus Real-Time PCR instrument (Applied Biosystems, Thermo Fisher Scientific, Dreieich) and SYBR Green in form of the Precision FASTMasterMix with ROX (Primer Design, Southhampton, U.K.). PCR amplification reactions were carried out in 20 µl reaction volumes and the protocol consisted of an initial denaturation at 95°C for 10 min, followed by 40 amplification cycles at 95°C for 15 s and 60°C for 1 min. The mRNA for acidic ribosomal protein RPLP0 (XS13) served as an internal reference gene for all rt-PCR reactions. Cycle time (Ct) was calculated by StepOne Software v2.0 (Applied Biosystems). For each gene, the $2^{-\Delta\Delta Ct}$ method [186] was performed to analyse relative quantities.

4.3.3. Results

4.3.3.1. Follow up of GL261 tumour-bearing mice and criteria established to choose euthanasia time point:

In vivo MRI studies were performed in all mice (n=31) to monitor tumour growth evolution and determine the different therapy response situations. Furthermore, the metabolomic information acquired by in vivo MRSI studies of the 20 cases described in chapter II was known. The four groups evaluated in this chapter are the following:

- In all responding IMS-TMZ-treated mice (n=12), the tumour volume met criteria for "stable disease" according to RECIST [187] adapted as described in [50].
- In all relapsing IMS-TMZ-treated mice (n=7), tumours transiently responded to treatment and subsequently, escaped from therapy showing clear regrowth.
- In all non-responding IMS-TMZ-treated mice (n=2), tumour volumes increased fast as vehicle treated tumours and no signs of transient growth arrest were observed.
- In all vehicle-treated (control) mice (n=10), tumour volumes increased fast, as expected.

The average tumour volume at therapy starting point (day 11 p.i.) was 7.4 ± 2.9 mm^3 for responding IMS-TMZ-treated mice; 8.1 ± 4.1 mm^3 for relapsing IMS-TMZ-treated mice; 11.0 ± 1.2 mm^3 for non-responding IMS-TMZ-treated mice; and 9.1 ± 8.4 mm^3 for control mice, with no significant differences between groups and no significant differences from volumes used by GABRMN in past studies. The average tumour volume at euthanasia time point was 58.6 ± 26.4 mm^3 for responding IMS-TMZ-treated mice (at day 23.5 ± 1.4 p.i.); 149.7 ± 22.6 mm^3 for relapsing mice (at day 40.3 ± 4.3 p.i.); 185.8 ± 48.6 mm^3 for non-responding mice (at day 23.0 ± 0.0 p.i.) and 71.61 ± 29.18 mm^3 for control mice (at day 18.3 ± 3.8 p.i.). At chosen time points, mice were euthanised by cervical dislocation, brain was removed, and tumour was resected. All collected samples are described in Table 4.1 and tumour volume evolution is shown in Figure 4.1

Group	Case	Tumour volume at therapy start point (mm³)	Tumour volume at endpoint (mm³)	Euthanasia (day p.i.)
Responding IMS-TMZ	C1412	12.1	87.2	23
	C1445	3.7	46.0	23
	C1447	6.2	94.9	28
	C1450	5.5	29.6	24
	C1451	11.6	54.1	23
	C1456	3.6	24.5	23
	C1458	10.0	107.2	23
	C1460	9.3	59.1	23
	C1463	4.4	35.6	23
	C1473	8.7	72.0	23
	C1504	7.3	49.1	23
	C1505	6.4	44.5	23
Relapsing IMS-TMZ	C1380	10.1	172.7	41
	C1383	4.4	183.9	49
	C1410	15.1	96.6	36
	C1486	6.2	141.1	38
	C1489	5.8	125.5	38
	C1491	4.0	185.7	38
	C1494	10.8	142.4	42
Non-responding IMS-TMZ	C1493	11.9	151.5	23
	C1496	10.2	220.1	23
IMS-vehicle	C1320	5.8	64.4	18
	C1344	4.3	29.3	17
	C1348	4.4	109.7	21
	C1457	1.1	54.9	23
	C1465	13.0	66.1	15
	C1466	1.2	72.4	23
	C1467	2.6	130.0	22
	C1471	12.6	78.1	17
	C1472	24.9	57.3	13
	C1474	20.9	61.3	14

Table 4.1. Description of responding IMS-TMZ, relapsing IMS-TMZ, non-responding IMS-TMZ and IMS-vehicle (control) treated mice, including tumour volume at therapy start point and at endpoint, and euthanasia day.
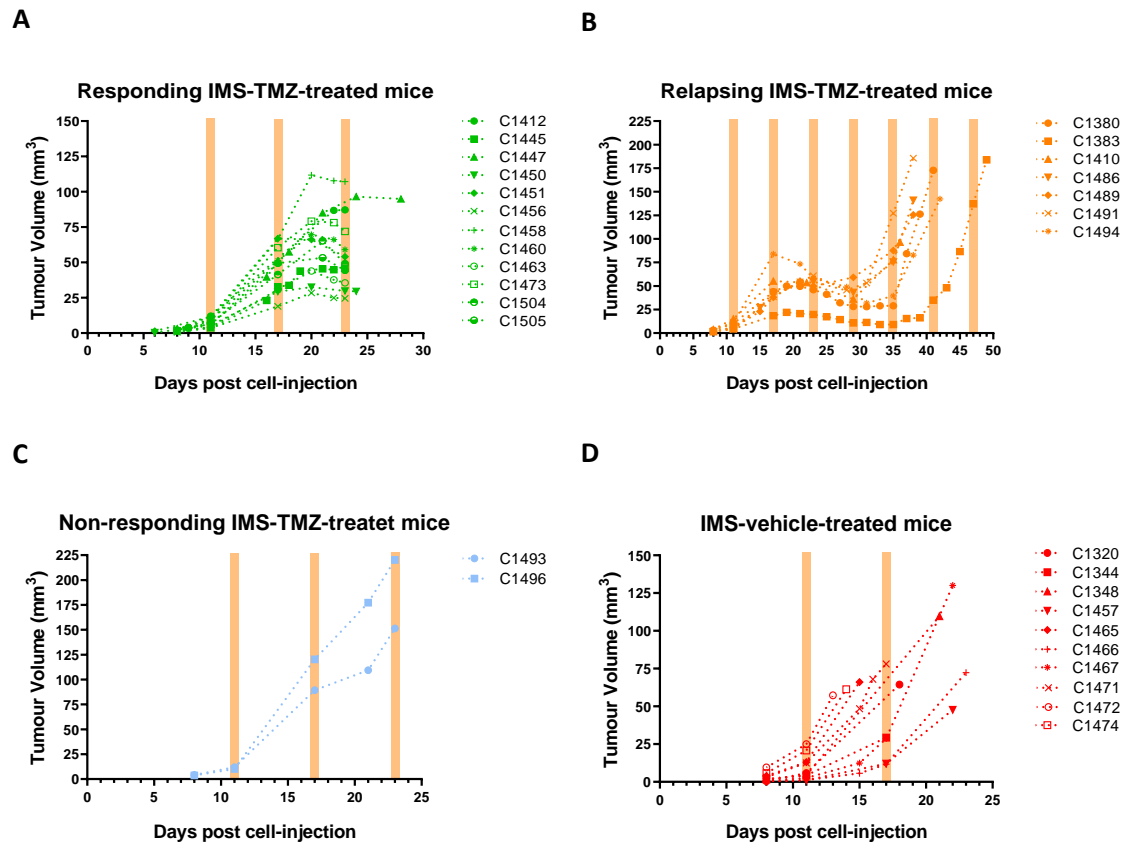
Figure 4.1. Tumour volume evolution (in mm³) of A) responding (n=12), B) relapsing after transient response (n=7), C) non-responding IMS-TMZ-treated mice (n=2) and D) vehicle-treated, control mice (n=10). In all responding cases, tumour volumes were in growth arrest at sacrifice time, in all relapsing cases, tumours responded to treatment and subsequently, escaped from the therapy, while in all non-responding and in all control cases, tumour volumes increased fast with no signs of growth arrest. Note that Y scales are adjusted for better data visualisation in each case, thus they are not equal in all graphs.

4.3.3.2. Global GAM population, as well as M1 and M2 subtypes, are increased in responding IMS-TMZ-treated tumours in comparison with other conditions

The GAM marker F4/80 was used to analyse global GAM population in tumour samples from IMS-TMZ-treated mice in three different conditions: responding, relapsing after transient response and non-responding to treatment, as well as vehicle-treated, control mice (Figure 4.2 A). We found that the F4/80 normalized content in the responding group was significantly higher (4.5-6.3-fold higher, depending on the groups compared) than the expression profile found in relapsing tumours, non-responding to IMS-TMZ treatment, as well as in control tumours, with p < 0.05 in all instances (Table 4.2). On the other hand, comparisons between relapsing, non-responding and control groups did not present significant differences. It is worth remembering that along this Chapter, for the non-responding group (n=2) it is not possible to make assumptions about values distribution, thus non-parametric tests were performed in these cases following the advice of the UAB Statistics Facility. Accordingly, any statistical inference with this group should be carefully interpreted due to the low number of individuals available yet to reach conclusions.

The M1 and M2 phenotypes were studied in the same cohorts through the analyses of the corresponding markers Nos2 and CD206. Regarding M1 GAMs (Figure 4.2 B), we found increased Nos2 gene expression in responding IMS-TMZ-treated tumours (0.06 ± 0.04 relative expression) which reached statistical significance when compared to relapsing and control tumours, with 0.01 ± 0.01 relative expression for both groups. Furthermore, non-responding tumours had a Nos2 relative expression of 0.02 ± 0.02, suggesting a lower M1 subpopulation in comparison to responding tumours, but no significant differences were found ($p = 0.2371$). The low number of cases in the non-responding group may hamper the interpretation of all statistical tests.

	Relative expression						
	F4/80	Nos2	CD206	PD-L1	M1/M2	M1/GAMs	M2/GAMs
Responding IMS-TMZ	0.79 ± 0.36	0.06 ± 0.04	0.23 ± 0.09	1.23 ± 0.52	0.29 ± 0.17	0.07 ± 0.03	0.32 ± 0.15
Relapsing IMS-TMZ	0.18 ± 0.11	0.01 ± 0.01	0.14 ± 0.11	0.47 ± 0.41	0.10 ± 0.05	0.08 ± 0.05	0.91 ± 0.72
Non-responding IMS-TMZ	0.13 ± 0.04	0.02 ± 0.02	0.11 ± 0.04	0.69 ± 0.70	0.16 ± 0.14	0.14 ± 0.13	0.86 ± 0.05
IMS-vehicle	0.18 ± 0.08	0.01 ± 0.01	0.13 ± 0.06	0.46 ± 0.16	0.11 ± 0.09	0.08 ± 0.05	0.84 ± 0.34

Table 4.2. Relative normalised expressions obtained in rt-PCR studies with responding, relapsing and non-responding IMS-TMZ as well as IMS-vehicle-treated (control) samples: average ± SD of F4/80, Nos2, CD206, and PD-L1 genes, and ratios of M1/M2, M1/GAMs and M2/GAMs, estimated as explained in Figure 4.2 caption.

Concerning M2 GAMs profile (Figure 4.2 C), results showed a different trend. We only observed significant differences between responding IMS-TMZ-treated and control mice (relative expressions 0.23 ± 0.09 and 0.13 ± 0.06, respectively). Other groups only reached a trend to significance when compared with the responding group: relapsing tumours with 0.14 ± 0.11 relative expression, and non-responding with 0.11 ± 0.04 ($p = 0.0789$ and $p = 0.0871$, respectively).

These results suggest that there is a larger GAM population in responding IMS-TMZ-treated mice in comparison with other groups, but M1 and M2 subpopulations did not increase in comparable proportions (see next section).
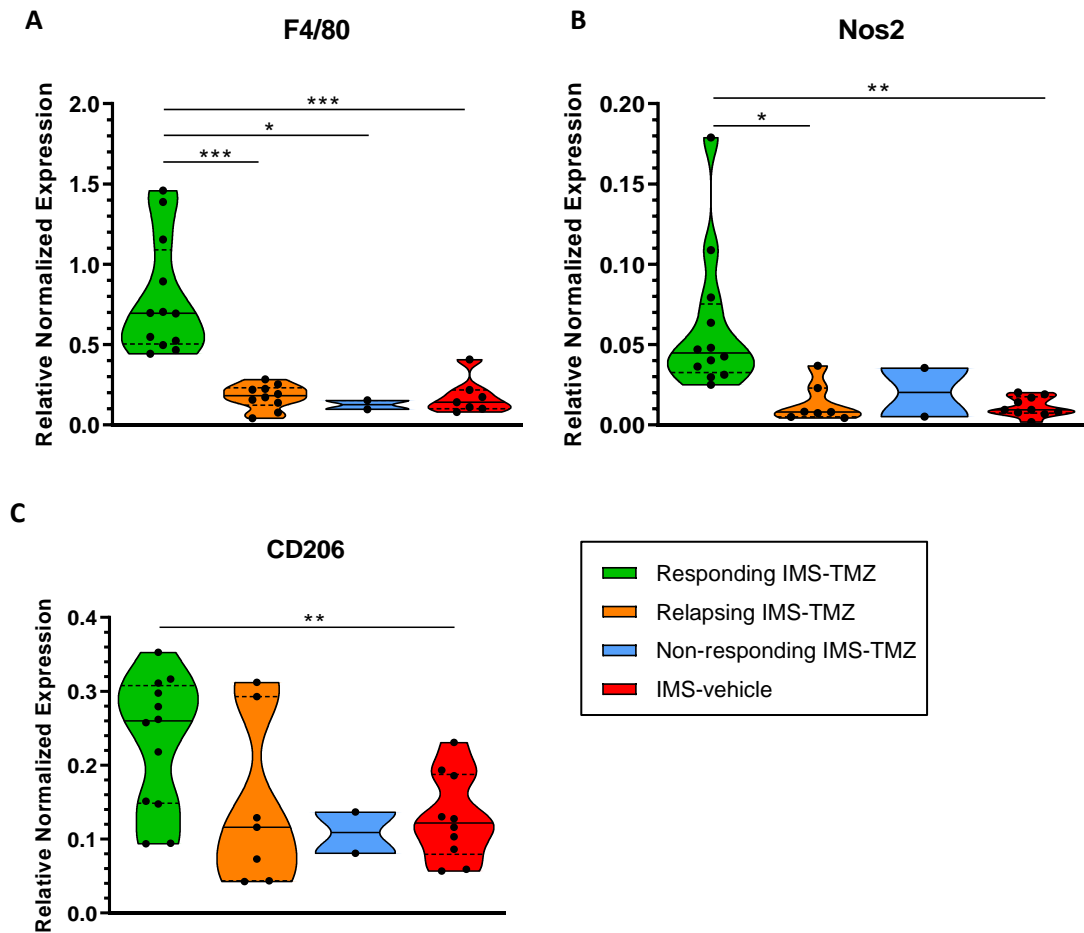
Figure 4.2. Violin plot for estimation of GAMs, M1 and M2 subpopulations in tumour samples from IMS-TMZ-treated mice responding, relapsing and non-responding to treatment, as well as IMS-vehicle-treated (control) mice. *A) Global GAM population was evaluated through F4/80 expression levels. Significant differences were observed between IMS-TMZ-treated responding groups and relapsing, non-responding and IMS-vehicle-treated groups (p < 0.05 in all instances). B) M1 GAM subtype population was evaluated through Nos2 gene expression levels. Significant differences were observed between responding IMS-TMZ-treated groups vs. relapsing (p = 0.013) and vs. control groups (p = 0.002), while comparison with non-responding group did not reach significance (p = 0.132). C) M2 GAM subtype population was evaluated through CD206 gene expression levels. Significant differences were observed only between responding IMS-TMZ-treated and control groups (p = 0.005), but a trend to significance was also found in comparisons of responding vs. relapsing (p = 0.079) and vs. non-responding groups (p = 0.088). Data are mean ± SD and significant differences between groups are indicated by asterisks (*** p ≤ 0.001, ** p < 0.005, * p < 0.05). Explanations for violin plots as in Figure 2 of Chapter II. Note that graphs are shown in different "y" scaling for better appreciation of data distribution.*

4.3.3.3. Assessing different GAM population subtypes regarding global GAM values

In order to analyse the predominant GAM population subtype in mice cohorts, M1/M2 ratio was calculated considering the ratio of Nos2 to CD206 (Figure 4.3 A). The M1/M2 ratio was found significantly higher in responding IMS-TMZ-treated tumours when compared to relapsing IMS-TMZ-treated tumours after transient response (*p* = 0.0090), as well as to IMS-vehicle-

treated tumours (p = 0.0022). Non-responding IMS-TMZ-treated tumours presented lower average expression value when compared to responding tumours, although no significant differences were observed (p = 0.3485), probably due to low number of cases in the non-responding group (n=2).

Furthermore, M1/GAM and M2/GAM ratios were analysed considering the ratios of Nos2 to F4/80 and CD206 to F4/80 expression levels, respectively. Regarding M1/GAM ratios, no significant differences were observed among different groups, although average expression level was higher in the non-responding group (Figure 4.3 B). However, when looking at the M2/GAM ratio (Figure 4.3 C), the IMS-TMZ-treated responding group presented an average ratio ca. 2.5-fold lower than other groups, reaching statistical significance when compared to relapsing (p < 0.0131) and non-responding (p = 0.0001) groups, and to IMS-vehicle-treated mice (p = 0.0005). On the other hand, the M2/GAM ratio achieved similar values in relapsing, non-responding and IMS-vehicle-treated tumours, with no significant difference between them. See Table 4.2 for M1/M2, M1/GAM and M2/GAM average ratios.

4.3.3.4. PD-L1 gene expression is increased in IMS-TMZ-treated tumours, and this increase may be correlated with GAM polarisation state

We analysed the PD-L1 gene expression in tumours from IMS-TMZ-treated mice responding, relapsing and non-responding to treatment and IMS-vehicle-treated mice (Figure 4.4 A). A significantly higher PD-L1 gene expression was observed in responding IMS-TMZ-treated mice (1.23 ± 0.52 relative expression), i.e., 2.6-fold higher when compared to relapsing (0.47 ± 0.41 relative expression) and control groups (0.46 ± 0.16 relative expression), with p = 0.0002 and p = 0.004, respectively. However, no significant differences (p = 0.440) were observed between IMS-TMZ-treated responding and non-responding groups, although a lower average PD-L1 expression level (0.69 ± 0.70) was found in non-responding tumours. Furthermore, in order to confirm whether PD-L1 gene expression levels were correlated with the polarisation state of GAMs as stated in Chapter II, Pearson correlation analyses were performed, and PD-L1 expression level was shown to be positively correlated to the M1/M2 ratio (p = 0.0095), confirming that in this experimental scenario, higher PD-L1 gene expression levels correlate with increased M1/M2 ratios (coloured map for expression levels can be found in Figure 4.4 B).
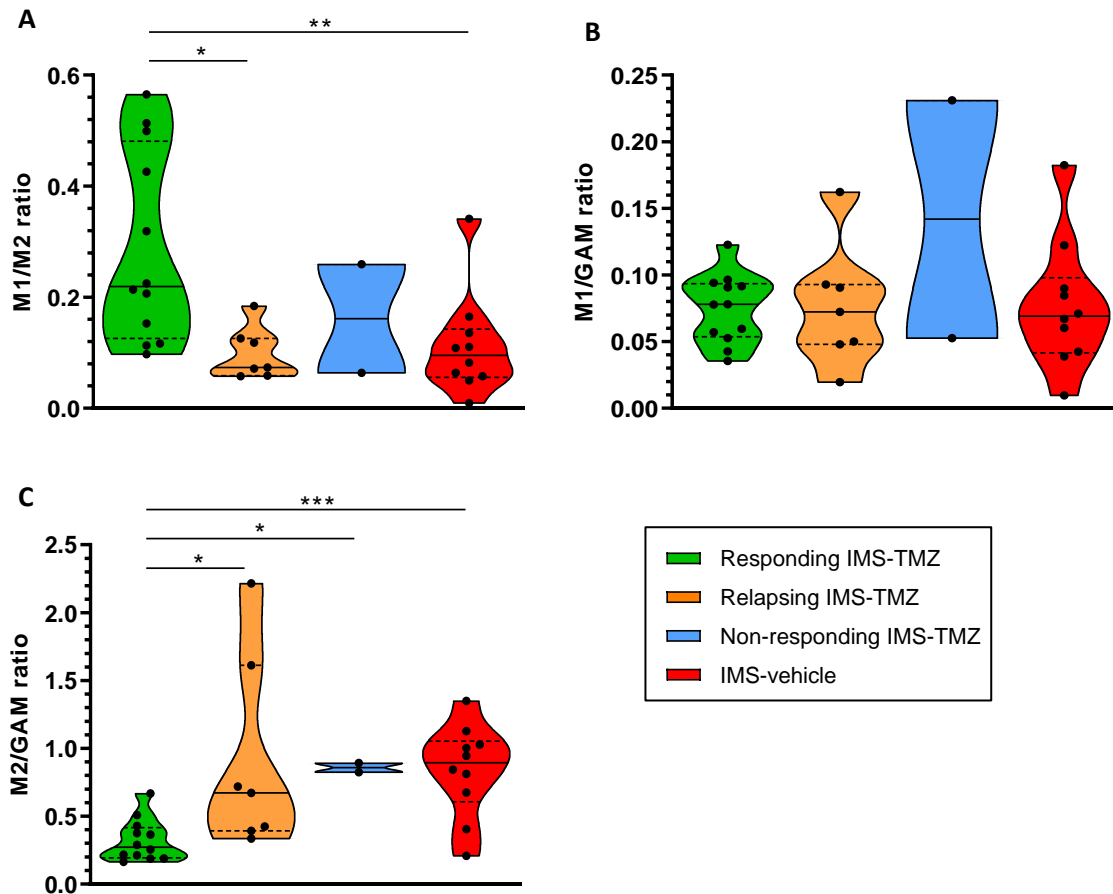
Figure 4.3. Results of the M1/M2, M1/GAM and M2/GAM ratios analyses in tumour samples from IMS-TMZ-treated mice responding, relapsing and non-responding to treatment, as well as from IMS-vehicle-treated (control) mice. *A) M1/M2 ratio was calculated using the relation of Nos2 to CD206 expression levels. Significant differences were observed between IMS-TMZ-treated responding vs. relapsing (p = 0.009) and vs. control groups (p = 0.002), while comparison with non-responding groups did not reach significance (p = 0.440). B) M1/GAM ratio was calculated using the relation of Nos2 to F4/80 expression levels. No significant differences were observed in comparison between groups. C) M2/GAM ratio was calculated using the relation of CD206 to F4/80 expression levels. Significant differences were observed between IMS-TMZ-treated responding vs. relapsing, vs. non-responding and vs. control groups (p<0.05 in all instances). Data are mean ± SD and significant differences between groups are indicated by asterisks (*** p ≤ 0.001, ** p < 0.005, * p < 0.05). Explanations for violin plots as in Figure 2 of Chapter II. Note that graphs are shown in different "y" scaling for better appreciation of data distribution.*
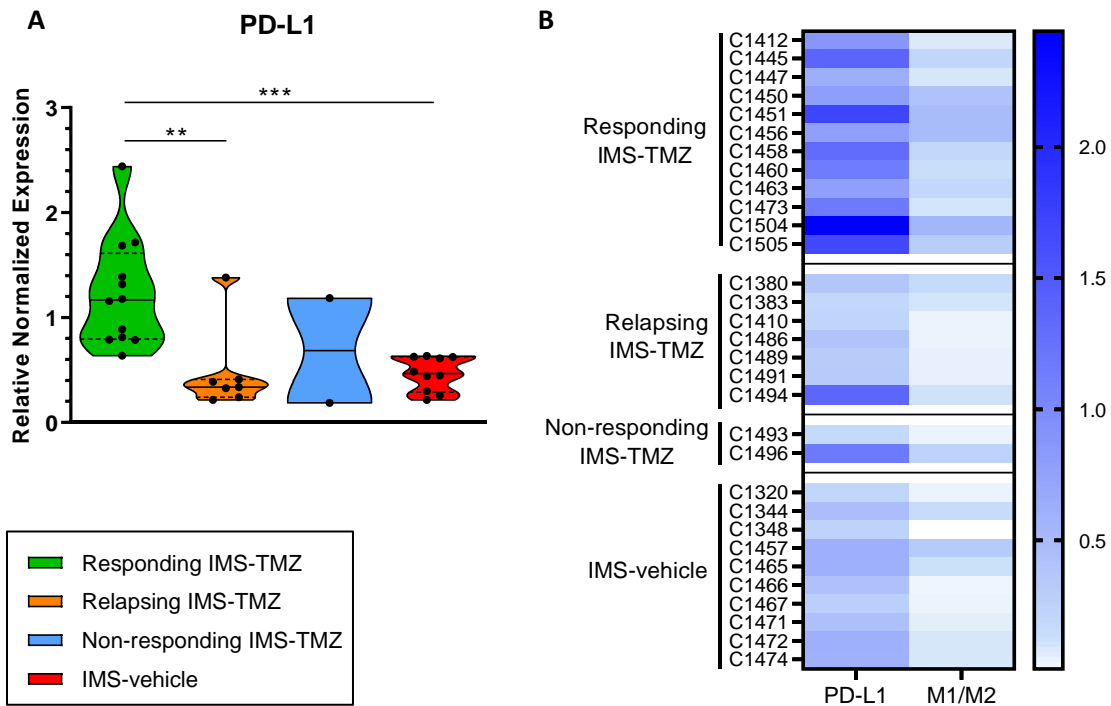
Figure 4.4. PD-L1 expression and its relationship with M1/M2 ratios. *A) Violin plot for PD-L1 level expression analyses in tumour samples from IMS-TMZ-treated mice responding, relapsing and non-responding to treatment, and control mice. Significant differences were observed between IMS-TMZ-treated responding vs relapsing and vs. control groups ($p < 0.005$ in all instances). Comparison between responding and non-responding groups was not significant ($p = 0.440$). Data are mean ± SD and significant differences between groups are indicated by asterisks (*** $p \leq 0.001$, ** $p < 0.005$). Explanations for violin plots as in Figure 2 of Chapter II. B) Visual coloured map for normalised expression representing PD-L1 gene expression level (from **Figure 4.4** A) and M1/M2 ratio (from Figure 4.3 A) in each individual case. Pearson correlation analysis in the whole group achieved statistical significance ($p = 0.0095$).*

4.3.3.5. ADAM8, ADAM10, ADAM17 and MMP14 genes present higher expression in responding IMS-TMZ-treated tumours, while MMP9 gene is higher expressed in non-responding IMS-TMZ-treated tumours

The expression levels of ADAM8, ADAM10, ADAM17, MMP9 and MMP14 genes were analysed by rt-PCR approaches (see Table 4.3 for relative expression values). We found an increase in the expression level of ADAM8, ADAM10, ADAM17 and MMP14 genes in IMS-TMZ-treated responding group vs. relapsing, non-responding and control tumours (Figure 4.5 A-C, E), reaching significance for some comparisons (please check Figure 4.5 caption). By contrast, no significant differences were detected between expression levels of relapsing, non-responding and control tumours. The expression of the aforementioned genes does not seem to be directly related to a local TMZ effect, since relapsing and non-responding were also treated with TMZ but did not present comparable expression levels to the responding tumours.

Regarding MMP9, we found significantly higher expression levels in the non-responding group vs. responding and relapsing tumours, as well as vs control tumours (Figure 4.5 D).

Conversely, this marker showed similar expression level in responding and relapsing IMS-TMZ-treated and IMS-vehicle-treated tumours. Again, results indicate that changes in the expression level of MMP9 are not linked with TMZ treatment or absence of treatment.

Furthermore, we found that protease genes ADAM8, ADAM10, ADAM17 and MMP14 presented a similar expression profile (Figure 4.6). As seen from Pearson correlations (see section 4.3.3.6 for details), all genes showed to be positively correlated. Interestingly, this correlation was not observed for MMP9 gene, which expression profile was distinctly different from those observed for ADAM8, ADAM10, ADAM17 and MMP14 genes.

	Relative expression				
	ADAM8	ADAM10	ADAM17	MMP9	MMP14
Responding IMS-TMZ	0.016 ± 0.012	0.068 ± 0.061	0.026 ± 0.017	0.005 ± 0.006	0.017 ± 0.008
Relapsing IMS-TMZ	0.004 ± 0.002	0.024 ± 0.010	0.012 ± 0.005	0.002 ± 0.002	0.004 ± 0.001
Non-responding IMS-TMZ	0.005 ± 0.004	0.032 ± 0.007	0.013 ± 0.006	0.038 ± 0.023	0.004 ± 0.000
IMS-vehicle	0.003 ± 0.002	0.016 ± 0.008	0.009 ± 0.003	0.002 ± 0.004	0.004 ± 0.002

Table 4.3. Relative normalised of ADAM8, 10 and 17, and MMP9 and 14 expression levels obtained in rt-PCR studies with responding, relapsing and non-responding IMS-TMZ and IMS-vehicle-treated (control) samples: values are average ± SD.
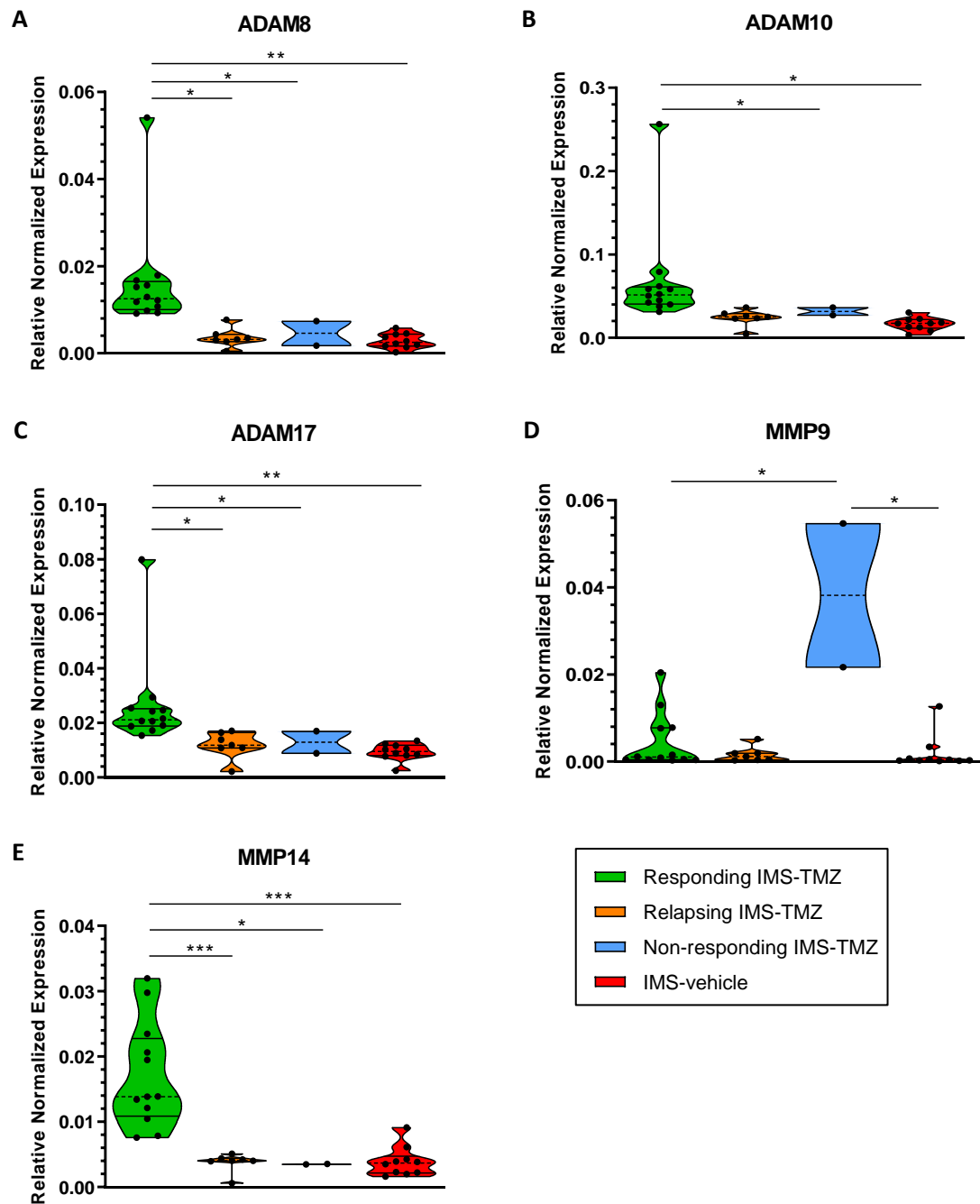
Figure 4.5. Violin plot for ADAMs and MMPs gene level expression in tumour samples from IMS-TMZ-treated mice responding, relapsing and non-responding to treatment and vehicle-treated (control) mice. *Results of A) ADAM8 expression levels, B) ADAM10 expression levels, C) ADAM17 expression levels. Significant differences were observed for responding vs. non-responding and for responding vs. control tumours for all ADAMs studied (p<0.05 in all instances). Moreover, the comparison responding vs. relapsing groups was also significant in case of ADAM8 and ADAM17. Comparisons for ADAMs expression levels between relapsing, non-responding, and control groups among themselves did not reach significance. Results of D) MMP9 expression levels and E) MMP14 expression levels. MMP9 levels were significantly higher in the non-responding group, reaching significance in comparison with responding and control groups (p < 0.05 in all instances), while responding, relapsing and control groups were not significantly different among themselves. For MMP14, significantly higher expression levels were found in responding group in comparison with relapsing, non-responding, and control groups (p<0.05 in all instances). Data are mean ± SD and significant differences between groups are indicated by asterisks (*** p ≤ 0.001, ** p < 0.005, * p <*

0.05). Explanations for violin plots as in Figure 2 of Chapter II. Note that graphs are shown in different "y" scaling for better appreciation of data distribution.
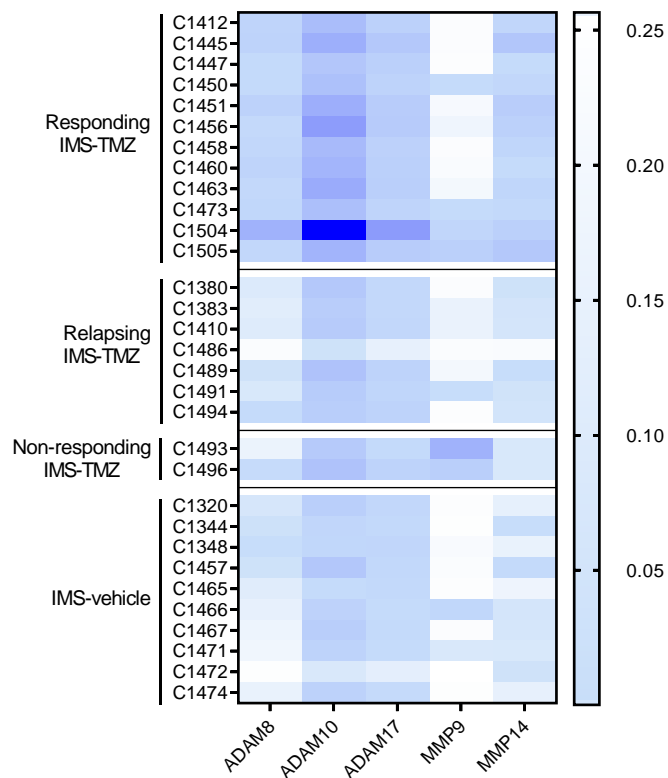
***Figure 4.6. Visual coloured map for normalised expression representing ADAM8, 10 and 17, and MMP9 and 14** (values from Figure* 4.5*¡Error! No se encuentra el origen de la referencia.) for each individual case.*

4.3.3.6. ADAM8, ADAM10, ADAM17 and MMP14 expression levels showed correlation with global GAM population, its polarisation state and PD-L1 gene expression

In order to investigate whether ADAMs – MMPs gene expressions were correlated with overall GAM population, M1/M2 profile and PD-L1 gene expression, Pearson's correlation analyses were performed considering all mice cohorts together. Significant correlation was found for the association of GAM, M1/M2 and PD-L1 to ADAM8, ADAM10, ADAM17 and MMP14 gene expression (all with $p < 0.0001$). The MMP9 gene presented a different trend, with no correlation found. Correlation analyses outputs can be found in Figures from Figure 4.7 to Figure 4.9.
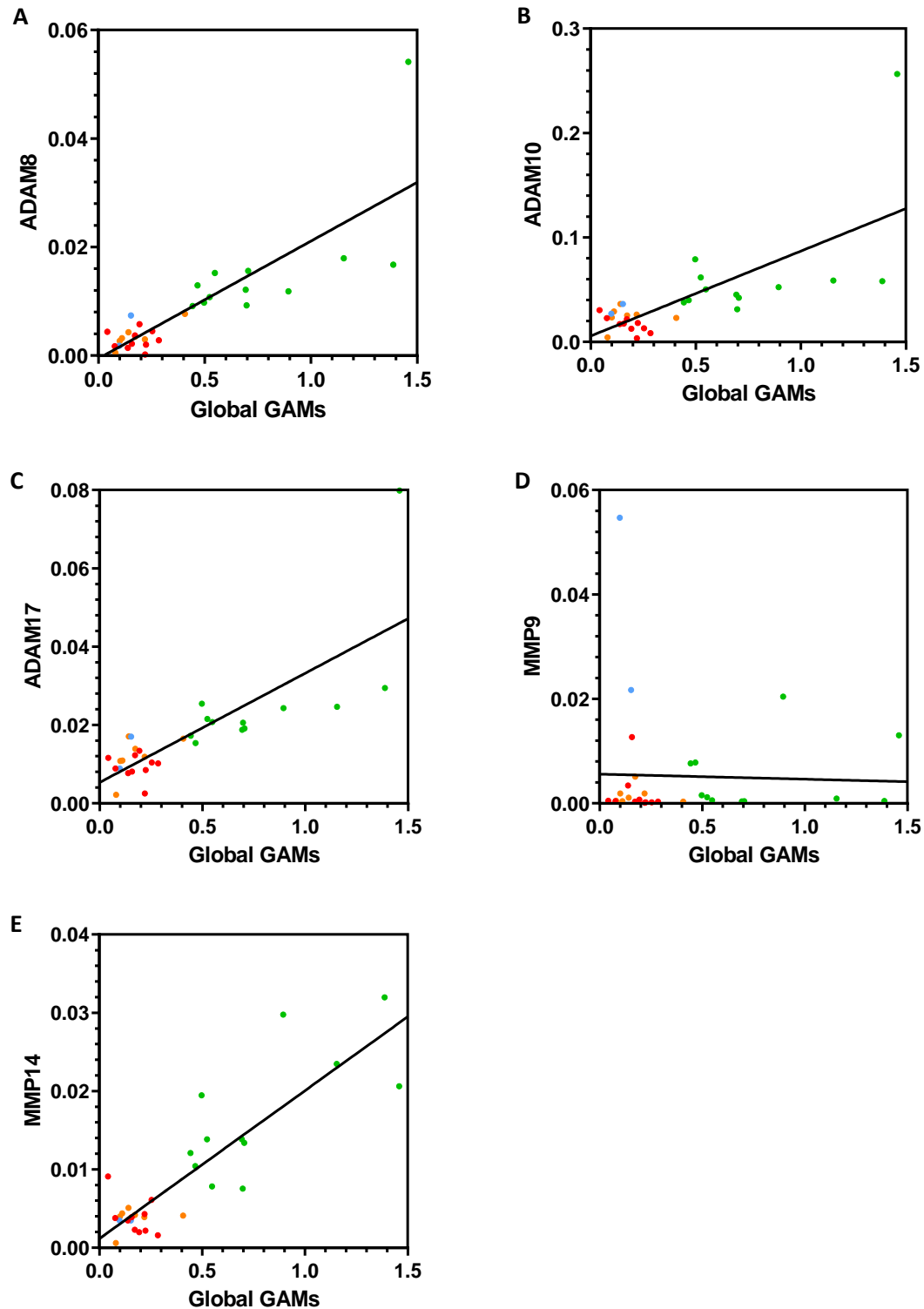
Figure 4.7. Pearson correlation analyses between ADAM8, ADAM10, ADAM17, MMP9 and MMP14 protease genes vs. global GAM population (F4/80 gene expression levels) considering all samples (IMS-TMZ-treated mice responding, relapsing and non-responding to treatment and control mice). Significance was found for the association between GAMs and A) ADAM8; B) ADAM10; C) and E) MMP14 expression levels (p < 0.0001 in all instances). No correlation was found for the association between D) GAMs/MMP9 (p = 0.8564). Colour code as in Figure 4.5.
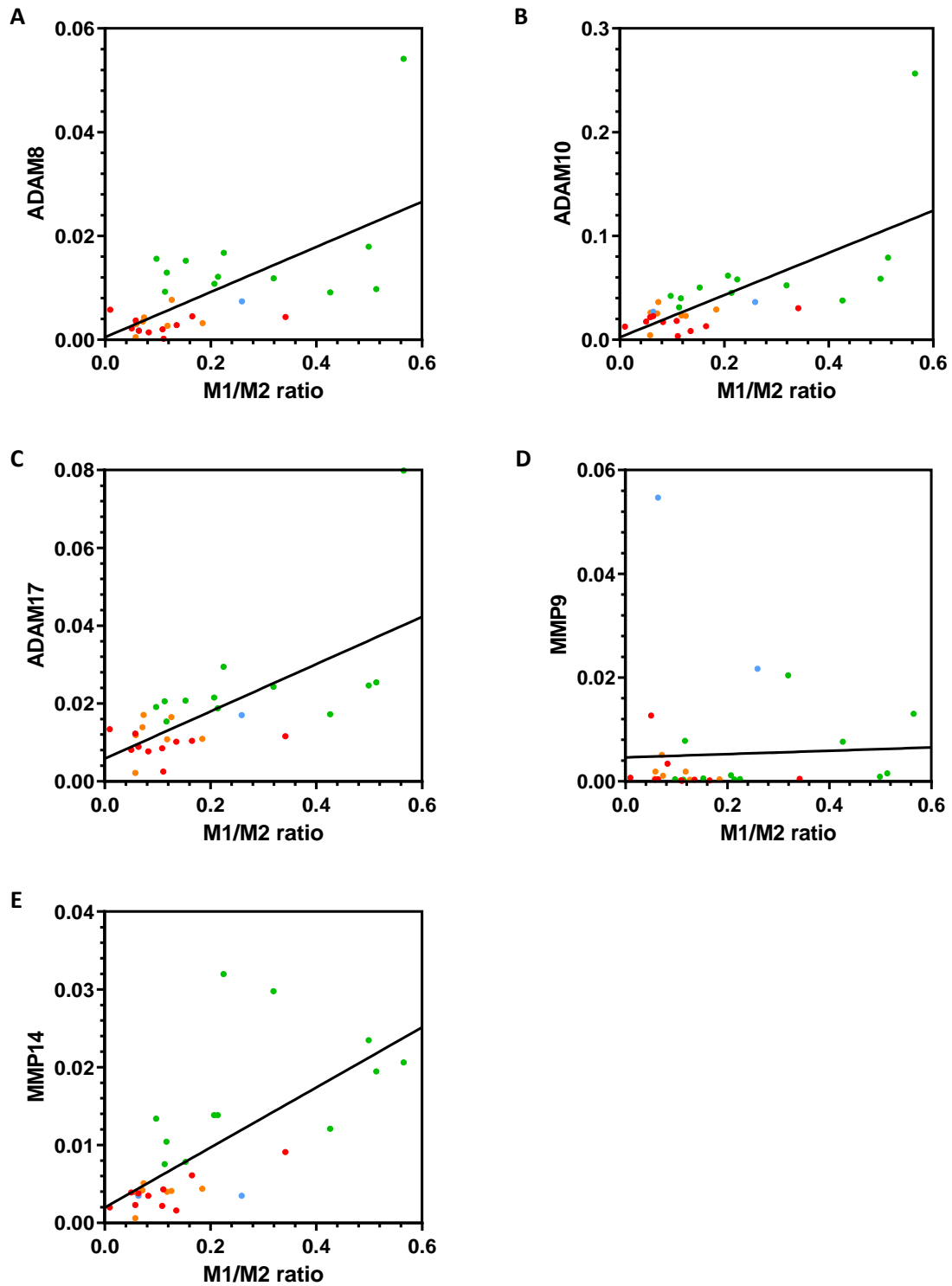
Figure 4.8. Pearson correlation analyses between ADAM8, ADAM10, ADAM17, MMP9 and MMP14 protease genes vs. M1/M2 (Nos2 to CD206 expression level ratios) considering all samples (IMS-TMZ-treated mice responding, relapsing and non-responding to treatment and control mice). Significance was found for the association between M1/M2 estimated ratio and A) ADAM8; B) ADAM10; C) and E) MMP14 expression levels (p < 0.0001 in all instances). No correlation was found for the association between D) M1/M2 and MMP9 (p = 0.8140). Colour code as in Figure 4.5.
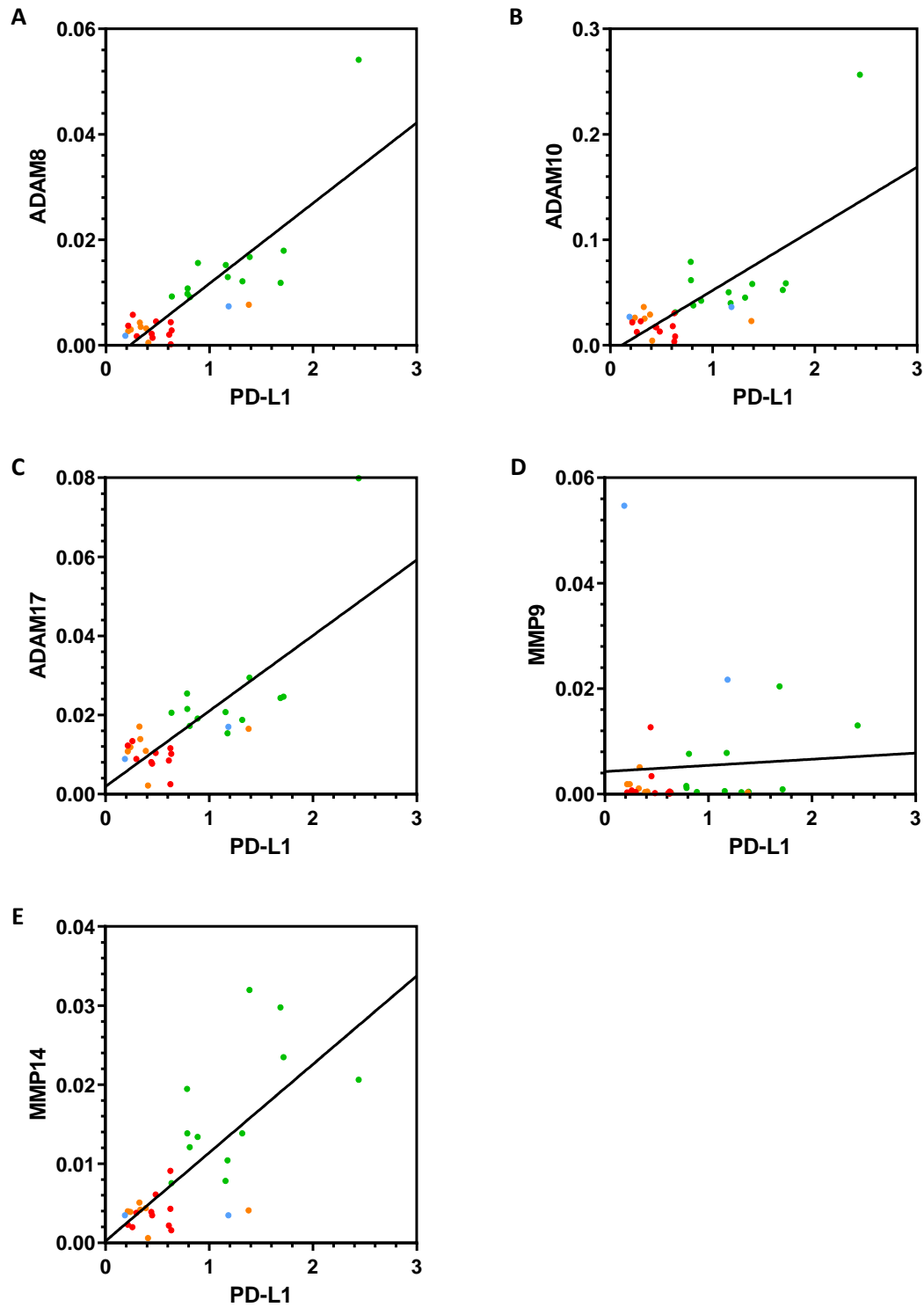
Figure 4.9. Pearson correlation analyses between ADAM8, ADAM10, ADAM17, MMP9 and MMP14 protease genes vs- PD-L1 expression (CD274 gene expression levels) considering all samples (IMS-TMZ-treated mice responding, relapsing and non-responding to treatment and control mice). Significance was found for the association between PD-L1 expression and A) ADAM8; B) ADAM10; C) and E) MMP14 gene expression levels (p < 0.0001 in all instances). No correlation was found for the association between D) PD-L1 and MMP9 (p = 0.7555). Colour code as in Figure 4.5.

4.3.4. Discussion

4.3.4.1. GAM populations may change during response to therapy and relapse

In this Chapter, we have analysed through rt-PCR approaches, tumour samples from mice belonging to different groups: IMS-TMZ-treated responding (n=12), relapsing (n=7) and non-responding (n=2) to treatment, as well as IMS-vehicle-treated (control) mice (n=10). One of our purposes was to characterise the microglia/macrophage population into the tumour site in different situations of response to therapy (i.e., responding, relapsing and non-responding), as well as in control tumours, with views to extend the published results reported in Chapter II. The number of cases in the non-responding group is low since it is not a usual finding to not present either transient or long-lasting responses to TMZ therapy, especially when mice are treated with the IMS-TMZ protocol (only ca. 10.2% of all treated mice do not respond to IMS-TMZ).

Our results, extended in this chapter in order to include subjects from the non-responding and relapsing groups, reinforce the idea of the microglia/macrophage role in tumour response. Still, an overall increase (ca. 5.1-fold change in average) in the content of microglia/macrophages was observed in IMS-TMZ-treated tumours responding to therapy, when compared to relapsing, non-responding and controls tumours, through F4/80 gene level expression. Furthermore, F4/80 does not seem to have differential expression when comparing relapsing or non-responding to therapy tumours to controls tumours (Figure 4.2 A). These results suggest that there is an increased GAM population in responding IMS-TMZ treated mice but not all TMZ-administered mice increased expression in the same way, with non-responding presenting even lower values. In other words, GAM content seems to correlate in our GB model with an "efficient" action of the IS triggered by an IMS TMZ administration. These results are in agreement with other published studies, which describe that certain chemotherapeutic agents can modulate immune infiltration into tumour sites being also related to tumour prognosis and/or response to therapy in colorectal [188,189], breast [190], ovarian [191,192], and brain [193–195] cancers.

Regarding different GAM phenotypes, as already discussed in Chapter II, changes in phenotype prevalence from M1 to M2 are associated with tumour progression in solid tumours [196,197]. Thus, the assessment of GAM polarisation profile with Nos2 and CD206 markers in tumours was extended to TMZ-treated relapsing and non-responding groups, in addition to responding and control tumours. Results showed that both M1 and M2 microglia/macrophages were present in all studied groups (Figure 4.2 B, C) but, as already suggested in Chapter II, the proportion of M1 and M2 GAMS was not the same across different groups. Results from this chapter confirm a significantly higher M1/M2 GAM ratio in IMS-TMZ-treated responding tumours compared with control tumours, and also when compared to relapsing IMS-TMZ-treated tumours. The ratio was also higher in responding mice when compared to non-responding, although significance was not achieved, which may be due to the low number of cases yet in the non-responding group. No significant differences were observed when comparing relapsing, non-responding and control tumours. Results seem to suggest that such

low M1/M2 ratios (i.e., pointing to a prevalence of M2 phenotype when comparing to responding tumours) are associated with a "lack of response", either from the beginning (non-responding) or arriving after transient response (relapsing), or with an IS unchecked active proliferation in control mice. In other words, the TME of responding tumours counts with a higher number of infiltrating IS cells with ability to start and sustain inflammatory responses as well as to exhibit antitumour activity, leading to tumour tissue disruption. Our results are in agreement with other authors which described the relation between the GAM polarisation in various cancer types and the outcome prognosis, showing a high content of M1 macrophages to be associated with best prognosis in treated ovarian cancer patients [198] or a high M2 infiltration to be a predicting poor prognosis [199]. Focusing on GB patients, it has been described that predominant M1 polarisation was associated with a better overall prognosis [200] and that the M1/M2 ratio was correlated with the survival rate after TMZ treatment [201]. Accordingly, in preclinical settings, therapeutic strategies able to increase the M1/M2 ratio were correlated with improved survival in glioma-bearing mice [202]. It is then clear that achieving suitable M1/M2 ratios is desirable and will be determinant for outcome in preclinical and clinical GB. It is worth pointing out that for obvious reasons, data are coming from different mice in each group, being impossible to collect this type of data along the time (i.e., same animal pre- and post-treatment, and during relapse if it is the case). However, we assume that a) control mice could be considered the "basal" situation of all mice pre-treatment, b) all mice presenting response (which we cannot know in advance if it would be a transient or long-lasting response with cure) would present similar changes in GAM ratios and switch in polarization profiles. Then, all mice that are relapsing after response have passed through the stage of "responding" with the corresponding increase in M1/M2 GAM ratio. In this sense, results suggest that a small percentage of mice even when treated with an effective therapeutic protocol such as IMS-TMZ described in Chapter I, are not able to mount a suitable antitumour immune system. Other mice present transient effective response detected by growth arrest following an adapted RECIST criteria (described in [50]), but relapse after this transient response. Some authors have described that there are human GB mutations which can be related to a prevailing M2 GAM recruitment which finally would lead to chemoresistance [203]. The switch to an M2-like phenotype can be also triggered by local factors such as cytokines [204], contributing to therapeutic resistance. In general, results described regarding M1 and M2 microglia/macrophage balance favouring an M2 phenotype is in agreement also with [114]. However, a word of caution may be raised regarding control GL261 GB tumours, since it was described in [114] that fluctuations can be observed in some immune populations, e.g., in M1 macrophages, relevant changes might take place between day 14 or 21 p.i. In addition, the methodological approaches used in our case and in the aforementioned work [114] are different, then a direct comparison is not straightforward.

4.3.4.2. PD-L1 gene expression in GL261 GB

PD-L1 expression level is considered a major prognostic biomarker for immune therapy in many cancers, such as renal carcinoma, colorectal cancer, lymphoma, head and neck carcinoma, bladder cancer, hepatocellular carcinoma and metastatic colorectal cancer, but still not in glioma [205]. In general, the most accepted predictive marker for therapy targeting PD-1/PD-L1 axis is the number of cytotoxic T-lymphocytes within the tumour and the expression level of PD-L1 in cancer cells [206]. This is not the case for GB: no reliable predictive marker has been described yet for GB. Unlike other solid tumours, the relationship between PD-L1 and different cell types such as lymphocytes remains largely elusive, probably reflecting the specific characteristics of the immune environment in the brain [207].

Our results suggest that there are significant differences (ca 2.6-fold change) regarding PD-L1 gene expression in IMS-TMZ-treated tumours responding to therapy compared to relapsing and control tumours. This expression was also 1.8-fold change higher in comparison with non-responding group values, although without significance. On the other hand, there were no significant differences between relapsing, non-responding, and control groups. Increased PD-L1 expression after chemotherapy has been already described [208–210], although there is variability about the reported results. In our case, average PD-L1 expression values were lower in control mice than in all TMZ-administered groups, but it only reached significance in case of IMS-TMZ treated responding mice. The large dispersion of values, and the low "n" yet in the non-responding group prevent us to affirm whether these small increments in relapsing and non-responding could be consistent. In fact, PD-L1 expression level values observed in relapsing and non-responding groups were much closer to control values.

A possible explanation for these differences between treated groups could be the implication of cytokines released by activated immune cells during therapy response. As described in the literature [139], upon T cell activation, they can migrate to the tumour site and produce cytokines such as IFN-γ, which leads to an increased expression of PD-L1 gene in tumour cells and other cells, including other T cells, within the tumour tissue. We have described in Chapter I immunohistochemistry analyses for TMZ-treated and control GL261 GB samples. In that case, mice were treated with a different TMZ administration protocol [49], not yet optimized to IMS-TMZ. Even in this scenario, GL261 tumours showed significant ($p < 0.05$) differences in CD3$^+$ immunohistochemistry staining in chosen fields while comparing TMZ-treated and control GL261 GB tumour-bearing mice. Regarding IMS-TMZ treated tumours responding to therapy, we would expect even higher infiltration of CD3$^+$ T cells into tumour tissue. This could finally lead to an increased PD-L1 gene overall expression in the whole tumour mass through production of IFN-γ by T lymphocytes, which would no longer be the case in relapsing and non-responding groups.

As mentioned in Chapter II, PD-L1 gene is expressed in a variety of cells, including macrophages. On macrophage surfaces, PD-L1 could have an antitumour role instead of

immunosuppressive, limiting excessive activation of T regulatory cells and protecting macrophages from killing by those T lymphocytes [211,212]. In the current chapter, the PD-L1 gene level expression was also related to M1/M2 ratio, showing a significant positive correlation among them (Figure 4.4 B), which indicates that increased PD-L1 content could be at least partially associated with increased M1-polarised macrophages. Responding tumours had a higher percentage of M1 macrophages, which could overexpress PD-L1 on their cell surface, protecting them from T lymphocyte attack. This M1 phenotype population is lower in relapsing and non-responding tumours, which could help to explain our results at least partially.

Furthermore, responding tumours contain a tumour cell population that has been damaged by TMZ and killed by host immune system cells elicited by released damage signals (i.e., lymphocytes and macrophages). These tumour cells die, leading to transient tumour mass decreases. Remaining tumour cells may react by overexpressing PD-L1 to protect from subsequent immune system attack, thus cells with high content of PD-L1 survive and expand, which is in line with PD-L1 expression level increasing in responding tumours. Periodic administration of TMZ might generate new immune system waves and cycles of cell killing repetition until tumours get cured or relapse: at that point tumours are either no longer sensitive to TMZ due to resistant dominant clones, or are able to evade immune system attack, leading to a relapsing tumour. Detailed mechanisms for GL261 GB relapsing still have to be elucidated. Still, the overexpression of metalloproteases (see section 4.3.4.3) may lead to the shedding of membrane-bound PD-L1, promoting the increase of soluble form PD-L1 (sPD-L1) with controversial consequences described [185], and which could inhibit T lymphocytes without need to reach cell-to-cell contact with tumour cells [213]. It remains unclear whether sPD-L1 levels in serum fluctuate during tumour progression or remission or whether they could serve as therapeutic biomarker in human glioma patients [214]. In the case of non-responding tumours, results show that the expression level of PD-L1 protein and gene is equivalent to vehicle-treated tumours suggesting that they would evade therapy by a different mechanism rather than using PD-L1 overexpression.

Last but not least, it is worth mentioning that Chapter I provided an estimation of the PD-L1 protein content through western-blot approaches, where control, relapsing and non-responding groups were analysed (no IMS-TMZ treated responding mice were included in the analysis in that case). Results showed that PD-L1 protein content was significantly higher (ca. 3-fold) in the relapsing IMS-TMZ-treated group when compared with the non-responding and control groups, while no differences were found between non-responding and control tumours. This trend was not observed in rt-PCR results. Non-linear relationships between RNA and protein level analyses of PD-L1 have been described by other authors [215], but it was not possible to further explore in detail in this work, e.g. splitting samples into two different parts for rt-PCR and Western-Blot studies. Future experiments using both measurement methods in the same samples may be of help to elucidate differences between these two methodological approaches.

4.3.4.3. ADAM and MMP gene expression in GL261 GB

ADAMs have been described to be implicated in many aspects of tumourigenesis. The 'shedding' activities of ADAMs, solubilizing cytokine ectodomains, growth factors, adhesion molecules, among others, help to highlight their central role in the extracellular regulation of cellular signalling. They can potentially regulate inflammatory responses, angiogenesis, and cell migration and proliferation, all of them relevant for tumour evolution. Indeed, data from cell and animal models of cancer indicate that ADAM proteolytic activities could drive several aspects of tumourigenesis [216]. On the other hand, MMPs can modulate cellular and signalling pathways by cleaving cytokines, chemokines and growth factors [217], while alterations in MMP expression and activity have been implicated in tumour progression and invasiveness [159].

In this Chapter, we evaluated the molecular profiles of ADAM8, ADAM10, ADAM17, MMP9 and MMP14 genes as well as their association with GB progression (i.e., response to therapy, or lack of response), GAMs population, and PD-L1 expression level within the TME. We found increased expression levels of ADAM8, ADAM10, ADAM17 and MMP14 genes in the IMS-TMZ responding group in comparison with relapsing, non-responding and control tumours (Figure 4.5 A-C, E). On the other hand, MMP9 gene expression level was found increased in the non-responding group in comparison with the other three groups (Figure 4.5 D). This differential expression can be also visually observed in the coloured map for normalized expressions in Figure 4.6. As in previous gene markers discussed in this chapter, changes in ADAMs and MMPs expression do not seem a direct local effect triggered by TMZ itself, since relapsing and non-responding groups did not present the same trend. Furthermore, ADAM8, ADAM10, ADAM17 and MMP14 gene expression levels were found positively associated with global GAM population (Figure 4.7), M1/M2 ratio (Figure 4.8) and PD-L1 gene expression level (Figure 4.9).

Our results show a positive association between ADAM8 expression level and global GAM population and M1/M2 ratio, with its expression level increased in IMS-TMZ treated, responding tumours. This is in agreement with work described in [218] who described colocalization of ADAM8 and CD68, a marker for macrophages/microglia in the brain, suggesting its functional relevance for tumour cells and GAMs in GB, probably contributing to neovascularization and angiogenesis. However, the same authors did not find a correlation between ADAM8 with a certain macrophage polarization state (M1/M2). Interestingly, ADAM8 is also described to be implicated in chemoresistance e.g., mediating resistance to DNA damaging drugs [148]. ADAM8 also proved to be involved in chemotherapy resistance in other contexts such as non-small cell lung cancer lines [219].

Regarding ADAM10, our results suggest a positive association between ADAM10 gene and global GAM population and M1/M2 ratio. In this sense, the expression of ADAM10 could contribute to the Th cell proliferation and differentiation, and in turn, IFN-γ secreted by Th cells stimulates M1 phenotype to exert antitumoural effects [118]. On the other hand, ADAM10 substrates were described to control a wide variety of processes, including persistent

Lymphocyte Activating 3 or T cell immunoglobulin and mucin domain-containing protein 3, which are markers of T cell exhaustion in tumour-infiltrating lymphocytes [220]. Results obtained by authors working with GB and ADAM10 analyses had controversial outputs, with ADAM10 correlating with GB progression [220] or with improved survival [200], although in this case overall results may be explained by more favourable macrophage polarization status (i.e. M1 prevailing, also in line with our results) detected in the human GB samples studied. As commented in the PD-L1 section, metalloproteases such as ADAM10 and ADAM17 were described to cleave PD-L1 in breast cancer cell lines [185] with release of sPD-L1. Furthermore, preclinical work with xenografts bearing colorectal cancer cells were described to benefit from targeted inhibition of active ADAM10, decreasing both tumour growth and relapse after chemotherapy [221]. Overall, this seems to indicate that although a negative role seems to be associated with an increased expression of ADAM10, a wider picture of other microenvironment actors may be needed in order to further elaborate about outcomes.

ADAM17 showed positive correlation with global GAM population and M1/M2 ratio. The role played by ADAM17 in the macrophage proliferation was already described in the introduction, related to their traffic [154] and proliferation [156] and it is aligned with our findings, suggesting a positive association between ADAM17 expression level and the global GAM population. Furthermore, its contribution to the differentiation of T lymphocytes towards Th cells through ADAM17 leads to the secretion of IFN-γ by Th cells, stimulating the M1 phenotype to exert antitumoural effects [118], which may help to explain the positive correlation between ADAM17 and M1/M2 ratio. Furthermore, ADAM17 expression levels were analysed in human GB samples and its expression was described to correlate with M1 polarization profile and better prognosis [200]. Conversely, other biological roles were described for ADAM17 and also ADAM10 which would help to explain their increased levels during an active response to therapy. In this context, it is likely that tumours are promoting changes in order to decrease host immune system attack. ADAM10 and ADAM17 are described to contribute to the immunosuppressive phenotype in glioma initiating cells in culture [222] accordingly, the increase in their expression levels could help to protect initiating cells from immune system attack.

Regarding the MMP9 gene level expression, increased values were found in the non-responding group in comparison with responding and relapsing groups and control group. This is in line with several studies reported in the literature. In human glioma samples, increased expression levels of MMP9 were associated with unfavourable clinical outcomes also reported in other cancer types such as gastric, colon and breast [223], being also used as a biomarker for different tumour types [224]. This agrees with overall results for MMP9 described in [200], suggestive of a worse prognosis in human GB samples. Furthermore, MMP9 inhibition in preclinical mouse models was described to promote anti-tumour immunity by altering physical and biochemical properties of tumours relevant to effector T-cell trafficking [225]. Authors [225]

hypothesize that MMP9 would limit antitumour response, at least in part, through degradation of tumour CXCR3 ligands, resulting in suboptimal trafficking of Th1 cells into tumours.

Results described in this chapter for MMP14 gene expression levels suggest increased expression in IMS-TMZ treated responding tumours in comparison with relapsing, non-responding and control tumours. Furthermore, a positive association was found between MMP14 expression level and global GAM population and M1/M2 ratio, in disagreement with authors in [200], who correlated this expression with a prevailing M2 phenotype and poor outcome in GB human samples studied. Previous studies have described that MMP14 is upregulated in different human tumours types [162,164–166] and glioma, where it was found correlated to glioma grade and to poor patient outcome [167,168]. Some studies have related MMP14 with the macrophage population, showing that increased levels of MMP14 are found in macrophage-rich regions of human atherosclerotic plaques [226]. Moreover, MMP14 seems to be upregulated in human peripheral blood monocytes and monocyte cell lines [227], while studies in vitro found that MMP14 promotes monocyte migration across the endothelium [228,229]. Besides, Andrew C. Newby hypothesised that macrophages with high MMP14 expression level could present the M1 phenotype [230], which is in agreement with our findings. Thus, MMP14 expression could be related to higher monocytes attraction to tumour tissue and macrophage polarisation towards a pro-inflammatory phenotype.

4.3.5. Conclusions

Results described in this chapter expand our knowledge about questions raised during the publication of Chapter II studies, both including different mice cohorts and analysing different microenvironment influencing factors. As main conclusions related to this chapter, we can list the following:

- Increased GAM infiltration, as well as M1/M2 ratios were confirmed in mice administered with IMS-TMZ and responding to therapy, suggesting a shift to antitumour phenotypes which would support their antitumour actions. Both parameters were in most cases significantly higher than in relapsing, non-responding or control groups. This confirms that GAM infiltration is not exclusively related to TMZ administration, but it is linked to an efficient host immune system action against tumours, triggered by TMZ.
- The M2/GAM ratio was shown to be significantly increased in actively proliferation situations such as control, relapsing and non-responding tumours, pointing to a protumoural phenotype supporting tumour progression.
- PD-L1 gene expression levels were higher in IMS-TMZ treated responding mice, reaching significance in comparison with relapsing and control mice, suggesting that tumour cells which were not killed in a therapeutic round may develop mechanisms to evade further host immune system attacks.

- PD-L1 expression levels measured in control, non-responding and relapsing mice did not follow the same trend described for protein measurements with western blot in Chapter I, i.e., were not significantly higher in relapsing tumours. The increase of experimental groups and further investigation on gene and protein expression measurements performed on fractions of the same samples will be needed in order to elucidate the cause for those differences

- Regarding metalloproteases, ADAM8, ADAM10, ADAM17 and MMP14 genes were highly expressed in IMS-TMZ-treated responding tumours compared with other groups. This expression was positively correlated with increased M2-to-M1 polarization profile and PD-L1 expression levels. The broad spectrum of biological activities associated to metalloproteases makes the interpretation of this data complex, and more studies will be needed to clarify whether this increased expression originates in tumour cells or host immune system cells and which role may be expected, being the same valid for PD-L1 expression.

- The MMP9 gene expression level was found increased in non-responding tumours in comparison with other groups, suggesting that its role related to invasion and angiogenesis could be determinant in fast tumour progression, even under efficient therapeutic schedules.

4.4. CHAPTER IV: ASSESSMENT OF CHANGES IN T-CELL AND NATURAL KILLER POPULATIONS IN GL261 GB DURING IMS-TMZ TREATMENT BY FLOW CYTOMETRY APPROACHES

4.4.1. Context and specific objectives

GB tumour cells secrete numerous chemokines, cytokines and growth factors and expose/release DAMPs that promote infiltration of various cells such as Th cells, Tc cells, Treg cells and NK cells within the tumour. These non-neoplastic cells are part of the TME, which has a crucial role in cancer growth and response to treatment [101].

The generation of new lymphocytes takes place in the bone marrow and the thymus, from which mature, but naïve, T cells are released to peripheral lymphoid organs, where they are primed by engaging with APCs. This priming phase leads to clonal expansion of T cells with antigen-specific effector functions, which then infiltrate tissues [207]. Tumour-infiltrating lymphocytes are primarily composed of Th, Tc, and Treg cells. Although T cell infiltration in GB is vastly outnumbered by GAMs (ca 1% in GL261 GB, unpublished GABRMN data, also [231]), multiple studies have proven a link between the type of infiltrating lymphocyte and GB progression [232–235].

Two major effector T cell populations exist, namely Th cells and Tc cells. Th cells express antigen receptors on their surface and can recognize antigen fragments presented by APCs. Once stimulated by antigen, Th cells proliferate and differentiate into active and memory, being able to orchestrate and modulate an antigen-specific immune response through their high plasticity and ability to produce cytokines [236]. Many studies have described Th cells to play an important role in the outcome of solid tumour diseases, including GB [237]. On the other hand, Tc cells can induce selective cell apoptosis through direct cell-cell interaction and targeted release of effector molecules, such as perforin and granzymes [238]. The infiltration and activation of Tc cells critically affect the development and progression of the tumour and they have been described to correlate positively with the survival rate of GB patients [239]. However, the infiltrated Tc cells in most tumours are exhausted or their activation inhibited due to the influence of the TME [240].

Treg are potent immunosuppressive cells that promote GB immune escape. Treg are not present in normal brain tissue, but a large number of immunosuppressive Treg are found in the GB microenvironment, relating the level of Treg infiltration to tumour pathological grade [241]. Treg can inhibit activation of naïve tumour-reactive T-lymphocytes (both Th and Tc) by secreting cytokines such as IL-10 and TGF-β and induce recruited Th cells in the TME to transform into new Treg. Thus, the presence of Treg cells may further contribute to the lack of effective immune activation against malignant GB [242]. One of the most important factors that determine Treg differentiation and maturation is FoxP3 (forkhead box P3). FoxP3 is also the main transcription factor through which Treg regulate the expression of IL-10 and TGF-β [243].

NK cells are powerful immune effectors that recognise target cells by the lack of MHC molecules on their surface and kill them without previous activation. NK cells contain both perforin-rich and granzyme-rich granules and are capable of lysing malignant cells by perforin/granzyme pathway or death receptor-related pathways [129]. NK cells are linked to brain tumour surveillance [244].

The specific objective of Chapter IV was to analyse responding samples from GL261 tumour-bearing mice treated with IMS-TMZ and vehicle, during a TRI peak increase close to the expected maximum point, evaluating, by flow cytometry, T cell subpopulations and NK infiltrated cells within the tumour site.

4.4.2.   Specific materials and methods

A total of 7 C57BL/6 mice (weighing 23.9 ± 1.8 g, aged 19.4 ± 0.8 weeks) were used for the studies described in this Chapter. The GL261 glioma generation, the IMS-TMZ treatment, and the *in vivo* MRI and MRSI studies were performed as described in Chapter II. Still, criteria regarding tumour appearance, Tumour Responding Index values and tumour volume changes for choosing suitable representatives were maintained, then the corresponding text will not be repeated in this section.

4.4.2.1. Flow Cytometry

In order to evaluate T cell subpopulations and NK cells infiltrated in tumours studied, tissue disaggregation and staining procedures were carried out following protocols from the facility *Servei de Cultius Cel·lulars, Producció d'Anticossos i Citometria (Universitat Autònoma de Barcelona)* under their advice and supervision, as follows:

A. Tumour disaggregation

A mechanical disaggregation was performed with scissors or scalpel to make small cuts on tumours in a 6 cm Petri dish. Then, further mechanical disaggregation was performed with a homogenizer (Labbox, Barcelona, Spain), with 1 ml of RPMI medium (Gibco, ThermoFisher, Spain) added. Cells were transferred to a 50 ml tube with a cell strainer to collect the cells and remove tumour debris. Petri dish was washed with RPMI to collect the residual cells with the needed volume to have a final volume of 10 ml medium in the tube. The tube was centrifuged at 400 x g for 5 minutes. After that, 5 ml of 0.17 M ammonium chloride solution were added to this tube for erythrocyte lysis and let sit for 5 minutes. After this time, 5 ml of RPMI were added and the tube was centrifuged at 400 x g for 5 minutes. The supernatant was discarded, and sediment was resuspended with 5 ml of RPMI and cells counted. For cell counting, a 1/100 dilution was made (10 µl of cells in 490 µl of RPMI, and, from there, making an additional 1:2 dilution with trypan blue). After counting, the suspension was adjusted to 1 million living cells / tube, in a final volume of 50 µl. The list of antibodies used for staining different cell populations can be found in Table 4.4.

Antibody	Reference		Provider
CD3	APC-Cy7 Hamster anti-mouse CD3e	561042	Becton Dickinson
CD4	PE Rat Anti-mouse CD4	561829	Becton Dickinson
CD8	FITC Rat Anti-mouse CD8a	553030	Becton Dickinson
CD49b	APC Rat anti-mouse CD49b	560628	Becton Dickinson
FoxP3	Alexa Fluor488 Rat anti-mouse Foxp3	560407	Becton Dickinson
FoxP3 Buffer	Mouse Foxp3 Buffer Set	560409	Becton Dickinson

Table 4.4. List of antibodies used for different cell populations staining.

B. Staining

B.1. Membrane staining: CD3, CD4, CD8, CD49b

For membrane staining, cytometer settings were optimized preparing 6 cytometry tubes with 50 µl of the cell suspension and the required amount of antibody as detailed in Table 4.5. The incubation was performed for 30 minutes in the dark. Then, 500 µl of PBS were added and solution centrifuged at 400 x g for 5 minutes. The supernatant was discarded and paraformaldehyde (0.4%) added. Suspension was stored at 4°C until acquisition by cytometer.

	Control	CD3	CD4	CD8	CD49b	CD3/CD4/CD8/CD49b
Cells (µl)	50	50	50	50	50	50
Antibody (µl)	0	2.5	2.5	1	2.5	2.5/2.5/1/2.5
PBS (µl)	50	47.5	47.5	49	47.5	41.5

Table 4.5. Solutions used for membrane staining.

B.2. Intracellular staining: Foxp3

For intracellular staining, 5 cytometry tubes were prepared with 50 µl of the cell suspension. Tubes were marked and the required amount of antibody was added (all steps are summarized in Table 4.6). The suspension was incubated for 30 minutes in the dark. After that, 1000 µl of PBS were added and the suspension centrifuged at 400 x g for 5 minutes. Supernatant was discarded and cells were fixed through addition of 2 ml of Foxp3 Fixation Mouse, previously diluted and stirred. The suspension was mixed and left for 30 minutes at 4 °C in the dark. Then, suspension was centrifuged at 400 x g for 5 minutes and fixation solution removed. Cells were washed, resuspending each pellet in 1 ml of FoxP3 Mouse permeabilization buffer, and stirring. The suspension was left for 30 minutes at 37 °C in the dark. After 30 minutes, suspension was centrifuged at 400 x g for 5 minutes and the permeabilizer was removed. Then 1 ml of PBS was added, and suspension centrifuged again at 400 x g for 5 minutes. FoxP3 antibody was added to the corresponding tube and shaken. Suspension was incubated for 20 minutes at room temperature and dark. After that, 1 ml of PBS was added, mixed and suspension centrifuged at 400 x g for 5 minutes and this step was repeated one more time. Finally, 0.5 ml of PBS was used

for resuspension and analysis was either performed immediately or suspension stored at 4 °C until acquisition at the cytometer.

	Control	CD3	CD4	Foxp3	CD3/CD4/Foxp3
Cells (µl)	50	50	50	50	50
CD3 or CD4 Antibody (µl)	0	2.5	2.5	-	2.5/2.5/-
PBS (µl)	50	47.5	47.5	50	45
30' Incubation at dark					
PBS (µl)	1000	1000	1000	1000	1000
Centrifugation 400xg 5' – discard supernatant					
Foxp3 Fixation mouse (µl)	2000	2000	2000	2000	2000
30' Incubation at 4°C and dark – Centrifugation 400xg 5' – discard supernatant					
Foxp3 Mouse permeabilization buffer (µl)	1000	1000	1000	1000	1000
30' Incubation at 37°C and dark – Centrifugation 400xg 5' – discard supernatant					
PBS (µl)	1000	1000	1000	1000	1000
Centrifugation 400xg 5'					
Foxp3 antibody	-	-	-	2.5	2.5
PBS (µl)	50	50	50	47.5	47.5
20' Incubation at room temperature and dark					
PBS (µl)	1000	1000	1000	1000	1000
Centrifugation 400xg 5'					
PBS (µl)	500	500	500	500	500
Store at 4°C until acquisition					

Table 4.6. Summary of the experimental procedure for intracellular Foxp3 staining.

C. Data acquisition

The acquisition was carried out by *Servei de Cultius Cel·lulars, Producció d'Anticossos i Citometria* experts using a BD FACSCanto flow cytometer (BD Biosciences, San Jose, CA) equipped with a solid-state blue laser (488 nm) and a He-Ne red laser (633nm).

The lymphocyte-like cell population was first selected by side scatters area (SSC-A, depends on cell structure) and forward scatters area (FSC-A, depends on cell size), and then by FSC-A and forward scatters height (FSC-H) to discard aggregates.

- In membrane marker analysis, T cells and NK cells were selected in a plot of CD3-allophycocyanin (APC)-Cy7 versus NK1-APC. From the CD3+ population, we selected CD4+ and CD8+ T cells in a plot of CD4-PE versus CD8-FITC (Figure 4.10).
- In intracellular marker analysis, Fox-P3-FITC positive cells were selected from CD3+/CD4+ population (Figure 4.11).

FITC and PE fluorescence were excited with the blue laser and emissions were measured with 530/30BP and 585/42BP filter equipped detectors, respectively. APC and APC-Cy7

fluorescence were excited with the red laser and emission measured with 660/20BP and 780/60BP filter equipped detectors, respectively.

Positive gates were set with negative controls. In all samples, more than 20,000 living cells were acquired. Data were analysed with the BD FACSDiva v5.0 and FlowJo v10.6.2 software.

D. <u>Cell counting</u>

In order to analyse the different subpopulations of T cells, the percentage of each cell type was determined and reported as a percentage of the parent cell type (for example, a cytotoxic T- cell should display both CD3 and CD8 positive staining). Cell size and cell morphology (shape and structure) were considered for selecting the group of cells compatible with lymphocytes and NK, as shown in Figure 4.10 and Figure 4.11.
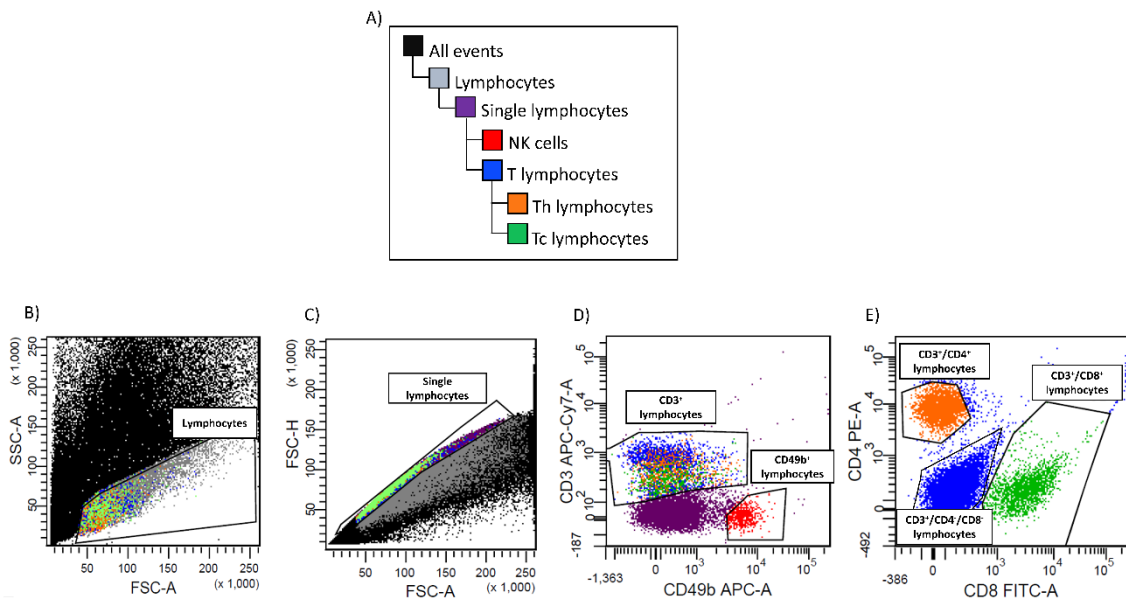
Figure 4.10. Map illustrating colour-coded cell populations clustered based on cell marker expression, representing data from a tumour sample stained for CD3, CD4, CD8 and CD49b. SSC abbreviation represents side scatters (depends on cell structure) and FSC abbreviation represents forward scatters (depends on cell size). The tissue illustrated was obtained from the IMS-vehicle-treated (control) case C1623. A) Coloured schematic overview of the different events detected by flow cytometry. B) All events were detected and plotted according to their SSC and FSC. C) All single cells with lymphocyte-like SSC and FSC were selected. D) Total T lymphocytes (CD3+ cells, dark blue, green, and orange) and NK cells (CD49b+ cells, red), E) Th lymphocytes (CD4+ cells, orange), Tc lymphocytes (CD8+ cells, green), and double-negative (DN) lymphocytes (CD3+/CD4-/CD8- cells, dark blue) were selected according to the marker expression.

C1612
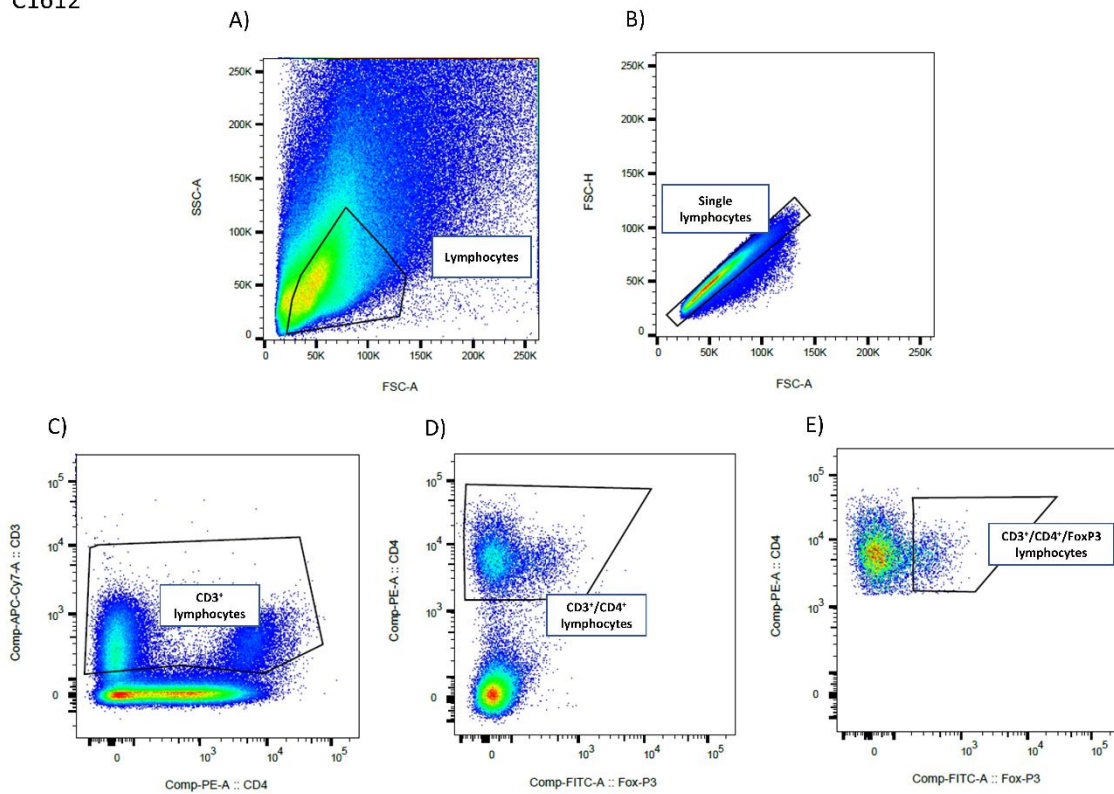
Figure 4.11. Map illustrating colour-coded cell populations that clustered based on cell marker expression, representing data from a tumour sample stained with CD3, CD4 and FoxP3 recognition. The tissue was obtained from the IMS-TMZ-treated case C1612. *A) All events were detected and plotted according to their SSC and FSC. B) All single cells with lymphocyte-like SSC and FSC were selected. C) Total $CD3^+$ T lymphocytes were taken according to their marker expression. D) Considering total T lymphocytes, Th lymphocytes ($CD3^+/CD4^+$) were selected. E) Lastly, Treg lymphocytes ($CD3^+/CD4^+/FoxP3^+$) were selected from the $CD3^+/CD4^+$ T lymphocyte population.*

4.4.3. Results

4.4.3.1. Follow up of GL261 tumour-bearing mice and endpoint criteria

In vivo MRI and MRSI studies were performed in all mice (n=7). Tumour volume was followed up by MRI, and MRSI acquisitions were carried out in order to measure the extent of response to treatment using the obtained nosological images, as explained in Chapters I and II. Extreme values for TRI were searched for, as well as homogeneous response levels, avoiding heterogeneous samples as much as possible.

- In all responding IMS-TMZ-treated mice (n=5), the tumour volume met criteria for "stable disease" according to RECIST [187] as described in adapted form in [50]. The time point chosen for TMZ-treated mice was when TRI values were equal or higher than 60%. Thus, average TRI values were 69.30 ± 11.43 %.
- In all vehicle-treated mice (n=2), tumour volumes increased fast and a TRI=0% (or as close as possible) was searched for. Thus, average TRI values were 5.28 ± 7.47 %.

The average tumour volume at therapy starting point (day 11 p.i.) was 17.4 ± 10.7 mm³ for responding IMS-TMZ-treated mice and 13.2 ± 7.5 mm³ for IMS-vehicle-treated mice, with no significant differences between groups[3]. At chosen time points, mice were euthanised by cervical dislocation, brain was removed, and tumour was resected. The average tumour volume at euthanasia was 94.7 ± 57.7 mm³, at day 23.2 ± 0.4 p.i., for responding IMS-TMZ-treated mice, and 88.3 ± 41.4 mm³, at day 16.0 ± 0.0 p.i., for IMS-vehicle treated (control) mice, with no significant differences with respect to the tumour volume between groups. All collected samples are described in Table 4.7 and tumour volume evolution is shown in Figure 4.12.

Group	Case	Tumour volume at therapy start point (mm³)	Tumour volume at endpoint (mm³)	Euthanasia (day p.i.)	TRI (%)
IMS-TMZ	C1606	14.2	83.7	23	64.7
	C1607	7.4	52.2	23	73.6
	C1610	31.8	136.7	23	60.0
	C1612	25.1	169.6	23	87.3
	C1615	8.5	31.5	24	60.9
IMS-vehicle	C1620	18.5	117.6	16	10.6
	C1622	7.9	59.1	16	0.0

Table 4.7. Description of responding IMS-TMZ (n=5) and IMS-vehicle treated mice (n=2), including tumour volume at therapy start point and at endpoint, euthanasia day and percentage of TRI shown at that time.
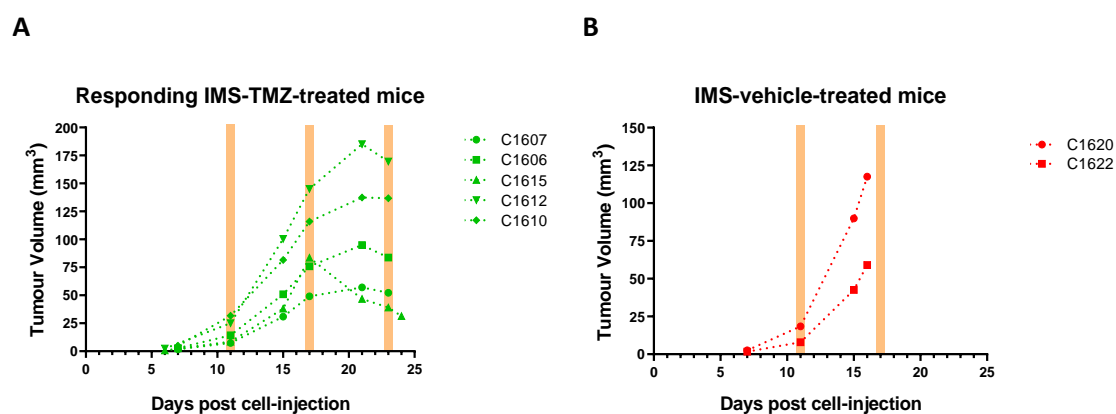
Figure 4.12. Tumour volume evolution (in mm³) of A) responding IMS-TMZ-treated mice (n=5) and B) IMS-vehicle-treated (control) mice (n=2). In all responding cases, tumour volumes were in growth arrest, while in all control cases, tumour volumes increased fast with no sign of growth arrest.

---

[3] Since flow cytometry procedures required considerable sample volume for rendering enough cells for analyses, the described tumours presented volumes significantly higher than volumes described in chapters I, II and III. This does not preclude that criteria for MRI and MRSI features were maintained and coherent along chapters.

4.4.3.2. Evaluating the different T cells subpopulations in responding IMS-TMZ-treated and vehicle-treated tumours

Total living cells were calculated through the cell viability estimated with trypan blue staining, while different T lymphocytes subpopulations were quantified considering $CD3^+/CD4^+/CD8^-$ as Th cells, $CD3^+/CD8^+/CD4^-$ as Tc cells, and $CD3^+CD4^+FoxP3^+$ as Treg cells.

Results showed non-significant differences in the number of living cells within the tumours between responding IMS-TMZ-treated samples and IMS-vehicle-treated (control) samples (p = 0.6190), with high dispersion of the values in both groups (Figure 4.13 A), ranging 72.0 - 95.2%. Furthermore, based on the combinations of surface markers, our flow cytometry results suggest that IMS-TMZ-treated tumours have a higher percentage of Th cells and Tc cells (with respect to $CD3^+$ parent cells) in comparison with control tumours (Figure 4.13 B, C). No significant differences were found (p = 0.0952 for both comparisons), although there was a trend to significance. Concerning to Treg cells, results point to similar infiltration of $CD3^+/CD4^+/FoxP3^+$ cells (with respect to $CD3^+/CD4^+$ parent cells) in both IMS-TMZ-treated and control tumours. No significant differences were found (p = 0.8571) for this comparison, probably due to considerable dispersion in the IMS-TMZ treated group (Figure 4.13 D).
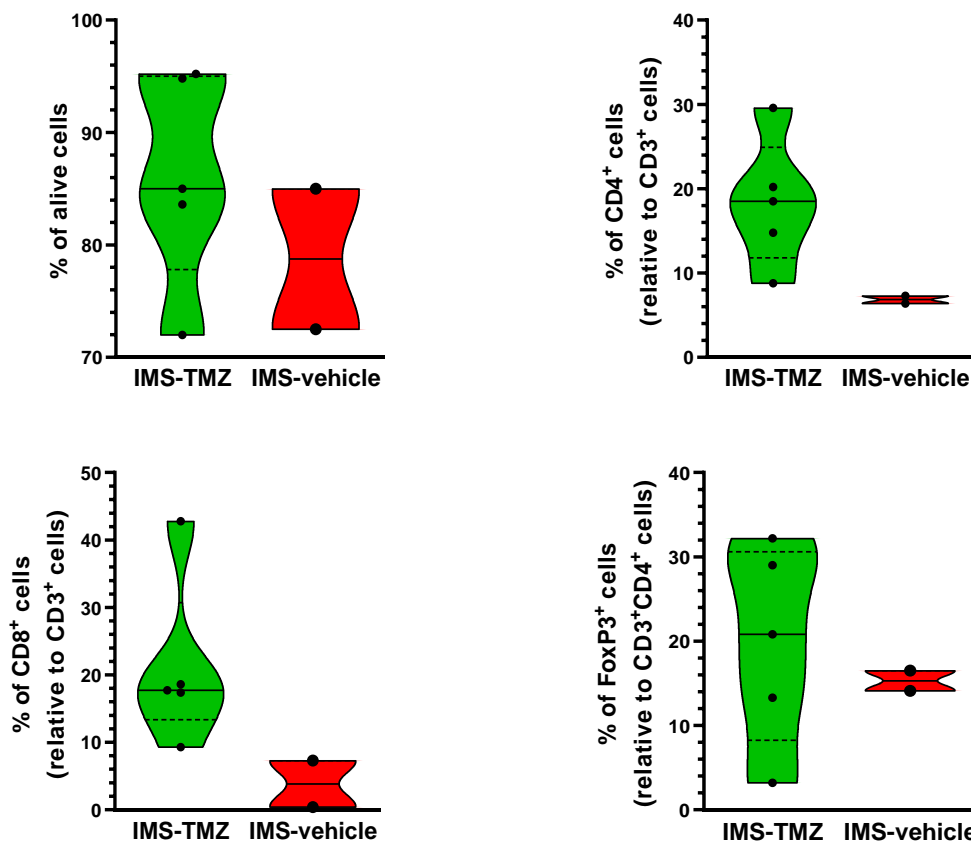
Figure 4.13. Violin plot for percentages of total alive cells, Th cells, Tc cells and Treg cells detected in IMS-TMZ-treated tumours (n=5) and IMS-vehicle-treated (control) tumours (n=2) by flow cytometry. A) Differences in the percentage of living cells detected by trypan blue test were non-significant (p = 0.6190) when comparing IMS-TMZ-treated tumours (89.1 ± 9.5 % of total cells) with vehicle-treated tumours (78.8 ± 8.8 % of total cells). B) Percentage of Th cells (CD3+/CD4+/CD8- cells with regard to CD3+ parent cells). There was a 2.7-fold increase between IMS-TMZ-treated compared to control tumours (18.4 ± 7.6 % vs. 6.9 ± 0.6 %, respectively), p = 0.0952. C) Percentage of Tc cells (CD3+/CD8+/CD4- cells with regard to CD3+ parent cells). There was a 5.5-fold increase between IMS-TMZ-treated and control tumours (21.2 ± 12.7 % vs. 3.9 ± 4.9 %, respectively). Differences were non-significant (p = 0.0952). The non-significance of the differences related to Th and Tc lymphocytes (close to tendency for significance (0.05 < p < 0.1)) is possibly due to the still low number of control mice analysed (n=2). D) Percentages of Treg cells (CD3+/CD4+/FoxP3+ cells with regard to CD3+/CD4+ parent cells). No significant differences were found (p = 0.8571) between IMS-TMZ-treated and control tumours (19.7 ± 11.8 % vs 15.3 ± 1.7 %, respectively). Data are mean ± SD. Explanations for violin plots as in Figure 2 of Chapter II. Note that graphs are shown in different "y" scaling for better appreciation of data distribution.

4.4.3.3. Evaluating the presence of NK cells in responding IMS-TMZ-treated and vehicle-treated tumours

Total NK were studied by flow cytometry considering the marker CD49b (with respect to total lymphocytes). The average values were similar for both IMS-TMZ-treated and vehicle-treated (control) tumours (Figure 4.14), respectively, 4.9 ± 1.7 % and 5.6 ± 0.4 % of total lymphocyte-like cells (p = 0.9524).
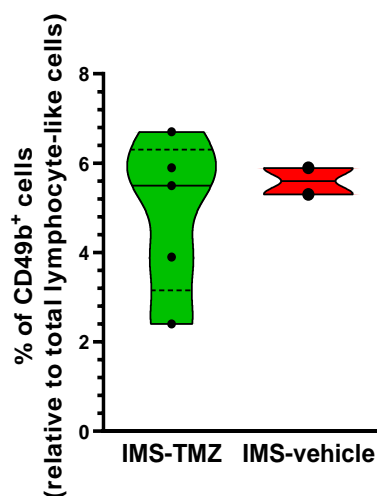
Figure 4.14. Violin plot for percentages of total NK cells (with regard to the total lymphocyte-like cells) by flow cytometry. No significant differences were found (p = 0.9524) between IMS-TMZ-treated tumours (n=5, 4.9 ± 1.7 % of total lymphocyte-like cells) and vehicle-treated (control) tumours (n=2, 5.6 ± 0.4 % of total lymphocyte-like cells). Data are mean ± SD. Explanations for violin plots as in Figure 2 of Chapter II.

Until enlarging the studied cohort to have higher numbers in both groups, drawing a "division line" between groups may be difficult. Moreover, the dispersion of some values can further blur this separation. Then, we have chosen two representative cases (one IMS-TMZ treated responding and one control) for further discussing the reported results. These cases were chosen since they showed the respectively larger measurable decrease or increase in tumour volumes compared to the previous day of measurement (-32.6% and +38.8%, respectively). Furthermore, from our experience, the volume evolution of C1615 showed a behaviour that would probably derive in a resolution/cure of the tumour if mouse was not euthanized for flow cytometry studies. The TRI for the selected cases was above 60% in the responding case, and 0% in the control case (Table 4.7). See also Figure 4.12 for tumour volume evolution of the selected cases. These cases would probably represent the extreme situations, especially regarding the responding case. The summary of results is shown in Table 4.8 below:

Case	Group	TRI	Th	Tc	Treg	NK
C1615	IMS-TMZ treated, responding	60.9%	20.2%	42.8%	3.2%	6.7%
C1622	IMS-vehicle treated, control	0.0%	7.3%	0.4%	14.1%	5.3%

Table 4.8. Flow cytometry individual values obtained for two representative cases.

The C1615 tumour (IMS-TMZ treated) showed a percentage of 20.2% for Th cells, 42.8% for Tc cells, and 3.2% for Treg cells, while the control tumour C1622 showed a percentage of 7.3% for Th cells, 0.4% for T cells, and 14.1% for Treg cells. This means a 2.8-fold increase for Th cells, a 107-fold increase for Tc cells, and a 4.4-fold decrease for Treg cells infiltrated in the tumour responding to therapy when compared to the control tumour. Regarding NK cells, we observed 6.7% for the treated responding case and a 5.3% for the control case, with a 1.3-fold increase.

4.4.4. Discussion

In this Chapter, we aimed to go a step beyond in our characterization of the tumour-associated microenvironment in response to IMS-TMZ therapy, guided by the MRSI-based nosological image. Then, samples from mice bearing tumours meeting MRI/MRSI criteria for responding (n=5) and control (n=2) groups were chosen for flow cytometry validation. Our purpose was to characterise the different subpopulations of T cells and the NK cells infiltrated into tumours, since the interplay between the tumour and its microenvironment is a dynamic process that strongly influences the progression and the outcome of several cancers, including GB [245].

It is currently widely accepted that successful antitumour immune response requires the presence and activation of components of the adaptative and innate immune system. Infiltrating immune cells can have different roles, from antitumour to immunosuppression, depending on

the cellular component involved. For example, Tc and Th lymphocytes are generally associated with favourable anti-tumour immune responses, while immunosuppressive effects are triggered by Treg lymphocytes. Thus, yet it is true that we have already described a significant increase in CD3$^+$ positively stained cells (a general marker for lymphocytes) in TMZ-treated responding samples [246], we wanted to investigate the distribution of different subsets comprised within the CD3$^+$ family. Accordingly, changes in the balance of different cell subsets would dramatically change outcome of tumours. It is also known that many tumours are associated with tertiary lymphoid structures, which have been observed near zones of infection and tumours [247]. Those are organized structures where immune system cells interact and activate each other, promoting a local sustained immune response. Indeed, the prognostic value associated to the presence of tumour-infiltrating lymphocytes has been described for breast cancer [248–250], pancreatic cancer [251], ovarian cancer [252], colorectal cancer [253], hepatocellular carcinoma [254] and melanoma [249], as well as high-grade glial tumours [255]. Results shown in this chapter IV work are in line with has been described in the literature, since responding IMS-TMZ-treated tumours increased the infiltrating Th and Tc subpopulation when compared to control tumours.

In our case, we were interested in checking whether our therapeutic strategy could increase (or modify population subsets) tumour infiltrating lymphocytes and whether the resulting effect would also match our MRSI-based biomarker. The results showed that, after sample disaggregation and preparation, the percentage of living cells was not significantly different between IMS-TMZ-treated tumours and control tumours (Figure 4.13 A) (p = 0.6190). Furthermore, values presented considerable dispersion in both groups. The IMS-TMZ treated responding tumours were experiencing a decrease in their tumour volume; some tumour cells are supposed to be in the process of damage/death due to efficient host immune system action. In this sense, cell debris belonging to dead tumour cells would be probably lost in the preparation steps (section 4.4.2.1 A). Moreover, in order to clarify the distribution of different T cell subsets within tumour tissue, here we have analysed the presence of helper, cytotoxic and regulatory T cells. Th and Tc lymphocytes are distinguished by their mutually exclusive expression of CD4 or CD8 co-receptors [256] while regulatory lymphocytes are characterized to be CD4$^+$, and recognized by the factor FoxP3 [243]. In the studies presented in this chapter, IMS-TMZ-treated responding tumours presented 2.7-fold increase of Th cells, combined with a 5.5-fold increase of Tc cells in comparison to control tumours (Figure 4.13 B, C, p = 0.0952 for both comparisons), showing a trend to significance. Increasing the number of cases in the control group may help to achieve significance in the future, but with the present results, the trend to increased lymphocyte infiltration triggered by IMS-TMZ chemotherapy is clear.

This agrees with changes in lymphocyte subpopulations after different therapeutic strategies described by other authors. For example, Dieci et al. [257] observed that lymphocyte infiltration after neoadjuvant chemotherapy in breast cancer correlated with better prognosis. This was also true for colorectal cancer, in which Matsutani et al. showed that the density of

CD8$^+$ cells attracted after neoadjuvant therapy (chemotherapy or chemo-radiotherapy) correlated positively with treatment efficacy [188]. In preclinical settings, an increase in tumour-infiltrating lymphocytes was also seen in GL261 GB combined treatment with TMZ and anti-PD-1 [258].

Still regarding lymphocytes, we cannot ignore that Figure 4.10 shows a relevant number of CD3$^+$ cells which do not seem to express neither CD8$^+$ not CD4$^+$ in their surface (double-negative, DN). The typology of such cells is unclear in this context and further studies may be needed to clarify their roles or origins. The existence of DN cells is described in the literature [259], and they can bear dual identity i.e. proinflammatory or immunosuppressive phenotype. The DN cells were described to inhibit cell proliferation and invasion when co-cultured with human pancreatic cancer cells. However, only a small fraction of cells matching this profile would be expected, and the relevant fraction found in this thesis will warrant further investigation.

Regarding NK cells, they are described to be crucial for the early phases of tumourigenesis. Since they represent a small proportion of the immune infiltrate, its prognostic value is limited compared to Tc and Th cells [260]. Our results show a slight decrease in the average amount of NK cells in IMS-TMZ treated mice in comparison with control mice, although a large value dispersion in the responding group prevented us to reach a conclusion about a clear trend during treatment/response. Still, as mentioned for lymphocytes, relative variation can be found depending on the euthanasia day in GL261 control mice [114].

High dose and/or dose intense chemo/radiotherapy resulting in toxic effects for the host immune system may lead to a failed resolution of the cancer treatment. In this sense, it has been demonstrated that TMZ and other alkylating agents in clinically relevant dosages promote a decrease in lymphocytes and qualitative dysfunction of T cells in melanoma and GB murine models [170]. Moreover, TMZ used at 50mg/Kg 5 days in a row in preclinical glioma models induced upregulation of markers of T-cell exhaustion such Lymphocyte Activating 3 or T cell immunoglobulin and mucin domain-containing protein 3, which was not seen with temozolomide in metronomic dose [261]. Overall, the actual landscape and data published suggest that some point has been missing in clinical settings, and the protocols currently used are counteracting in host immune system action, probably preventing to get better outcomes in GB patients.

Our immune-respectful IMS-TMZ every-6-day administration protocol showed, in this sense, the ability to bring together the beneficial effects of TMZ while avoiding the undesired consequences of continuous administration. This protocol was even able to cure GL261 GB bearing mice (Section 4, Chapter I), which was not possible in our hands with the original "5-2-2" protocol [49,50,60]. The 6–day-repeating chemotherapeutic schedule had been previously described to be effective against subcutaneous GL261 GB [173], using cyclophosphamide. In this

work from Wu & Waxman, metronomic schedule proved capable to provide balance between tumour cell toxicity while minimizing immune cell ablation without rebound of Tregs or loss of antitumour CD8+ T-cell responses. Ignoring this balance might prevent tumour curation and long-term immune memory mounting and should probably be a take-home message for future clinical improvement.

A word of caution in this sense may be raised regarding the preclinical use of modified cells expressing exogenous genes such as luciferase, which may elicit anti-tumour responses (e.g., increasing CD8$^+$ cells) even in absence of treatment [262], providing overrated responses that will not be translated in the case of immunocompetent preclinical models or human patients.

4.4.5. Conclusions

In this Chapter, we have demonstrated that IMS-TMZ administration was able to trigger changes in local immune system elements within tumours (especially lymphocyte subsets) in samples chosen guided by our MRSI-based biomarker. The main conclusions related to this chapter were as follows:

- Both Tc and Th percentage populations increase in IMS-TMZ treated responding mice, in line with the satisfactory response detected both by volumetric measurements in MRI and Tumour Responding Index calculated with our MRSI-based nosological approaches. We could only achieve a trend to significance, probably due to the still low number of cases analysed.
- Average percentage of Treg cells was also higher in IMS-TMZ treated responding mice, but with considerable data dispersion. This increase was non-significant and warrants further investigation since metronomic therapeutic schedules were described to rather decrease the number of functional Tregs.
- Natural Killer cells, in the same line of Tregs, showed an opposed trend, with slightly higher average values in control samples when compared with IMS-TMZ treated samples. Variations due to euthanasia day cannot be discarded and this should be further investigated for all immune cell types.
- The existence of a double-negative population (CD3$^+$/CD8$^-$/CD4$^-$) is worth of further investigation since their percentage over the CD3$^+$ population might not be neglected, and the described role for DNs in literature is ambiguous.

5. GENERAL DISCUSSION

Glioblastomas are the most common and fatal malignant primary brain tumours in adults. Despite aggressive therapy based on maximal safe resection, followed by radio and chemotherapy and adjuvant chemotherapy with temozolomide, the outcome of GB patients remains poor, with a median survival of fewer than 15 months. Second-line or alternative treatments being tested (e.g., immunotherapy, antiangiogenic treatment, targeted therapy and combination regimens) are not significantly improving therapeutic outcome, having only discrete effects, thus clinical guidelines have not changed too much since the TMZ advent [263]. Moreover, due to the disease severity and treatment needs (hospitalization, chemo-radiotherapy, and introduction of tailored or new adjuvant therapies), GB patient costs are a burden to the health system [264]. Thus, it seems that two key aspects may be improved in the management of GB patients, which would involve a relief to the health system: the development of therapeutic personalized approaches and the refinement of follow-up protocols.

The standard first-line therapeutic approaches in clinical, with few exceptions, seems to be rooted in the established Stupp guidelines [14,23,265]. Some alternative trials have been done (or are in progress) approaching TMZ metronomic schedules but they are often based in recurrent GB patients, which make things more complex since recurrent patients may have higher mutational loads and developed resistance (e.g. of clinical trials: NCT00501891, NCT02770378 and NCT01308632).

Regarding follow-up approaches, the clinical guidelines for tumour response or progression are mostly focused on anatomical parameters (i.e., imaging), that might lack precision at some early points, precisely in moments in which fast and informed decisions may condition the final GB patient outcome [266]. Monitoring therapy response in GB is generally carried out through non-invasive approaches such as magnetic resonance since it avoids repeated biopsy procedures, which are not exempt of risk. Considering that the participation of the host immune system in response to therapy is currently a well-accepted concept, some approaches have been developed towards imaging local immune system action such as the combination of [^{18}F]FET (detects amino acid metabolism) with [^{18}F]DPA-714 PET (reveals ligands targeting the 18kDa translocator protein in GAMs, tumour cells, astrocytes and endothelial cells) and MRI, together with immune-phenotyping to monitor TMZ treatment response *in vivo* and to analyse possible therapy-induced reactive changes in the TME [195]. This suggests that a combination of PET/MRI would be ideal, but it is unclear whether the best therapeutic approach was launched and/or if this type of approach can be translated as is to the health system. Still, having in mind that the interplay between the tumour and its immune microenvironment is a dynamic process, a non-ionizing imaging method would be preferred in case several sequential explorations would be needed. This would be the ideal case for MRI/MRSI, but not for PET. Other immune-PET approaches have been reported (e.g., PET using Zr-labelled PEGylated single-domain antibody fragments to explore the dynamics and distribution of intratumoural Tc cells and CD11b+

myeloid cells in a colorectal mouse adenocarcinoma model [267]), but none has reached clinics yet. The real challenge associated with the present clinical pipeline follow-up is that a precious time is wasted due to the uncertainty related to the MRI criteria applied for follow-up, and this is relevant for patients' outcome.

It is well known that the MRS(I) local changes can precede MRI anatomical changes in both preclinical and clinical studies. In preclinical settings, our group benefited from MRSI to produce nosological images that monitored the GB response to TMZ [50]. Regarding clinical studies, Jalbert et al. [268] have used anatomic, diffusion, perfusion, and metabolomic MR data to improve clinical assessment for patients with recurrent low-grade glioma. Still, we are also aware that a combination of MRI and MRSI parameters can be combined -or jointly analysed - for even more precise information in brain-related studies (see for example Li et al. [269], where authors combined the biochemical tissue discrimination of MRSI with the high resolution of MRI for brain tumour diagnosis). It is expected that MRSI can help to guide or explain MRI findings and our group has also started to explore this possibility with satisfactory results [270].

Some authors have tried to address this timely need of information during chemoradiotherapy with functional MRI studies in patients [271] obtaining promising results since the technique can differentiate between early treatment responders and non-responders through detection of the tumour biology and vascular state of the tumour microenvironment during therapy. Despite the clear methodological strengths, some limitations may take place since these approaches are based on a voxel-by-voxel analysis to assess per cent of regional changes over time, which requires highly precise image registration and typically exclude voxels that are not present in both the baseline and intra-treatment tumour volumes. In this respect, MRSI can offer an approach capable to be promptly translational and inform about metabolomics changes related to therapy without the need for an initial baseline. These pattern changes have been characterized by our group in preclinical settings although they should be further validated in clinical settings.

In this sense, previous result from our group showed an oscillatory behaviour of the MRSI-based pattern when using the standard three-cycle TMZ administration protocol in GL261 GB tumour-bearing mice [49]. The frequency of these oscillations, reflecting changes in the metabolomic spectral patterns, matches the length of the immune cycle in the mouse brain, described to be of ca 6 days [107]. The presence of host immune system elements is a good prognostic factor for GB outcome, since more cells with ability to start and sustain inflammatory responses infiltrating the tumour means more tumour tissue disruption. In this sense, even RANO criteria for evaluating therapy response has adapted and evolved to an iRANO set of criteria that are based on immune-related response criteria [272].

Immune system activity is not only achieved with novel immunotherapeutic approaches, but this is also a well described effect even under the standard chemo-radiotherapy. In this respect, many authors have described that TMZ presents a potential immunogenic effect [35–

40] since it promotes the release/exposure of immunogenic signals by tumour cells, launching the cancer-immune cycle and leading to tumour cell killing. Although TMZ is the standard chemotherapeutic treatment for GB patients, the overall molecular mechanism underlying its antitumoral effects should be still investigated. The beneficial effect of TMZ in preclinical/clinical settings was traditionally attributed to its cytotoxic effect as a DNA alkylating agent and methylating agent of macromolecules, triggering different modalities of cell death, such as autophagy or apoptosis [31,273]. However, TMZ was described to display a predominantly cytostatic effect, rather than cytotoxic [26,33,40,274] suggesting that other effects beyond the DNA alkylation potential are occurring, thus any transient response may rely on mechanisms different from tumour cell killing. Those effects could be related to TMZ ability to produce immunogenic cell death/damage that leads to a positive outcome in anticancer therapy [35–40]. This means that TMZ does not need to directly kill all tumour cells: eliciting host immune response against neoplastic cells by producing a certain amount of damage in order to trigger release/exposure of DAMPs and attract immune cells within the tumour site would be enough [275–277]. Accordingly, the activation of both innate and adaptative immunity antitumour effects in the host would eventually lead to an efficient response.

Having in mind **a)** previous studies from our group with cultured GL261 GB cells demonstrating that TMZ acts mostly as a cytostatic drug [33], **b)** the role of the TME in the response to therapy (Introduction, section 1.3), especially the host immune system, **c)** the oscillatory behaviour of MRSI-based changes during therapy response in longitudinal studies with TMZ-treated GL261 GB bearing mice [49], matching the length of the immune cycle in mice [107], we defined our main focus in this work. We aimed to confirm the oscillating pattern in GL261 GB treated with immune respectful TMZ cycles. In addition, we devoted efforts to the biological validation of the MRSI-based nosological images during transient/permanent response to TMZ, in order to enhance its potential translation as a surrogate biomarker enabling personalised therapeutic decisions, based on metabolomic information. Considering that spectroscopic information is not straightforward to process and interpret, one of the main challenges for incorporating metabolomics in clinical pipelines as a biomarker is to produce an imaging-like output easy to be understood by radiologists, such as our nosological images of response. However, in addition to producing suitable outputs, metabolomic pattern changes behind those outputs should be characterized and explained in terms of cellular/molecular features.

It is important to bear in mind, while investigating the possible origin of the MRSI-based changes, that MRSI is a volumetric technique. This means that cellular populations significantly contributing to the tumour mass (e.g., tumour cells, macrophages) will be the most determinant in this detected pattern (see Figure 5.1). However, we cannot forget the cell subsets that represent a smaller percentage of the tumour volume, such as lymphocytes, and other influencing factors, such as immunosuppressor proteins or metalloproteases, that have also a

relevant impact on the MRSI observed metabolomic patterns indirectly, since they can affect the whole tumour microenvironment and produce structural changes in tissues.
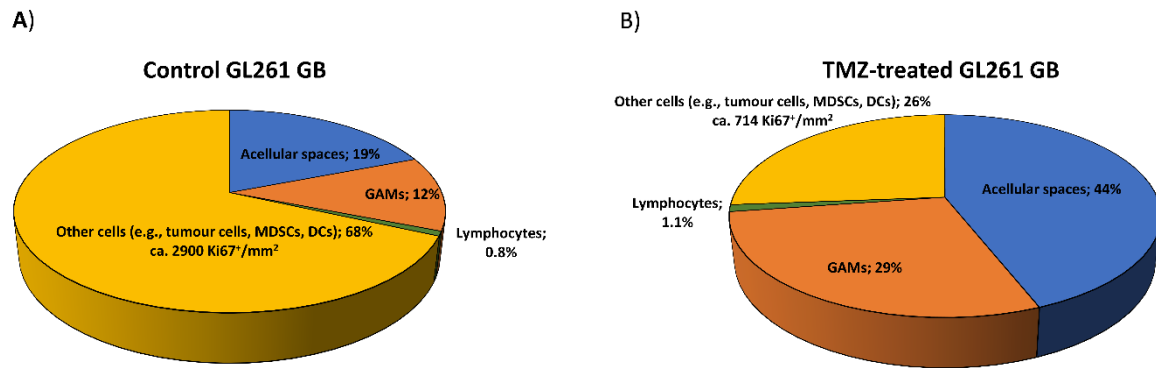
Figure 5.1. Calculated volumetric distribution of different tissular components and acellular spaces in A) Control and B) TMZ-treated, responding, GL261 tumours. The percentage attributed to "other cells" was estimated by difference with other elements. Cases chosen for the "responding" cohort were cases characterized as "high response" from [49]. Data from [49]and unpublished GABRMN calculations.

Host immunity involves several cellular populations and local factors, and the interplay between the tumour and its microenvironment is a dynamic process. One of the main tumour tissue populations is glioma-associated microglia/macrophages, whose M1 GAMs phenotype was linked with a better overall prognosis [199,200,278] while the M2 GAMs phenotype was associated with glioma progression [198] in studies with clinical glioma samples. Another cell component involved in the GB patient prognosis is the lymphocyte population. Tc lymphocytes and Th lymphocytes are generally associated with proinflammatory action, and their presence has been described as a good prognostic factor for high-grade glial tumours [255]. By opposite, Treg lymphocytes play an immunosuppressive role within the tumour site [115]. Regarding NK cells, these lymphocytes are described to be essential for the anti-tumour innate immune response [129]. In addition to cell populations, there are molecules that might regulate the immune system activity, such as the inhibitory immune checkpoint composed by the PD-L1/PD-1 axis, which protects tumour cells and macrophages from being killed by immune system cells [135–137]. It is also important to consider the role of different metalloproteases, responsible for a large number of biological activities associated with the immune system. For example, ADAMs have been described to modulate the activities of membrane cytokines and growth factors, their receptors, and cell adhesion molecules [143], playing a pivotal role in the regulation of tumour proliferation and inflammation [141]. On the other hand, MMPs can modulate various signalling pathways by cleaving cytokines, chemokines and growth factors, acting on cell proliferation, migration, differentiation, apoptosis, angiogenesis, tissue repair, and immune response [157].

Regarding that, first, in Chapter I, we have addressed some basic histopathological studies in GL261 GB bearing-tumour mice treated with TMZ. We found that TMZ-treated tumours showed an increase in the global T lymphocyte population (CD3^{+} stained cells) as well as the area

occupied by microglia/macrophage population (Iba^{+} stained cells) in comparison to untreated samples. Moreover, the MRSI-detected responsive zones could achieve values up to 42% of area occupancy by microglia/macrophages while unresponsive zones could reach values as low as 1.4%. Thereby, we have confirmed that the contribution of microglia/macrophages populations is not negligible at all in tumour environments responding to therapy. Moreover, in Chapter I, we applied in a longitudinal protocol for the noninvasive assessment of therapy response under IMS therapy administration (i.e., the immune system respectful schedule, every 6 days), in order to assess reproducibility of the oscillatory response pattern observed previously. The oscillatory behaviour along the period of the transient response to therapy was fully confirmed. On the opposite, these oscillations decreased or disappear prior to -or during- tumour relapse in IMS-treated cases and were definitely absent in vehicle-treated cases. These results suggest that TMZ administration "resets" the host immune system cycle and the recorded TRI oscillations could be at least partially due to local metabolic changes resulting from the immune system activity within the tumour tissue.

Then, we wanted to gain more insight into this validation. Considering that the GAM population could contribute to the differential metabolomic patterns detected in vivo by MRSI-based analysis in GL261 GB and knowing that this population may present different phenotypic profiles, in Chapter II we have studied samples from GL261 GB-bearing mice treated with IMS-TMZ or IMS-vehicle to characterise the microglia/macrophage population into the tumour site. Despite both treated and control tumours presented relevant GAM content, IMS-TMZ-treated tumours responding to therapy showed a significantly higher global GAM population. Moreover, a significantly higher ratio of M1/M2 GAM content was found in IMS-TMZ-treated samples. These findings, added to the fact that the different microglia/macrophage phenotypes use different metabolic pathways [201,279], suggest that the GAM population is a suitable candidate to be at least partially responsible for the MRSI-detected spectral pattern changes.

Having in mind other different host immune system elements and to better characterize contribution to responding and control samples, in Chapter IV we have analysed the different subpopulations of T lymphocytes within tumours responding to IMS-TMZ therapy and IMS-vehicle treated. We found that responding IMS-TMZ-treated tumour samples increased the infiltrating Th and Tc subpopulation when compared to control tumours. Although lymphocytes would represent only a small fraction of the GB mass volume (ca 1% in GL261 GB, unpublished GABRMN data) and may not have a direct impact on spectral pattern changes observed by MRSI, they can indeed affect other populations that certainly represent a high volume of the tumour, such as tumour cells or GAMs. Then, we need to achieve a global view about immune system-related changes during response to therapy that overall, can help to explain the MRSI-based pattern changes recorded.

Since the PD-L1/PD-1 axis can also modulate the TME, contributing indirectly to the detected metabolomic changes, in Chapter II we have analysed the PD-L1 gene expression in

IMS-TMZ-treated and vehicle-treated GL261 GB groups. We found a significantly higher PD-L1 gene expression in responding IMS-TMZ-treated tumours compared to tumours treated with vehicle. Moreover, a significant positive correlation was found between PD-L1 gene expression level and the M1/M2 ratio, which points that increased PD-L1 content could be associated with an increased M1-polarised GAM population. It has been described that PD-L1 can be expressed by macrophages [280], exerting a protective effect during the interaction between the macrophage presenting tumour antigen and the effector T cell [212]. In this way, PD-L1 would prevent macrophages from being killed by T cells, thereby contributing to the increased GAM population, especially to the M1 subpopulation. This would be mirrored in the MRSI-observed spectral pattern.

Regarding different metalloproteases, in Chapter III we have evaluated the molecular profiles of ADAM8, ADAM10, ADAM17, MMP9 and MMP14 genes, and their association with GAM population and PD-L1 gene. Our findings revealed an increased expression level of ADAM8, ADAM10, ADAM17 and MMP14 genes in the IMS-TMZ responding group in comparison with control tumours. Moreover, these gene expression levels were found positively correlated to the global GAM population and PD-L1 gene expression. ADAM8, ADAM10, ADAM17 and MMP14 could have a relevant impact on the MRSI observed metabolomic patterns since they influence other immune system cells. Namely, it has been described that

a) ADAM8 is expressed in monocytes [145],
b) ADAM10 may contribute to the Th cell proliferation/differentiation with consequent M1 GAMs stimulation [118],
c) ADAM17 plays a role in macrophage proliferation [154,156] and differentiation of T lymphocyte toward Th cells [118], stimulating indirectly the polarisation of GAMs towards the M1 phenotype to exert an antitumour effect,
d) MMP14 promotes monocyte migration to the tumour site [228,229] and could be related to the macrophage polarization toward a proinflammatory phenotype [230].

Furthermore, in Chapter III we have also approached the global GAM population, its different subtypes, and the PD-L1, ADAM8, ADAM10, ADAM17, MMP9 and MMP14 gene expression level in tumours that relapsed or were unresponsive to the IMS-TMZ treatment. These groups showed the same trend as control tumours for all parameters evaluated, except for MMP9 (described to limit antitumor response [225]), which was found to increase in non-responding IMS-TMZ-treated tumours. These results discard that the TMZ treatment was the direct cause for the gene expression levels found in responding IMS-TMZ-treated tumours, and the determinant for changes in expression levels seem to be efficient host immune response against tumour cells.

Examining altogether, our data (main findings summarised in Figure 5.2) supports that the MRSI-observed spectral patterns in tumours that efficiently responded to therapy (i.e., the green pattern in nosological images) can be correlated with an effective activation of different

host immune system elements against the tumour, while MRSI-observed spectral patterns in control tumours (i.e., the red nosological images) can be associated to a lower extent of local immune action, observed in a basal way and which could take place in tumours with considerable immunogenic capacity such as GL261 [281].
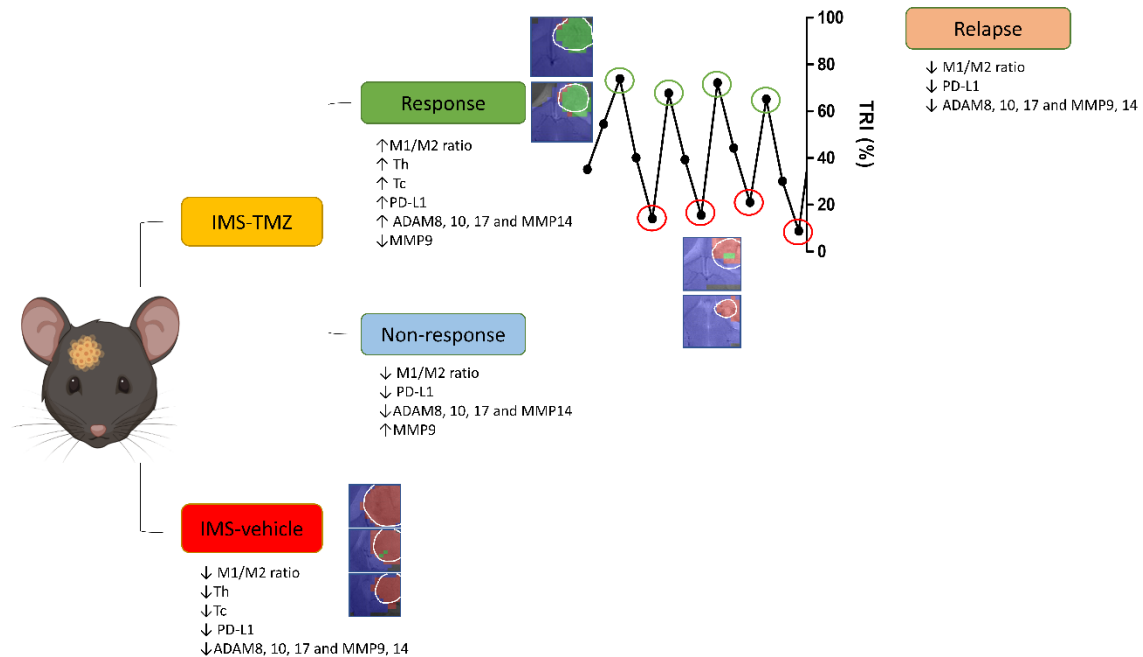
Figure 5.2. Summary of the results obtained in this thesis. *We found an increase of M1/M2 GAMs ratio, an overall increase in the number of Th and Tc lymphocytes, as well as a high expression level of PD-L1, ADAM8, ADAM10, ADAM17 and MMP14 genes in tumours responding to IMS-TMZ treatment, at the peak response positions (green ovals, oscillating with a circaseptan period [282]). The M1/M2 ratio, as well as the expression level of PD-L1, ADAM8, ADAM10, ADAM17, MMP9 and MMP14 genes, were found to be decreased in "valley" timepoints during response, in those tumours that had transiently responded to therapy and subsequently, escaped from therapy (red ovals). The same expression profile was observed for non-responding IMS-TMZ-treated tumours, except for the metalloprotease gene MMP9, which was found highly expressed in this group. On the other hand, IMS-vehicle-treated tumours showed lower M1/M2 GAMs ratio, an overall decrease in the number of Th and Tc cells and a lower expression level of PD-L1, ADAM8, ADAM10, ADAM17, MMP9 and MMP14 genes. These results point to a suitable immune system action in tumours showing a transient response to therapy while this action is no longer able to control tumour cell growth in relapsing tumours. In non-responding and control tumours, the immune system is not sufficiently active against tumour cells.*

However, in order to advance towards a possible proposal of the surrogate biomarker for a clinical use, a larger validation will be required. It is worth investigating a) the origin of the reported PD-L1 gene expression level, b) the unclear role of double-negative CD3^{+} cells, c) the activation/exhaustion state of the host immune system cells and their different subtypes, and, finally, d) how those changes overall impact the MRSI-based biomarker. Furthermore, mice cohorts need to be enlarged to confirm some of our findings which are based in a still low number of subjects. It will be also relevant to elucidate the immune system local changes taking place in IMS-TMZ-treated tumours when they enter an oscillation "valley", i.e., low TRI values after a peak response, meaning that the MRSI-based spectral pattern was found to correlate to the equivalent, metabolomically, to non-responding tissue. These aspects and the study of other preclinical models, such as the CT-2A or SB28 GB models, will be the subject of future PhD thesis

in our group. Another subject of possible study would be the differences and similarities between preclinical GB and human GB (e.g., the mutational load of GL261 [61] is much higher than an untreated human GB [62], which could trigger by itself a differential stimulation of the host immune system. Finally, we are aware that a translational proposal of our biomarker including long and repeated MRSI explorations in patients, followed by validation, would not be easy/feasible. Currently, this is only feasible in preclinical models. In order to propose a translational protocol, more information will be needed regarding the minimum number of explorations and whether this could be translated into an imaging protocol in methodological strategies such as radiomics, provided they were suitably guided and trained from metabolomics approaches. We are confident that our method would be able to provide early and confident information about sustained host antitumour immune system, which cannot be spotted by any current non-invasive imaging technique, and then, readily translatable into clinics.

6. GENERAL CONCLUSION

We have observed in the immunocompetent GL261 GB preclinical model that an immune respectful administration schedule may not only improve survival, but even produce cure in GL261 GB-afflicted mice. Furthermore, the IMS protocol was able to raise strong immune memory effects against new tumour-rechallenges in these cured mice. Moreover, we have explored the tumour immune microenvironment guided by MRSI-based biomarker appearance. Results support the idea that the host immune system activation is closely related to the beneficial outcome reached from IMS-TMZ therapeutic schedules and could at least partially explain spectral pattern changes observed by the MRSI-based biomarker. Further studies will be needed in order to clarify additional molecular/cellular elements explaining the MRSI-based findings, extending the investigation to other preclinical models and therapeutic approaches, in the search for a robust clinical translational proposal.

7.   REFERENCES

1. Global cancer observatory. Available online: https://gco.iarc.fr/.
2. Fitzmaurice, C.; Abate, D.; Abbasi, N.; Abbastabar, H.; Abd-Allah, F.; Abdel-Rahman, O.; Abdelalim, A.; Abdoli, A.; Abdollahpour, I.; Abdulle, A.S.M.; et al. Global, Regional, and National Cancer Incidence, Mortality, Years of Life Lost, Years Lived With Disability, and Disability-Adjusted Life-Years for 29 Cancer Groups, 1990 to 2017. *JAMA Oncol.* **2019**, *5*, 1749–1768, doi:10.1001/jamaoncol.2019.2996.
3. Weller, M.; Wick, W.; Aldape, K.; Brada, M.; Berger, M.; Pfister, S.M.; Nishikawa, R.; Rosenthal, M.; Wen, P.Y.; Stupp, R.; et al. Glioma. *Nat. Rev. Dis. Prim.* **2015**, *1*, 15017, doi:10.1038/nrdp.2015.17.
4. Omuro, A.; DeAngelis, L.M. Glioblastoma and other malignant gliomas: A clinical review. *JAMA - J. Am. Med. Assoc.* **2013**, *310*, 1842–1850, doi:10.1001/jama.2013.280319.
5. Huse, J.T.; Holland, E.C. Targeting brain cancer: Advances in the molecular pathology of malignant glioma and medulloblastoma. *Nat. Rev. Cancer* **2010**, *10*, 319–331, doi:10.1038/nrc2818.
6. World Health Organization WHO Classification of Tumours Editorial Board. Classification of Tumours of the Central Nervous System. In *5th ed. Lyon: International Agency for Research on Cancer*; 2021.
7. Stoyanov, G.S.; Dzhenkov, D.; Ghenev, P.; Iliev, B.; Enchev, Y.; Tonchev, A.B. Cell biology of glioblastoma multiforme: from basic science to diagnosis and treatment. *Med. Oncol.* **2018**, *35*, 27, doi:10.1007/s12032-018-1083-x.
8. Ostrom, Q.T.; Cioffi, G.; Gittleman, H.; Patil, N.; Waite, K.; Kruchko, C.; Barnholtz-Sloan, J.S. CBTRUS Statistical Report: Primary Brain and Other Central Nervous System Tumors Diagnosed in the United States in 2012-2016. *Neuro. Oncol.* **2019**, *21*, V1–V100, doi:10.1093/neuonc/noz150.
9. Louis, D.N.; Perry, A.; Wesseling, P.; Brat, D.J.; Cree, I.A.; Figarella-Branger, D.; Hawkins, C.; Ng, H.K.; Pfister, S.M.; Reifenberger, G.; et al. The 2021 WHO Classification of Tumors of the Central Nervous System: a summary. *Neuro. Oncol.* **2021**, *23*, 1231–1251, doi:10.1093/neuonc/noab106.
10. Tan, A.C.; Ashley, D.M.; López, G.Y.; Malinzak, M.; Friedman, H.S.; Khasraw, M. Management of glioblastoma: State of the art and future directions. *CA. Cancer J. Clin.* **2020**, *70*, 299–312, doi:10.3322/caac.21613.
11. Hanif, F.; Muzaffar, K.; Perveen, K.; Malhi, S.M.; Simjee, S.U. Glioblastoma Multiforme : A Review of its Epidemiology and Pathogenesis through Clinical Presentation and Treatment. *Asian Pac J Cancer Prev.* **2017**, *18*, 3–9, doi:10.22034/APJCP.2017.18.1.3.
12. Tan, A.C.; Ashley, D.M.; López, G.Y.; Malinzak, M.; Friedman, H.S.; Khasraw, M. Management of glioblastoma: State of the art and future directions. *CA. Cancer J. Clin.* **2020**, *70*, 299–312, doi:10.3322/caac.21613.
13. Gilard, V.; Tebani, A.; Dabaj, I.; Laquerrière, A.; Fontanilles, M.; Derrey, S.; Marret, S.; Bekri, S. Diagnosis and Management of Glioblastoma: A Comprehensive Perspective. *J. Pers. Med.* **2021**, *11*, 258, doi:10.3390/jpm11040258.
14. Stupp, R.; Hegi, M.E.; Mason, W.P.; van den Bent, M.J.; Taphoorn, M.J.; Janzer, R.C.; Ludwin, S.K.; Allgeier, A.; Fisher, B.; Belanger, K.; et al. Effects of radiotherapy with concomitant and adjuvant temozolomide versus radiotherapy alone on survival in glioblastoma in a randomised phase III study: 5-year analysis of the EORTC-NCIC trial. *Lancet Oncol.* **2009**, *10*, 459–466, doi:10.1016/S1470-2045(09)70025-7.
15. Karschnia, P.; Vogelbaum, M.A.; van den Bent, M.; Cahill, D.P.; Bello, L.; Narita, Y.; Berger, M.S.; Weller, M.; Tonn, J.C. Evidence-based recommendations on categories for extent of resection in diffuse glioma. *Eur. J. Cancer* **2021**, *149*, 23–33, doi:10.1016/j.ejca.2021.03.002.

16. Mann, J.; Ramakrishna, R.; Magge, R.; Wernicke, A.G. Advances in Radiotherapy for Glioblastoma. *Front. Neurol.* **2018**, *8*, 748, doi:10.3389/fneur.2017.00748.

17. Narayana, A.; Yamada, J.; Berry, S.; Shah, P.; Hunt, M.; Gutin, P.H.; Leibel, S.A. Intensity-modulated radiotherapy in high-grade gliomas: Clinical and dosimetric results. *Int. J. Radiat. Oncol. Biol. Phys.* **2006**, *64*, 892–897, doi:10.1016/j.ijrobp.2005.05.067.

18. Sologuren, I.; Rodríguez-Gallego, C.; Lara, P.C. Immune effects of high dose radiation treatment: Implications of ionizing radiation on the development of bystander and abscopal effects. *Transl. Cancer Res.* **2014**, *3*, 18–31, doi:10.3978/j.issn.2218-676X.2014.02.05.

19. Frey, B.; Rubner, Y.; Kulzer, L.; Werthmöller, N.; Weiss, E.M.; Fietkau, R.; Gaipl, U.S. Antitumor immune responses induced by ionizing irradiation and further immune stimulation. *Cancer Immunol. Immunother.* **2014**, *63*, 29–36, doi:10.1007/s00262-013-1474-y.

20. Baumann, M.; Krause, M.; Thames, H.; Trott, K.; Zips, D. Cancer stem cells and radiotherapy. *Int. J. Radiat. Biol.* **2009**, *85*, 391–402, doi:10.1080/09553000902836404.

21. Olivares-Urbano, M.A.; Griñán-Lisón, C.; Marchal, J.A.; Núñez, M.I. CSC Radioresistance: A Therapeutic Challenge to Improve Radiotherapy Effectiveness in Cancer. *Cells* **2020**, *9*, 1651, doi:10.3390/cells9071651.

22. Ricci, M.S.; Zong, W. Chemotherapeutic Approaches for Targeting Cell Death Pathways. *Oncologist* **2006**, *11*, 342–357, doi:10.1634/theoncologist.11-4-342.

23. Stupp, R.; Brada, M.; van den Bent, M.J.; Tonn, J.-C.; Pentheroudakis, G. High-grade glioma: ESMO Clinical Practice Guidelines for diagnosis, treatment and follow-up. *Ann. Oncol.* **2014**, *21*, iii93–iii101, doi:10.1093/annonc/mdu050.

24. Newlands, E.S.; Stevens, M.F.G.; Wedge, S.R.; Wheelhouse, R.T.; Brock, C. Temozolomide: A review of its discovery, chemical properties, pre-clinical development and clinical trials. *Cancer Treat. Rev.* **1997**, *23*, 35–61, doi:10.1016/S0305-7372(97)90019-0.

25. Villano, J.L.; Seery, T.E.; Bressler, L.R. Temozolomide in malignant gliomas: Current use and future targets. *Cancer Chemother. Pharmacol.* **2009**, *64*, 647–655, doi:10.1007/s00280-009-1050-5.

26. Strobel, H.; Baisch, T.; Fitzel, R.; Schilberg, K.; Siegelin, M.D.; Karpel-Massler, G.; Debatin, K.-M.; Westhoff, M.-A. Temozolomide and Other Alkylating Agents in Glioblastoma Therapy. *Biomedicines* **2019**, *7*, 69, doi:10.3390/biomedicines7030069.

27. Hombach-Klonisch, S.; Mehrpour, M.; Shojaei, S.; Harlos, C.; Pitz, M.; Hamai, A.; Siemianowicz, K.; Likus, W.; Wiechec, E.; Toyota, B.D.; et al. Glioblastoma and chemoresistance to alkylating agents: Involvement of apoptosis, autophagy, and unfolded protein response. *Pharmacol. Ther.* **2018**, *184*, 13–41, doi:10.1016/j.pharmthera.2017.10.017.

28. Zhang, J.; F.G. Stevens, M.; D. Bradshaw, T. Temozolomide: Mechanisms of Action, Repair and Resistance. *Curr. Mol. Pharmacol.* **2012**, *5*, 102–114, doi:10.2174/1874-470211205010102.

29. Hegi, M.E.; Diserens, A.-C.; Gorlia, T.; Hamou, M.-F.; de Tribolet, N.; Weller, M.; Kros, J.M.; Hainfellner, J.A.; Mason, W.; Mariani, L.; et al. MGMT Gene Silencing and Benefit from Temozolomide in Glioblastoma. *N. Engl. J. Med.* **2005**, *352*, 997–1003, doi:10.1056/nejmoa043331.

30. Nassiri, F.; Aldape, K.; Zadeh, G. The multiforme of glioblastoma. *Neuro. Oncol.* **2018**, *20*, 437–438, doi:10.1093/neuonc/noy025.

31. Roos, W.P.; Batista, L.F.Z.; Naumann, S.C.; Wick, W.; Weller, M.; Menck, C.F.M.; Kaina, B. Apoptosis in malignant glioma cells triggered by the temozolomide-induced DNA lesion O6-methylguanine. *Oncogene* **2007**, *26*, 186–197, doi:10.1038/sj.onc.1209785.

32. De Salvo, M.; Maresca, G.; D'agnano, I.; Marchese, R.; Stigliano, A.; Gagliassi, R.; Brunetti, E.; Raza, G.H.; De Paula, U.; Bucci, B. Temozolomide induced c-Myc-mediated apoptosis

via Akt signalling in MGMT expressing glioblastoma cells. *Int. J. Radiat. Biol.* **2011**, *87*, 518–33, doi:10.3109/09553002.2011.556173.

33. Villamañan, L.; Martínez-escardó, L.; Arús, C.; Yuste, V.J.; Candiota, A.P. Successful partnerships: Exploring the potential of immunogenic signals triggered by TMZ, CX-4945, and combined treatment in Gl261 glioblastoma cells. *Int. J. Mol. Sci.* **2021**, *22*, 3453, doi:10.3390/ijms22073453.

34. Liikanen, I.; Ahtiainen, L.; Hirvinen, M.L.; Bramante, S.; Cerullo, V.; Nokisalmi, P.; Hemminki, O.; Diaconu, I.; Pesonen, S.; Koski, A.; et al. Oncolytic adenovirus with temozolomide induces autophagy and antitumor immune responses in cancer patients. *Mol. Ther.* **2013**, *21*, 1212–1223, doi:10.1038/mt.2013.51.

35. Fritzell, S.; Sandén, E.; Eberstål, S.; Visse, E.; Darabi, A.; Siesjö, P. Intratumoral temozolomide synergizes with immunotherapy in a T cell-dependent fashion. *Cancer Immunol. Immunother.* **2013**, *62*, 1463–1474, doi:10.1007/s00262-013-1449-z.

36. Curtin, J.F.; Liu, N.; Candolfi, M.; Xiong, W.; Assi, H.; Yagiz, K.; Edwards, M.R.; Michelsen, K.S.; Kroeger, K.M.; Liu, C.; et al. HMGB1 Mediates Endogenous TLR2 Activation and Brain Tumor Regression. *PLoS Med.* **2009**, *6*, e1000010, doi:10.1371/journal.pmed.1000010.

37. Kim, T.G.; Kim, C.H.; Park, J.S.; Park, S.D.; Kim, C.K.; Chung, D.S.; Hong, Y.K. Immunological factors relating to the antitumor effect of temozolomide chemoimmunotherapy in a murine glioma model. *Clin. Vaccine Immunol.* **2010**, *17*, 143–153, doi:10.1128/CVI.00292-09.

38. Karachi, A.; Dastmalchi, F.; Mitchell, D.A.; Rahman, M. Temozolomide for immunomodulation in the treatment of glioblastoma. *Neuro. Oncol.* **2018**, *20*, 1566–1572, doi:10.1093/neuonc/noy072.

39. Opzoomer, J.W.; Sosnowska, D.; Anstee, J.E.; Spicer, J.F.; Arnold, J.N. Cytotoxic chemotherapy as an immune stimulus: A molecular perspective on turning up the immunological heat on cancer. *Front. Immunol.* **2019**, *10*, 1654, doi:10.3389/fimmu.2019.01654.

40. von Roemeling, C.A.; Wang, Y.; Qie, Y.; Yuan, H.; Zhao, H.; Liu, X.; Yang, Z.; Yang, M.; Deng, W.; Bruno, K.A.; et al. Therapeutic modulation of phagocytosis in glioblastoma can activate both innate and adaptive antitumour immunity. *Nat. Commun.* **2020**, *11*, 1508, doi:10.1038/s41467-020-15129-8.

41. Hicks, W.H.; Bird, C.E.; Traylor, J.I.; Shi, D.D.; El Ahmadieh, T.Y.; Richardson, T.E.; McBrayer, S.K.; Abdullah, K.G. Contemporary Mouse Models in Glioma Research. *Cells* **2021**, *10*, 712, doi:10.3390/cells10030712.

42. Antunes, L.; Angioi-Duprez, K.S.; Bracard, S.R.; Klein-Monhoven, N.A.; Le Faou, A.E.; Duprez, A.M.; Plénat, F.M. Analysis of Tissue Chimerism in Nude Mouse Brain and Abdominal Xenograft Models of Human Glioblastoma Multiforme: What Does It Tell Us About the Models and About Glioblastoma Biology and Therapy? *J. Histochem. Cytochem.* **2000**, *48*, 847–858, doi:10.1177/002215540004800613.

43. Huszthy, P.C.; Daphu, I.; Niclou, S.P.; Stieber, D.; Nigro, J.M.; Sakariassen, P.O.; Miletic, H.; Thorsen, F.; Bjerkvig, R. In vivo models of primary brain tumors: pitfalls and perspectives. *Neuro. Oncol.* **2012**, *14*, 979–993, doi:10.1093/neuonc/nos135.

44. Ciezka, M.; Acosta, M.; Herranz, C.; Canals, J.M.; Pumarola, M.; Candiota, A.P.; Arús, C. Development of a transplantable glioma tumour model from genetically engineered mice: MRI/MRS/MRSI characterisation. *J. Neurooncol.* **2016**, *129*, 67–76, doi:10.1007/s11060-016-2164-3.

45. Oh, T.; Fakurnejad, S.; Sayegh, E.T.; Clark, A.J.; Ivan, M.E.; Sun, M.Z.; Safaee, M.; Bloch, O.; James, C.D.; Parsa, A.T. Immunocompetent murine models for the study of glioblastoma immunotherapy. *J. Transl. Med.* **2014**, *12*, 107, doi:10.1186/1479-5876-12-107.

46. Semenkow, S.; Li, S.; Kahlert, U.D.; Raabe, E.H.; Xu, J.; Arnold, A.; Janowski, M.; Oh, B.C.; Brandacher, G.; Bulte, J.W.M.; et al. An immunocompetent mouse model of human

glioblastoma. *Oncotarget* **2017**, *8*, 61072–61082, doi:10.18632/oncotarget.17851.

47. Ferrer-Font, L. Tuning response to therapy in preclinical gl261 glioblastoma through ck2 targeting and temozolomide metronomic approaches, Universitat Autònoma de Barcelona, 2017.

48. Szatmári, T.; Lumniczky, K.; Désaknai, S.; Trajcevski, S.; Hídvégi, E.J.; Hamada, H.; Sáfrány, G. Detailed characterization of the mouse glioma 261 tumor model for experimental glioblastoma therapy. *Cancer Sci.* **2006**, *97*, 546–553, doi:10.1111/j.1349-7006.2006.00208.x.

49. Arias-Ramos, N.; Ferrer-Font, L.; Lope-Piedrafita, S.; Mocioiu, V.; Julià-Sapé, M.; Pumarola, M.; Arús, C.; Candiota, A.P. Metabolomics of therapy response in preclinical glioblastoma: A multi-slice MRSI-based volumetric analysis for noninvasive assessment of temozolomide treatment. *Metabolites* **2017**, *7*, pii: E20, doi:10.3390/metabo7020020.

50. Delgado-Goñi, T.; Ortega-Martorell, S.; Ciezka, M.; Olier, I.; Candiota, A.; Julià-Sapé, M.; Fernández, F.; Pumarola, M.; Lisboa, P.; Arús, C. MRSI-based molecular imaging of therapy response to temozolomide in preclinical glioblastoma using source analysis. *NMR Biomed.* **2016**, *29*, 732–743, doi:10.1002/nbm.3521.

51. Simões, R.V.; Ortega-Martorell, S.; Delgado-Goñi, T.; Fur, Y. Le; Pumarola, M.; Candiota, A.P.; Martín, J.; Stoyanova, R.; Cozzone, P.J.; Julià-Sapé, M.; et al. Improving the classification of brain tumors in mice with perturbation enhanced (PE)-MRSI. *Integr. Biol.* **2012**, *4*, 183–191, doi:10.1039/c2ib00079b.

52. Wu, S.; Calero-Pérez, P.; Arús, C.; Candiota, A.P. Anti-pd-1 immunotherapy in preclinical gl261 glioblastoma: Influence of therapeutic parameters and non-invasive response biomarker assessment with mrsi-based approaches. *Int. J. Mol. Sci.* **2020**, *21*, 8775, doi:10.3390/ijms21228775.

53. Towner, R.A.; Ihnat, M.; Saunders, D.; Bastian, A.; Smith, N.; Pavana, R.K.; Gangjee, A. A new anti-glioma therapy, AG119: pre-clinical assessment in a mouse GL261 glioma model. *BMC Cancer* **2015**, *15*, 522, doi:10.1186/s12885-015-1538-9.

54. Reardon, D.A.; Gokhale, P.C.; Klein, S.R.; Ligon, K.L.; Rodig, S.J.; Ramkissoon, S.H.; Jones, K.L.; Conway, A.S.; Liao, X.; Zhou, J.; et al. Glioblastoma Eradication Following Immune Checkpoint Blockade in an Orthotopic, Immunocompetent Model. *Cancer Immunol. Res.* **2016**, *4*, 124–135, doi:10.1158/2326-6066.CIR-15-0151.

55. Xu, M.; Yao, Y.; Hua, W.; Wu, Z.; Zhong, P.; Mao, Y.; Zhou, L.; Luo, F.; Chu, Y. Mouse glioma immunotherapy mediated by A2B5+ GL261 cell lysate-pulsed dendritic cells. *J. Neurooncol.* **2014**, *116*, 497–504, doi:10.1007/s11060-013-1334-9.

56. Kober, C.; Rohn, S.; Weibel, S.; Geissinger, U.; Chen, N.G.; Szalay, A.A. Microglia and astrocytes attenuate the replication of the oncolytic vaccinia virus LIVP 1.1.1 in murine GL261 gliomas by acting as vaccinia virus traps. *J. Transl. Med.* **2015**, *13*, 216, doi:10.1186/s12967-015-0586-x.

57. M. Seligman, A.; Shear, J. Studies in carcinogenesis. *Am. J. Cancer* **1939**, *37*, 364–396.

58. Scott, O.C.A. Tumor Transplantation and Tumor Immunity: A Personal View. *Cancer Res.* **1991**, *51*, 757–763.

59. Ausman, J.I.; Shapiro, W.R.; Rall, D.P. Studies on the Chemotherapy of Experimental Brain Tumors: Development of an Experimental Model. *Cancer Res.* **1970**, *30*, 2394–2400.

60. Delgado-Goñi, T.; Julià-Sapé, M.; Candiota, A.P.; Pumarola, M.; Arús, C. Molecular imaging coupled to pattern recognition distinguishes response to temozolomide in preclinical glioblastoma. *NMR Biomed.* **2014**, *27*, 1333–1345, doi:10.1002/nbm.3194.

61. Genoud, V.; Marinari, E.; Nikolaev, S.I.; Castle, J.C.; Bukur, V.; Dietrich, P.Y.; Okada, H.; Walker, P.R. Responsiveness to anti-PD-1 and anti-CTLA-4 immune checkpoint blockade in SB28 and GL261 mouse glioma models. *Oncoimmunology* **2018**, *7*, e1501137, doi:10.1080/2162402X.2018.1501137.

62. Schumacher, T.N.; Schreiber, R.D. Neoantigens in cancer immunotherapy. *Science (80-.).* **2015**, *348*, 69–74, doi:10.1126/science.aaa4971.

63. Pich, O.; Muiños, F.; Lolkema, M.P.; Steeghs, N.; Gonzalez-Perez, A.; Lopez-Bigas, N. The mutational footprints of cancer therapies. *Nat. Genet.* **2019**, *51*, 1732–1740, doi:10.1038/s41588-019-0525-5.

64. Weishaupt D, M.B.; Köchli, V.D. *How Does MRI Work? An introduction to the Physics and Function of Magnetic Resonance Imaging*; Second edi.; Springer New York LLC, 2006; ISBN 978-3-540-37845-7.

65. Dhermain, F.G.; Hau, P.; Lanfermann, H.; Jacobs, A.H.; van den Bent, M.J. Advanced MRI and PET imaging for assessment of treatment response in patients with gliomas. *Lancet Neurol.* **2010**, *9*, 906–920, doi:10.1016/S1474-4422(10)70181-2.

66. Kiessling, F.; Morgenstern, B.; Zhang, C. Contrast Agents and Applications to Assess Tumor Angiogenesis In Vivo by Magnetic Resonance Imaging. *Curr. Med. Chem.* **2006**, *14*, 77–91, doi:10.2174/092986707779313516.

67. Pichler, B.J.; Wehrl, H.F.; Judenhofer, M.S. Latest advances in molecular imaging instrumentation. *J. Nucl. Med.* **2008**, *49*, 5–23, doi:10.2967/jnumed.108.045880.

68. Horská, A.; Barker, P.B. Imaging of brain tumors: MR spectroscopy and metabolic imaging. *Neuroimaging Clin. N. Am.* **2010**, *20*, 293–310, doi:10.1016/j.nic.2010.04.003.

69. Weybright, P.; Maly, P.; Gomez-Hassan, D.; Blaesing, C.; Sundgren, P.C. MR spectroscopy in the evaluation of recurrent contrast-enhancing lesions in the posterior fossa after tumor treatment. *Neuroradiology* **2004**, *46*, 541–549, doi:10.1007/s00234-004-1195-1.

70. Hajek, M.; Dezortova, M. Introduction to clinical in vivo MR spectroscopy. *Eur. J. Radiol.* **2008**, *67*, 185–193, doi:10.1016/j.ejrad.2008.03.002.

71. Govindaraju, V.; Young, K.; Maudsley, A.A. Proton NMR chemical shifts and coupling constants for brain metabolites. *NMR Biomed.* **2000**, *13*, 129–153, doi:10.1002/1099-1492(200005)13:3<129::AID-NBM619>3.0.CO;2-V.

72. Hattingen, E.; Jurcoane, A.; Bähr, O.; Rieger, J.; Magerkurth, J.; Anti, S.; Steinbach, J.P.; Pilatus, U. Bevacizumab impairs oxidative energy metabolism and shows antitumoral effects in recurrent glioblastomas: A 31P/ 1H MRSI and quantitative magnetic resonance imaging study. *Neuro. Oncol.* **2011**, *13*, 1349–1363, doi:10.1093/neuonc/nor132.

73. Nelson, S.J. Assessment of therapeutic response and treatment planning for brain tumors using metabolic and physiological MRI. *NMR Biomed.* **2011**, *24*, 734–749, doi:10.1002/nbm.1669.

74. Julià-Sapé, M.; Candiota, A.P.; Arús, C. Cancer metabolism in a snapshot: MRS(I). *NMR Biomed.* **2019**, *32*, e4054, doi:10.1002/nbm.4054.

75. Nelson, S.J.; Kadambi, A.K.; Park, I.; Li, Y.; Crane, J.; Olson, M.; Molinaro, A.; Roy, R.; Butowski, N.; Cha, S.; et al. Association of early changes in 1H MRSI parameters with survival for patients with newly diagnosed glioblastoma receiving a multimodality treatment regimen. *Neuro. Oncol.* **2017**, *19*, 430–439, doi:10.1093/neuonc/now159.

76. Hourani, R.; Horská, A.; Albayram, S.; Brant, L.J.; Melhem, E.; Cohen, K.J.; Burger, P.C.; Weingart, J.D.; Carson, B.; Wharam, M.D.; et al. Proton magnetic resonance spectroscopic imaging to differentiate between nonneoplastic lesions and brain tumors in children. *J. Magn. Reson. Imaging* **2006**, *23*, 99–107, doi:10.1002/jmri.20480.

77. Anwar, M.; Molinaro, A.M.; Morin, O.; Chang, S.M.; Haas-Kogan, D.A.; Nelson, S.J.; Lupo, J.M. Identifying Voxels at Risk for Progression in Glioblastoma Based on Dosimetry, Physiologic and Metabolic MRI. *Radiat. Res.* **2017**, *188*, 303–313, doi:10.1667/RR14662.1.

78. Zarinabad, N.; Abernethy, L.J.; Avula, S.; Davies, N.P.; Rodriguez Gutierrez, D.; Jaspan, T.; MacPherson, L.; Mitra, D.; Rose, H.E.L.; Wilson, M.; et al. Application of pattern recognition techniques for classification of pediatric brain tumors by in vivo 3T 1H-MR spectroscopy—A multi-center study. *Magn. Reson. Med.* **2018**, *79*, 2359–2366, doi:10.1002/mrm.26837.

79. Zhu, H.; Barker, P.B. MR Spectroscopy and Spectroscopic Imaging of the Brain. *Methods Mol. Biol.* **2010**, *711*, 203–226, doi:10.1007/978-1-61737-992-5_9.

80.   Verma, A.; Kumar, I.; Verma, N.; Aggarwal, P.; Ojha, R. Magnetic resonance spectroscopy - Revisiting the biochemical and molecular milieu of brain tumors. *BBA Clin.* **2016**, *5*, 170–178, doi:10.1016/j.bbacli.2016.04.002.

81.   Cecil, K.M. Proton Magnetic Resonance Spectroscopy: Technique for the Neuroradiologist. *Neuroimaging Clin. N. Am.* **2013**, *23*, 381–392, doi:10.1016/j.nic.2012.10.003.

82.   Maniega, S.M.; Cvoro, V.; Armitage, P.A.; Marshall, I.; Bastin, M.E.; Wardlaw, J.M. Choline and creatine are not reliable denominators for calculating metabolite ratios in acute ischemic stroke. *Stroke* **2008**, *39*, 2467–2469, doi:10.1161/STROKEAHA.107.507020.

83.   Tong, Z.; Yamaki, T.; Harada, K.; Houkin, K. In vivo quantification of the metabolites in normal brain and brain tumors by proton MR spectroscopy using water as an internal standard. *Magn. Reson. Imaging* **2004**, *22*, 1017–1024, doi:10.1016/j.mri.2004.02.006.

84.   Glunde, K.; Bhujwalla, Z.M.; Ronen, S.M. Choline metabolism in malignant transformation. *Nat. Rev. Cancer* **2011**, *11*, 835–848, doi:10.1038/nrc3162.

85.   Bi, J.; Chowdhry, S.; Wu, S.; Zhang, W.; Masui, K.; Mischel, P.S. Altered cellular metabolism in gliomas — an emerging landscape of actionable co-dependency targets. *Nat. Rev. Cancer* **2020**, *20*, 57–70, doi:10.1038/s41568-019-0226-5.

86.   Quintero, M.; Cabañas, M.E.; Arús, C. A possible cellular explanation for the NMR-visible mobile lipid (ML) changes in cultured C6 glioma cells with growth. *Biochim. Biophys. Acta - Mol. Cell Biol. Lipids* **2007**, *1771*, 31–44, doi:10.1016/j.bbalip.2006.10.003.

87.   Pérez, Y.; Lahrech, H.; Cabañas, M.E.; Barnadas, R.; Sabós, M.; Rémy, C.; Arús, C. Measurement by nuclear magnetic resonance diffusion of the dimensions of the mobile lipid compartment in C6 cells. *Cancer Res.* **2002**, *62*, 5672–5677.

88.   Soares, D.P.; Law, M. Magnetic resonance spectroscopy of the brain: review of metabolites and clinical applications. *Clin. Radiol.* **2009**, *64*, 12–21, doi:10.1016/j.crad.2008.07.002.

89.   Candiota, A.P.; Majós, C.; Julià-Sapé, M.; Cabañas, M.; Acebes, J.J.; Moreno-Torres, A.; Griffiths, J.R.; Arús, C. Non-invasive grading of astrocytic tumours from the relative contents of myo-inositol and glycine measured by in vivo mrs. *J. Belgian Soc. Radiol.* **2011**, *94*, 319–329, doi:10.5334/jbr-btr.698.

90.   Anastasiou, D. Tumour microenvironment factors shaping the cancer metabolism landscape. *Br. J. Cancer* **2017**, *116*, 277–286, doi:10.1038/bjc.2016.412.

91.   Hattingen, E.; Lanfermann, H.; Quick, J.; Franz, K.; Zanella, F.E.; Pilatus, U. 1H MR spectroscopic imaging with short and long echo time to discriminate glycine in glial tumours. *Magn. Reson. Mater. Physics, Biol. Med.* **2009**, *22*, 33–41, doi:10.1007/s10334-008-0145-z.

92.   Bertholdo, D.; Watcharakorn, A.; Castillo, M. Brain Proton Magnetic Resonance Spectroscopy: Introduction and Overview. *Neuroimaging Clin. N. Am.* **2013**, *23*, 359–380, doi:10.1016/j.nic.2012.10.002.

93.   Howe, F.A.; Barton, S.J.; Cudlip, S.A.; Stubbs, M.; Saunders, D.E.; Murphy, M.; Wilkins, P.; Opstad, K.S.; Doyle, V.L.; McLean, M.A.; et al. Metabolic profiles of human brain tumors using quantitative in vivo 1H magnetic resonance spectroscopy. *Magn. Reson. Med.* **2003**, *49*, 223–232, doi:10.1002/mrm.10367.

94.   Quintero, M.; Cabañas, M.E.; Arús, C. 13C-labelling studies indicate compartmentalized synthesis of triacylglycerols in C6 rat glioma cells. *Biochim. Biophys. Acta - Mol. Cell Biol. Lipids* **2010**, *1801*, 693–701, doi:10.1016/j.bbalip.2010.03.013.

95.   Cudalbu, C.; Behar, K.L.; Bhattacharyya, P.K.; Bogner, W.; Borbath, T.; Graaf, R.A.; Gruetter, R.; Henning, A.; Juchem, C.; Kreis, R.; et al. Contribution of macromolecules to brain 1 H MR spectra: Experts' consensus recommendations. *NMR Biomed.* **2021**, *34*, e4393, doi:10.1002/nbm.4393.

96.   Hakumäki, J.M.; Poptani, H.; Sandmair, A.-M.; Ylä-Herttuala, S.; Kauppinen, R.A. 1H MRS detects polyunsaturated fatty acid accumulation during gene therapy of glioma:

Implications for the in vivo detection of apoptosis. *Nat. Med.* **1999**, *5*, 1323–1327, doi:10.1038/15279.

97. El-Deredy, W. Pattern Recognition Approaches in Biomedical and Clinical Magnetic Resonance Spectroscopy: A Review. *NMR Biomed.* **1997**, *10*, 99–124.

98. Tate, A.R.; Griffiths, J.R.; Martínez-Pérez, I.; Moreno, A.; Barba, I.; Cabañas, M.E.; Watson, D.; Alonso, J.; Bartumeus, F.; Isamat, F.; et al. Towards a method for automated classification of 1H MRS spectra from brain tumours. *NMR Biomed.* **1998**, *11*, 177–191, doi:10.1002/(SICI)1099-1492(199806/08)11:4/5<177::AID-NBM534>3.0.CO;2-U.

99. Ortega-Martorell, S.; Lisboa, P.J.G.; Vellido, A.; Simões, R. V.; Pumarola, M.; Julià-Sapé, M.; Arús, C. Convex Non-Negative Matrix Factorization for Brain Tumor Delimitation from MRSI Data. *PLoS One* **2012**, *7*, e47824, doi:10.1371/journal.pone.0047824.

100. De Edelenyi, F.S.; Rubin, C.; Estève, F.; Grand, S.; Décorps, M.; Lefournier, V.; Le Bas, J.-F.; Rémy, C. A new approach for analyzing proton magnetic resonance spectroscopic images of brain tumors: nosologic images. *Nat. Med.* **2000**, *6*, 1287–1289, doi:10.1038/81401.

101. Gieryng, A.; Pszczolkowska, D.; Walentynowicz, K.A.; Rajan, W.D.; Kaminska, B. Immune microenvironment of gliomas. *Lab. Investig.* **2017**, *97*, 498–518, doi:10.1038/labinvest.2017.19.

102. Broekman, M.L.; Maas, S.L.N.; R. Abels, E.; Mempel, T.R.; M. Krichevsky, A.; O. Breakefield, X. Multidimensional communication in the microenvirons of glioblastoma. *Nat. Rev. Neurol.* **2018**, *14*, 482–495, doi:10.1038/s41582-018-0025-8.Multidimensional.

103. Chen, D.S.; Mellman, I. Oncology meets immunology: The cancer-immunity cycle. *Immunity* **2013**, *39*, 1–10, doi:10.1016/j.immuni.2013.07.012.

104. Haabeth, O.A.W.; Tveita, A.A.; Fauskanger, M.; Schjesvold, F.; Lorvik, K.B.; Hofgaard, P.O.; Omholt, H.; Munthe, L.A.; Dembic, Z.; Corthay, A.; et al. How Do CD4+ T Cells Detect and Eliminate Tumor Cells That Either Lack or Express MHC Class II Molecules? *Front. Immunol.* **2014**, *5*, doi:10.3389/fimmu.2014.00174.

105. Motta, J.M.; Rumjanek, V.M. Sensitivity of Dendritic Cells to Microenvironment Signals. *J. Immunol. Res.* **2016**, *2016*, 4753607, doi:10.1155/2016/4753607.

106. Balan, S.; Saxena, M.; Bhardwaj, N. *Dendritic cell subsets and locations*; 1st ed.; Elsevier Inc., 2019; Vol. 348; ISBN 9780128183519.

107. Karman, J.; Ling, C.; Sandor, M.; Fabry, Z. Initiation of immune responses in brain is promoted by local dendritic cells. *J. Immunol.* **2004**, *173*, 2353–2361, doi:10.4049/jimmunol.173.4.2353.

108. Chen, H.; Li, M.; Guo, Y.; Zhong, Y.; He, Z.; Xu, Y.; Zou, J. Immune response in glioma's microenvironment. *Innov. Surg. Sci.* **2021**, *5*, 115–125, doi:10.1515/iss-2019-0001.

109. Chen, L.; Flies, D.B. Molecular mechanisms of T cell co-stimulation and co-inhibition. *Nat. Rev. Immunol.* **2013**, *13*, 227–242, doi:10.1038/nri3405.

110. Motz, G.T.; Coukos, G. Deciphering and Reversing Tumor Immune Suppression. *Immunity* **2013**, *39*, 61–73, doi:10.1016/j.immuni.2013.07.005.

111. Hambardzumyan, D.; Gutmann, D.H.; Kettenmann, H. The role of microglia and macrophages in glioma maintenance and progression. *Nat. Neurosci.* **2016**, *19*, 20–27, doi:10.1038/nn.4185.

112. Lisi, L.; Ciotti, G.M.P.; Braun, D.; Kalinin, S.; Currò, D.; C, D.R.; Coli, A.; Mangiola, A.; Anile, C.; Dl, F.; et al. Expression of iNOS , CD163 and ARG-1 taken as M1 and M2 markers of microglial polarization in human glioblastoma and the surrounding normal parenchyma. *Neurosci. Lett.* **2017**, *645*, 106–112, doi:10.1016/j.neulet.2017.02.076.

113. Bingle, L.; Brown, N.J.; Lewis, C.E. The role of tumour-associated macrophages in tumour progression: Implications for new anticancer therapies. *J. Pathol.* **2002**, *196*, 254–265, doi:10.1002/path.1027.

114. McKelvey, K.J.; Hudson, A.L.; Prasanna Kumar, R.; Wilmott, J.S.; Attrill, G.H.; Long, G. V.; Scolyer, R.A.; Clarke, S.J.; Wheeler, H.R.; Diakos, C.I.; et al. Temporal and spatial

modulation of the tumor and systemic immune response in the murine Gl261 glioma model. *PLoS One* **2020**, *15*, e0226444, doi:10.1371/journal.pone.0226444.

115. Wang, H.; Zhou, H.; Xu, J.; Lu, Y.; Ji, X.; Yao, Y.; Chao, H.; Zhang, J.; Zhang, X.; Yao, S.; et al. Different T-cell subsets in glioblastoma multiforme and targeted immunotherapy. *Cancer Lett.* **2021**, *496*, 134–143, doi:10.1016/j.canlet.2020.09.028.

116. Dranoff, G. Cytokines in cancer pathogenesis and cancer therapy. *Nat. Rev. Cancer* **2004**, *4*, 11–22, doi:10.1038/nrc1252.

117. Palucka, K.; Banchereau, J. Cancer Immunotherapy via Dendritic Cells. In *Interaction of Immune and Cancer Cells*; Klink, M., Ed.; Springer Vienna: Vienna, 2014; pp. 75–89 ISBN 978-3-7091-1299-1.

118. Topalian, S.L.; Taube, J.M.; Anders, R.A.; Pardoll, D.M. Mechanism-driven biomarkers to guide immune checkpoint blockade in cancer therapy. *Nat. Rev. Cancer* **2016**, *16*, 275–287, doi:10.1038/nrc.2016.36.

119. Kershaw, M.H.; Westwood, J.A.; Darcy, P.K. Gene-engineered T cells for cancer therapy. *Nat. Rev. Cancer* **2013**, *13*, 525–541, doi:10.1038/nrc3565.

120. Bevan, M.J. Helping the CD8+ T-cell response. *Nat. Rev. Immunol.* **2004**, *4*, 595–602, doi:10.1038/nri1413.

121. Farhood, B.; Najafi, M.; Mortezaee, K. CD8+ cytotoxic T lymphocytes in cancer immunotherapy: A review. *J. Cell. Physiol.* **2019**, *234*, 1–13, doi:10.1002/jcp.27782.

122. Tumeh, P.C.; Harview, C.L.; Yearley, J.H.; Shintaku, I.P.; Emma, J.; Taylor, M.; Robert, L.; Chmielowski, B.; Spasic, M.; Henry, G.; et al. PD-1 blockade induces responses by inhibiting adaptive immune resistance. *Nature* **2014**, *515*, 568–571, doi:10.1038/nature13954.PD-1.

123. Gotwals, P.; Cameron, S.; Cipolletta, D.; Cremasco, V.; Crystal, A.; Hewes, B.; Mueller, B.; Quaratino, S.; Sabatos-Peyton, C.; Petruzzelli, L.; et al. Prospects for combining targeted and conventional cancer therapy with immunotherapy. *Nat. Rev. Cancer* **2017**, *17*, 286–301, doi:10.1038/nrc.2017.17.

124. Thomas, D.A.; Massagué, J. TGF-β directly targets cytotoxic T cell functions during tumor evasion of immune surveillance. *Cancer Cell* **2005**, *8*, 369–380, doi:10.1016/j.ccr.2005.10.012.

125. Tay, R.E.; Richardson, E.K.; Toh, H.C. Revisiting the role of CD4+ T cells in cancer immunotherapy—new insights into old paradigms. *Cancer Gene Ther.* **2020**, doi:10.1038/s41417-020-0183-x.

126. Gottschalk, C.; Mettke, E.; Kurts, C. The role of invariant natural killer T cells in dendritic cell licensing, cross-priming, and memory CD8+ T cell generation. *Front. Immunol.* **2015**, *6*, 379, doi:10.3389/fimmu.2015.00379.

127. El Andaloussi, A.; Han, Y.; Lesniak, M.S. Prolongation of survival following depletion of CD4+ CD25+ regulatory T cells in mice with experimental brain tumors. *J. Neurosurg.* **2006**, *105*, 430–437, doi:10.1111/cas.14069.

128. Braza, F.; Durand, M.; Degauque, N.; Brouard, S. Regulatory T Cells in Kidney Transplantation: New Directions? *Am. J. Transplant.* **2015**, *15*, 2288–2300, doi:10.1111/ajt.13395.

129. Chávez-Galán, L.; Arenas-Del Angel, M.C.; Zenteno, E.; Chávez, R.; Lascurain, R. Cell death mechanisms induced by cytotoxic lymphocytes. *Cell. Mol. Immunol.* **2009**, *6*, 15–25, doi:10.1038/cmi.2009.3.

130. Golán, I.; Rodríguez de la Fuente, L.; Costoya, J. NK Cell-Based Glioblastoma Immunotherapy. *Cancers (Basel).* **2018**, *10*, 522, doi:10.3390/cancers10120522.

131. Sharma, P.; Hu-Lieskovan, S.; Wargo, J.A.; Ribas, A. Primary, Adaptive, and Acquired Resistance to Cancer Immunotherapy. *Cell* **2017**, *168*, 707–723, doi:10.1016/j.cell.2017.01.017.

132. Rowshanravan, B.; Halliday, N.; Sansom, D.M. CTLA-4: a moving target in immunotherapy. *Blood* **2018**, *131*, 58–67, doi:10.1182/blood-2017-06-741033.

133. Lim, M.; Xia, Y.; Bettegowda, C.; Weller, M. Current state of immunotherapy. *Nat. Rev. Clin. Oncol.* **2018**, *15*, 422–442, doi:10.1038/s41571-018-0003-5.

134. Zhang, X.; Zhu, S.; Li, T.; Liu, Y.; Chen, W.; Chen, J. Targeting immune checkpoints in malignant glioma. *Oncotarget* **2017**, *8*, 7157–7174, doi:10.18632/oncotarget.12702.

135. Keir, M.E.; Butte, M.J.; Freeman, G.J.; Sharpe, A.H. PD-1 and Its Ligands in Tolerance and Immunity. *Annu. Rev. Immunol.* **2008**, *6*, 677–704, doi:10.1146/annurev.immunol.26.021607.090331.

136. Mirghorbani, M.; Van Gool, S.; Rezaei, N. Myeloid-derived suppressor cells in glioma. *Expert Rev. Neurother.* **2013**, *13*, 1395–1406, doi:10.1586/14737175.2013.857603.

137. Antonios, J.P.; Soto, H.; Everson, R.G.; Moughon, D.; Orpilla, J.R.; Shin, N.P.; Sedighim, S.; Treger, J.; Odesa, S.; Tucker, A.; et al. Immunosuppressive tumor-infltrating myeloid cells mediate adaptive immune resistance via a PD-1/PD-L1 mechanism in glioblastoma. *Neuro. Oncol.* **2017**, *19*, 796–807, doi:10.1093/neuonc/now287.

138. Varricchi, G.; Galdiero, M.R.; Marone, G.; Criscuolo, G.; Triassi, M.; Bonaduce, D.; Marone, G.; Tocchetti, C.G. Cardiotoxicity of immune checkpoint inhibitors. *ESMO Open* **2017**, *2*, e000247, doi:10.1136/esmoopen-2017-000247.

139. Sharma, P.; Allison, J.P. The future of immune checkpoint therapy. *Science (80-.).* **2015**, *348*, 56–61.

140. Zaravinos, A. An updated overview of HPV-associated head and neck carcinomas. *Oncotarget* **2014**, *5*, 3956–3969, doi:10.18632/oncotarget.1934.

141. Brocker, C.N.; Vasiliou, V.; Nebert, D.W. Evolutionary divergence and functions of the ADAM and ADAMTS gene families. *Hum. Genomics* **2009**, *4*, 43–55, doi:10.1186/1479-7364-4-1-43.

142. Giebeler, N.; Zigrino, P. A Disintegrin and Metalloprotease (ADAM): Historical Overview of Their Functions. *Toxins (Basel).* **2016**, *8*, 122, doi:10.3390/toxins8040122.

143. Murphy, G. The ADAMs: Signalling scissors in the tumour microenvironment. *Nat. Rev. Cancer* **2008**, *8*, 929–941, doi:10.1038/nrc2459.

144. Lambrecht, B.N.; Vanderkerken, M.; Hammad, H. The emerging role of ADAM metalloproteinases in immunity. *Nat. Rev. Immunol.* **2018**, *18*, 745–758, doi:10.1038/s41577-018-0068-5.

145. Gómez-Gaviro, M.; Domínguez-Luis, M.; Canchado, J.; Calafat, J.; Janssen, H.; Lara-Pezzi, E.; Fourie, A.; Tugores, A.; Valenzuela-Fernández, A.; Mollinedo, F.; et al. Expression and Regulation of the Metalloproteinase ADAM-8 during Human Neutrophil Pathophysiological Activation and Its Catalytic Activity on L-Selectin Shedding. *J. Immunol.* **2007**, *178*, 8053–8063, doi:10.4049/jimmunol.178.12.8053.

146. Schlomann, U.; Rathke-Hartlieb, S.; Yamamoto, S.; Jockusch, H.; Bartsch, J.W. Tumor necrosis factor α induces a metalloprotease-disintegrin, ADAM8 (CD 156): Implications for neuron-glia interactions during neurodegeneration. *J. Neurosci.* **2000**, *20*, 7964–7971, doi:10.1523/jneurosci.20-21-07964.2000.

147. Bartsch, J.W.; Wildeboer, D.; Koller, G.; Naus, S.; Rittger, A.; Moss, M.L.; Minai, Y.; Jockusch, H. Tumor necrosis factor-α (TNF-α) regulates shedding of TNF-α receptor 1 by the metalloprotease-disintegrin ADAM8: Evidence for a protease-regulated feedback loop in neuroprotection. *J. Neurosci.* **2010**, *30*, 12210–12218, doi:10.1523/JNEUROSCI.1520-10.2010.

148. Conrad, C.; Benzel, J.; Dorzweiler, K.; Cook, L.; Schlomann, U.; Zarbock, A.; Slater, E.P.; Nimsky, C.; Bartsch, J.W. ADAM8 in invasive cancers: links to tumor progression, metastasis, and chemoresistance. *Clin. Sci.* **2019**, *133*, 83–99, doi:10.1042/CS20180906.

149. Britton, G.J.; Ambler, R.; Clark, D.J.; Hill, E. V; Tunbridge, H.M.; McNally, K.E.; Burton, B.R.; Butterweck, P.; Sabatos-Peyton, C.; Hampton-O'Neil, L.A.; et al. PKCθ links proximal T cell and Notch signaling through localized regulation of the actin cytoskeleton. *Elife* **2017**, *6*, e20003, doi:10.7554/eLife.20003.

150. Britton, G.J.; Ambler, R.; Clark, D.J.; Hill, E. V.; Tunbridge, H.M.; McNally, K.E.; Burton,

B.R.; Butterweck, P.; Sabatos-Peyton, C.; Hampton-O'Neil, L.A.; et al. PKCθ links proximal T cell and Notch signaling through localized regulation of the actin cytoskeleton. *Elife* **2017**, *6*, e20003, doi:10.7554/eLife.20003.

151. Wiley, H.S.; Woolf, M.F.; Opresko, L.K.; Burke, P.M.; Will, B.; Morgan, J.R.; Lauffenburger, D.A. Removal of the membrane-anchoring domain of epidermal growth factor leads to intracrine signaling and disruption of mammary epithelial cell organization. *J. Cell Biol.* **1998**, *143*, 1317–1328, doi:10.1083/jcb.143.5.1317.

152. Borrell-Pagès, M.; Rojo, F.; Albanell, J.; Baselga, J.; Arribas, J. TACE is required for the activation of the EGFR by TGF-α in tumors. *EMBO J.* **2003**, *22*, 1114–1124, doi:10.1093/emboj/cdg111.

153. West, M.A.; Prescott, A.R.; Kui, M.C.; Zhou, Z.; Rose-John, S.; Scheller, J.; Watts, C. TLR ligand-induced podosome disassembly in dendritic cells is ADAM17 dependent. *J. Cell Biol.* **2008**, *182*, 993–1005, doi:10.1083/jcb.200801022.

154. Scheller, J.; Chalaris, A.; Garbers, C.; Rose-John, S. ADAM17: A molecular switch to control inflammation and tissue regeneration. *Trends Immunol.* **2011**, *32*, 380–387, doi:10.1016/j.it.2011.05.005.

155. Black, R.A.; Rauch, C.T.; Kozlosky, C.J.; Peschon, J.J.; Slack, J.L.; Wolfson, M.F.; Castner, B.J.; Stocking, K.L.; Reddy, P.; Srinivasan, S.; et al. A metalloproteinase disintegrin that releases tumour-necrosis factor-alpha from cells. *Nature* **1997**, *385*, 729–733.

156. Lichtenthaler, S.F.; Lemberg, M.K.; Fluhrer, R. Proteolytic ectodomain shedding of membrane proteins in mammals—hardware, concepts, and recent developments. *EMBO J.* **2018**, *37*, e99456, doi:10.15252/embj.201899456.

157. Vihinen, P.; Kähäri, V.M. Matrix metalloproteinases in cancer: Prognostic markers and therapeutic targets. *Int. J. Cancer* **2002**, *99*, 157–166, doi:10.1002/ijc.10329.

158. Vincenti, M.P.; Brinckerhoff, C.E. Signal transduction and cell-type specific regulation of matrix metalloproteinase gene expression: Can MMPs be good for you? *J. Cell. Physiol.* **2007**, *213*, 355–364, doi:10.1002/jcp.21208.

159. Cui, N.; Hu, M.; Khalil, R.A. Biochemical and Biological Attributes of Matrix Metalloproteinases. *Prog Mol Biol Transl Sci* **2017**, *147*, 1–73, doi:10.1016/bs.pmbts.2017.02.005.

160. Löffek, S.; Schilling, O.; Franzke, C.-W. Biological role of matrix metalloproteinases: a critical balance. *Eur. Respir. J.* **2011**, *38*, 191–208, doi:10.1183/09031936.00146510.

161. Martin, M.D.; Matrisian, L.M. The other side of MMPs: Protective roles in tumor progression. *Cancer Metastasis Rev.* **2007**, *26*, 717–724, doi:10.1007/s10555-007-9089-4.

162. Zarrabi, K.; Dufour, A.; Li, J.; Kuscu, C.; Pulkoski-Gross, A.; Zhi, J.; Hu, Y.; Sampson, N.S.; Zucker, S.; Cao, J. Inhibition of Matrix Metalloproteinase 14 (MMP-14)-mediated Cancer Cell Migration. *J. Biol. Chem.* **2011**, *286*, 33167–33177, doi:10.1074/jbc.M111.256644.

163. Sampieri, C.L.; Nuttall, R.K.; Young, D.A.; Goldspink, D.; Clark, I.M.; Edwards, D.R. Activation of p38 and JNK MAPK pathways abrogates requirement for new protein synthesis for phorbol ester mediated induction of select MMP and TIMP genes. *Matrix Biol.* **2008**, *27*, 128–138, doi:10.1016/j.matbio.2007.09.004.

164. Kondratiev, S.; Gnepp, D.R.; Yakirevich, E.; Sabo, E.; Annino, D.J.; Rebeiz, E.; Laver, N. V. Expression and prognostic role of MMP2, MMP9, MMP13, and MMP14 matrix metalloproteinases in sinonasal and oral malignant melanomas. *Hum. Pathol.* **2008**, *39*, 337–343, doi:10.1016/j.humpath.2007.07.003.

165. Chen, T.Y.; Li, Y.C.; Liu, Y.F.; Tsai, C.M.; Hsieh, Y.H.; Lin, C.W.; Yang, S.F.; Weng, C.J. Role of MMP14 gene polymorphisms in susceptibility and pathological development to hepatocellular carcinoma. *Ann. Surg. Oncol.* **2011**, *18*, 2348–2356, doi:10.1245/s10434-011-1574-x.

166. Weng, C.J.; Chen, M.K.; Lin, C.W.; Chung, T. Te; Yang, S.F. Single nucleotide polymorphisms and haplotypes of MMP-14 are associated with the risk and pathological

development of oral cancer. *Ann. Surg. Oncol.* **2012**, *19*, 319–327, doi:10.1245/s10434-011-1736-x.

167. Wang, L.; Yuan, J.; Tu, Y.; Mao, X.; He, S.; Fu, G.; Zong, J.; Zhang, Y. Co-expression of MMP-14 and MMP-19 predicts poor survival in human glioma. *Clin. Transl. Oncol.* **2013**, *15*, 139–145, doi:10.1007/s12094-012-0900-5.

168. Xie, H.; Xue, Y.; Liu, L.; Wang, P.; Liu, Y.; Ying, H. Expressions of matrix metalloproteinase-7 and matrix metalloproteinase-14 associated with the activation of extracellular signal-regulated kinase1/2 in human brain gliomas of different pathological grades. *Med. Oncol.* **2011**, *28*, 433–438, doi:10.1007/s12032-010-9660-7.

169. Scharovsky, O.G.; Mainetti, L.E.; Rozados, V.R. Metronomic chemotherapy: Changing the paradigm that more is better. *Curr. Oncol.* **2009**, *16*, 7–15, doi:10.3747/co.v16i2.420.

170. Litterman, A.J.; Zellmer, D.M.; Grinnen, K.L.; Hunt, M.A.; Dudek, A.Z.; Salazar, A.M.; Ohlfest, J.R. Profound Impairment of Adaptive Immune Responses by Alkylating Chemotherapy. *J. Immunol.* **2013**, *190*, 6259–6268, doi:10.4049/jimmunol.1203539.

171. Hanahan, D.; Bergers, G.; Bergsland, E. Less is more, regularly: metronomic dosing of cytotoxic drugs can target tumor angiogenesis in mice. *J. Clin. Invest.* **2000**, *105*, 1045–1047, doi:10.1172/JCI9872.

172. Ferrer-Font, L.; Villamañan, L.; Arias-Ramos, N.; Vilardell, J.; Plana, M.; Ruzzene, M.; Pinna, L.A.; Itarte, E.; Arús, C.; Candiota, A.P. Targeting protein kinase CK2: Evaluating CX-4945 potential for GL261 glioblastoma therapy in immunocompetent mice. *Pharmaceuticals* **2017**, *10*, 24, doi:10.3390/ph10010024.

173. Wu, J.; Waxman, D.J. Metronomic cyclophosphamide eradicates large implanted GL261 gliomas by activating antitumor Cd8 + T-cell responses and immune memory. *Oncoimmunology* **2015**, *4*, e1005521, doi:10.1080/2162402X.2015.1005521.

174. Pasquier, E.; Kavallaris, M.; André, N. Metronomic chemotherapy: New rationale for new directions. *Nat. Rev. Clin. Oncol.* **2010**, *7*, 455–465, doi:10.1038/nrclinonc.2010.82.

175. Pasquier, E.; Tuset, M.P.; Street, J.; Sinnappan, S.; MacKenzie, K.L.; Braguer, D.; Andre, N.; Kavallaris, M. Concentration- and schedule-dependent effects of chemotherapy on the angiogenic potential and drug sensitivity of vascular endothelial cells. *Angiogenesis* **2013**, *16*, 373–386, doi:10.1007/s10456-012-9321-x.

176. Emmenegger, U.; Man, S.; Shaked, Y.; Francia, G.; Wong, J.W.; Hicklin, D.J.; Kerbel, R.S. A comparative analysis of low-dose metronomic cyclophosphamide reveals absent or low-grade toxicity on tissues highly sensitive to the toxic effects of maximum tolerated dose regimens. *Cancer Res.* **2004**, *64*, 3994–4000, doi:10.1158/0008-5472.CAN-04-0580.

177. Browder, T.; Butterfield, C.E.; Kräling, B.M.; Shi, B.; Marshall, B.; O'Reilly, M.S.; Folkman, J. Antiangiogenic scheduling of chemotherapy improves efficacy against experimental drug-resistant cancer. *Cancer Res.* **2000**, *60*, 1878–86.

178. Asadzadeh, Z.; Safarzadeh, E.; Safaei, S.; Baradaran, A.; Mohammadi, A.; Hajiasgharzadeh, K.; Derakhshani, A.; Argentiero, A.; Silvestris, N.; Baradaran, B. Current Approaches for Combination Therapy of Cancer: The Role of Immunogenic Cell Death. *Cancers (Basel).* **2020**, *12*, 1047, doi:10.3390/cancers12041047.

179. Ferrer-Font, L.; Arias-Ramos, N.; Lope-Piedrafita, S.; Julià-Sapé, M.; Pumarola, M.; Arús, C.; Candiota, A.P. Metronomic treatment in immunocompetent preclinical GL261 glioblastoma: effects of cyclophosphamide and temozolomide. *NMR Biomed.* **2017**, *30(9)*, doi:10.1002/nbm.3748.

180. Simões, R.V.; García-Martín, M.L.; Cerdán, S.; Arús, C. Perturbation of mouse glioma MRS pattern by induced acute hyperglycemia. *NMR Biomed.* **2008**, *21*, 251–264, doi:10.1002/nbm.

181. Delgado-Goñi, T.; Martín-Sitjar, J.; Simões, R. V.; Acosta, M.; Lope-Piedrafita, S.; Arús, C. Dimethyl sulfoxide (DMSO) as a potential contrast agent for brain tumors. *NMR Biomed.* **2013**, *26*, 173–184, doi:10.1002/nbm.2832.

182. Garofalo, S.; D'Alessandro, G.; Chece, G.; Brau, F.; Maggi, L.; Rosa, A.; Porzia, A.; Mainiero,

F.; Esposito, V.; Lauro, C.; et al. Enriched environment reduces glioma growth through immune and non-immune mechanisms in mice. *Nat. Commun.* **2015**, *6*, 6623, doi:10.1038/ncomms7623.

183. Watters, J.J.; Schartner, J.M.; Badie, B. Microglia function in brain tumors. *J. Neurosci. Res.* **2005**, *81*, 447–455, doi:10.1002/jnr.20485.

184. Wesolowska, A.; Kwiatkowska, A.; Slomnicki, L.; Dembinski, M.; Master, A.; Sliwa, M.; Franciszkiewicz, K.; Chouaib, S.; Kaminska, B. Microglia-derived TGF- b as an important regulator of glioblastoma invasion-an inhibition of TGF- b -dependent effects by shRNA against human TGF- b type II receptor. *Oncogene* **2008**, *27*, 918–930, doi:10.1038/sj.onc.1210683.

185. Romero, Y.; Wise, R.; Zolkiewska, A. Proteolytic processing of PD-L1 by ADAM proteases in breast cancer cells. *Cancer Immunol. Immunother.* **2020**, *69*, 43–55, doi:10.1007/s00262-019-02437-2.

186. Rao, X.; Huang, X.; Zhou, Z.; Lin, X. An improvement of the 2ˆ(-delta delta CT) method for quantitative real-time polymerase chain reaction data analysis. *Biostat. Bioinforma. Biomath.* **2013**, *3*, 71–85.

187. Eisenhauer, E. a; Therasse, P.; Bogaerts, J.; Schwartz, L.H.; Sargent, D.; Ford, R.; Dancey, J.; Arbuck, S.; Gwyther, S.; Mooney, M.; et al. New response evaluation criteria in solid tumours: Revised RECIST guideline (version 1.1). *Eur. J. Cancer* **2009**, *45*, 228–247, doi:10.1016/j.ejca.2008.10.026.

188. Matsutani, S.; Shibutani, M.; Maeda, K.; Nagahara, H.; Fukuoka, T.; Nakao, S.; Hirakawa, K.; Ohira, M. Significance of tumor-infiltrating lymphocytes before and after neoadjuvant therapy for rectal cancer. *Cancer Sci.* **2018**, *109*, 966–979, doi:10.1111/cas.13542.

189. Wilkinson, K.; Ng, W.; Roberts, T.L.; Becker, T.M.; Lim, S.H.-S.; Chua, W.; Lee, C.S. Tumour immune microenvironment biomarkers predicting cytotoxic chemotherapy efficacy in colorectal cancer. *J. Clin. Pathol.* **2021**, *74*, 625–634, doi:10.1136/jclinpath-2020-207309.

190. Ladoire, S.; Mignot, G.; Dabakuyo, S.; Arnould, L.; Apetoh, L.; Rébé, C.; Coudert, B.; Martin, F.; Bizollon, M.H.; Vanoli, A.; et al. In situ immune response after neoadjuvant chemotherapy for breast cancer predicts survival. *J. Pathol.* **2011**, *224*, 389–400, doi:10.1002/path.2866.

191. Liu, R.; Hu, R.; Zeng, Y.; Zhang, W.; Zhou, H.-H. Tumour immune cell infiltration and survival after platinum-based chemotherapy in high-grade serous ovarian cancer subtypes: A gene expression-based computational study-NC-ND license. *EBioMedicine* **2020**, *51*, 102602, doi:10.1016/j.ebiom.2019.102602.

192. Mesnage, S.J.L.; Auguste, A.; Genestie, C.; Dunant, A.; Pain, E.; Drusch, F.; Gouy, S.; Morice, P.; Bentivegna, E.; Lhomme, C.; et al. Neoadjuvant chemotherapy (NACT) increases immune infiltration and programmed death-ligand 1 (PD-L1) expression in epithelial ovarian cancer (EOC). *Ann. Oncol.* **2017**, *28*, 651–657, doi:10.1093/annonc/mdw625.

193. Nesseler, J.P.; Schaue, D.; McBride, W.H.; Lee, M.H.; Kaprealian, T.; Niclou, S.P.; Nickers, P. Irradiation to Improve the Response to Immunotherapeutic Agents in Glioblastomas. *Adv. Radiat. Oncol.* **2019**, *4*, 268–282, doi:10.1016/j.adro.2018.11.005.

194. Sahebjam, S.; Sharabi, A.; Lim, M.; Kesarwani, P.; Chinnaiyan, P. Immunotherapy and radiation in glioblastoma. *J. Neurooncol.* **2017**, *134*, 531–539, doi:10.1007/s11060-017-2413-0.

195. Foray, C.; Valtorta, S.; Barca, C.; Winkeler, A.; Roll, W.; Müther, M.; Wagner, S.; Gardner, M.L.; Hermann, S.; Schäfers, M.; et al. Imaging temozolomide-induced changes in the myeloid glioma microenvironment. *Theranostics* **2021**, *11*, 2020–2033, doi:10.7150/thno.47269.

196. Sica, A.; Mantovani, A. Science in medicine Macrophage plasticity and polarization : in vivo veritas. *J. Clin. Invest.* **2012**, *122*, 787–795, doi:10.1172/JCI59643DS1.

197. Dan, H.; Liu, S.; Liu, J.; Liu, D.; Yin, F.; Wei, Z.; Wang, J.; Zhou, Y.; Jiang, L.; Ji, N.; et al.

RACK1 promotes cancer progression by increasing the M2/M1 macrophage ratio via the NF-κB pathway in oral squamous cell carcinoma. *Mol. Oncol.* **2020**, *14*, 795–807, doi:10.1002/1878-0261.12644.

198. Macciò, A.; Gramignano, G.; Cherchi, M.C.; Tanca, L.; Melis, L.; Madeddu, C. Role of M1-polarized tumor-associated macrophages in the prognosis of advanced ovarian cancer patients. *Sci. Rep.* **2020**, *10*, 6096, doi:10.1038/s41598-020-63276-1.

199. Zhang, B.; Guoqing Yao, I.; Yafei Zhang, I.; Juan Gao, I.; Bo Yang, I.; Zhiguo Rao, I.; Jianfei Gao, I.I. M2-Polarized tumor-associated macrophages are associated with poor prognoses resulting from accelerated lymphangiogenesis in lung adenocarcinoma. *Clin. (Sao Paulo)* **2011**, *66*, 1879–1886, doi:10.1590/S1807-59322011001100006.

200. Gjorgjevski, M.; Hannen, R.; Carl, B.; Li, Y.; Landmann, E.; Buchholz, M.; Bartsch, J.W.; Nimsky, C. Molecular profiling of the tumor microenvironment in glioblastoma patients : correlation of microglia / macrophage polarization state with metalloprotease expression profiles and survival. *Biosci. Rep.* **2019**, *39*, BSR20182361, doi:10.1042/BSR20182361.

201. Geisenberger, C.; Mock, A.; Warta, R.; Rapp, C.; Schwager, C.; Korshunov, A.; Nied, A.K.; Capper, D.; Brors, B.; Jungk, C.; et al. Molecular profiling of long-term survivors identifies a subgroup of glioblastoma characterized by chromosome 19/20 co-gain. *Acta Neuropathol.* **2015**, *130*, 419–434, doi:10.1007/s00401-015-1427-y.

202. Stessin, A.M.; Clausi, M.G.; Zhao, Z.; Lin, H.; Hou, W.; Jiang, Z.; Duong, T.Q.; Tsirka, S.E.; Ryu, S. Repolarized macrophages, induced by intermediate stereotactic dose radiotherapy and immune checkpoint blockade, contribute to long-term survival in glioma-bearing mice. *J. Neurooncol.* **2020**, *147*, 547–555, doi:10.1007/s11060-020-03459-y.

203. Kazantseva, M.; Eiholzer, R.A.; Mehta, S.; Taha, A.; Bowie, S.; Roth, I.; Zhou, J.; Joruiz, S.M.; Royds, J.A.; Hung, N.A.; et al. Elevation of the TP53 isoform Δ133p53β in glioblastomas: an alternative to mutant p53 in promoting tumor development. *J. Pathol.* **2018**, *246*, 77–88, doi:10.1002/path.5111.

204. De Boeck, A.; Ahn, B.Y.; D'Mello, C.; Lun, X.; Menon, S. V.; Alshehri, M.M.; Szulzewsky, F.; Shen, Y.; Khan, L.; Dang, N.H.; et al. Glioma-derived IL-33 orchestrates an inflammatory brain tumor microenvironment that accelerates glioma progression. *Nat. Commun.* **2020**, *11*, 4997, doi:10.1038/s41467-020-18569-4.

205. Chen, R.Q.; Liu, F.; Qiu, X.Y.; Chen, X.Q. The prognostic and therapeutic value of PD-L1 in glioma. *Front. Pharmacol.* **2019**, *9*, 1503, doi:10.3389/fphar.2018.01503.

206. Chen, P.-L.; Roh, W.; Reuben, A.; Cooper, Z.A.; Spencer, C.N.; Prieto, P.A.; Miller, J.P.; Bassett, R.L.; Gopalakrishnan, V.; Wani, K.; et al. Analysis of Immune Signatures in Longitudinal Tumor Samples Yields Insight into Biomarkers of Response and Mechanisms of Resistance to Immune Checkpoint Blockade. *Cancer Discov.* **2016**, *6*, 827–837, doi:10.1158/2159-8290.CD-15-1545.

207. Huang, J.; Liu, F.; Liu, Z.; Tang, H.; Wu, H.; Gong, Q.; Chen, J. Immune checkpoint in glioblastoma: Promising and challenging. *Front. Pharmacol.* **2017**, *8*, 242, doi:10.3389/fphar.2017.00242.

208. Zhang, P.; Su, D.M.; Liang, M.; Fu, J. Chemopreventive agents induce programmed death-1-ligand 1 (PD-L1) surface expression in breast cancer cells and promote PD-L1-mediated T cell apoptosis. *Mol. Immunol.* **2008**, *45*, 1470–1476, doi:10.1016/j.molimm.2007.08.013.

209. Katsuya, Y.; Horinouchi, H.; Asao, T.; Kitahara, S.; Goto, Y.; Kanda, S.; Fujiwara, Y.; Nokihara, H.; Yamamoto, N.; Watanabe, S. ichi; et al. Expression of programmed death 1 (PD-1) and its ligand (PD-L1) in thymic epithelial tumors: Impact on treatment efficacy and alteration in expression after chemotherapy. *Lung Cancer* **2016**, *99*, 4–10, doi:10.1016/j.lungcan.2016.05.007.

210. Leduc, C.; Adam, J.; Louvet, E.; Sourisseau, T.; Dorvault, N.; Bernard, M.; Maingot, E.;

Faivre, L.; Cassin-Kuo, M.-S.; Boissier, E.; et al. TPF induction chemotherapy increases PD-L1 expression in tumour cells and immune cells in head and neck squamous cell carcinoma. *ESMO Open* **2018**, *3*, e000257, doi:10.1136/esmoopen-2017-000257.

211. Lu, D.; Ni, Z.; Liu, X.; Feng, S.; Dong, X.; Shi, X.; Zhai, J.; Mai, S.; Jiang, J.; Wang, Z.; et al. Beyond T Cells: Understanding the Role of PD-1/PD-L1 in Tumor-Associated Macrophages. *J. Immunol. Res.* **2019**, *2019*, Article ID 1919082, doi:10.1155/2019/1919082.

212. Singhal, S.; Stadanlick, J.; Annunziata, M.J.; Rao, A.S.; Pratik, S.; Brien, S.O.; Moon, E.K.; Cantu, E.; Danet-, G.; Ra, H.; et al. Human tumor-associated monocytes/macrophages and their regulation of T cell responses in early-stage lung cancer. *Sci. Transl. Med.* **2019**, *11*, eaat1500, doi:10.1126/scitranslmed.aat1500.Human.

213. Han, B.; Dong, L.; Zhou, J.; Yang, Y.; Guo, J.; Xuan, Q.; Gao, K.; Xu, Z.; Lei, W.; Wang, J.; et al. The clinical implication of soluble PD-L1 (sPD-L1) in patients with breast cancer and its biological function in regulating the function of T lymphocyte. *Cancer Immunol. Immunother.* **2021**, *70*, 2893–2909, doi:10.1007/s00262-021-02898-4.

214. Liu, S.; Zhu, Y.; Zhang, C.; Meng, X.; Sun, B.; Zhang, G.; Fan, Y.; Kang, X. The Clinical Significance of Soluble Programmed Cell Death-Ligand 1 (sPD-L1) in Patients With Gliomas. *Front. Oncol.* **2020**, *10*, doi:10.3389/fonc.2020.00009.

215. Yuan, J.; Zhang, J.; Zhu, Y.; Li, N.; Tian, T.; Li, Y.; Li, Y.; Li, Z.; Lai, Y.; Gao, J.; et al. Programmed death-ligand-1 expression in advanced gastric cancer detected with RNA in situ hybridization and its clinical significance. *Oncotarget* **2016**, *7*, 39671–39679, doi:10.18632/oncotarget.9381.

216. Duffy, M.J.; Mullooly, M.; O'Donovan, N.; Sukor, S.; Crown, J.; Pierce, A.; McGowan, P.M. The ADAMs family of proteases: new biomarkers and therapeutic targets for cancer? *Clin. Proteomics* **2011**, *8*, 9, doi:10.1186/1559-0275-8-9.

217. Young, D.; Das, N.; Anowai, A.; Dufour, A. Matrix Metalloproteases as Influencers of the Cells' Social Media. *Int. J. Mol. Sci.* **2019**, *20*, 3847, doi:10.3390/ijms20163847.

218. Li, Y.; Guo, S.; Zhao, K.; Conrad, C.; Driescher, C.; Rothbart, V.; Schlomann, U.; Guerreiro, H.; Bopp, M.H.; König, A.; et al. ADAM8 affects glioblastoma progression by regulating osteopontin-mediated angiogenesis. *Biol. Chem.* **2021**, *402*, 195–206, doi:10.1515/hsz-2020-0184.

219. Zhang, W.; Wan, M.; Ma, L.; Liu, X.; He, J. Protective effects of ADAM8 against cisplatin-mediated apoptosis in non-small-cell lung cancer. *Cell Biol. Int.* **2013**, *37*, 47–53, doi:10.1002/cbin.10011.

220. Smith, T.M.; Tharakan, A.; Martin, R.K. Targeting ADAM10 in Cancer and Autoimmunity. *Front. Immunol.* **2020**, *11*, 499, doi:10.3389/fimmu.2020.00499.

221. Atapattu, L.; Saha, N.; Chheang, C.; Eissman, M.F.; Xu, K.; Vail, M.E.; Hii, L.; Llerena, C.; Liu, Z.; Horvay, K.; et al. An activated form of ADAM10 is tumor selective and regulates cancer stem-like cells and tumor growth. *J. Exp. Med.* **2016**, *213*, 1741–1757, doi:10.1084/jem.20151095.

222. Wolpert, F.; Tritschler, I.; Steinle, A.; Weller, M.; Eisele, G. A disintegrin and metalloproteinases 10 and 17 modulate the immunogenicity of glioblastoma-initiating cells. *Neuro. Oncol.* **2014**, *16*, 382–391, doi:10.1093/neuonc/not232.

223. Xue, Q.; Cao, L.; Chen, X.-Y.; Zhao, J.; Gao, L.; Li, S.-Z.; Fei, Z. High expression of MMP9 in glioma affects cell proliferation and is associated with patient survival rates. *Oncol. Lett.* **2017**, *13*, 1325–1330, doi:10.3892/ol.2017.5567.

224. Huang, H. Matrix Metalloproteinase-9 (MMP-9) as a Cancer Biomarker and MMP-9 Biosensors: Recent Advances. *Sensors* **2018**, *18*, 3249, doi:10.3390/s18103249.

225. Juric, V.; O'Sullivan, C.; Stefanutti, E.; Kovalenko, M.; Greenstein, A.; Barry-Hamilton, V.; Mikaelian, I.; Degenhardt, J.; Yue, P.; Smith, V.; et al. MMP-9 inhibition promotes anti-tumor immunity through disruption of biochemical and physical barriers to T-cell trafficking to tumors. *PLoS One* **2018**, *13*, e0207255, doi:10.1371/journal.pone.0207255.

226. Rajavashisth, T.B.; Xu, X.-P.; Jovinge, S.; Meisel, S.; Xu, X.-O.; Chai, N.-N.; Fishbein, M.C.; Kaul, S.; Cercek, B.; Sharifi, B.; et al. Membrane Type 1 Matrix Metalloproteinase Expression in Human Atherosclerotic Plaques. *Circulation* **1999**, *99*, 3103–3109, doi:10.1161/01.cir.99.24.3103.

227. Faisal Khan, K.M.; Howe, L.R.; Falcone, D.J. Extracellular matrix-induced cyclooxygenase-2 regulates macrophage proteinase expression. *J. Biol. Chem.* **2004**, *279*, 22039–22046, doi:10.1074/jbc.M312735200.

228. Matías-Román, S.; Gálvez, B.G.; Genís, L.; Yáñez-Mó, M.; De La Rosa, G.; Sánchez-Mateos, P.; Sánchez-Madrid, F.; Arroyo, A.G. Membrane type 1-matrix metalloproteinase is involved in migration of human monocytes and is regulated through their interaction with fibronectin or endothelium. *Blood* **2005**, *105*, 3956–3964, doi:10.1182/blood-2004-06-2382.

229. Sithu, S.D.; English, W.R.; Olson, P.; Krubasik, D.; Baker, A.H.; Murphy, G.; D'Souza, S.E. Membrane-type 1-matrix metalloproteinase regulates intracellular adhesion molecule-1 (ICAM-1)-mediated monocyte transmigration. *J. Biol. Chem.* **2007**, *282*, 25010–25019, doi:10.1074/jbc.M611273200.

230. Newby, A.C. Metalloproteinase expression in monocytes and macrophages and its relationship to atherosclerotic plaque instability. *Arterioscler. Thromb. Vasc. Biol.* **2008**, *28*, 2108–2114, doi:10.1161/ATVBAHA.108.173898.

231. Orrego, E.; Castaneda, C.A.; Castillo, M.; Bernabe, L.A.; Casavilca, S.; Chakravarti, A.; Meng, W.; Garcia-Corrochano, P.; Villa-Robles, M.R.; Zevallos, R.; et al. Distribution of tumor-infiltrating immune cells in glioblastoma. *CNS Oncol.* **2018**, *7*, CNS21, doi:10.2217/cns-2017-0037.

232. Sayour, E.J.; McLendon, P.; McLendon, R.; De Leon, G.; Reynolds, R.; Kresak, J.; Sampson, J.H.; Mitchell, D.A. Increased proportion of FoxP3+ regulatory T cells in tumor infiltrating lymphocytes is associated with tumor recurrence and reduced survival in patients with glioblastoma. *Cancer Immunol. Immunother.* **2015**, *64*, 419–427, doi:10.1007/s00262-014-1651-7.

233. Yang, I.; Tihan, T.; Han, S.J.; Wrensch, M.R.; Wiencke, J.; Sughrue, M.E.; Parsa, A.T. CD8+ T-cell infiltrate in newly diagnosed glioblastoma is associated with long-term survival. *J. Clin. Neurosci.* **2010**, *17*, 1381–1385, doi:10.1016/j.jocn.2010.03.031.

234. Kmiecik, J.; Poli, A.; Brons, N.H.C.; Waha, A.; Eide, G.E.; Enger, P.Ø.; Zimmer, J.; Chekenya, M. Elevated CD3+ and CD8+ tumor-infiltrating immune cells correlate with prolonged survival in glioblastoma patients despite integrated immunosuppressive mechanisms in the tumor microenvironment and at the systemic level. *J. Neuroimmunol.* **2013**, *264*, 71–83, doi:10.1016/j.jneuroim.2013.08.013.

235. Lohr, J.; Ratliff, T.; Huppertz, A.; Ge, Y.; Dictus, C.; Ahmadi, R.; Grau, S.; Hiraoka, N.; Eckstein, V.; Ecker, R.C.; et al. Effector T-cell infiltration positively impacts survival of glioblastoma patients and is impaired by tumor-derived TGF-β. *Clin. Cancer Res.* **2011**, *17*, 4296–4308, doi:10.1158/1078-0432.CCR-10-2557.

236. Zhu, J. T helper cell differentiation, heterogeneity, and plasticity. *Cold Spring Harb. Perspect. Biol.* **2018**, *10*, a030338, doi:10.1101/cshperspect.a030338.

237. Kumar, R.; Kamdar, D.; Madden, L.; Hills, C.; Crooks, D.; O'Brien, D.; Greenman, J. Th1/Th2 cytokine imbalance in meningioma, anaplastic astrocytoma and glioblastoma multiforme patients. *Oncol. Rep.* **2006**, *15*, 1513–1516, doi:10.3892/or.15.6.1513.

238. Mohme, M.; Neidert, M.C. Tumor-Specific T Cell Activation in Malignant Brain Tumors. *Front. Immunol.* **2020**, *11*, 205, doi:10.3389/fimmu.2020.00205.

239. Ueda, R.; Kohanbash, G.; Sasaki, K.; Fujita, M.; Zhu, X.; Kastenhuber, E.R.; McDonald, H.A.; Potter, D.M.; Hamilton, R.L.; Lotze, M.T.; et al. Dicer-regulated microRNAs 222 and 339 promote resistance of cancer cells to cytotoxic T-lymphocytes by down-regulation of ICAM-1. *Proc. Natl. Acad. Sci.* **2009**, *106*, 10746–10751, doi:10.1073/pnas.0811817106.

240. Beck, R.J.; Slagter, M.; Beltman, J.B. Contact-dependent killing by cytotoxic T lymphocytes

is insufficient for EL4 tumor regression in vivo. *Cancer Res.* **2019**, *79*, 3406–3416, doi:10.1158/0008-5472.CAN-18-3147.

241. Grauer, O.M.; Nierkens, S.; Bennink, E.; Toonen, L.W.J.; Boon, L.; Wesseling, P.; Sutmuller, R.P.M.; Adema, G.J. CD4+FoxP3+ regulatory T cells gradually accumulate in gliomas during tumor growth and efficiently suppress antiglioma immune responsesin vivo. *Int. J. Cancer* **2007**, *121*, 95–105, doi:10.1002/ijc.22607.

242. Chen, J.; Ganguly, A.; Mucsi, A.D.; Meng, J.; Yan, J.; Detampel, P.; Munro, F.; Zhang, Z.; Wu, M.; Hari, A.; et al. Strong adhesion by regulatory T cells induces dendritic cell cytoskeletal polarization and contact-dependent lethargy. *J. Exp. Med.* **2017**, *214*, 327–338, doi:10.1084/jem.20160620.

243. Kim, C.H. FOXP3 and Its Role in the Immune System. In *Advances in Experimental Medicine and Biology*; 2009; Vol. 665, pp. 17–29 ISBN 9781441915986.

244. Dominguez-Valentin, M.; Navarro, A.G.; Rahman, A.M.; Kumar, S.; Retière, C.; Ulvestad, E.; Kristensen, V.; Lund-Johansen, M.; Lie, B.A.; Enger, P.Ø.; et al. Identification of a natural killer cell receptor allele that prolongs survival of cytomegalovirus-positive glioblastoma patients. *Cancer Res.* **2016**, *76*, 5326–5336, doi:10.1158/0008-5472.CAN-16-1162.

245. Huang, B.; Zhang, H.; Gu, L.; Ye, B.; Jian, Z.; Stary, C.; Xiong, X. Advances in Immunotherapy for Glioblastoma Multiforme. *J. Immunol. Res.* **2017**, *2017*, 3597613, doi:10.1155/2017/3597613.

246. Wu, S.; Calero-Pérez, P.; Villamañan, L.; Arias-Ramos, N.; Pumarola, M.; Ortega-Martorell, S.; Julià-Sapé, M.; Arús, C.; Candiota, A.P. Anti-tumour immune response in GL261 glioblastoma generated by Temozolomide Immune-Enhancing Metronomic Schedule monitored with MRSI-based nosological images. *NMR Biomed.* **2020**, *33*, e4229, doi:10.1002/nbm.4229.

247. Paijens, S.T.; Vledder, A.; de Bruyn, M.; Nijman, H.W. Tumor-infiltrating lymphocytes in the immunotherapy era. *Cell. Mol. Immunol.* **2021**, *18*, 842–859, doi:10.1038/s41423-020-00565-9.

248. Ahn, S.; Chung, Y.R.; Seo, A.N.; Kim, M.; Woo, J.W.; Park, S.Y. Changes and prognostic values of tumor-infiltrating lymphocyte subsets after primary systemic therapy in breast cancer. *PLoS One* **2020**, *15*, e0233037, doi:10.1371/journal.pone.0233037.

249. Melssen, M.; Slingluff, C.L. Vaccines targeting helper T cells for cancer immunotherapy. *Curr. Opin. Immunol.* **2017**, *47*, 85–92, doi:10.1016/j.coi.2017.07.004.

250. Mahmoud, S.M.A.; Paish, E.C.; Powe, D.G.; Macmillan, R.D.; Grainge, M.J.; Lee, A.H.S.; Ellis, I.O.; Green, A.R. Tumor-infiltrating CD8+ lymphocytes predict clinical outcome in breast cancer. *J. Clin. Oncol.* **2011**, *29*, 1949–1955, doi:10.1200/JCO.2010.30.5037.

251. Orhan, A.; Vogelsang, R.P.; Andersen, M.B.; Madsen, M.T.; Hölmich, E.R.; Raskov, H.; Gögenur, I. The prognostic value of tumour-infiltrating lymphocytes in pancreatic cancer: a systematic review and meta-analysis. *Eur. J. Cancer* **2020**, *132*, 71–84, doi:10.1016/j.ejca.2020.03.013.

252. Sato, E.; Olson, S.H.; Ahn, J.; Bundy, B.; Nishikawa, H.; Qian, F.; Jungbluth, A.A.; Frosina, D.; Gnjatic, S.; Ambrosone, C.; et al. Intraepithelial CD8+ tumor-infiltrating lymphocytes and a high CD8+/regulatory T cell ratio are associated with favorable prognosis in ovarian cancer. *Proc. Natl. Acad. Sci.* **2005**, *102*, 18538–18543, doi:10.1073/pnas.0509182102.

253. Pagès, F.; Kirilovsky, A.; Mlecnik, B.; Asslaber, M.; Tosolini, M.; Bindea, G.; Lagorce, C.; Wind, P.; Marliot, F.; Bruneval, P.; et al. In situ cytotoxic and memory T cells predict outcome in patients with early-stage colorectal cancer. *J. Clin. Oncol.* **2009**, *27*, 5944–5951, doi:10.1200/JCO.2008.19.6147.

254. Ding, W.; Xu, X.; Qian, Y.; Xue, W.; Wang, Y.; Du, J.; Jin, L.; Tan, Y. Prognostic value of tumor-infiltrating lymphocytes in hepatocellular carcinoma. *Medicine (Baltimore).* **2018**, *97*, e13301, doi:10.1097/MD.0000000000013301.

255. Kim, A.R.; Choi, K.S.; Kim, M.S.; Kim, K.M.; Kang, H.; Kim, S.; Chowdhury, T.; Yu, H.J.; Lee,

C.E.; Lee, J.H.; et al. Absolute quantification of tumor-infiltrating immune cells in high-grade glioma identifies prognostic and radiomics values. *Cancer Immunol. Immunother.* **2021**, *70*, 1995–2008, doi:10.1007/s00262-020-02836-w.

256. Yu, J.S.; Lee, P.K.; Ehtesham, M.; Samoto, K.; Black, K.L.; Wheeler, C.J. Intratumoral T cell subset ratios and Fas ligand expression on brain tumor endothelium. *J. Neurooncol.* **2003**, *64*, 55–61, doi:10.1158/0008-5472.

257. Dieci, M. V.; Criscitiello, C.; Goubar, A.; Viale, G.; Conte, P.; Guarneri, V.; Ficarra, G.; Mathieu, M.C.; Delaloge, S.; Curigliano, G.; et al. Prognostic value of tumor-infiltrating lymphocytes on residual disease after primary chemotherapy for triple-negative breast cancer: A retrospective multicenter study. *Ann. Oncol.* **2014**, *25*, 611–618, doi:10.1093/annonc/mdt556.

258. Dai, B.; Qi, N.; Li, J.; Zhang, G. Temozolomide combined with PD-1 Antibody therapy for mouse orthotopic glioma model. *Biochem. Biophys. Res. Commun.* **2018**, *501*, 871–876, doi:10.1016/j.bbrc.2018.05.064.

259. D'Acquisto, F.; Crompton, T. CD3+CD4-CD8- (double negative) T cells: Saviours or villains of the immune response? *Biochem. Pharmacol.* **2011**, *82*, 333–340, doi:10.1016/j.bcp.2011.05.019.

260. Molgora, M.; Cortez, V.S.; Colonna, M. Killing the Invaders: NK Cell Impact in Tumors and Anti-Tumor Therapy. *Cancers (Basel).* **2021**, *13*, 595, doi:10.3390/cancers13040595.

261. Karachi, A.; Yang, C.; Dastmalchi, F.; Sayour, E.J.; Huang, J.; Azari, H.; Long, Y.; Flores, C.; Mitchell, D.A.; Rahman, M. Modulation of temozolomide dose differentially affects T-cell response to immune checkpoint inhibition. *Neuro. Oncol.* **2019**, *21*, 730–741, doi:10.1093/neuonc/noz015.

262. Sanchez, V.E.; Lynes, J.P.; Walbridge, S.; Wang, X.; Edwards, N.A.; Nwankwo, A.K.; Sur, H.P.; Dominah, G.A.; Obungu, A.; Adamstein, N.; et al. GL261 luciferase-expressing cells elicit an anti-tumor immune response: an evaluation of murine glioma models. *Sci. Rep.* **2020**, *10*, 11003, doi:10.1038/s41598-020-67411-w.

263. Birzu, C.; French, P.; Caccese, M.; Cerretti, G.; Idbaih, A.; Zagonel, V.; Lombardi, G. Recurrent Glioblastoma: From Molecular Landscape to New Treatment Perspectives. *Cancers (Basel).* **2020**, *13*, 47, doi:10.3390/cancers13010047.

264. Goel, N.J.; Bird, C.E.; Hicks, W.H.; Abdullah, K.G. Economic implications of the modern treatment paradigm of glioblastoma: an analysis of global cost estimates and their utility for cost assessment. *J. Med. Econ.* **2021**, *24*, 1018–1024, doi:10.1080/13696998.2021.1964775.

265. Stupp, R.; Mason, W.P.; van den Bent, M.J.; Weller, M.; Fisher, B.; Taphoorn, M.J.B.; Belanger, K.; Brandes, A.A.; Marosi, C.; Bogdahn, U.; et al. Radiotherapy plus Concomitant and Adjuvant Temozolomide for Glioblastoma. *N. Engl. J. Med.* **2005**, *352*, 987–996, doi:10.1056/NEJMoa043330.

266. Zikou, A.; Sioka, C.; Alexiou, G.A.; Fotopoulos, A.; Voulgaris, S.; Argyropoulou, M.I. Radiation Necrosis, Pseudoprogression, Pseudoresponse, and Tumor Recurrence: Imaging Challenges for the Evaluation of Treated Gliomas. *Contrast Media Mol. Imaging* **2018**, *2018*, 6828396, doi:10.1155/2018/6828396.

267. Rashidian, M.; LaFleur, M.W.; Verschoor, V.L.; Dongre, A.; Zhang, Y.; Nguyen, T.H.; Kolifrath, S.; Aref, A.R.; Lau, C.J.; Paweletz, C.P.; et al. Immuno-PET identifies the myeloid compartment as a key contributor to the outcome of the antitumor response under PD-1 blockade. *Proc. Natl. Acad. Sci. U. S. A.* **2019**, *116*, 16971–16980, doi:10.1073/pnas.1905005116.

268. Jalbert, L.E.; Neill, E.; Phillips, J.J.; Lupo, J.M.; Olson, M.P.; Molinaro, A.M.; Berger, M.S.; Chang, S.M.; Nelson, S.J. Magnetic resonance analysis of malignant transformation in recurrent glioma. *Neuro. Oncol.* **2016**, *18*, 1169–1179, doi:10.1093/neuonc/now008.

269. Li, Y.; Liu, X.; Wei, F.; Sima, D.M.; Van Cauter, S.; Himmelreich, U.; Pi, Y.; Hu, G.; Yao, Y.; Van Huffel, S. An advanced MRI and MRSI data fusion scheme for enhancing

unsupervised brain tumor differentiation. *Comput. Biol. Med.* **2017**, *81*, 121–129, doi:10.1016/j.compbiomed.2016.12.017.

270. Núñez, L.M.; Romero, E.; Julià-Sapé, M.; Ledesma-Carbayo, M.J.; Santos, A.; Arús, C.; Candiota, A.P.; Vellido, A. Unraveling response to temozolomide in preclinical GL261 glioblastoma with MRI/MRSI using radiomics and signal source extraction. *Sci. Rep.* **2020**, *10*, 19699, doi:10.1038/s41598-020-76686-y.

271. Ly, K.I.; Vakulenko-Lagun, B.; Emblem, K.E.; Ou, Y.; Da, X.; Betensky, R.A.; Kalpathy-Cramer, J.; Duda, D.G.; Jain, R.K.; Chi, A.S.; et al. Probing tumor microenvironment in patients with newly diagnosed glioblastoma during chemoradiation and adjuvant temozolomide with functional MRI. *Sci. Rep.* **2018**, *8*, 17062, doi:10.1038/s41598-018-34820-x.

272. Okada, H.; Weller, M.; Huang, R.; Finocchiaro, G.; Gilbert, M.R.; Wick, W.; Ellingson, B.M.; Hashimoto, N.; Pollack, I.F.; Brandes, A.A.; et al. Immunotherapy response assessment in neuro-oncology: a report of the RANO working group. *Lancet Oncol.* **2015**, *16*, e534–e542, doi:10.1016/S1470-2045(15)00088-1.

273. Kleijn, A.; van den Bossche, W.; Haefner, E.S.; Belcaid, Z.; Burghoorn-Maas, C.; Kloezeman, J.J.; Pas, S.D.; Leenstra, S.; Debets, R.; de Vrij, J.; et al. The Sequence of Delta24-RGD and TMZ Administration in Malignant Glioma Affects the Role of CD8+ T Cell Anti-tumor Activity. *Mol. Ther. - Oncolytics* **2017**, *5*, 11–19, doi:10.1016/j.omto.2017.02.002.

274. Günther, W.; Pawlak, E.; Damasceno, R.; Arnold, H.; Terzis, A.J. Temozolomide induces apoptosis and senescence in glioma cells cultured as multicellular spheroids. *Br. J. Cancer* **2003**, *88*, 463–469, doi:10.1038/sj.bjc.6600711.

275. Colangelo, T.; Polcaro, G.; Ziccardi, P.; Muccillo, L.; Galgani, M.; Pucci, B.; Rita Milone, M.; Budillon, A.; Santopaolo, M.; Mazzoccoli, G.; et al. The miR-27a-calreticulin axis affects drug-induced immunogenic cell death in human colorectal cancer cells. *Cell Death Dis.* **2016**, *7*, e2108, doi:10.1038/cddis.2016.29.

276. Dichmann, S.; Idzko, M.; Zimpfer, U.; Hofmann, C.; Ferrari, D.; Luttmann, W.; Virchow, C.; Di Virgilio, F.; Norgauer, J. Adenosine triphosphate-induced oxygen radical production and CD11b up- regulation: Ca++ mobilization and actin reorganization in human eosinophils. *Blood* **2000**, *95*, 973–978, doi:10.1182/blood.v95.3.973.003k47_973_978.

277. Lotze, M.T.; Tracey, K.J. High-mobility group box 1 protein (HMGB1): Nuclear weapon in the immune arsenal. *Nat. Rev. Immunol.* **2005**, *5*, 331–342, doi:10.1038/nri1594.

278. Vidyarthi, A.; Agnihotri, T.; Khan, N.; Singh, S.; Tewari, M.K.; Radotra, B.D.; Chatterjee, D.; Agrewala, J.N. Predominance of M2 macrophages in gliomas leads to the suppression of local and systemic immunity. *Cancer Immunol. Immunother.* **2019**, *68*, 1995–2004, doi:10.1007/s00262-019-02423-8.

279. Zeiner, P.S.; Preusse, C.; Golebiewska, A.; Zinke, J.; Iriondo, A.; Muller, A.; Kaoma, T.; Filipski, K.; Müller-Eschner, M.; Bernatz, S.; et al. Distribution and prognostic impact of microglia/macrophage subpopulations in gliomas. *Brain Pathol.* **2019**, *29*, 513–529, doi:10.1111/bpa.12690.

280. Bloch, O.; Crane, C.A.; Kaur, R.; Safaee, M.; Rutkowski, M.J.; Parsa, A.T. Gliomas promote immunosuppression through induction of B7-H1 expression in tumor-associated macrophages. *Clin Cancer Res* **2013**, *19*, 3165–3175, doi:10.1158/1078-0432.CCR-12-3314.

281. Khalsa, J.K.; Cheng, N.; Keegan, J.; Chaudry, A.; Driver, J.; Bi, W.L.; Lederer, J.; Shah, K. Immune phenotyping of diverse syngeneic murine brain tumors identifies immunologically distinct types. *Nat. Commun.* **2020**, *11*, 3912, doi:10.1038/s41467-020-17704-5.

282. Haus, E.; Lakatua, D.J.; Swoyer, J.; Sackett-Lundeen, L. Chronobiology in hematology and immunology. *Am. J. Anat.* **1983**, *168*, 467–517, doi:10.1002/aja.1001680406.

IDEXX BioAnalytics

IDEXX

FINAL REPORT OF LABORATORY EXAMINATION
Mörikestr. 28/3, D 71636 Ludwigsburg, Germany
+49 (0)7141 64 83585
idexxbioanalytics-europe@idexx.com   www.idexxbioanalytics.eu/

Received: 5/3/2019
Completed: 5/8/2019

Submitted By

Ana Paula Candiota
Universitat Autonoma de Barcelona
Edifici cs campus UAB
Cerdanyola del Vallès
Barcelona 08193 Spain

Phone: 00935814126
Email: AnaPaula.Candiota@uab.cat; idexx-radil-results@idexx.com

Specimen
Description
Species: mouse
Description: cells
Number of Specimens/Animals: 1

ID	Client ID	Add l ID
1	GL261-1	GL261

Services/Tests Performed: IMPACT II PCR Profile (1); CellCheck - mouse (mouse STR profile and interspeciescontamination test) (1)

PCR evaluation for: Ectromelia, EDIM, LCMV, LDEV, MAV1, MAV2, mCMV, MHV, MNV, MPV, MVM, *Mycoplasma pulmonis*, *Mycoplasma* sp., Polyoma, PVM, REO3, Sendai, TMEV

Genetic evaluation for: Interspecies Contamination Test, Mouse STR Profile

Summary: Cell Check results are provided in the data results section for each

sample.All other test results were negative. Please see the report for details.

If you have questions, please call +49 (0)7141 64 83585

PCR EVALUATION

cells	1
Ectromelia	-
EDIM	-
LCMV	-
LDEV	-
MAV1	-
MAV2	-
mCMV	-
MHV	-
MNV	-
Mycoplasma pulmonis	-
Mycoplasma sp.	-
MVM	-
MPV	-
Polyoma	-
PVM	-
REO3	-
Sendai	-
TMEV	-

Legend: + = positive - = negative id:id = pooled sample range id+id+id = non-range pooled sample NT or blank = no test performed wps =weak positive XX = Testing in progress

CELL CHECK

Species-specific PCR Evaluation

Species	1
mouse	+
rat	-
human	-
Chinese hamster	-
African green monkey	-

Marker Analysis

Marker Name	1	
	SampleResults	GL261 (IBA profile)
MCA-4-2	20.3, 21.3	20.3, 21.3
MCA-5-5	17	17
MCA-6-4	18	18
MCA-6-7	14	14
MCA-9-2	18, 19	18, 19

Marker Name	1	
	SampleResults	GL261 (IBA profile)
MCA-12-1	17	17
MCA-15-3	22.3, 24.3	22.3, 24.3
MCA-18-3	16	16
MCA-X-1	29	29

Sample ID	Remarks
1	The sample was confirmed to be of mouse origin and no mammalian interspecies contamination was detected. Agenetic profile was generated for the sample by using a panel of STR markers for genotyping. The sample profile matches identically to the genetic profile established for this cell line.

ANNEX II
SUPERVISION OF LABORATORY ANIMALS

Procedure: CEEAH-3665

MONITORING PARAMETERS (scale: 0-3 points):

<u>Wight loss</u>

0) Normal weight
1) Less than 10% loss
2) Between 10 and 15% loss
3) Consistent or rapid, exceeding 20% loss maintained for 72 h.

<u>Physical appearance</u>

0) Normal
1) More than 10% dehydration, body condition 2 (BC; see further for details), skin tenting
2) Erected hair. Cyanosis
3) Hunched back. Loss of muscle mass

<u>Clinical signs</u>

0) None
1) Circular motion of the animal
2) Mucous secretions and/or bleeding form any orifice. Detectable hypertrophy of organs (lymph nodes, spleen, liver).
3) Shortness of breath (particularly if accompanied by nasal discharge and/or cyanosis). Cachexia

<u>Changes in behavior</u>

0) No
1) Inability to move normally
2) Inability to get to the food/ drink, isolation from the rest of the animals in the cage
3) Unconsciousness or comatose. Lack of response (dying)

<u>Wounds</u>

0) No
1) Scratches
2) Nonhealing wounds. Infection at surgical site
3) Ulcerating, festering wounds. Ulcerating necrotic tumours

The animal condition according to the parameters and overall score:

a) 0 points: Healthy animal
b) 1-2 points: Minor signs, follow stablished protocol
c) 3-11 points: Daily supervision of the animal. Analgesics* or euthanization of the animal**
d) 12-30 points: euthanasia**

*Analgesic: Meloxicam (subcutaneously: 1 mg/kg)

**The *Servei d'Estabulari* veterinary staff will inform a group member as soon as possible to consider halting of the protocol/ experiment.

NOTE: As the tumour grows, it affects in the motor function of the brain. Animals may suffer from: paresis, decreased strength, plegia, paralysis. In these cases, food and water (i.e., hydrogel or water-soaked food) should be placed inside the cage to facilitate access by the animal.

Body Condition (BC):

BC 1

Mouse is emaciated.
- *Skeletal structure extremely prominent; little or no flesh cover.*
- *Vertebrae distinctly segmented.*

BC 2

Mouse is under conditioned.
- *Segmentation of vertebral column evident.*
- *Dorsal pelvic bones are readily palpable.*

BC 3

Mouse is well-conditioned.
- *Vertebrae and dorsal pelvis not prominent; palpable with slight pressure.*

BC 4

Mouse is over conditioned.
- *Spine is a continuous column.*
- *Vertebrae palpable only with firm pressure.*

BC 5

Mouse is obese.
- *Mouse is smooth and bulky.*
- *Bone structure disappears under flesh and subcutaneous fat.*